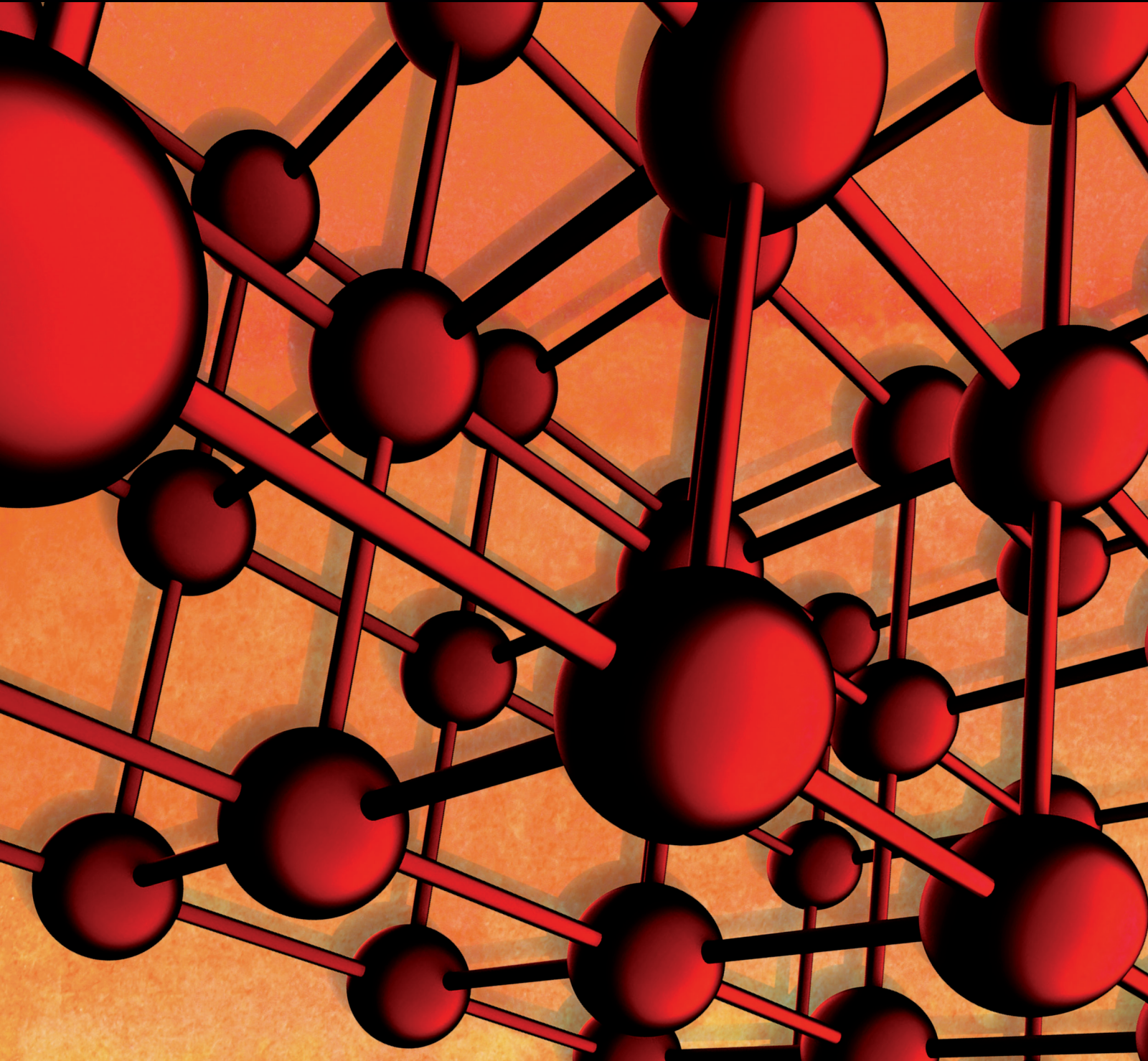


Advances in Materials Science and Engineering

Green Composite Materials

Guest Editors: Hao Wang, Peter Schubel, Xiaosu Yi, Jin Zhu, Chad Ulven, and Yiping Qiu





Green Composite Materials

Advances in Materials Science and Engineering

Green Composite Materials

Guest Editors: Hao Wang, Peter Schubel, Xiaosu Yi, Jin Zhu,
Chad Ulven, and Yiping Qiu



Copyright © 2015 Hindawi Publishing Corporation. All rights reserved.

This is a special issue published in “Advances in Materials Science and Engineering.” All articles are open access articles distributed under the Creative Commons Attribution License, which permits unrestricted use, distribution, and reproduction in any medium, provided the original work is properly cited.

Editorial Board

- Dimitrios G. Aggelis, Belgium
Jarir Aktaa, Germany
K. G. Anthymidis, Greece
Amit Bandyopadhyay, USA
Arun Bansil, USA
Massimiliano Barletta, Italy
Jozef Bednarcik, Germany
Avi Bendavid, Australia
Jamal Berakdar, Germany
Giovanni Berselli, Italy
Alessandra Bianco, Italy
Susmita Bose, USA
H.-Günter Brokmeier, Germany
Steve Bull, UK
Peter Chang, Canada
Daolun Chen, Canada
Gabriel Cuello, France
Narendra B. Dahotre, USA
João P. Davim, Portugal
Francesco Delogu, Italy
Seshu B. Desu, USA
Yong Ding, USA
Aziz Dinia, France
Kaveh Edalati, Japan
Gilbert Fantozzi, France
Massimo Fresta, Italy
E. Freysz, France
Sergi Gallego, Spain
Santiago Garcia-Granda, Spain
Filippo Giannazzo, Italy
Daniel Guay, Canada
Hiroki Habazaki, Japan
Joke Hadermann, Belgium
Satoshi Horikoshi, Japan
Rui Huang, USA
Jacques Huot, Canada
- Michele Iafisco, Italy
Katsuyuki Kida, Japan
Jae-Ho Kim, Korea
Akihiko Kimura, Japan
Takayuki Kitamura, Japan
Hongchao Kou, China
Prashant Kumta, USA
Luciano Lamberti, Italy
Heinrich Lang, Germany
Pavel Lejcek, Czech Republic
Cristina Leonelli, Italy
Markku Leskela, Finland
Ying Li, USA
Wei Liu, France
Yunqi Liu, China
Meilin Liu, Georgia
Ying Liu, USA
Jun Liu, China
Fernando Lusquiños, Spain
Peter Majewski, Australia
Philippe Miele, France
Hossein Moayed, Malaysia
Paul Munroe, Australia
Rufino M. Navarro, Spain
Luigi Nicolais, Italy
Hiroshi Noguchi, Japan
Chérif Nouar, France
José L. Ocaña, Spain
Tsutomu Ohzuku, Japan
Olanrewaju Ojo, Canada
Xiaoqing Pan, USA
Anna Paradowska, Australia
Gianluca Percoco, Italy
Jean-Francois Pierson, France
Simon C. Potter, Canada
Manijeh Razeghi, USA
- Anna Richelli, Italy
Antonio Riveiro, Spain
Pascal Roussel, France
Timo Sajavaara, Finland
Antti Salminen, Finland
Fawzy H. Samuel, Canada
Carlo Santulli, Italy
Franz-Josef Schmitt, Germany
Jainagesh A. Sekhar, USA
Fridon Shubitidze, USA
Charles C. Sorrell, Australia
Costas M. Soukoulis, USA
Sam-Shajing Sun, USA
Kohji Tashiro, Japan
Somchai Thongtem, Thailand
Achim Trampert, Germany
Filip Tuomisto, Finland
Stuart Turner, Belgium
Krystyn Van Vliet, USA
Rui Vilar, Portugal
Holger von Wenckstern, Germany
Rui Wang, China
Qiang Wang, China
Rong Wang, USA
Lu Wei, China
Jörg M. K. Wiezorek, USA
Wei Wu, USA
Hemmige S. Yathirajan, India
Wenbin Yi, China
Belal F. Yousif, Australia
Jinghuai Zhang, China
Li Zhang, China
Ming-Xing Zhang, Australia
Wei Zhou, China

Contents

Green Composite Materials, Hao Wang, Peter Schubel, Xiaosu Yi, Jin Zhu, Chad Ulven, and Yiping Qiu
Volume 2015, Article ID 487416, 1 page

Impacts of Limestone Particle Size on the Performance of Flexible Wood Fiber Composite Floor,
Hongcheng He, Jinling Nie, and Jing Wang
Volume 2015, Article ID 804729, 5 pages

Impact of Layer-by-Layer Self-Assembly Clay-Based Nanocoating on Flame Retardant Properties of Sisal Fiber Cellulose Microcrystals, Chun Wei, Sihua Zeng, Yuyuan Tan, Wu Wang, Jian Lv, and Hongxia Liu
Volume 2015, Article ID 691290, 7 pages

Development of a Zero-Cement Binder Using Slag, Fly Ash, and Rice Husk Ash with Chemical Activator, M. R. Karim, M. F. M. Zain, M. Jamil, and F. C. Lai
Volume 2015, Article ID 247065, 14 pages

Removal of Organic Dyes by Nanostructure ZnO-Bamboo Charcoal Composites with Photocatalysis Function, Xinliang Yu, Aimiao Qin, Lei Liao, Rui Du, Ning Tian, Song Huang, and Chun Wei
Volume 2015, Article ID 252951, 6 pages

Effect of Three Bioenzymes on Compaction, Consistency Limits, and Strength Characteristics of a Sedimentary Residual Soil, Tanveer Ahmed Khan and Mohd Raihan Taha
Volume 2015, Article ID 798965, 9 pages

Effect of Fiber Waviness on Tensile Strength of a Flax-Sliver-Reinforced Composite Material, Taweesak Piyatuchsananon, Akira Furuya, Baosheng Ren, and Koichi Goda
Volume 2015, Article ID 345398, 8 pages

Ground Hemp Fibers as Filler/Reinforcement for Thermoplastic Biocomposites, Amir Etaati, Selvan Pather, Moloud Rahman, and Hao Wang
Volume 2015, Article ID 513590, 11 pages

Role of Metals Content in Spinach in Enhancing the Conductivity and Optical Band Gap of Chitosan Films, Irwana Nainggolan, Devi Shantini, Tulus Ikhsan Nasution, and Mohd Nazree Derman
Volume 2015, Article ID 702815, 8 pages

Composites Based Green Poly(L-Lactic Acid) and Dioctyl Phthalate: Preparation and Performance, Yan-Hua Cai, Li-Sha Zhao, and Yan-Hua Zhang
Volume 2015, Article ID 289725, 5 pages

Preparation of PAN Spinning Solution with Fine Dispersion of Cellulose Microparticles, Jee-Woo Yang, Jong Sung Won, Da Young Jin, Ji Eun Lee, Won Ho Park, and Seung Goo Lee
Volume 2015, Article ID 534241, 8 pages

Effects of Low Volume Fraction of Polyvinyl Alcohol Fibers on the Mechanical Properties of Oil Palm Shell Lightweight Concrete, Ming Kun Yew, Hilmi Bin Mahmud, Bee Chin Ang, and Ming Chian Yew
Volume 2015, Article ID 425236, 11 pages



Influence of Molarity and Chemical Composition on the Development of Compressive Strength in POFA Based Geopolymer Mortar, S. M. Alamgir Kabir, U. Johnson Alengaram, Mohd Zamin Jumaat, Afia Sharmin, and Azizul Islam
Volume 2015, Article ID 647071, 15 pages

Waste Cellulose from Tetra Pak Packages as Reinforcement of Cement Concrete, Gonzalo Martínez-Barrera, Carlos E. Barrera-Díaz, Erick Cuevas-Yañez, Víctor Varela-Guerrero, Enrique Viguera-Santiago, Liliana Ávila-Córdoba, and Miguel Martínez-López
Volume 2015, Article ID 682926, 6 pages

Editorial

Green Composite Materials

Hao Wang,¹ Peter Schubel,² Xiaosu Yi,³ Jin Zhu,⁴ Chad Ulven,⁵ and Yiping Qiu⁶

¹Centre of Excellence in Engineered Fibre Composites, University of Southern Queensland, Toowoomba, QLD 4350, Australia

²Division of Materials, Mechanics and Structures, University of Nottingham, Nottingham NG96PA, UK

³Beijing Institute of Aeronautical Materials, Beijing 100095, China

⁴Ningbo Institute of Industrial Technology, Chinese Academy of Sciences, Ningbo 315201, China

⁵North Dakota State University, Fargo, ND 58108-6050, USA

⁶College of Textiles, Donghua University, Shanghai 201620, China

Correspondence should be addressed to Hao Wang; hao.wang@usq.edu.au

Received 16 May 2015; Accepted 18 May 2015

Copyright © 2015 Hao Wang et al. This is an open access article distributed under the Creative Commons Attribution License, which permits unrestricted use, distribution, and reproduction in any medium, provided the original work is properly cited.

Global awareness of environmental issues has resulted in the emergence of sustainable and environmentally friendly green materials, which are renewable resources based, recyclable, and biodegradable. These green composite materials can be polymer based or cement based. In the polymer based green composites, natural fibres, such as hemp, flax, jute, kenaf, and sisal, have been used to replace conventional synthetic fibres. On the other hand, bioresins have been derived from starch, vegetable oils, and protein to replace petroleum based polymers. Cement based composites utilise new binders, such as geopolymers and recycled aggregators. The use of renewable and recycled resources reduces the need for petrochemicals and minerals, resulting in reduced natural resources depletion. Commercial products and applications are now emerging for these green composites.

Green composites are regarded as the next generation of sustainable composite materials, gaining significant attention from both academia and industry. This special issue is just a snapshot to present some of the latest progress in green composites fabrication, characterisation, testing, and applications.

The special issue contains eight papers on polymer based green composites, including hemp, flax, and sisal fibre reinforced composites, and polylactic acid and chitosan biopolymers. It also contains five papers on cement based composites, including geopolymers from slag, fly ash, metakaolin, and rice hush ash. There are also papers across these two areas, which use oil palm shell and waste cellulose in cement and concrete.

We hope the information provided in this special issue is useful and offers stimulation to the new development of green composite materials and the promotion of these materials to industrial applications.

*Hao Wang
Peter Schubel
Xiaosu Yi
Jin Zhu
Chad Ulven
Yiping Qiu*

Research Article

Impacts of Limestone Particle Size on the Performance of Flexible Wood Fiber Composite Floor

Hongcheng He,¹ Jinling Nie,¹ and Jing Wang²

¹Hunan Academy of Forestry, Shaoshan South Road, Changsha, Hunan 410004, China

²Centre of Excellence in Engineered Composite, University of Southern Queensland, Toowoomba, QLD 4350, Australia

Correspondence should be addressed to Hongcheng He; xbd9818@163.com and Jing Wang; jing.wang@usq.edu.au

Received 25 June 2014; Revised 20 August 2014; Accepted 24 August 2014

Academic Editor: Jin Zhu

Copyright © 2015 Hongcheng He et al. This is an open access article distributed under the Creative Commons Attribution License, which permits unrestricted use, distribution, and reproduction in any medium, provided the original work is properly cited.

Sustainable wood floor (WFF), produced from natural plants, is a sort of novel green and ecofriendly composite floor, which has been attracting more and more attention in the world. WFF also gives a solution of utilizations of agricultural wastes, such as bamboo mats and hemp hurd. The additive limestone powder plays key role in the performance of flexible bamboo composite floor, so, in this paper, the effects of limestone size and size distributions were investigated. The best particle size distributions of limestone are 25 wt% of 48 μm , 25 wt% of 106 μm , and 50 wt% of 160 μm . The as-obtained WFF has good elasticity, good affinity, and strong comfortableness as well as free formaldehyde release.

1. Introduction

With globally rapid development of industrialization and urbanization, energy saving and greenhouse gas (GHG) mitigation have become ones of the most extensive issues [1–5]. Flexible wood fiber floor, prepared by special processing technology using nature fibers (such as bamboo, hemp, cotton, and other woods), PVC, limestone powders, flexible agent, and raw materials, is one kind of new green and environmental protection composite floors [6]. Natural fibres can also be widely applied furniture veneer, integral cupboard, and decorative materials [7, 8].

The natural fibre reinforced composites have competitive advantages, such as (i) being green and ecofriendly: the products do not contain urea formaldehyde, phenolic aldehyde, or aldehydes resin and are free of formaldehyde [9] and it is also free of wastewater and exhaust gas release during the manufacturing process; (ii) having excellent abrasive resistance [10]: the wear-resisting revolution is as high as 300,000, compared with traditional floor materials 13,000 and the high-performance aggrandizement wood floor 20,000; (iii) having higher quality and better elasticity [11]: this product could become thinner, lighter, and stronger than

conventional materials, so that it enables the modern high buildings weight-bearing and space saving [8] and due to the good elastic recovery under heavy shock load, the work-related injury can be dramatically reduced and, at the same time, the elastic recovery may reduce the damage to the floor; (iv) being waterproof, antiskid, antibacterial and [12–14]: the natural fibres are easily modified and treated to change their surface physical and chemical structure, so this composite floor has excellent waterproof and antibacterial properties and the flame retardant can reach the B1 level of GB8624-1997 [15]; (v) being antistatic: due to the natural characteristic of natural fibers and limestone, the floor can be permanently antistatic [16]; (vi) being mute and noise reducing [17]: WFF contains abundant wood fibers which have good sound absorbability, so this composite could be utilized to produce sound absorbing decorative board [18].

During the development of wood fibre floor, the addition of limestone is a must to enhance the mechanical properties and improve other functional features. However, the impacts of limestone particle size and the size distribution on the performance of composite floor are still not clear. This paper is the first to systematically investigate those impact factors.

TABLE 1: The dimension of bamboo fibre.

	Length, μm	Width, μm	Inner diameter, μm	Length-width ratio
Average	89.84	36.60	29.42	2.45
Coefficient of variation	24%	13%	14%	27%

TABLE 2: Effects of limestone particle size and size distribution on the performance of wood composite floor.

Number	Size/mesh (portion)	MOR/MPa	MOE/MPa	Shock strength/MPa	IB/MPa	Density/g/cm ³	TS/%	Thermal expansion ratio/%
1	No limestone added	16.6	1396	10.9	2.98	1.18	1.55	1.83
2	48 (100)	18.7	1436	11.9	2.35	1.13	0.56	1.33
3	106 (100)	20.6	1723	13.6	1.98	0.98	0.78	1.16
4	160 (100)	28.3	1950	19.9	1.26	0.75	1.69	0.92
5	48 (25)	27.2	1679	13.6	1.68	0.72	1.56	0.98
	106 (25)							
	160 (50)							
6	48 (30)	23.5	1586	13.1	1.76	0.65	1.38	1.13
	106 (25)							
	160 (45)							
7	48 (35)	21.6	1532	12.5	1.81	0.61	1.33	1.21
	106 (25)							
	160 (40)							

2. Materials and Methods

2.1. Materials. Bamboo fiber (moisture 8%, ash less than 3%) was obtained from Shandong Xincheng Wood Fiber Powder Corporation (China). PVC was received from Qilu Petrochemical Company (China). Limestone powder (particle size 48 μm , 106 μm , and 160 μm) was supplied by Hebei Lingshou Tianhao Minerals Processing Factory. Vinyl chloride-vinyl acetate copolymer (EVA-1) was purchased from Beijing Hua'er Corporation. The polar fibre dimension is shown in Table 1 and the fibre was used as received.

2.2. Equipment and Instruments. WFF was carried out by using independent flexible bamboo fiber floor production line; the mechanic properties were tested by WDT-5 tension and compression spring tester; DMA242 was applied to characterize the mechanical properties of materials as a function of time and temperature.

2.3. Test Methodologies of Mechanical Properties. To test modulus of rupture (MOR) and modulus of elasticity (MOE), samples were prepared according to the standard of GB/T9341-2000. Standard of ASTM D 256-06 was applied to measure shock strength. Other properties such as the internal bond (IB) strength, sample density, the thickness swelling (TS) rate of water absorption, and the hold screw force were carried out referring to the standard of GB-T 117718-2009, GB/T1033.1-2008 GB/T1034-1998, and GB 11718.9-1989, respectively. The thickness swelling ratio was tested at 20°C for 24 hours.

2.4. Preparation of Wood Floor

2.4.1. Technological Process. See Figure 1.

2.4.2. Main Process Parameters and Facilities. Figure 2 shows the main preparing process of wood floor and wooden homogeneity hollow coiling molding. The main facilities required in those process are listed as powder microwave dryer, mixing agitator, kneading extruder, high sheeting open miller, high calendaring and coating machine, oil pressure cooling and shaping machine, traction and cutting machine, mould press machine, edge cutter, and coater.

To prepare wood floor, wood powder was milled to 80–120 mesh in size and dried at 100°C for 1 hour, with the moisture being less than 8%. The dried powder then was mixed with EVA-1, PVC, and limestone for 30 min and cured at 100–180°C for 15–20 min, 80–120°C for 5–10 min, 60–100°C for 3–5 min, and 30–50°C for 3–5 min, respectively, followed by edge cutting and polishing. In all samples preparation, the ratio of bamboo fiber powder, limestone, PVC resin, and accessories is 30 : 40 : 25 : 5.

3. Results and Discussion

The impacts of limestone particle size and size distribution on the performance of wood fibre reinforced composite floor are shown in Table 2 and Figure 3. All results are average values tested three times. Table 2 shows that all features improved after limestone particle was added to the composites. During the manufacturing of flexible bamboo fiber composite floor,

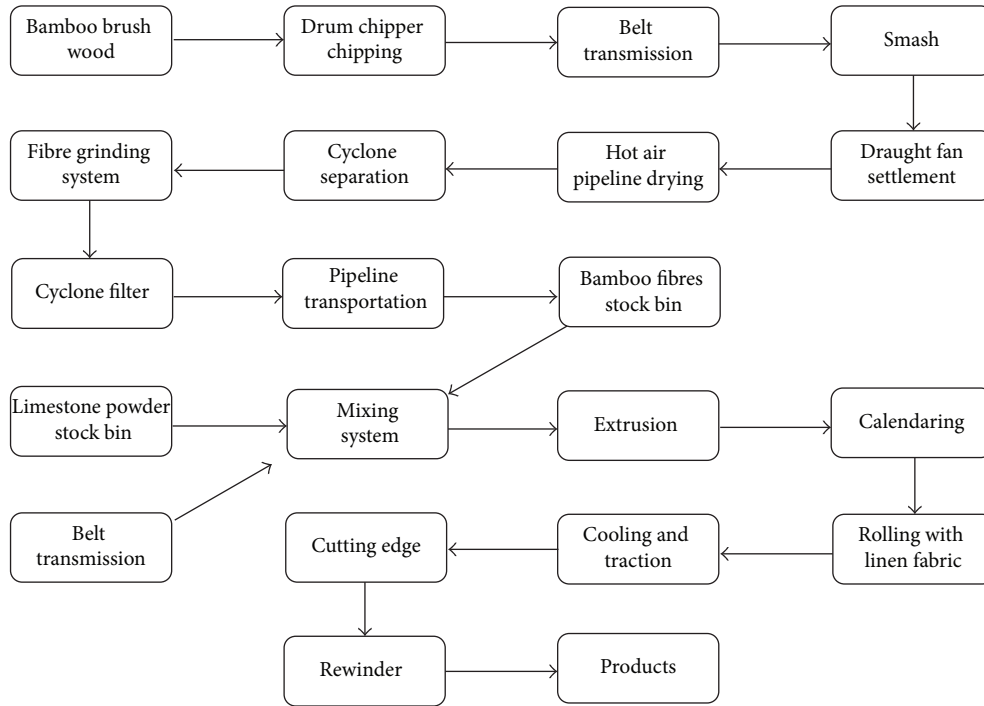


FIGURE 1: The strategy of wood composite panel preparation.

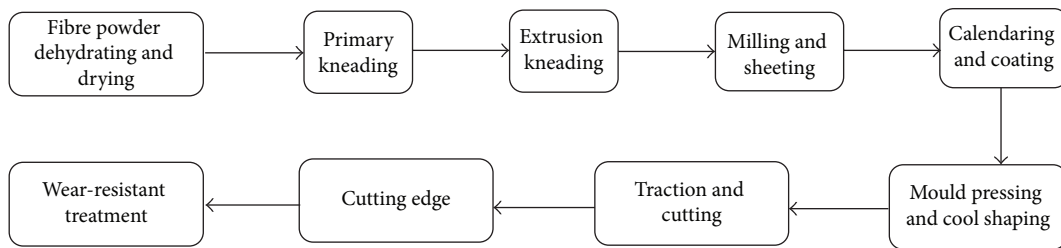


FIGURE 2: Wood floor and wooden fiber homogeneity hollow coiling molding process.

the size of limestone and the size distribution play key role on the mechanical properties of obtained composites. It is clear from Figures 3(a), 3(b), and 3(c) that composites reinforced with smaller sized limestone have lower modulus of rupture (MOR) and modulus of elasticity (MOE), meanwhile, the internal bonding (IB) strength shows decreasing trend with the increase of limestone size. Because the smaller sized powders have larger specific surface area (porosity), the smaller sized limestone has better adhesion strength with resin. As a result, its physical property is closer to plastic with better flexibility. The larger sized limestone contributes higher MOR and MOE to the composite.

To carry out better composite floor, different sized limestone powder was mixed to reinforce composite mats. When the ratio of different sized limestone powder 48 μm/106 μm/160 μm is 25/25/50, the obtained composite mats have not only optimum MOR, MOE, and internal bonding strength, but also better flexibility and enough

strength, which makes it a great potential in the application as composite floor.

Figure 3(d) shows that the shock strength of WFF increases with the increase of particle size. The shock strength reaches the largest value when the limestone particle size is 160 μm. However, for the mixture limestone powder, the content increase of large sized particle results in the decrease of shock strength. Meanwhile, the high ratio of big sized limestone powder leads to the density declining (Figure 3(e)). This is because that with the increase of large sized powder content/distribution, the number of pores and fibres in the composite will increase so that the interface bonding strength will decrease.

Figures 3(f) and 3(g) reveal the effects of limestone size and size distribution on the TS and thermo expansion ratio. They state that the increase of small sized powder ratio leads to the increase of TS and thermal expansion rate of obtained composites. The reason is that the smaller sized particle has

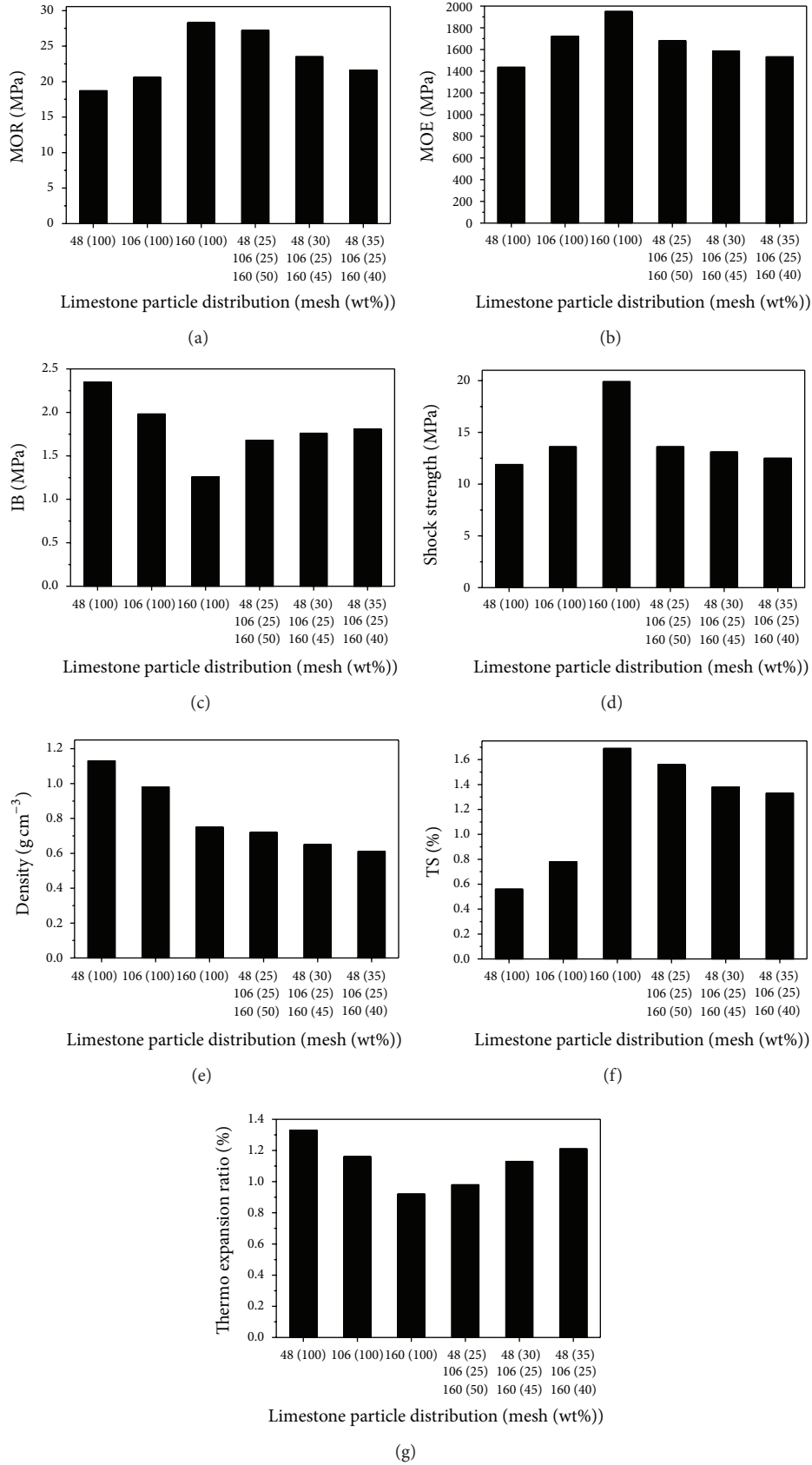


FIGURE 3: Effects of limestone particle size and size distribution on (a) MOR; (b) MOE; (c) IB; (d) shock strength; (e) density; (f) TS; and (g) thermo expansion rate.

better combination dens which will decrease the swelling ratio of water absorption. On the other hand, with the increase of particle size (or large sized particle distribution), the lattice distortion at the interfacial zone will become harder because large limestone requires higher thermally deforming; as a result, the thermal expansion becomes lower [19].

4. Conclusions

The optimum features of flexible bamboo fiber composite floor prepared in this paper were tested as follows: bending strength 28.3 MPa, MOE 1950 MPa, shock strength 19.9 KJ/m², internal bonding strength 2.35 MPa, TS 0.56%, thermal expansion rate 0.92, and density 0.61 g/cm³.

The performance of wood composite floor was affected by the limestone size and size distribution. Considering and comparing all impact factors, the optimum limestone powder size ratio is concluded as 48 μm (25 portion), 106 μm (25 portion), and 160 μm (50 portion).

The as-prepared wood composite floor material has good elasticity, affinity, and strong comfortableness. This composite was tested to match the China national standards requirement for man-made floor materials and has potential commercialization.

Conflict of Interests

The authors declare that there is no conflict of interests regarding the publication of this paper.

Acknowledgment

The project was financially supported by Chinese State Forestry Administration 948 Project, Natural Wood Reinforced Composite Key Technology Introduction (2011-4-11).

References

- [1] B. Jiang, Z. Sun, and M. Liu, "China's energy development strategy under the low-carbon economy," *Energy*, vol. 35, no. 11, pp. 4257–4264, 2010.
- [2] S. Luo and A. N. Netravali, "Interfacial and mechanical properties of environment-friendly "green" composites made from pineapple fibers and poly(hydroxybutyrate-co-valerate) resin," *Journal of Materials Science*, vol. 34, no. 15, pp. 3709–3719, 1999.
- [3] S. Luo and A. N. Netravali, "Mechanical and thermal properties of environment-friendly "green" composites made from pineapple leaf fibers and poly(hydroxybutyrate-co-valerate) resin," *Polymer Composites*, vol. 20, no. 3, pp. 367–378, 1999.
- [4] S. Nam and A. N. Netravali, "Green composites. I. Physical properties of ramie fibers for environment-friendly green composites," *Fibers and Polymers*, vol. 7, no. 4, pp. 372–379, 2006.
- [5] Y. Wang, W. Ji, X. Yu et al., "The impact of urbanization on the annual average temperature of the past 60 years in Beijing," *Advances in Meteorology*, vol. 2014, Article ID 374987, 9 pages, 2014.
- [6] J. Holbery and D. Houston, "Natural-fiber-reinforced polymer composites in automotive applications," *JOM*, vol. 58, no. 11, pp. 80–86, 2006.
- [7] U. L. Ahlstedt, E. Lussi, and S. A. Ryden, "Method of making decorative laminated products such as tiles, panels or webs from cellulosic materials," US Patent 4,420,351, 1983.
- [8] R. K. Cullen, M. M. Singh, and J. Summerscales, "Characterisation of natural fibre reinforcements and composites," *Journal of Composites*, vol. 2013, Article ID 416501, 4 pages, 2013.
- [9] H. Kalaycioglu and G. Nemli, "Producing composite particle-board from kenaf (*Hibiscus cannabinus* L.) stalks," *Industrial Crops and Products*, vol. 24, no. 2, pp. 177–180, 2006.
- [10] M. Saxena, R. K. Morchhale, P. Asokan, and B. K. Prasad, "Plant fiber industrial waste reinforced polymer composites as a potential wood substitute material," *Journal of Composite Materials*, vol. 42, no. 4, pp. 367–384, 2008.
- [11] I. S. Aji, S. M. Sapuan, E. S. Zainudin, and K. Abdan, "Kenaf fibres as reinforcement for polymeric composites: a review," *International Journal of Mechanical and Materials Engineering*, vol. 4, no. 3, pp. 239–248, 2009.
- [12] M. Sain, S. H. Park, F. Suhara, and S. Law, "Flame retardant and mechanical properties of natural fibre-PP composites containing magnesium hydroxide," *Polymer Degradation and Stability*, vol. 83, no. 2, pp. 363–367, 2004.
- [13] K. R. Cordell, "Waterproof fabric," US Patent 6,274,520, 2001.
- [14] W. L. Morrison, "Antimicrobial blended yarns and fabrics comprised of naturally occurring fibers," US Patent 3,959,556, 1976.
- [15] W.-L. Tian, Y.-Q. Wu, W.-X. Peng, and Y.-C. Hu, "Study on low-toxicity fire-retardant treated technology of wood," in *Proceedings of the 3rd International Conference on Bioinformatics and Biomedical Engineering (ICBBE '09)*, pp. 1–5, Beijing, China, June 2009.
- [16] C. L. Kissel, "Antistatic textile compositions and sol/gel/polymer compositions," US Patent 5,004,563, 1991.
- [17] H.-S. Yang, D.-J. Kim, and H.-J. Kim, "Rice straw-wood particle composite for sound absorbing wooden construction materials," *Bioresource Technology*, vol. 86, no. 2, pp. 117–121, 2003.
- [18] H. C. He and C. Chen, "Study on forming process of plant fiber multilayer decorative board (I)- Effect of fiber content on the properties," *Applied Mechanics and Materials*, vol. 468, pp. 3–7, 2014.
- [19] R. Arpón, J. M. Molina, R. A. Saravanan, C. García-Cordovilla, E. Louis, and J. Narciso, "Thermal expansion behaviour of aluminium/SiC composites with bimodal particle distributions," *Acta Materialia*, vol. 51, no. 11, pp. 3145–3156, 2003.

Research Article

Impact of Layer-by-Layer Self-Assembly Clay-Based Nanocoating on Flame Retardant Properties of Sisal Fiber Cellulose Microcrystals

Chun Wei,¹ Sihua Zeng,^{1,2} Yuyuan Tan,¹ Wu Wang,¹ Jian Lv,¹ and Hongxia Liu¹

¹Key Laboratory of New Processing Technology for Nonferrous Metals and Materials, Ministry of Education, Ministry-Province Jointly Constructed Cultivation Base for State Key Laboratory of Processing for Nonferrous Metal and Featured Materials, College of Materials Science and Engineering, Guilin University of Technology, Guilin 541004, China

²Sichuan EM Technology Co., Ltd., Mianyang 621000, China

Correspondence should be addressed to Chun Wei; 1005668130@qq.com

Received 8 August 2014; Revised 30 September 2014; Accepted 14 October 2014

Academic Editor: Hao Wang

Copyright © 2015 Chun Wei et al. This is an open access article distributed under the Creative Commons Attribution License, which permits unrestricted use, distribution, and reproduction in any medium, provided the original work is properly cited.

The renewable cationic polyelectrolyte chitosan (CH) and anionic nanomontmorillonite (MMT) layers were alternately deposited on the surface of sisal fiber cellulose microcrystals (SFCM) via layer-by-layer (LBL) self-assembly method. The structure and properties of the composites were characterized by zeta potential, thermal gravimetric analysis (TGA), X-ray diffraction (XRD), field emission scanning electron microscopy (FESEM), Fourier transform infrared spectrometer (FTIR), microcalorimeter (MCC), and so forth. The zeta potential results show that the cellulose microcrystalline surface charge reversed due to the adsorption of CH and MMT nanoplatelets during multilayer deposition. MMT characteristic diffraction peaks appear in XRD patterns of SFCM(CH/MMT)₅ and SFCM(CH/MMT)₁₀ composites. Additionally, FESEM reveals that the SFCM(CH/MMT)₁₀ surface is covered with a layer of material containing Si, which has been verified by elemental analysis. TGA results show that the initial decomposition (weight loss of 5%) temperature of SFCM(CH/MMT)₅ is increased by 4°C compared to that of pure SFCM. On the other hand, carbon residue percentage of SFCM(CH/MMT)₁₀ is 25.1%, higher than that of pure SFCM (5.4%) by 19.7%. Eventually, it is testified by MCC measurement that CH/MMT coating can significantly reinforce the flame retardant performance of SFCM.

1. Introduction

Cellulose is the most abundant natural renewable resource [1, 2] and has been recently concerned and developed as raw material with the gradual depletion of oil resources and increasing emphasis on environment-friendliness, green materials, and sustainable development. However, these natural fibers have properties of facile thermal degradation and flammability, which limit its application in many fields. Hence, it is necessary to effectively modify cellulose to improve the heat resistance and flame resistance of natural fibers, especially polymer-based reinforced natural fiber composite [3, 4].

Layer-by-layer self-assembly (LBL) is a rapidly developed simple and versatile surface modification method in the 90s of the last century [5, 6]. This facile method can be performed

in mild reaction conditions, without limitations of the size and shape of substrate, and it has other advantages: flexible film composition and controllable thickness, stable film performance, and so forth. Thanks to these properties, multilayer films with different characteristics, such as hydrophobicity [7, 8], controlled drug release [9, 10], chemical sensing [11, 12], antibacterial property [13, 14], and flame resistance [15–17], can be built through this method.

Montmorillonite (MMT) is typical layered silicate clay consisting of two Si–O tetrahedrals and a layer of Al–O octahedron amid them. Because partial Al³⁺ cation within the octahedron are replaced by Mg²⁺ and others, the surface negative charge among montmorillonite layers is excess, resulting in the fact that Na⁺, Ca²⁺, and other cations are readily absorbed onto montmorillonite layers to maintain the charge balance itself. The unique layered structure and excellent heat

resistance of MMT make it widely used in the preparation of brand-new high-performance polymer/clay nanocomposites [18]. Compared with conventional filled polymers, MMT can improve mechanical properties [19], gas barrier properties, solvent resistance, and heat resistance of the polymer matrix [20], and a potential flame retardant capacity [21] might be existent.

In this study, a strategy of using sisal fiber cellulose microcrystal (SFCM) as a substrate and alternately adsorbing positively charged polyelectrolyte chitosan (CH) and negatively charged inorganic nanolayer MMT onto the surface of SFCM via LBL technique has been proposed. The effect of CH/MMT coating on the thermal performance and flame retardant properties of SFCM was systematically investigated, aiming at applying SFCM to high-performance composite materials.

2. Experimental

2.1. Materials. Sisal fibers were obtained from Guangxi Sisal Company, China. Chitosan (medium viscosity of 200–400 mPa·S) was purchased from Aladdin Reagent Company. Sodium MMT clay was provided by Zhejiang Fenghong New Materials Co., Ltd., with an average size of 1180 nm. Acetic acid (AR) with a hydrochloric acid (AR) and sulfuric acid (AR) was obtained from Xilong Chemical Co. Both deionized water and sisal fiber microcrystalline cellulose (SFCM) were homemade [22]; SFCM is a rod-like structure with a diameter of about 10 μm and a length of about 50–150 μm .

2.2. Layer-by-Layer Self-Assembly Method. SFCM charging process is as follows. SFCM was added to an aqueous H_2SO_4 solution with a concentration of 45%, and the mixture was then stirred under 50°C for 2 min before it was filtered and washed for 4 times. The precipitation was dried at 50°C.

MMT solution preparation is as follows. 5 g of montmorillonite powder was dissolved in 1000 mL of distilled water by vigorous agitation. The suspension was placed at room temperature for 24 h of swelling, and then it was processed with ultrasonic sound generated from an ultrasonic cleaner for 3 h. After centrifugation, at a rate of 8000 rad/min for 5 min, with a high speed centrifuge, the upper clear liquid was collected. SFCMs were alternately adsorbed positively charged polyelectrolyte chitosan (CH) and negatively charged inorganic nanolayer MMT onto the surface of SFCM via LBL technique, as shown in Figure 1.

2.3. Preparation of $\text{SFCM}(\text{CH}/\text{MMT})_n$ Composites. 0.5 g of sulfuric acid-treated SFCM was thoroughly dispersed in 100 mL of CH solution (0.2 wt%, containing 1 v/v% of acetic acid), which was then magnetically stirred for 10 min. Afterwards, wash and vacuum filtration were alternatively performed for 4 times using 1 v/v% of acetic acid solution (dissolved in deionized water). Then, the solid was dispersed into 100 mL of MMT solution (pH not adjusted) and then magnetically stirred for 30 min. After being washed in deionized water for four times, sample was tested for zeta potential measurement. Similarly, $\text{SFCM}(\text{CH}/\text{MMT})_n$ composite

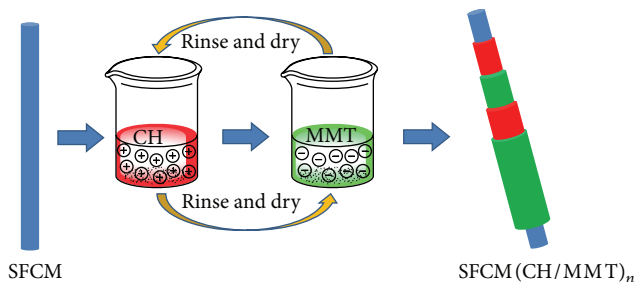


FIGURE 1: Layer-by-layer self-assembly process of $\text{SFCM}(\text{CH}/\text{MMT})_n$.

materials ($n = 1, 5, \text{ and } 10$, resp.) were prepared for the following characterizations.

2.4. Characterization. X-ray diffraction (XRD) spectra were taken on a Holland PANalytical X-Pert PRO X-ray diffractometer with $\text{Cu K}\alpha$ radiation from 3° ~40°. Zeta potential was determined using a Zetasizer Nano ZS90 nanoparticle size and zeta potential analyzer (Malvern Company, British). Thermal gravimetric (TGA) test, for the weight loss curve ranging from 50 to 700°C, was conducted by a NETZSCH STA-449C thermal gravimetric analyzer (NETZSCH Company, Germany) at a heating rate of 10°C/min under the nitrogen. Fourier transformed infrared spectroscopy (FTIR) was obtained using a NICOLET NEXUS 470 FT-IR spectrometer (Perkin-Elmer Company, United States), and samples were prepared using KBr for flaking. Field emission electron microscopy (FESEM) was operated using a Hitachi S-4800 field emission scanning electron microscope provided by Hitachi High-Technologies Corporation. Microscale combustion calorimetry (MCC) was conducted using an MCC-2 (Govmark, Farmingdale, NY) microscale combustion calorimeter, and the sample was heated from 100 to 700°C with a heating rate of 1°C/s under the nitrogen atmosphere, and samples are decomposed anaerobically to release volatile combustible gases under high temperatures, which can be combusted in N_2/O_2 (8 : 2) atmosphere.

3. Results and Discussion

3.1. Impact of CH/MMT Coating on SFCM Zeta Potential. Zeta potential online monitoring can be used to characterize the dynamic adsorption of chitosan and montmorillonite suspensions on SFCM surface. The residual CH and MMT solution would affect the zeta potential of the samples, so we can confirm that the measurement of the zeta potential of $\text{SFCM}(\text{CH}/\text{MMT})_n$ adsorption was acted after the samples have been washed in deionized water for some time in order to remove the residual of the CH or MMT.

Figure 2 shows that the adsorption of each CH/MMT layer will turn the negative (or positive) potential into a positive (or negative) one. This potential reverse indicates that CH/MMT has been assembled to SFCM surface. Further, as the number of adsorption layers increases, absolute amount of the surface zeta charges becomes gradually smaller. This is

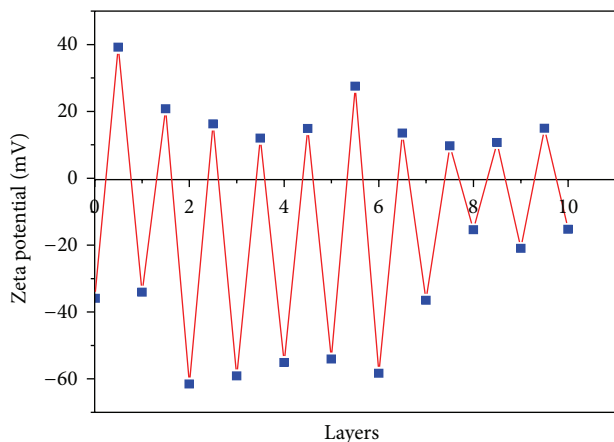


FIGURE 2: Changes of zeta potential at alternative absorption steps of CH and MMT.

probably because the MMT clay layer deposited on cellulose surface formed a relatively flat deposition surface where there are less nanotopological structures [23] compared with the pure polymer electrolyte self-assembly, so that less polymer chains will be deposited on this plane, resulting in the declined absolute amount of surface zeta charges as above mentioned.

3.2. Effect of CH/MMT Coating on SFCM Composite Crystal Structure. For further describing the assembly of CH/MMT coating on SFCM surface, XRD was carried out to characterize pure MMT, SFCM, SFCM(CH/MMT)₅, and SFCM(CH/MMT)₁₀. As shown in Figure 3, between small angles 3° and 10°, an MMT diffraction peak corresponding to pure MMT at $2\theta = 6.8^\circ$ occurs. According to the Bragg equation ($2d\sin\theta = n\lambda$), pure MMT interplanar spacing is 13.1 Å, whereas an MMT diffraction peak of SFCM(CH/MMT)₅ and SFCM(CH/MMT)₁₀ appears where $2\theta = 4.8^\circ$ and 5.0° , which has not been observed in the pattern of pure SFCM. Compared to pure MMT, MMT diffraction peak of SFCM(CH/MMT)₅ and SFCM(CH/MMT)₁₀ is shifted to a smaller angle. It is elucidated from the peak shift toward small angle that the interplanar spacing of MMT in CH/MMT nanocoating layer is larger than that in pure MMT. The reason might be that CH amid MMT sheets or the peeling of MMT layer during sonication process increases the distance between layers, which is consistent with Li et al.'s report [24]. Exceptionally, peaks intensity corresponding to SFCM(CH/MMT)₅ and SFCM(CH/MMT)₁₀ is much weaker than the peak intensity of pure MMT. The reason might be the following: the absorbed MMT has a low content and fewer deposition layers, and thus the CH/MMT coating is so thin that MMT layered structure, within the coating, cannot be converted from amorphousness into ordered structure [15].

3.3. Influence of CH/MMT Coating on Thermal Properties of SFCM. To clarify the impact of CH/MMT nanocoating on thermal performance of SFCM, pure SFCM and SFCM(CH/MMT)_n composites ($n = 1, 5, \text{ and } 10$) were tested

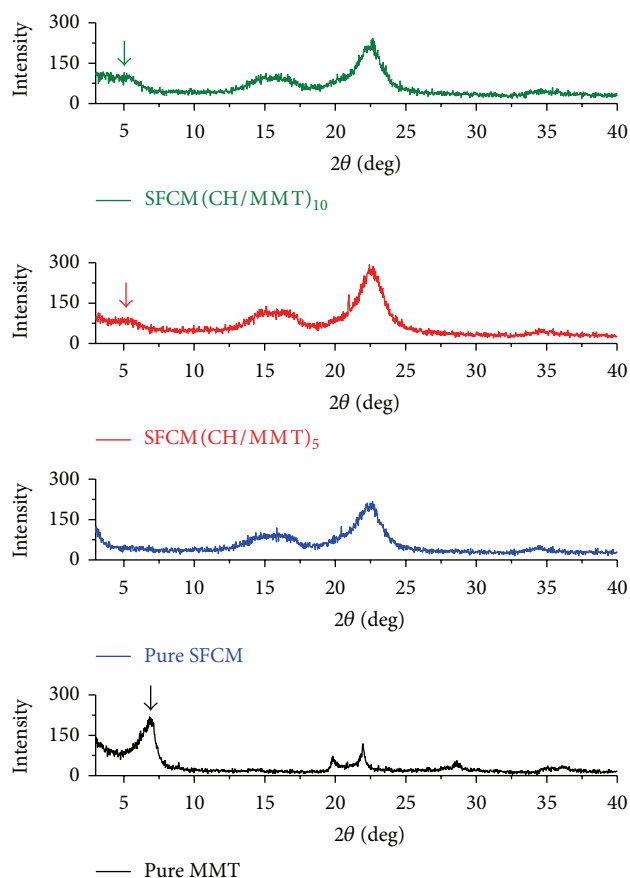


FIGURE 3: X-ray diffraction patterns of pure MMT, pure SFCM, SFCM(CH/MMT)₅, and SFCM(CH/MMT)₁₀.

by TGA analysis (Figure 4). Before 340°C, TGA curves of SFCM, before and after treatment, are almost the same. The characteristic thermal parameters selected were the temperature for 5% and 10% weight loss. The results are summarized in Table 1. Table 1 shows that thermal properties of the treated SFCM are slightly better than those of untreated SFCM. At a weight loss of 10%, compared with pure SFCM, decomposition temperatures of SFCM(CH/MMT)₁, SFCM(CH/MMT)₅, and SFCM(CH/MMT)₁₀ composites are elevated by 3, 4, and 3°C, respectively. On the other hand, between 340 and 700°C, it is found that the char yield of coated SFCM(CH/MMT)_n is higher than that of pure SFCM. Moreover, as adsorption layers increase, char yield rises as well. At 700°C, compared with pure SFCM, char yields of SFCM(CH/MMT)₁, SFCM(CH/MMT)₅, and SFCM(CH/MMT)₁₀ are increased by 9.6%, 12.0%, and 19.7%, respectively. This increase may be ascribed to the nanolayer of MMT that forms a sheet of carbon residue covering the surface of cellulose during heating process, because of which heat was insulated, protecting an amount of cellulose microcrystals from destruction.

3.4. Fourier Transform Infrared (FTIR) Analysis. Carbon residue, after TGA test, of pure SFCM, SFCM(CH/MMT)₅, and SFCM(CH/MMT)₁₀ was subjected to FTIR testing. As it is shown in Figure 5, for TGA residual carbon of

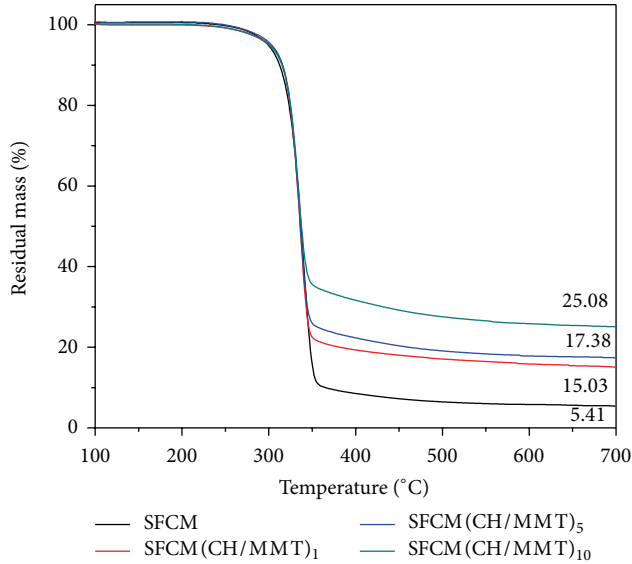


FIGURE 4: TGA plots of SFCM coated with different number of CH/MMT bilayers.

TABLE 1: TGA results for SFCM coated with different number of CH/MMT bilayers.

Samples	Temperature at 5 wt% loss (°C)	Temperature at 10 wt% loss (°C)	Residue (wt%)
SFCM	299	312	5.4
SFCM(CH/MMT) ₁	302	315	15.0
SFCM(CH/MMT) ₅	303	316	17.4
SFCM(CH/MMT) ₁₀	300	315	25.1

SFCM(CH/MMT)₁₀, stretching vibration peaks corresponding to methyl and methylene on cellulose appeared at 2970 and 2925 cm^{-1} [25], while these peaks of pure SFCM and SFCM(CH/MMT)₅ are almost negligible. This implies that, with the increase of CH/MMT layers, cellulose microcrystals was protected in the process of thermal degradation. In addition, there is another peak at 1050 cm^{-1} for TG residual carbon of SFCM(CH/MMT)₅ and SFCM(CH/MMT)₁₀, which may be Si-O-Si stretching vibration peak of MMT or stretching vibration absorption peak of the cellulose C-C skeleton, indicating that the TG residual carbon of SFCM(CH/MMT)₁₀ might be composed of cellulose microcrystalline and MMT [26].

3.5. Morphology and Surface Element Analysis of SFCM and SFCM(CH/MMT)₁₀ Composite. Field emission scanning electron micrographs of pure SFCM (Figure 6(a)) and its TGA carbon residue (Figure 6(c)) and SFCM(CH/MMT)₁₀ (Figure 6(b)) and its TGA carbon residue (Figure 6(d)) are given. It can be observed that the surface of pure SFCM is continuous cellulose structure with clear texture, clean surface, and regular structure, whereas the cellulose surface is coated with fold-like layers in Figure 6(b) and it is unable to clearly see continuous and clear-textured cellulose skeleton. For this reason, surface element analysis for pure SFCM and

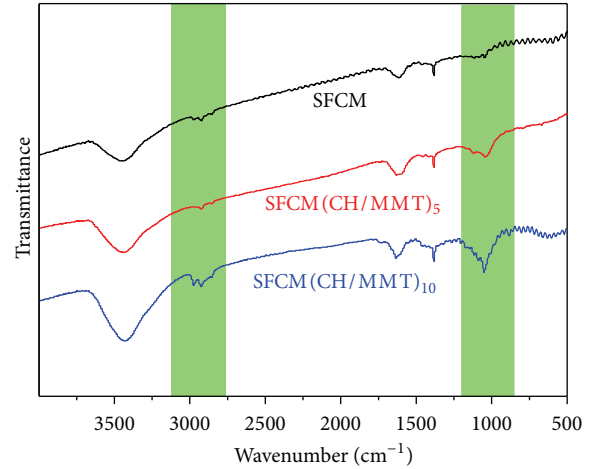


FIGURE 5: FTIR spectra of char residues of pure SFCM, SFCM(CH/MMT)₅, and SFCM(CH/MMT)₁₀ (charred in N_2 at 700°C).

SFCM(CH/MMT)₁₀ samples was shown in Figures 7(a) and 7(b). Figure 7(a) verifies the presence of elements C and O on the surface of pure SFCM without Si. However, in Figure 7(b), besides C and O, Si, Mg, Al, and other elements were also detected on the surface of SFCM(CH/MMT)₁₀, demonstrating that the fold layers in Figure 6(b) should be MMT nanolayers.

Clear spiral contraction texture of pure SFCM can be observed in Figure 6(c), and this is because of the severe contraction of cellulose during heating process. On the other hand, composite SFCM(CH/MMT)₁₀ surface shrinkage has been significantly weakened, and this may be due to a thermal insulation coke layer which was formed during the heating of CH/MMT coating. This layer has satisfying insulation properties, inhibiting the heat from being transferred to the internal cellulose, that is, a protective effect.

3.6. Impact of CH/MMT Coating on Flame Retardant Performance of SFCM. To study the effect of CH/MMT on combustion properties of pure SFCM, SFCM(CH/MMT)₅, and SFCM(CH/MMT)₁₀, powder samples were tested through microscale combustion calorimetry (MCC). The combustion properties of the samples will be characterized on the basis of the released heat, heat release rate, and other parameters. In Figure 8 and Table 2, compared with pure SFCM, both temperature of initial decomposition and heat release rate of SFCM(CH/MMT)₅ and SFCM(CH/MMT)₁₀ were slightly decreased. Moreover, both total released heat and maximum heat release rate of SFCM(CH/MMT)₅ and SFCM(CH/MMT)₁₀ composites are lower than those of pure SFCM, where the maximum heat release rate of SFCM(CH/MMT)₁₀ is lower than that of pure cellulose by 47.5 W/g, and the total released heat of SFCM(CH/MMT)₅ and SFCM(CH/MMT)₁₀ is lower than that of pure SFCM by more than 21%.

It is concluded that the presence of CH/MMT coating enhanced the flame retardant performance of SFCM to some

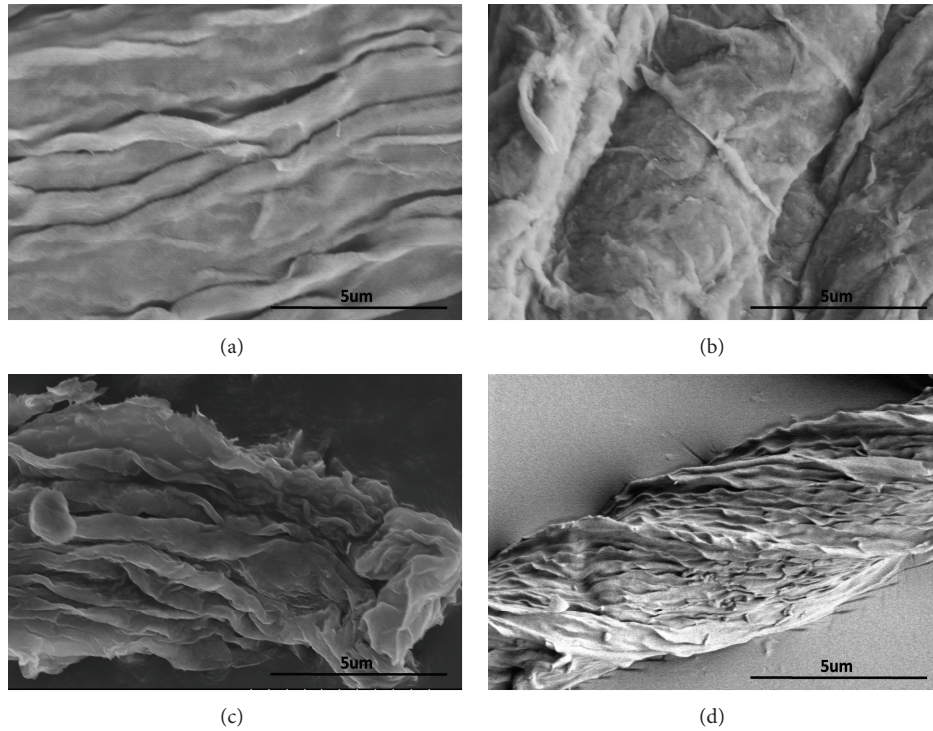


FIGURE 6: FESEM images of (a) pure SFCM, (b) SFCM(CH/MMT)₁₀, and (c) char residues of pure SFCM and (d) SFCM(CH/MMT)₁₀ (charred in N₂ at 700°C).

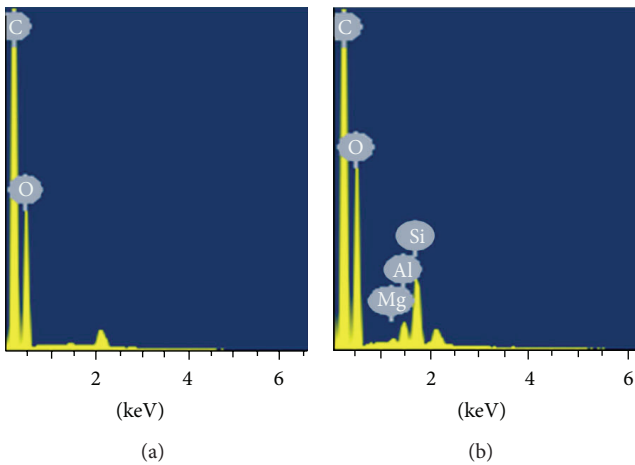


FIGURE 7: Superficial elemental distribution of (a) pure SFCM and (b) SFCM(CH/MMT)₁₀.

extent. It is elucidated that MMT inorganic layer does not react with the cellulose, so MMT mainly functions as a physical barrier on the surface of cellulose, during the combustion process of SFCM(CH/MMT)_n, of which flame retardant effect is limited. Hence, in terms of flame retardant performance, the composites cannot match with intumescent P-N fire retardant that can react with cellulose [27], which has also been confirmed by literatures related to retardant coating fabricated by inorganic nanoparticles, such as SiO₂ [28] or POSS [29].

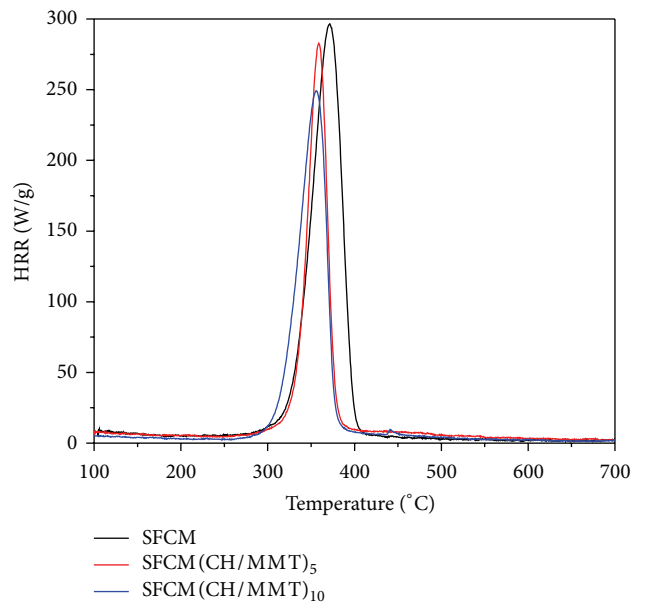


FIGURE 8: Heat release rate versus temperature for pure SFCM, SFCM(CH/MMT)₅, and SFCM(CH/MMT)₁₀.

4. Conclusion

CH/MMT coating on the surface of SFCM was prepared by LBL self-assembly method and our results reveal that the assembly of CH/MMT coating could increase heat resistance

TABLE 2: MCC results of pure SFCM, SFCM(CH/MMT)₅, and SFCM(CH/MMT)₁₀.

Samples	pkHRR (°C)	pkHRR (W/g)	Total HR (kJ/g)
SFCM	371.2	296.6	15.0
SFCM(CH/MMT) ₅	318.2	282.7	11.3
SFCM(CH/MMT) ₁₀	302.4	249.1	11.7

and flame retardancy of SFCM. TGA results demonstrate that the thermal performance of treated SFCM is commonly superior to that of untreated SFCM. With the increase of the number of adsorbed layers, carbon residue increases. Meanwhile, MCC results indicate that the existence of CH/MMT coating has significantly improved flame retardant capability of SFCM.

Conflict of Interests

The authors declare that there is no conflict of interests regarding the publication of this paper.

Acknowledgments

The authors would like to acknowledge the National Natural Science Foundation of China (Grant nos. 21264005, 21204013, 51263005, and 51163003), Guangxi Natural Science Foundation of China (Grant nos. 2013GXNSFDA019008 and 2014GXNSFAA118321), Guangxi Small Highland Innovation Team of Talents in Colleges and Universities, and Innovation Team of Guangxi Universities' Talent Highland for financial support.

References

- X. F. Li, E. Y. Ding, and G. K. Li, "A method of preparing spherical nano-crystal cellulose with mixed crystalline forms of cellulose I and II," *Chinese Journal of Polymer Science*, vol. 19, no. 3, pp. 291–296, 2001.
- M. Larssona, Q. Zhou, and A. Larssona, "Different types of microfibrillated cellulose as filler materials in polysodium acrylate superabsorbents," *Chinese Journal of Polymer Science*, vol. 29, no. 4, pp. 407–413, 2011.
- A. Sutka, S. Kukle, J. Gravitis, R. Milašius, and J. Malašauskiene, "Nanofibre electrospinning poly(vinyl alcohol) and cellulose composite mats obtained by use of a cylindrical electrode," *Advances in Materials Science and Engineering*, vol. 2013, Article ID 932636, 6 pages, 2013.
- B. Madsen and E. K. Gamstedt, "Wood versus plant fibers: similarities and differences in composite applications," *Advances in Materials Science and Engineering*, vol. 2013, Article ID 564346, 14 pages, 2013.
- Y. Wang, A. S. Angelatos, and F. Caruso, "Template synthesis of nanostructured materials via layer-by-layer assembly," *Chemistry of Materials*, vol. 20, no. 3, pp. 848–858, 2008.
- X. Zhang, H. Chen, and H. Y. Zhang, "Layer-by-layer assembly: from conventional to unconventional methods," *Chemical Communications*, no. 14, pp. 1395–1405, 2007.
- J. Bravo, L. Zhai, Z. Wu, R. E. Cohen, and M. F. Rubner, "Transparent superhydrophobic films based on silica nanoparticles," *Langmuir*, vol. 23, no. 13, pp. 7293–7298, 2007.
- R. M. Jisr, H. H. Rmaile, and J. B. Schlenoff, "Hydrophobic and ultrahydrophobic multilayer thin films from perfluorinated polyelectrolytes," *Angewandte Chemie*, vol. 44, no. 5, pp. 782–785, 2005.
- K. C. Wood, J. Q. Boedicker, D. M. Lynn, and P. T. Hammond, "Tunable drug release from hydrolytically degradable layer-by-layer thin films," *Langmuir*, vol. 21, no. 4, pp. 1603–1609, 2005.
- Y. Yan, G. K. Such, A. P. R. Johnston, H. Lomas, and F. Caruso, "Toward therapeutic delivery with layer-by-layer engineered particles," *ACS Nano*, vol. 5, no. 6, pp. 4252–4257, 2011.
- Q. Gao, Y. Y. Guo, W. Y. Zhang, H. L. Qi, and C. X. Zhang, "An amperometric glucose biosensor based on layer-by-layer GOx-SWCNT conjugate/redox polymer multilayer on a screen-printed carbon electrode," *Sensors and Actuators B: Chemical*, vol. 153, no. 1, pp. 219–225, 2011.
- A. Salimi and A. Noorbakhsh, "Layer by layer assembly of glucose oxidase and thiourea onto glassy carbon electrode: fabrication of glucose biosensor," *Electrochimica Acta*, vol. 56, no. 17, pp. 6097–6105, 2011.
- C. M. Dvoracek, G. Sukhonosova, M. J. Benedikt, and J. C. Grunlan, "Antimicrobial behavior of polyelectrolyte-surfactant thin film assemblies," *Langmuir*, vol. 25, no. 17, pp. 10322–10328, 2009.
- J. A. Lichter, K. J. van Vlietpa, and M. F. Rubner, "Design of antibacterial surfaces and interfaces: polyelectrolyte multilayers as a multifunctional platform," *Macromolecules*, vol. 42, no. 22, pp. 8573–8586, 2009.
- G. Laufer, F. Carosio, R. Martinez, G. Camino, and J. C. Grunlan, "Growth and fire resistance of colloidal silica-polyelectrolyte thin film assemblies," *Journal of Colloid and Interface Science*, vol. 356, no. 1, pp. 69–77, 2011.
- Y.-C. Li, S. Mannen, A. B. Morgan et al., "Intumescent all-polymer multilayer nanocoating capable of extinguishing flame on fabric," *Advanced Materials*, vol. 23, no. 34, pp. 3926–3931, 2011.
- A. Laachachi, V. Ball, K. Apaydin, V. Toniazzo, and D. Ruch, "Diffusion of polyphosphates into (poly(allylamine)-montmorillonite) multilayer films: flame retardant-intumescent films with improved oxygen barrier," *Langmuir*, vol. 27, no. 22, pp. 13879–13887, 2011.
- M. Durandish and A. Alipour, "Investigation into morphology, microstructure and properties of SBR/EPDM/ORGANO montmorillonite nanocomposites," *Chinese Journal of Polymer Science (English Edition)*, vol. 31, no. 4, pp. 660–669, 2013.
- H. Yang and Q. Zheng, "Structure stability of organic montmorillonite used for preparing polyethylene/montmorillonite nanocomposite," *Journal of Materials Science Letters*, vol. 22, no. 20, pp. 1431–1433, 2003.
- L. Xia, J. Xiong, B. Shentu, and Z. Weng, "Thermal-oxidative degradation and accelerated aging behavior of polyamide 6/epoxy resin-modified montmorillonite nanocomposites," *Journal of Applied Polymer Science*, vol. 131, no. 19, 2014.
- X. J. Zhang, F. Ren, L. Q. Zhang, D. Dong, K. Jiang, and Y. Lu, "Effects of the loading levels of organically modified montmorillonite on the flame-retardant properties of asphalt," *Journal of Applied Polymer Science*, vol. 131, no. 21, 2014.
- J. I. Morán, V. A. Alvarez, V. P. Cyras, and A. Vázquez, "Extraction of cellulose and preparation of nanocellulose from sisal fibers," *Cellulose*, vol. 15, no. 1, pp. 149–159, 2008.

- [23] G. Laufer, M. A. Priolo, C. Kirkland, and J. C. Grunlan, "High oxygen barrier, clay and chitosan-based multilayer thin films: an environmentally-friendly foil replacement," *Green Materials*, vol. 1, no. 1, pp. 4–10, 2013.
- [24] Y.-C. Li, J. Schulz, S. Mannen et al., "Flame retardant behavior of polyelectrolyte-clay thin film assemblies on cotton fabric," *ACS Nano*, vol. 4, no. 6, pp. 3325–3337, 2010.
- [25] Z. Lin, S. Rennecker, and D. P. Hindman, "Nanocomposite-based lignocellulosic fibers 1. Thermal stability of modified fibers with clay-polyelectrolyte multilayers," *Cellulose*, vol. 15, no. 2, pp. 333–346, 2008.
- [26] T. Zhang, H. Yan, M. Peng, L. Wang, H. Ding, and Z. Fang, "Construction of flame retardant nanocoating on ramie fabric via layer-by-layer assembly of carbon nanotube and ammonium polyphosphate," *Nanoscale*, vol. 5, no. 7, pp. 3013–3021, 2013.
- [27] G. Laufer, C. Kirkland, A. B. Morgan, and J. C. Grunlan, "Intumescent multilayer nanocoating, made with renewable polyelectrolytes, for flame-retardant cotton," *Biomacromolecules*, vol. 13, no. 9, pp. 2843–2848, 2012.
- [28] F. Carosio, G. Laufer, J. Alongi, G. Camino, and J. C. Grunlan, "Layer-by-layer assembly of silica-based flame retardant thin film on PET fabric," *Polymer Degradation and Stability*, vol. 96, no. 5, pp. 745–750, 2011.
- [29] Y.-C. Li, S. Mannen, J. Schulz, and J. C. Grunlan, "Growth and fire protection behavior of POSS-based multilayer thin films," *Journal of Materials Chemistry*, vol. 21, no. 9, pp. 3060–3069, 2011.

Research Article

Development of a Zero-Cement Binder Using Slag, Fly Ash, and Rice Husk Ash with Chemical Activator

M. R. Karim,¹ M. F. M. Zain,² M. Jamil,² and F. C. Lai³

¹Department of Civil Engineering, Dhaka University of Engineering and Technology, Gazipur 1700, Bangladesh

²Department of Architecture, University Kebangsaan Malaysia, 43600 Bangi, Selangor, Malaysia

³ATM, Sika Kimia Sdn Bhd, 71800 Nilai, Negeri Sembilan, Malaysia

Correspondence should be addressed to M. R. Karim; reza_civil128@yahoo.com and M. F. M. Zain; fauzi@vllis.eng.ukm.my

Received 22 October 2014; Accepted 20 February 2015

Academic Editor: Hao Wang

Copyright © 2015 M. R. Karim et al. This is an open access article distributed under the Creative Commons Attribution License, which permits unrestricted use, distribution, and reproduction in any medium, provided the original work is properly cited.

The increasing demand and consumption of cement have necessitated the use of slag, fly ash, rice husk ash (RHA), and so forth as a supplement of cement in concrete construction. The aim of the study is to develop a zero-cement binder (Z-Cem) using slag, fly ash, and RHA combined with chemical activator. NaOH, Ca(OH)₂, and KOH were used in varying weights and molar concentrations. Z-Cem was tested for its consistency, setting time, flow, compressive strength, XRD, SEM, and FTIR. The consistency and setting time of the Z-Cem paste increase with increasing RHA content. The Z-Cem mortar requires more superplasticizer to maintain a constant flow of 110 ± 5% compared with OPC. The compressive strength of the Z-Cem mortar is significantly influenced by the amounts, types, and molar concentration of the activators. The Z-Cem mortar achieves a compressive strength of 42–44 MPa at 28 days with 5% NaOH or at 2.5 molar concentrations. The FTIR results reveal that molecules in the Z-Cem mortar have a silica-hydrate (Si-H) bond with sodium or other inorganic metals (i.e., sodium/calcium-silica-hydrate-alumina gel). Therefore, Z-Cem could be developed using the aforementioned materials with the chemical activator.

1. Introduction

Cement and concrete are important materials for rapid urbanization. Concrete is considered as one of the key elements in the social, economic, and infrastructural development of human society. Ordinary Portland cement- (OPC-) based concrete is one of the significant construction materials in the globe. Up to now, we are still dependent on cement and concrete for the construction of many infrastructures such as buildings, towers, roads, bridges, flyovers, tunnels, industries, and river training works. Approximately 25 billion tons of concrete are produced and consumed annually all over the world. Cement consumption increased to 2.9 billion tons globally in a year and is predicted to increase to 4 billion tons by 2020 [1]. An alternative technology for the production of concrete without the use of cement does not currently exist. OPC is an energy-intensive material after steel and aluminum. OPC emits huge quantities of CO₂ gas to the atmosphere, about 7% of global emission [2]. These phenomena have necessitated the use of supplementary and/or

pozzolanic materials such as slag, fly ash (FA), and rice husk ash (RHA) in cement and concrete manufacturing. However, the use of pozzolanic materials, either natural, agricultural, or industrial by-products, in the production of composite cements has gained increasing interest because of various ecological, economical, technical, and diversified product quality reasons [3]. Sustainable concrete manufactured from pozzolanic materials is one of the solutions recommended by several researchers in the past few decades [2, 4, 5].

Pozzolans are fine materials that contain silica and/or alumina. They do not exhibit any cementing properties of their own, only in the presence of calcium oxide or calcium hydroxide. Silica and alumina in pozzolans also react and form cementitious materials [6]. Huge quantities of pozzolanic materials are regularly produced as wastes in every part of the world. All of these pozzolanic wastes are usually discharged into ponds, rivers, and lagoons without any commercial return. For instance, slag is a pozzolana generated as industrial by-product from steel industries. Approximately 100 million tons of slag is produced annually

worldwide. However, only 35 million tons of slag is used and the rest is disposed [2]. FA is another by-product generated from coal-operated power stations. About 900 million tons of FA is produced annually worldwide [5]. RHA is generated as a waste from rice-processing mills. Approximately 110 million tons [7] of rice husk (about 20% of 550 million tons of rice) and 16 million tons to 22 million tons of RHA are produced globally. No potential and/or alternative uses have been proposed for RHA. These wastes are not only accountable for spending huge expenses for transportation and/or removal but are also the cause of enormous environmental pollutions. These pozzolanic materials contain a high amount of silica and alumina in amorphous or crystal forms. Many researchers have recommended the use of these pozzolans as supplement of cement and as constituent of concrete because of their engineering, technical, financial, and environmental significance. The utilization of slag [8], FA [9], and RHA [10] significantly improves the strength and durability of mortar and concrete. A quaternary-blended cement was developed by Lai [11] by using slag, palm oil fuel ash, RHA, and timber ash with 66% OPC replacement, which was also used in high-strength (100 MPa to 120 MPa), sustainable, and high-performance concrete. Ehrenberg and Geiseler [12] reported that in manufacturing blended cement, the inclusion of slag and FA considerably reduces energy demand and CO₂ emission. Therefore, the use of pozzolans in cement and concrete construction is a valuable and appropriate step for solving or minimizing the important issues on CO₂ emission, sustainable concrete, environmental pollution, and demand/consumption of cement.

Pozzolans were used as partial replacement of cement in most of the past research. Some studies were conducted on the production of geopolymer concrete [13–16]. Geopolymer concrete is produced from aggregates with FA/slag that are activated using highly concentrated sodium hydroxide with sodium silicate (or potassium hydroxide with potassium silicate). The curing process of geopolymer concrete is usually performed at approximately 60°C to 90°C. Recently, Karim et al. [17, 18] reported a preliminary investigation for the development of an alternative cementitious binder by using slag + FA [17] and slag + palm oil fuel ash + RHA with only 5% sodium hydroxide [18] and calcium hydroxide by weight of binder, separately. However, they did not investigate the effects of types and contents (by weight and molar concentration) of the activator and its different content on the strength of the alternative cementitious binder. Considering all of these parameters, the current study investigates the possibility of developing a zero-cement binder (Z-Cem) using slag, FA, and RHA through the mechanical (i.e., grinding of materials) and chemical (using chemical activators) activation technique. To activate these materials, sodium hydroxide (NaOH), calcium hydroxide (Ca(OH)₂), and potassium hydroxide (KOH) were used by weight of Z-Cem and by their molar concentrations.

2. Materials and Methodology

2.1. Materials. Ground granulated blast furnace slag, FA, and RHA were used as raw materials. OPC type I was used to

compare the different properties of Z-Cem (i.e., physical, chemical, binding, flow, compressive strength, morphological, and microstructure). The slag was provided by a local cement company. FA was obtained from Klang power station, Selangor, Malaysia. RHA was produced using a special type of furnace available at the concrete and structure laboratory in University Kebangsaan Malaysia. The details of the furnace were reported by Zain et al. [19]. Standard sand manufactured by Societe Nouvelle Du Littoral, France (certified by the international organization of standardization) was used as fine aggregate for the preparation of the mortar. NaOH, KOH, and Ca(OH)₂ flakes of analytical grade, which were used as chemical activators, were obtained from Merck. Viscocrete 315 brand obtained from Sika Manufacturer was used as a superplasticizer (SP) to increase and maintain a sufficient flow for casting. The Viscocrete 315 is a high-range water reducer based on polycarboxylate-ether (PCE). It is a low-viscosity liquid that has been formulated by the manufacturer for use as received. Drinking water that is available in the concrete laboratory was used for the preparation of the mortar and in curing purposes.

2.2. Tests on Materials. The physical and chemical properties of the materials and those of Z-Cem were determined in different laboratories. The following tests and instruments were used to examine several properties of materials: the fineness of the materials was determined using an automatic Blaine machine. The grain size of the materials was analyzed using Malvern Mastersizer 2000. The amorphous or crystal phase of the materials was examined using X-ray diffraction (XRD) test. The chemical composition of materials was determined using X-ray fluorescence (XRF) test with a Bruker brand XRF machine. The morphological view and shape of the particles of the materials were examined by scanning electron microscopy (SEM) analysis by using Supra 55 VP (ZEISS).

2.3. Preparation of Paste and Mortar Specimens. Table 1 presents five different mixing proportions of the raw materials (i.e., slag, FA, RHA, SP, activators, and sand) for the development of Z-Cem. The fineness of Z-Cem was significantly improved by grinding RHA in a grinding machine. However, slag and FA were used as received from the industry. NaOH, KOH, and Ca(OH)₂ were used as chemical activators. The water-to-binder ratio (W/B) was kept at 0.55 to obtain a reasonable flow for easily casting. The solution-to-binder (S/B) ratio of the activator was kept as required to maintain a constant flow of 110 ± 5% for the mortars. The paste and mortar were mixed and prepared using a Hobart mixing apparatus according to ASTM C305 specification [20] via the two methods described below. The activators were used by weight (%) of Z-Cem and by their molar concentrations. Given that the same amount (%) of Ca(OH)₂, KOH, and NaOH produces different molar concentrations in the same amount of water, we used them in the same molar concentration.

2.3.1. Preparation of Mortar Using Activator by Weight. The activators were used according to the weight of the Z-Cem

TABLE 1: Materials used for the preparation of Z-Cem and OPC mortars (wt.%).

Binder	Raw materials (%)				SP	Activators	BSEN 196-1		ASTM C109	
	Slag	FA	RHA	OPC			W/B	Sa/B	S/B	Sa/B
Z-Cem 1	60	40	0	0	According to necessity	NaOH or KOH or Ca(OH) ₂	0.55	3.0	0.55 to 0.62	2.75
Z-Cem 2	55	35	10	0						
Z-Cem 3	50	30	20	0						
Z-Cem 4	40	30	30	0						
Z-Cem 5	70	20	10	0						
Cement	0	0	0	100	—	—	0.50	3.0	0.50	2.75

binder (i.e., 2.5%, 5.0%, and 7.5%). The W/B, S/B, and sand-to-binder (Sa/B) ratios are listed in Table 1. The required activator was dissolved in water. Generally, Ca(OH)₂ dilutes instantly, whereas KOH and NaOH need a little more time to be diluted. The NaOH flakes were diluted within 60 ± 10 seconds. The Z-Cem mortars can be cast easily for a minimum flow of 50%. Thus, to maintain a minimum mortar flow of 50% for easy casting, SP was used in various doses when necessary. After dilution of the activator, all raw materials (powder sample of Z-Cem, sand, chemical activator, water, and SP) were mixed using a Hobart mixture machine based on ASTM C305 [20] testing specification. Mortar prisms of 40 mm × 40 mm × 160 mm in size were prepared according to BS EN196-1 [21] testing procedure. Mortar specimens of 50 mm × 50 mm × 50 mm in size were also cast according to ASTM C109 specification [22]. The mortars were poured into the moulds and were compacted using a mechanical shaking table.

2.3.2. Preparation of Mortar Using Activator with Different Molar Concentrations. The mortar was prepared using different molar concentrations of the activators. The activators were produced at 1.0, 2.5, 5.0, and 7.5 M before preparing the Z-Cem mortar. Mortar cubes were cast according to ASTM C109 [22] specification by using the required materials in Table 1. The mortar was poured into the cube molds and was uniformly compacted using a vibrator table. Finally, molds of the Z-Cem mortars were opened after two days because the specimens could collapse if immersed into water for less than two days. The mortar specimens were then immersed in a water tank at room temperature of $25 \pm 2^\circ\text{C}$ for curing until desired testing ages of 3, 7, 14, and 28 days.

2.4. Testing of Paste and Mortar. The consistency and setting time of the pastes were determined according to ASTM C187 [23] and ASTM C191 [24] by using a Vicat apparatus. Mortar flow spread test was performed using a flow table based on the ASTM C1437 testing procedure [25]. The compressive strength of the mortar was determined according to BS EN196-1 [21] and ASTM C109 [22] testing procedures by using a universal testing machine (unit test Sdn Bhd brand with 1000 kN capacity). The mortar was also evaluated using SEM and XRD analysis. To determine the types of chemical bonding characteristics in the mortar, Fourier transform infrared (FTIR) test was performed using a PerkinElmer machine.

3. Results and Discussion

3.1. Properties of Materials. Various material properties such as chemical composition, fineness, specific gravity, XRD analysis, SEM analysis, and strength are presented and discussed below.

3.1.1. Chemical Composition. Table 2 presents the chemical properties of the materials. Among all materials, RHA contains the highest amount of silica (87.55%). The loss on ignition (LOI) is higher for FA but is less than 10%, as mentioned in ASTM C618 [6]. The SO₃ content of these materials is less than 4% based on the same standard, whereas the SO₃ content is nearly 1% for Z-Cems. LOI falls within the ASTM limit for all Z-Cem samples. Z-Cem has more than double amounts of silica, three to four times of alumina, and one-half to one-third part of the CaO content compared with OPC. The sum of the major oxides (SiO₂ + Al₂O₃ + Fe₂O₃) of Z-Cems ranges between 50% and 70%, which is greater than 50% (minimum) according to ASTM C618 for Class-C pozzolan [6]. Thus, Z-Cem could be considered as Class-C pozzolana.

3.1.2. Fineness. The particle sizes of the pozzolanic materials and Z-Cem samples are also shown in Table 2. The average particle sizes of slag, FA, RHA (ungrounded, UG), RHA (grounded, G), and OPC are 14.87, 14.45, 8.80, 6.72, and 16.79 μm, respectively. These results indicate that the slag, FA, and RHA (G) have smaller particle sizes compared with OPC. The materials have high specific surface areas (lower grain size), except for FA. The slag has an extensively high specific surface area of 1.155 m²/cm³, which is more than 1.5 times that of OPC. All of the Z-Cem samples have an average particle size of 10 ± 2 μm. All of the Z-Cems also have fineness that is 3.5 times greater than that of OPC. Z-Cems have specific surface areas that are 2.5 times greater than that of the OPC sample.

3.1.3. Microstructure of Materials. Figure 1 presents the SEM images of the raw materials. The SEM image of the slag shows square and diamond shapes, whereas the OPC sample has box-type and stone-type shapes. FA, as received from the industry, contains mostly spherical particles with rough surfaces. The SEM image of RHA (UG) shows very porous and spongy structures, which explain their high specific surfaces. The particles of RHA (UG) are angular, cellular, and

TABLE 2: Chemical and physical properties of the materials (wt.%).

(a) Chemical properties and oxide compositions (%)												
Materials	SiO ₂	Al ₂ O ₃	Fe ₂ O ₃	CaO	MgO	SO ₃	Na ₂ O	K ₂ O	P ₂ O ₅	TiO ₂	MnO	LOI
Slag	33.75	16.76	0.55	45.40	6.71	1.29	0.12	0.44	—	—	—	3.10
FA	58.95	20.24	5.18	3.04	0.52	0.48	0.14	1.32	0.65	1.08	0.12	3.16
RHA	87.55	0.39	0.20	1.03	0.67	0.57	0.05	2.85	1.31	0.02	0.07	3.14
OPC	20.94	4.63	4.46	67.17	2.53	2.98	0.04	0.15	—	—	—	1.29
*Z-Cem 1	43.41	17.91	2.39	28.22	4.05	0.92	0.13	0.78	—	—	—	3.13
*Z-Cem 2	47.59	16.12	2.12	25.92	3.78	0.89	0.13	0.98	—	—	—	3.12
*Z-Cem 3	51.76	14.33	1.86	23.62	3.50	0.86	0.12	1.17	—	—	—	3.11
*Z-Cem 4	57.23	12.73	1.82	19.22	2.93	0.80	0.11	1.41	—	—	—	3.11
*Z-Cem 5	43.70	15.54	1.43	32.21	4.66	1.00	0.12	0.84	—	—	—	3.09

*Calculated values.

(b) Physical properties								
	Specific gravity	Grain size (μm)			Fineness (m^2/gm)		Specific surface area (m^2/cm^3)	Pore volume (cm^3/gm)
		d_{10}	d_{50}	d_{90}	Blaine	BET		
Slag	2.84	2.65	14.87	37.57	0.3935	1.98	1.155	0.00617
FA	2.42	3.27	14.45	64.33	0.3567	2.34	0.785	0.00444
RHA (UG)	1.96	1.99	8.80	38.75	0.5780	—	1.225	—
RHA (G)	2.09	1.66	6.72	29.20	0.6975	12.70	1.502	0.00674
OPC	3.15	3.34	16.79	47.37	0.2302	1.54	0.715	0.00312
Z-Cem 1	2.65	1.24	11.23	65.19	0.8529	—	1.83	—
Z-Cem 2	2.59	1.24	11.03	70.61	0.8507	—	1.87	—
Z-Cem 3	2.55	1.10	9.28	46.83	0.9309	—	2.03	—
Z-Cem 4	2.49	1.03	8.90	47.20	0.9503	—	2.09	—
Z-Cem 5	2.68	1.32	11.65	66.32	0.8326	—	1.80	—

spongy. The SEM image of grounded RHA (G) is presented in Figure 1(d), which indicates that most plerospheres and large, irregular-shaped particles of RHA samples were crushed into smaller sizes after grinding. Therefore, Z-Cems produced from these pozzolanic materials contain very irregularly shaped particles with a porous cellular surface, which consequently increases the fineness and surface area of Z-Cem.

3.1.4. Morphology of Materials. Figure 2 shows the XRD patterns of the pozzolanic materials and OPC. RHA mainly contains amorphous materials with a small quantity of crystalline phase as cristobalite (high-temperature phase of SiO₂) and sylvite. The XRD pattern of the slag shows a crystalline phase of amorphous silica. The XRD pattern of FA shows that it is mainly composed of crystalline phases such as quartz and mullite. Only a few small peaks could be identified as crystalline silica, which is different from the XRD patterns of the slag and RHA. The amorphous silica present in these materials is responsible for the pozzolanic activity. Similar observations have been reported by other researchers [26, 27].

3.1.5. Strength Activity Index of Pozzolans. According to ASTM C311, the strength activity index (SAI) is the ratio between the compressive strength of a mortar containing substitute materials 20% by mass of binder and the average compressive strength of a reference cement mortar at

a designated age [28]. The SAI of the raw materials (FA and RHA) was determined according to this standard. Slag activity index, which is defined as similar to the SAI, only differs by 50% replacement of slag [29]. The compressive strength of the mortar was determined according to ASTM C109 [22]. The SAI of the materials was determined and the results are presented in Table 3. The results show that the SAI of slag is more than 100% for both 7 and 28 days. Thus, slag is considered as grade 100 based on ASTM C989 [29] classification. The SAI of FA mortars is just over 75% at 7 days; however, the value is over 88% at 28 days. Therefore, FA is considered as class F according to ASTM C618 [6] specification. The SAI of RHA (UG) is below 50% at 7 days and more than 63% at 28 days. The SAI of RHA was low because original and/or RHA (UG) were used in preparing the testing mortar. Usually, the SAI of any pozzolans can be improved by grinding or increasing their fineness, which can easily be seen from Table 3. Thus, the SAI of RHA (G) is much higher than that of RHA (UG) samples. Pozzolans can be activated greatly by improving their fineness [10, 30, 31].

3.2. Consistency of Paste. According to ASTM C187, consistency is defined as the amount of water required for a paste to penetrate the Vicat testing needle (10 mm in diameter) by 10 mm [23]. Table 4 provides the obtained consistencies of OPC and Z-Cem pastes. Table 4 indicates

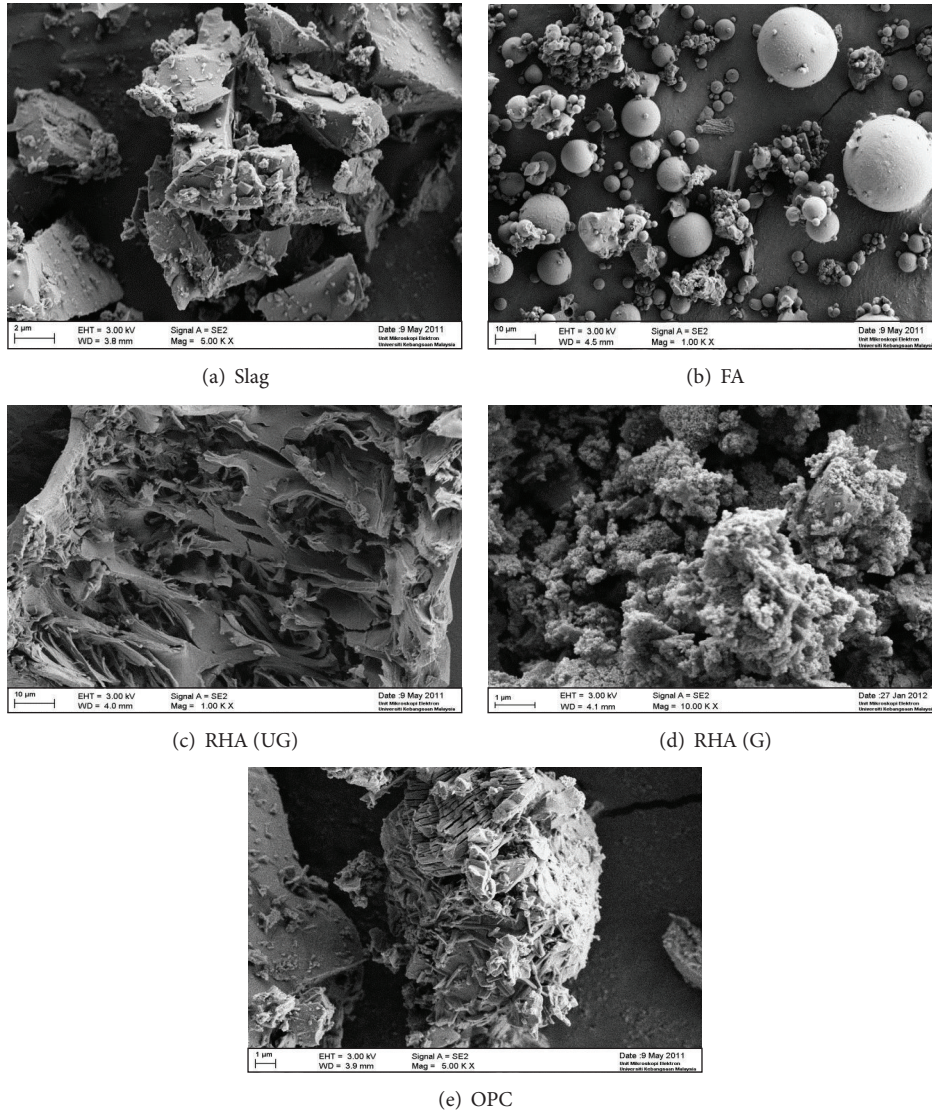


FIGURE 1: SEM images of the used materials.

TABLE 3: Strength activity index of pozzolans.

Materials	Strength activity at 7 days		Strength activity at 28 days	
	Activity index	ASTM requirement	Activity index	ASTM requirement
Slag	100.44	95 for 120 grade	103.88	95 for 100 grade
FA	75.36	75 for Class F	88.07	75 for Class F
RHA	48.58	—	63.04	—
RHA (G)	86.76	—	101.61	—

that the consistency of OPC is 30.5%, whereas that of Z-Cem pastes show increased values. Z-Cem pastes, as obtained from the slag, FA, and RHA, show a higher consistency (or more water demand) compared with OPC. The consistency for Z-Cem pastes varies between 32.5% and 42.5%. The Z-Cem paste possesses more consistency because of the porous and spongy particles of RHA (Figures 1(c) and 1(d)), more voids in the particles, and greater fineness of Z-Cem. Usually,

consistency increases for any blended paste of pozzolan with OPC. Ganesan et al. [32] reported that the consistency of RHA-blended pastes gradually increases with the addition of RHA. A similar finding was also reported by Cheerarot and Jaturapitakkul [33]. They claimed that the consistency of FA-blended paste is higher than that of OPC. Therefore, the greater consistency of the paste of Z-Cem (as produced from the blended materials of slag, FA, and RHA) is rational.

TABLE 4: Consistency and setting time of Z-Cem and OPC.

Binder	Normal consistency (%)	Setting time (h:min) with 5% activators					
		Ca(OH) ₂	Initial KOH	NaOH	Ca(OH) ₂	Final KOH	NaOH
Z-Cem 1	32.5	5:45	1:50	0:21	8:10	3:40	1:30
Z-Cem 2	35.8	7:10	3:40	0:42	—	—	2:20
Z-Cem 3	39.0	—	—	0:50	—	—	3:15
Z-Cem 4	42.5	—	—	1:10	—	—	3:40
Z-Cem 5	33.5	6:05	2:05	0:30	8:40	4:20	2:05
OPC	30.5	—	2:35	—	—	5:25	—

—: not determined exactly because setting time is more than 12 hours.

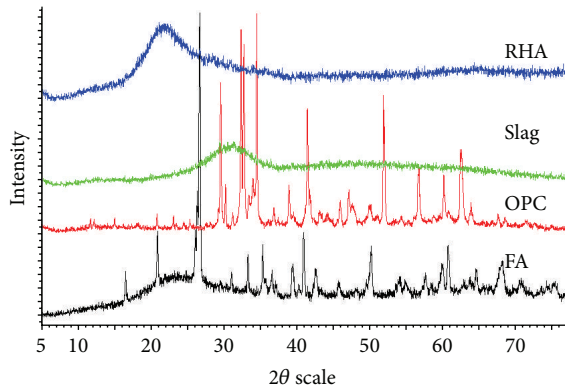


FIGURE 2: XRD patterns of the used materials.

3.3. Setting Time of Paste. The initial and final setting times of OPC and Z-Cem pastes are presented in Table 4. The setting time of Z-Cem is lesser when slag and FA are used but increases when RHA is added to Z-Cems (for Z-Cem 2, Z-Cem 3, Z-Cem 4, and Z-Cem 5). The initial setting time of OPC pastes is 155 min. The initial setting time of 30% RHA (Z-Cem 4) is the highest among all of the Z-Cem binders. The final setting time also increases for Z-Cem 4. The final setting times of Z-Cem pastes are within the ASTM C150 limit for the final setting time of OPC (≤ 375 min) [34]. An excess amount of silica increases the strength of the cement but prolongs its setting time. Larger quantities of alumina quicken the setting time but weaken the cement [35]. For the same reasons, among all of the Z-Cem pastes, Z-Cem 1 sets early because of the larger amount of alumina and lesser amount of silica. By contrast, Z-Cem 4 takes a longer time to set because it has more silica content and less alumina (as shown in Table 2). Although Z-Cems contain higher silica contents than that of OPC, Z-Cems set earlier than OPC. The setting time of Z-Cem is not only affected or controlled by its silica and alumina contents but also by the amount/concentration of the activator. Even though the same amount of activator was used in all of the Z-Cem pastes, the concentration of the activator was reduced for Z-Cem 2, Z-Cem 3, Z-Cem 4, and Z-Cem 5 because more amount of water was used (i.e., greater values of normal consistency of Z-Cem 2, Z-Cem 3, Z-Cem 4, and Z-Cem 5). Therefore, the setting times of Z-Cem 2, Z-Cem 3,

Z-Cem 4, and Z-Cem 5 gradually increase. The coarser particle size of FA and the spongy particle size of RHA could be the reasons for the longer setting time of the paste because they absorb more amount of water (can be seen from the normal consistency data), thereby resulting in the delay of the hydration process. Usually, smaller-sized particles react quickly than coarser particles. Thus, particles with a diameter between 1 and 10 μm will react within 1 day and 1 month, respectively, whereas particles over 50 μm will not completely react with the presence of sufficient amount of water [36]. The setting time of FA-blended paste increases compared with that of OPC [37]. Among the activators, NaOH contributes to the earlier setting of the Z-Cem because of its smaller cation (Na^+) compared with the other activators.

3.4. Flow of Mortar. Tables 5 and 6 show the measured flow of the mortar in different Z-Cem mixes and OPC in which the mortars were prepared according to BS EN196-1 [21] and ASTM C109 [22] testing standards, respectively. The flow value of the mortars depends on various factors including mix proportion, fineness of Z-Cem, amount of used SP, and types of activators. The flow value of the OPC mortar is over 80% without SP. For the utilization of NaOH, the flow decreases for Z-Cems 3 and 4 mortars, even though SP was added in the mortars. Although 3.5% SP was used in Z-Cem 4, its flow is less compared with those of other Z-Cems and OPC mortars. The lesser flow rate of the Z-Cem mortar is due to more water demand from slag, FA, and RHA, which were used in preparing Z-Cem. To maintain a constant flow of $110 \pm 5\%$, the highest amount of the activator's solution and SP are required with the use of NaOH, whereas $\text{Ca}(\text{OH})_2$ and KOH require less amount of solution. Similar observation has been reported in the literatures for mortar [38] and paste [39] prepared with potassium-based activators, which exhibits greater flow compared with those prepared with sodium-based activator. The lesser flow of mortar containing NaOH may be caused by the following reasons:

- (i) among the activators, NaOH has the smallest cation (Na^+), which may attract the molecules/constituents of the binder and the mortar and, consequently, reduce the flow of mortar;
- (ii) the lower flow tendency and the higher water demand are due to the porous and spongy nature of these

TABLE 5: Flow and SP requirements for 0.55 W/B ratio with Sa/B ratio of 3.0.

Binder	SP (%)	Flow (%) for using 5% activators by wt. of binder		
		Ca(OH) ₂	KOH	NaOH
Z-Cem 1	1.0	79	78	73
Z-Cem 2	1.0	68	59	51
Z-Cem 3	2.5	62	58	48
Z-Cem 4	3.5	74	70	58
Z-Cem 5	1.0	80	76	71
OPC	0.0	81		

TABLE 6: Activator's solution and SP requirement to maintain constant flow (110 ± 5%).

Binder	2.5 M Ca(OH) ₂ solution			2.5 M KOH solution			2.5 M NaOH solution		
	B/S	SP (%)	Flow	B/S	SP (%)	Flow	B/S	SP (%)	Flow
Z-Cem 1	0.55	4.0	113	0.58	4.0	109	0.62	4.2	112
Z-Cem 2	0.55	4.2	111	0.58	4.2	108	0.62	4.3	106
Z-Cem 3	0.55	4.5	106	0.58	4.4	113	0.62	4.5	109
Z-Cem 4	0.55	4.7	110	0.58	4.6	108	0.62	4.8	105
Z-Cem 5	0.55	4.2	108	0.58	4.0	107	0.62	4.2	106
OPC	Flow – 107, SP 0.0%								

materials (particularly for RHA) and the higher fineness or larger surface area; thus, more amount of water is required. Several researchers have reported that more amount of water is required to obtain the desired consistency; a lower flow ability is common among pozzolans [40, 41].

3.5. SP Requirement of Mortar. The amounts of SP are presented in Tables 5 and 6. Table 5 indicates that the Z-Cem mortar requires more SP. Moreover, SP requirement is varied for different Z-Cem mortars. This result could be due to the high fineness and porous surface of FA and RHA. In the Z-Cem mortar, SP requirement is greatly influenced by RHA content and the activators. For example, with NaOH, Z-Cem 1 (60% slag, 40% FA, and 0% RHA) shows 73% flow with 1% SP, whereas Z-Cem 4 (40% slag, 30% FA, and 30% RHA) provides 58% flow with 3.5% SP. Table 6 presents the SP content required for the mortar prepared with 2.5 M solution to maintain a constant flow of $110 \pm 5\%$, as specified in ASTM C109 [22]. The results show that compared with KOH and NaOH, Ca(OH)₂ produces a constant flow ($110 \pm 5\%$) with less S/B and SP content for the same Z-Cem mortar (i.e., Ca(OH)₂ requires less amount of solution and SP). Thus, the flow of the Z-Cem mortar is also greatly influenced by different activators. Among the three activators, Ca(OH)₂ possesses the highest flow ability. Given the application of molar-concentrated solution, SP requirement also increases within creasing RHA content (i.e., Z-Cem 2 to Z-Cem 5). Pozzolanic materials require greater amount of SP [41, 42].

3.6. Compressive Strength of Mortar. The compressive strengths of Z-Cem mortars are significantly influenced by the amount, type, and concentrations of activators, as discussed below.

3.6.1. Strength of Mortar as Influenced by Amount of Activators. To investigate the effect of the amount of activators (by weight of binder) on the strength of the mortar, Z-Cem 4 with three different activators was used because this mix gives the best compressive strength (Table 7). Mortar cubes were cast according to ASTM C109 [22]. Figure 3 presents the compressive strengths of the mortar with different activator contents. The figure demonstrates that when the same amount of activators was used, the strength of the Z-Cem mortar is less with Ca(OH)₂, whereas KOH and NaOH give better results. The rate of strength development of the Z-Cem mortar with KOH is slow compared with those of Ca(OH)₂ and NaOH at early ages, up to 7 days. It could be expected that there would be a retardation of reaction kinetics due to the utilization of potassium-based activator [38].

Due to the wide range of factors affecting the mechanical strength of the alkali activated binders and/or geopolymer, and the physical and chemical differences of the materials (slag, fly ash, metakaolin, and activators) and curing temperature used in the different researches, it is difficult to make direct comparison between strengths and other properties reported by the various authors. However, considering the relationship between the strength with molarity of activators and the types of activators, obtained results of this study have been compared with the others research findings in the relevant sections.

Figure 3 shows that Z-Cem achieves lesser strength at lower doses of activators (2.5%). A lower amount (2.5%) may not be sufficient to activate all of the molecules of Z-Cem. Besides, no significant effects on the strength development are observed with the addition of higher amount (7.5%) of Ca(OH)₂ and NaOH. The strengths of the mortars were almost the same for doses of 5.0% and 7.5% of the activators. However, at a dose of 7.5%, KOH imparted the highest strength to the Z-Cem mortar at 28 days but shows reduced

TABLE 7: Strength of mortar as influenced by types of activators.

Mortar	Activators (5% by weight)	Compressive strength (MPa) at different ages			
		3 days	7 days	14 days	28 days
Z-Cem 1	Ca(OH) ₂	—	2.61	6.59	18.10
	KOH	—	4.66	5.45	20.26
	NaOH	9.21	13.25	18.12	22.12
Z-Cem 2	Ca(OH) ₂	—	2.38	5.60	6.10
	KOH	—	3.32	6.20	26.35
	NaOH	10.24	14.65	20.12	28.32
Z-Cem 3	Ca(OH) ₂	—	5.22	10.42	13.35
	KOH	—	15.20	22.55	30.60
	NaOH	12.12	16.22	21.23	33.12
Z-Cem 4	Ca(OH) ₂	—	5.50	13.76	20.65
	KOH	—	9.53	19.10	27.46
	NaOH	13.87	20.12	34.15	42.24
Z-Cem 5	Ca(OH) ₂	—	6.30	12.70	14.90
	KOH	—	12.40	28.21	30.52
	NaOH	10.12	14.12	26.13	30.22
OPC	—	24.94	30.32	35.08	44.08

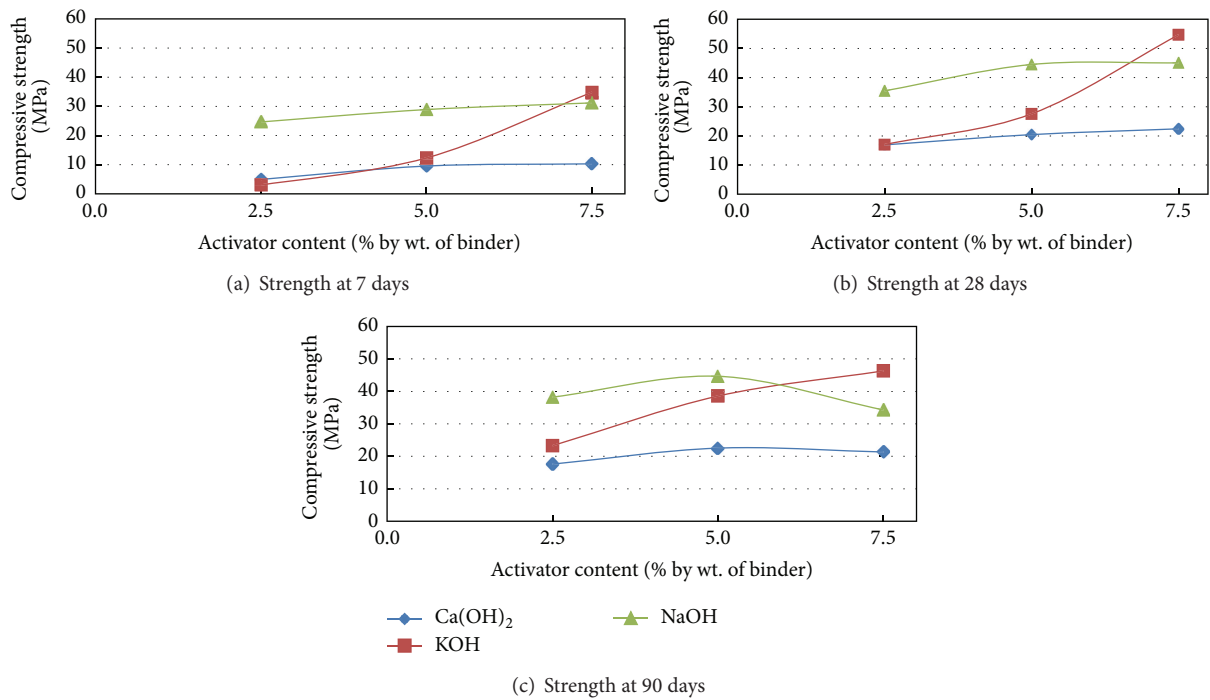


FIGURE 3: Compressive strength of mortar (Z-Cem 4) as influenced by amount of activators.

strength at 90 days. The strength of the mortar remains the same or decreases, which is most probably due to the excess amounts of activators that did not participate in the chemical reaction or weak intrabonds that have formed between them. These weak bonds may collapse at prolonged periods of time.

3.6.2. Strength of Mortar as Influenced by Types of Activators. To investigate the effect of different types of activators on the strength of the Z-Cem mortar, mortar prisms were cast

according to BS EN196-1 [21] standard. Table 7 presents the compressive strengths of Z-Cem mortars with different activators at various ages of mortar. Although 7.5% KOH imparts the best strength to the Z-Cem mortar, it develops the strength of the mortar very slowly at an earlier age. Therefore, activators were used by 5% weight of binder because this percentage of activators (NaOH and Ca(OH)₂) imparts better strength to the Z-Cem mortar (Figure 3). Table 7 shows that the strength development of the Z-Cem mortar is slow at

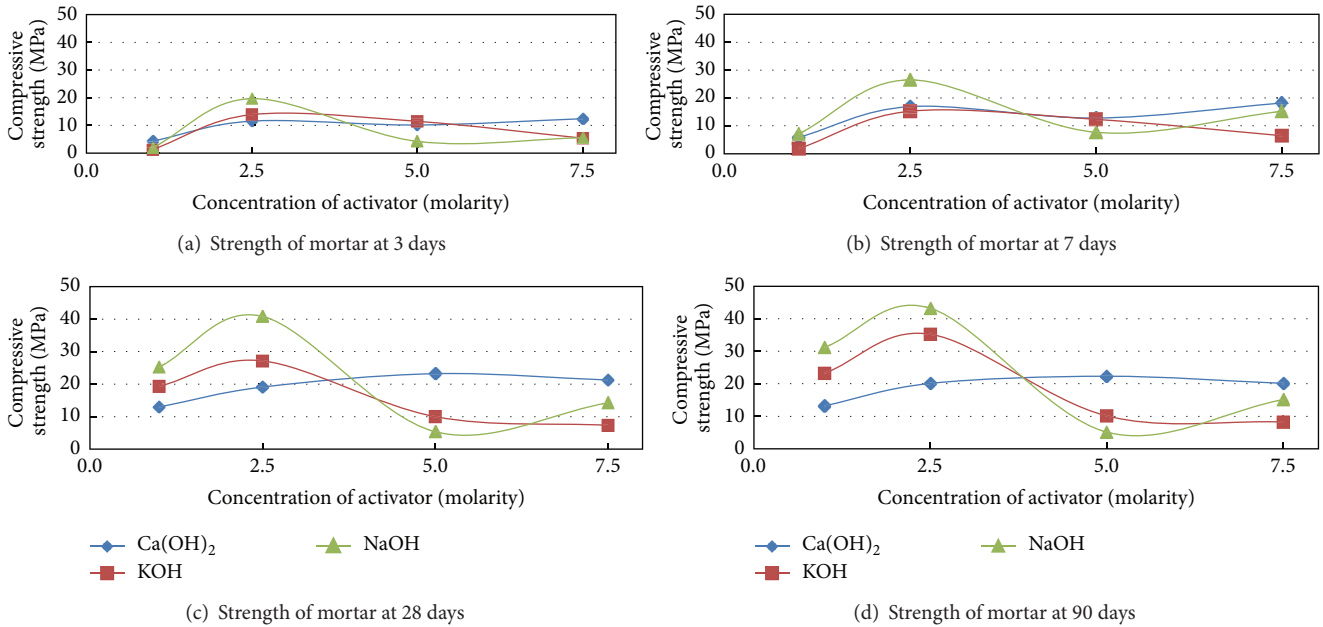


FIGURE 4: Strength of mortar (Z-Cem 4) for different concentrations of activators.

an early age (3 days), particularly for $\text{Ca}(\text{OH})_2$ and KOH , but it is considerable for the same amount of NaOH (5% weight of binder). Z-Cem 4 achieves the highest compressive strength (42.24 MPa at 28 days) with NaOH . The strength development of Z-Cem mortars with NaOH is similar to that of OPC, in which a reasonable strength is achieved at early and later ages. The Z-Cem 1 mortar has lesser strength compared with the OPC mortar. The compressive strengths of the Z-Cem 4 mortar at 3 and 7 days are greater than those specified in ASTM C150 (the minimum strength of OPC type I cement is 12.0 and 19.0 MPa at days 3 and 7, resp.) [34]. The Z-Cem mortars achieve considerable strengths because of greater fineness, which is an important property in increasing the strength of the mortar and the chemical action of activators. The grinding technique of slag and RHA could be demonstrated as a kind of mechanical activation for Z-Cem. Thus, grinding and the particle size of pozzolans are vital factors in increasing the strength of the mortar. Kiattikomol et al. [43] reported that a mortar with 20% OPC replacement had greater strength with higher fineness of FA. A comparable strength was found in other studies where greater fineness was observed in grounded RHA. OPC mortar and concrete with finer RHA were reported to have better strengths [10, 31, 44]. However, in the present study, the strength of the Z-Cem 1 (without RHA) mortar is less but increases with the presence of RHA (for Z-Cem 2, Z-Cem 3, Z-Cem 4, and Z-Cem 5). RHA might function as another activator for Z-Cem. Therefore, the developed strength of Z-Cem may be due to the following combined reasons:

- (i) better strength which was observed because of the presence of more silica in Z-Cem. Thus, Z-Cem 4 achieves the highest compressive strength because of its greater silica and lesser alumina contents [35] that

can be seen from the oxide composition of Z-Cem (Table 2);

- (ii) the chemical cross-linking action of RHA;
- (iii) the grinding effects of materials that lead to the increase in surface area or greater fineness of Z-Cem;
- (iv) effect of the binary or ternary blends of pozzolans in Z-Cem, because Joshi and Kadu [45] reported that FA-based geopolymer concrete (activated by 12 M–14 M NaOH solution) achieves a compressive strength of 14 MPa due to heat curing at 75°C for 24 hours. Ravikumar et al. [46] also found that FA-based geopolymer concrete (activated by 8 M NaOH solution) achieves a compressive strength of 29 MPa due to heat curing at 75°C for 48 hours;
- (v) chemical action of NaOH , $\text{Ca}(\text{OH})_2$, and KOH .

The strength development rate of the Z-Cem mortar is faster with NaOH , followed by $\text{Ca}(\text{OH})_2$ and KOH at an early age of up to 14 days. Thus, NaOH contributes to gain strength quickly which is similar argument as reported by Oh et al. [16] and Fernandez-Jimenez et al. [47]. This result may be due to the following reasons: (i) among the activators, NaOH has the smallest cation (Na^+), which may attract the molecules/constituents of the binder and the mortar, and consequently increase the intrabond of molecules in the mortar. To obtain better strength, a similar argument was reported by Pimraksa et al. [48] where they utilized NaOH . Rodríguez et al. [38] have reported that mortars produced with sodium-based activator present higher strength than those with potassium-based activator. Table 7 also indicates that with the same amount of the activator (5% by weight), NaOH contributes to the development of the highest strength

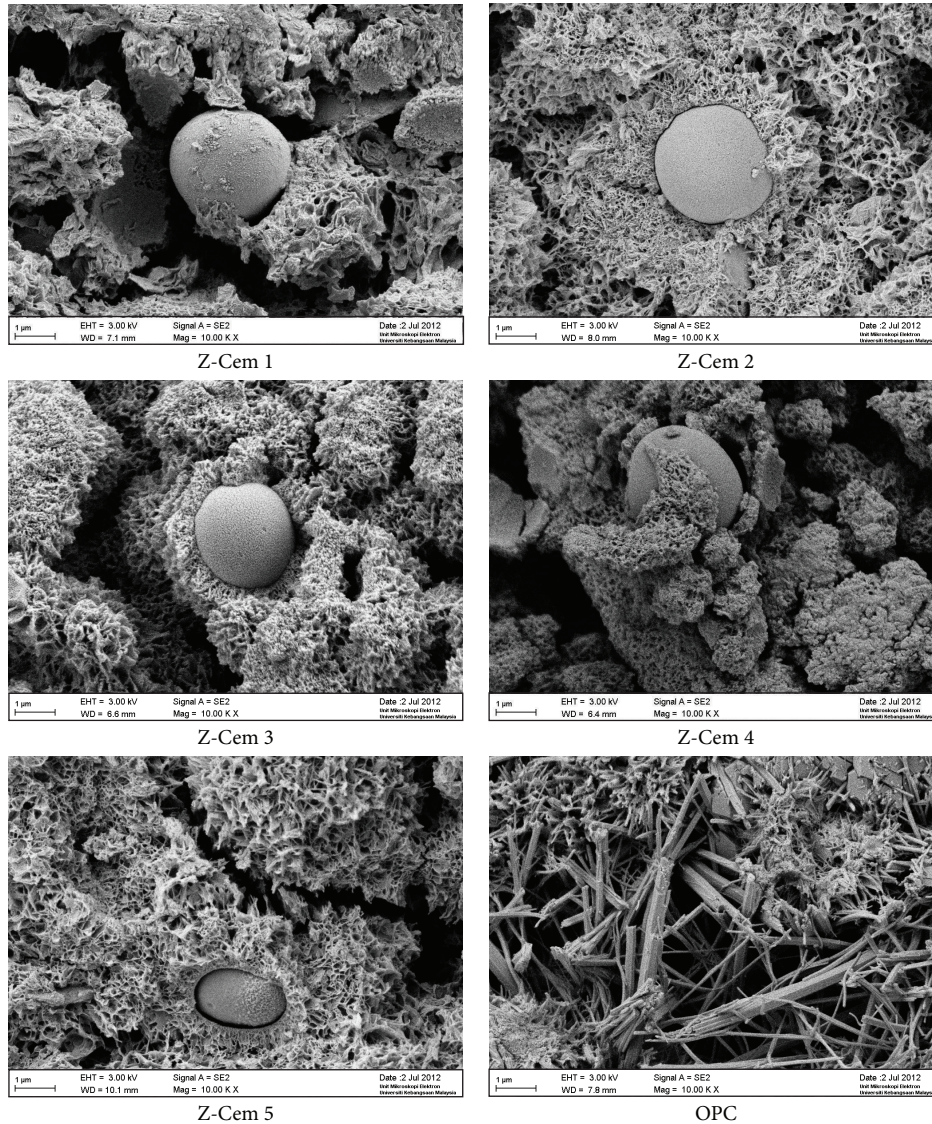


FIGURE 5: SEM images of OPC and Z-Cem mortars at 28 days of curing age.

of mortar among the activators. Therefore, to obtain a reasonable strength of the Z-Cem mortar, the use of grounded pozzolans with NaOH activator is the best technique.

3.6.3. Effects of Concentration of Activator on Mortar Strength.

To investigate the effects of the concentration of activators on the strength of the mortar, Z-Cem 4 was considered because it has the highest compressive strength. Mortar cubes were prepared according to ASTM C109 [22]. The compressive strengths of those specimens are presented in Figure 4. The figure shows that strength of mortar is influenced significantly by the concentration of activators which is similar conclusion reported by other researchers [46, 49]. However, the strength of the mortar is less when $\text{Ca}(\text{OH})_2$ is used with different concentrations. By contrast, the strength of the Z-Cem mortar is better with different molar concentrations of KOH and NaOH. The rate of strength

development of the Z-Cem mortar is slow for KOH compared with those of $\text{Ca}(\text{OH})_2$ and NaOH at early ages, up to 7 days and concentrations of 1.0 and 2.5 M. Rodríguez et al. [38] claimed that a retardation of reaction kinetics occurs due to the utilization of potassium-based activator. The higher concentrated solutions (over 5.0 M concentrations) of activators are insignificant in increasing the strength of the Z-Cem mortar, even though the strength of the mortar was reduced for 5.0 and 7.5 M activators. This result may be due to following causes:

- (i) a lower concentration (1.0 M) may not be sufficient to activate all of the molecules of Z-Cem;
- (ii) for a higher molarity (5.0 and 7.5 M), excess amounts of activators remain without forming weak intra-bonds inside the Z-Cem mortar. Residual activators or weak bonds of activators may collapse when the mortar is immersed in water for curing. As a result,

the strength of the mortar remains the same or decreases.

The Z-Cem mortar achieves the highest strength with 2.5 M activators. Therefore, based on experimental results, NaOH contributes in developing the highest strength of the Z-Cem mortar with 2.5 M solutions at all ages.

The strength of the mortar was determined using two testing methods (ASTM C109 and BS EN196-1). These two different methods were used to observe the effect of fixed W/B ratio and fixed flow on the strength of the Z-Cem mortar. Thus, the flow of the mortar was also determined using those methods. For a particular Z-Cem, no significant or remarkable strength variation is observed because of the fixed W/B ratio and flow. No more specific reasons are available to determine strength of mortar by using the two testing methods.

3.7. SEM Observation of Mortar. The SEM images of OPC and Z-Cem mortars at 28 days of curing are presented in Figure 5. SEM images of Z-Cem exhibit honeycomb type heterogeneous gel structure with embedded varying morphologies associated with hollow cavities, the same as geopolymer structure. A similar argument has been reported by Rodríguez et al. [38] for the alkali activated binder. In Figure 5, large differences in the microstructures of OPC and Z-Cem mortars are observed. The microstructures of the Z-Cem mortars change from large pores and/or honey combs to homogeneous small pores because of the increase in RHA content. Z-Cem 1 does not contain RHA, whereas Z-Cem 2, Z-Cem 3, Z-Cem 4, and Z-Cem 5 contain 10%, 20%, 30%, and 10% RHA, respectively. With the increase in RHA content, the pores in Z-Cem are reduced and confined. Spherical shape of FA particles (Figure 1(b)) could be another reason to densify the microstructure of Z-Cem mortars. Therefore, the strength development of the Z-Cem mortars is not only dependent on the chemical activator but also related to the amount of RHA and FA which contribute to the increase in silica content (Table 2). Fine particles of RHA, slag, and spherical particles of FA fill the small pores of Z-Cem and consequently increase the density of the mortar, which also leads to the increase in the compressive strength of the Z-Cem mortar. The existence of ettringite is observed in the SEM image of OPC, whereas ettringite is absent in the SEM images of the Z-Cem mortars, it contains sponge-type gel structure. Therefore, the strength development processes of Z-Cem and OPC mortars are likely not similar.

3.8. XRD Analysis of Mortar. Figure 6 presents the XRD patterns of the OPC and Z-Cem mortars at 28 days of curing. The Z-Cem mortars contain mainly crystalline materials with a small quantity of amorphous phase. The XRD patterns of the Z-Cem mortars also indicate that the mortars mainly contain silica in different forms. The Z-Cem mortars show peaks of silica, quartz, and syngenite at angles of 21°, 27°, and 38° at 2 θ . Aluminum sulfate hydrate and albite peaks are observed in the Z-Cem 1 and 4 mortars at angles of 24° and 28°, respectively, at 2 θ . By contrast, the peak of calcite is observed in the OPC samples at angles of 28° at 2 θ . Ca(OH)₂

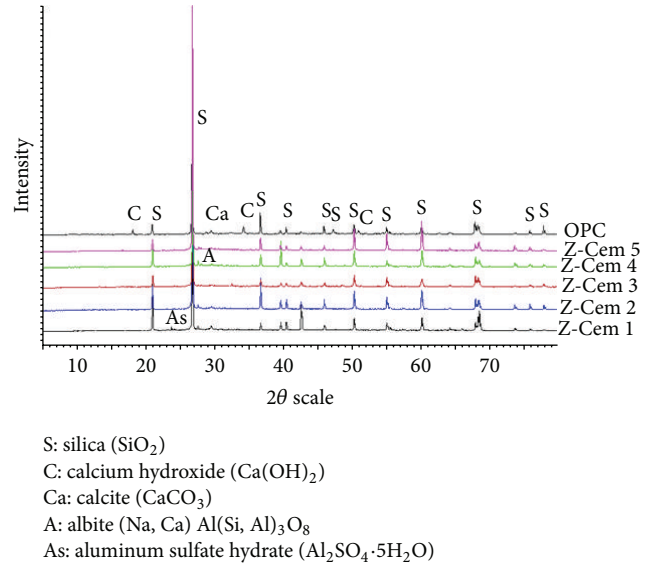


FIGURE 6: XRD pattern of the mortars at 28 days of curing age.

peaks are found in the OPC samples at angles of 18°, 34°, and 51° at 2 θ . Therefore, the peaks of OPC and Z-Cem mortars are alike throughout the analyzed angles with little dissimilarity.

3.9. FTIR Analysis of Mortar. To identify the chemical bonds in the molecules, FTIR analysis was performed in OPC and Z-Cem mortars. Figure 7 presents the results of the FTIR analysis. The characteristic bands were observed in Z-Cem 1 at wavelengths of 3958, 3822, 3724, 3625, 3478, 3371, 3103, 2996, 2750, 2663, 2452, 2367, 2275, 2159, 1949, 1818, 1454, 1366, 1118, 1029, 851, 648, and 420 cm⁻¹. Whereas OPC shows characteristic bands at wavelengths of 3942, 3827, 3703, 3618, 3463, 3274, 3177, 2972, 2751, 2654, 2557, 2450, 2357, 2133, 1938, 1816, 1516, 1437, 1295, 1218, 1117, 1020, 873, 646, 566, and 414 cm⁻¹. Almost the same wavelengths were observed for Z-Cem 3, 4, and 5 mortars. The band at 3822 cm⁻¹ or 3625 cm⁻¹ may be due to the presence of calcium hydroxide. The band near 3625, 3478, and 3371 cm⁻¹ (3300 cm⁻¹ to 3640 cm⁻¹) has been reported to be mainly due to the hydrogen bond vibration in either H-OH or Si-OH groups [50, 51]. The absorption at band near 1600 cm⁻¹ may be due to the presence of free water molecules, which indicates that water molecules are freely absorbed in the cement pores or are attached on the surface of calcium silicate hydrate (C-S-H). The band near 1440 cm⁻¹ is most probably due to the presence of a carbonate (CO₃²⁻) group. The broad band ranging from 950 cm⁻¹ to 1200 cm⁻¹ is due to the existence of a C-S-H structure (band at 3450 and 1600 cm⁻¹ represent C-S-H). The band at 984 cm⁻¹ may be due to the presence of a Si-O bond (i.e., sodium metasilicate (Na₂SiO₃·5H₂O)) [52]. Bands at approximately 880 cm⁻¹ are due to the presence of calcite. The bands at 648 cm⁻¹ may be due to Al-O vibrations of aluminate mineral components. The bands near 420 cm⁻¹ may be due to the existence of a Si-O bond. Similar observations have also been reported in past studies [50, 51]. Therefore, most of the

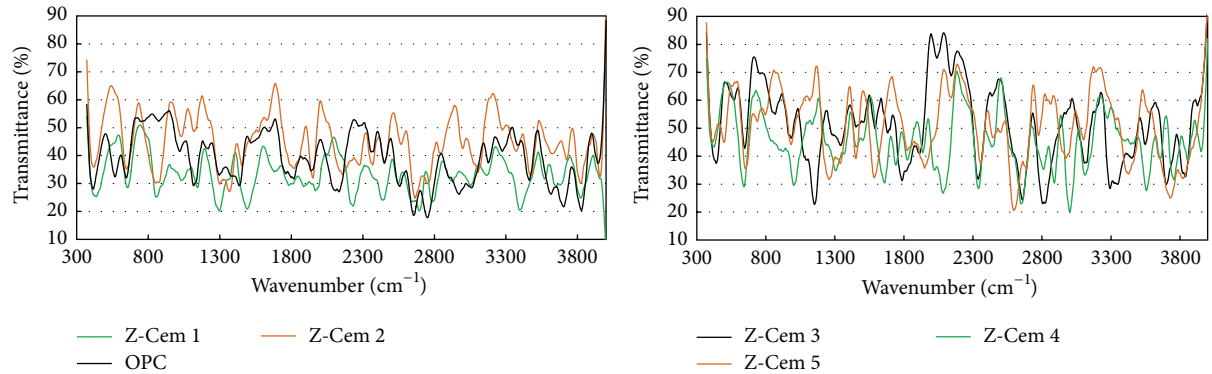


FIGURE 7: FTIR data of OPC and Z-Cem mortars.

molecules in the Z-Cem mortar are observed to have a silica-hydrate (Si-H) bond with sodium or other inorganic metals (i.e., sodium/calcium-silica-hydrate-alumina gel).

4. Conclusions

Based on the overall test results, the following conclusions are drawn from this study.

- (i) Slag and FA contain moderate amounts of SiO_2 , whereas RHA has a high percentage of SiO_2 . Z-Cem (combination of slag, FA, and RHA) contains over 50% major oxides ($\text{SiO}_2 + \text{Al}_2\text{O}_3 + \text{Fe}_2\text{O}_3$). As a result, Z-Cem functions as a binder with the presence of chemical activators such as NaOH, KOH, or $\text{Ca}(\text{OH})_2$ at an ambient temperature.
- (ii) Slag, FA, and RHA could be used as Z-Cem binders with the presence of a chemical activator provided that these materials should be processed properly while maintaining a high fineness value (combined Blaine fineness should be more than $8000 \text{ cm}^2/\text{gm}$).
- (iii) Z-Cem shows a reasonable consistency and setting time. The initial and final setting times of Z-Cem 4 (slag 40%, FA 30%, and RHA 30%) with 5% NaOH are 70 and 220 min., respectively. The flow value of the mortar of Z-Cem is satisfactory with the presence of SP.
- (iv) The strength of the Z-Cem mortars is significantly influenced by the amount, molar concentration, and type of activators. When the same amount or molar concentration of activators is used, NaOH contributes in achieving the highest strength of the Z-Cem mortar, except 7.5% KOH.
- (v) The mortar of Z-Cem 4 with NaOH has the highest strength. A minimum of 2.5% and/or 1.0 M solution of NaOH is required to obtain reasonable strength, which is more than 25 MPa at 28 days. NaOH could be used by 5% weight of binder or 2.5 M solution to obtain better and acceptable strength of more than 42 MPa at 28 days. The utilization of an activator of more than 5% by weight of binder or over 5.0 M is

insignificant to increase the strength of the Z-Cem mortar.

- (vi) The FTIR results reveal that molecules in the Z-Cem mortar are connected and linked with a silica-hydrate (Si-H) bond with sodium or other inorganic metals (i.e., sodium/calcium-silica-hydrate-alumina gel).
- (vii) The test results ensure that Z-Cem could be developed using locally available slag, FA, and RHA combined with the chemical activator. If slag, FA, and RHA are used as supplement for cement, the demand of cement should be reduced. Therefore, these materials can be consumed properly as Z-Cem binders that could also be used as sustainable binders in the near future.

Conflict of Interests

The authors declare that there is no conflict of interests regarding the publication of this paper.

Acknowledgments

The authors would like to express satisfaction to the Almighty Allah for performing this research. In particular, the authors appreciate and are grateful to the financial support and experimental assistance provided by the University Kebangsaan Malaysia; Ministry of Higher Education; Fundamental Research Grant Scheme; and Department of Civil and Structural Engineering in performing this research. The first author would like to thank Dhaka University of Engineering and Technology for permitting his study leave for the research.

References

- [1] P. Chana, "Low carbon cements: the challenges and opportunities," in *Proceedings of the Future Cement conference & Exhibition*, pp. 1–7, London, UK, February 2011.
- [2] P. K. Mehta, "Concrete technology for sustainable development," *Concrete International*, vol. 21, no. 11, pp. 47–52, 1999.
- [3] M. Öner, K. Erdogdu, and A. Günlü, "Effect of components fineness on strength of blast furnace slag cement," *Cement and Concrete Research*, vol. 33, no. 4, pp. 463–469, 2003.

- [4] M. Nehdi, "Ternary and quaternary cements for sustainable development," *Concrete International*, vol. 23, no. 4, pp. 35–42, 2001.
- [5] V. M. Malhotra, "Reducing CO₂ emissions," *ACI Concreter International*, vol. 28, no. 9, pp. 42–45, 2006.
- [6] ASTM C618, "Standard specification for coal fly ash and raw or calcined natural pozzolan for use as a mineral admixture in concrete," in *Annual Book of ASTM Standard 04.02*, pp. 310–313, 2001.
- [7] Torbed, "Energy technology application description, energy & amorphous silica production from rice husk," April 2011, <http://www.torftech.com/pdf/application%20description%20-%20rice%20hulls.pdf>.
- [8] A. Oner and S. Akyuz, "An experimental study on optimum usage of GGBS for the compressive strength of concrete," *Cement and Concrete Composites*, vol. 29, no. 6, pp. 505–514, 2007.
- [9] A. Oner, S. Akyuz, and R. Yildiz, "An experimental study on strength development of concrete containing fly ash and optimum usage of fly ash in concrete," *Cement and Concrete Research*, vol. 35, no. 6, pp. 1165–1171, 2005.
- [10] A. N. Givi, S. A. Rashid, F. N. A. Aziz, and M. A. M. Salleh, "Assessment of the effects of rice husk ash particle size on strength, water permeability and workability of binary blended concrete," *Construction and Building Materials*, vol. 24, no. 11, pp. 2145–2150, 2010.
- [11] F. C. Lai, "High volume quaternary blended cement for sustainable high performance concrete," in *Proceedings of the 34th Conference on Our World in Concrete & Structure*, vol. 80, pp. 175–180, August 2009.
- [12] A. Ehrenberg and Geiseler, "Jokologische Eigenschaften von Hochofenzement, Bstion-Informationen," vol. 37, no. 4, pp. 51–63, In Bensted and Barnes, *Structure and Performance of Cement*, 2nd Eds, Spon press, London and New York, pp. 310–25.
- [13] D. Hardjito, S. E. Wallah, D. M. J. Sumajouw, and B. V. Rangan, "On the development of fly ash-based geopolymer concrete," *ACI Materials Journal*, vol. 101, no. 6, pp. 467–472, 2004.
- [14] D. Hardjito, S. E. Wallah, D. M. J. Sumajouw, and B. V. Rangan, "Fly ash-based geopolymer concrete: study of slender reinforced columns," *Journal of Materials Science*, vol. 42, no. 9, pp. 3124–3130, 2007.
- [15] P. Duxson, A. Fernández-Jiménez, J. L. Provis, G. C. Lukey, A. Palomo, and J. S. J. van Deventer, "Geopolymer technology: the current state of the art," *Journal of Materials Science*, vol. 42, no. 9, pp. 2917–2933, 2007.
- [16] J. E. Oh, P. J. M. Monteiro, S. S. Jun, S. Choi, and S. M. Clark, "The evolution of strength and crystalline phases for alkali-activated ground blast furnace slag and fly ash-based geopolymers," *Cement and Concrete Research*, vol. 40, no. 2, pp. 189–196, 2010.
- [17] M. R. Karim, M. F. M. Zain, M. Jamil, and F. C. Lai, "An experimental study on utilization of slag and fly ash as an alternative cementitious binder," *Journal of Scientific Research*, vol. 2, no. 11, pp. 620–625, 2012.
- [18] M. R. Karim, M. F. M. Zain, M. Jamil, and F. C. Lai, "Fabrication of a non-cement binder using slag, palm oil fuel ash and rice husk ash with sodium hydroxide," *Construction and Building Materials*, vol. 49, pp. 894–902, 2013.
- [19] M. F. M. Zain, M. N. Islam, F. Mahmud, and M. Jamil, "Production of rice husk ash for use in concrete as a supplementary cementitious material," *Construction and Building Materials*, vol. 25, no. 2, pp. 798–805, 2011.
- [20] ASTM C 305-06, "American society for testing and materials," in *Annual Book of ASTM Standards, Cement, Lime, Gypsum*, vol. 04.01, pp. 228–230, 2009.
- [21] BSI, "Methods of testing cement, part 1: determination of strength," EN 196-1:2005, British Standards Institution, 2005.
- [22] ASTM C109, "Standard test methods for compressive strength of hydraulic cement using 50mm cube specimens," *Annual book of ASTM standard 04.01*, pp. 78–85, 2009.
- [23] ASTM C187, "Standard test methods for normal consistency of hydraulic cement," in *Annual Book of ASTM Standard, Cement, Lime, Gypsum*, vol. 04.01, pp. 181–183, 2009.
- [24] ASTM C191, "Standard test methods for setting time of hydraulic cement by Vicat needle," in *Annual Book of ASTM Standard Cement, Lime, Gypsum*, vol. 04.01, pp. 186–191, 2009.
- [25] ASTM C1437-07, "American society for testing and materials, Annual book of ASTM standards, Cement, lime, gypsum," vol. 04.01, pp. 622–23, 2009.
- [26] Q. Feng, H. Yamamichi, M. Shoya, and S. Sugita, "Study on the pozzolanic properties of rice husk ash by hydrochloric acid pretreatment," *Cement and Concrete Research*, vol. 34, no. 3, pp. 521–526, 2004.
- [27] A. Salas, S. Delvasto, R. M. de Gutierrez, and D. Lange, "Comparison of two processes for treating rice husk ash for use in high performance concrete," *Cement and Concrete Research*, vol. 39, no. 9, pp. 773–778, 2009.
- [28] ASTM C311, "Standard test methods for sampling and testing of fly ash or natural pozzolan for use in Portland-cement concrete," in *ASTM C311-05, Annual Book of ASTM Standard*, vol. 04.02, pp. 207–215, 2006.
- [29] ASTM C989, *Standard Specification for Ground Granulated Blast-Furnace Slag for Use in Concrete and Mortars*, vol. 04.02, 2006.
- [30] P. Chindaprasirt, C. Jaturapitakkul, and U. Rattanasak, "Influence of fineness of rice husk ash and additives on the properties of lightweight aggregate," *Fuel*, vol. 88, no. 1, pp. 158–162, 2009.
- [31] G. R. de Sensale, "Strength development of concrete with rice-husk ash," *Cement and Concrete Composites*, vol. 28, no. 2, pp. 158–160, 2006.
- [32] K. Ganesan, K. Rajagopal, and K. Thangavel, "Rice husk ash blended cement: assessment of optimal level of replacement for strength and permeability properties of concrete," *Construction and Building Materials*, vol. 22, no. 8, pp. 1675–1683, 2008.
- [33] R. Cheerarat and C. Jaturapitakkul, "A study of disposed fly ash from landfill to replace Portland cement," *Waste Management*, vol. 24, no. 7, pp. 701–709, 2004.
- [34] ASTM C150, "Standard specification for Portland cement," in *Annual Book of ASTM Standard*, vol. 04.01, pp. 152–157, 2009.
- [35] B. C. Punmia, A. K. Jain, Kr. Arun, and A. M. Jain, "Basic Civil Engineering," Firewall Media, p. 117, 2003.
- [36] Science of Concrete, <http://iti.northwestern.edu/cement/index.html>.
- [37] W. Tangchirapat, T. Saeting, C. Jaturapitakkul, K. Kiattikomol, and A. Siripanichgorn, "Use of waste ash from palm oil industry in concrete," *Waste Management*, vol. 27, no. 1, pp. 81–88, 2007.
- [38] E. D. Rodríguez, S. A. Bernal, J. L. Provis, J. Paya, J. M. Monzo, and M. V. Borrachero, "Effect of nanosilica-based activators on the performance of an alkali-activated fly ash binder," *Cement and Concrete Composites*, vol. 35, no. 1, pp. 1–11, 2013.
- [39] J. W. Phair and J. S. J. Van Deventer, "Effect of silicate activator pH on the leaching and material characteristics of waste-based

- inorganic polymers," *Minerals Engineering*, vol. 14, no. 3, pp. 289–304, 2001.
- [40] S. Y. Ahmad and Z. Shaikh, "Portland-pozzolana cement from sugarcane bagasse ash," in *Lime and Other Alternative Cements*, pp. 172–179, Neville Hill, London, UK, 1992.
- [41] P. Chindapasirt, S. Rukzon, and V. Sirivivatnanon, "Resistance to chloride penetration of blended Portland cement mortar containing palm oil fuel ash, rice husk ash and fly ash," *Construction and Building Materials*, vol. 22, no. 5, pp. 932–938, 2008.
- [42] S. Rukzon and P. Chindapasirt, "An experimental investigation of the carbonation of blended portland cement palm oil fuel ash mortar in an indoor environment," *Indoor and Built Environment*, vol. 18, no. 4, pp. 313–318, 2009.
- [43] K. Kiattikomol, C. Jaturapitakkul, S. Songpiriyakij, and S. Chutubtim, "A study of ground coarse fly ashes with different finenesses from various sources as pozzolanic materials," *Cement and Concrete Composites*, vol. 23, no. 4-5, pp. 335–343, 2001.
- [44] D. D. Bui, J. Hu, and P. Stroeven, "Particle size effect on the strength of rice husk ash blended gap-graded Portland cement concrete," *Cement and Concrete Composites*, vol. 27, no. 3, pp. 357–366, 2005.
- [45] S. V. Joshi and M. S. Kadu, "Role of alkaline activator in development of eco-friendly fly ash based geopolymer concrete," *International Journal of Environmental Science and Development*, vol. 3, no. 5, pp. 417–421, 2012.
- [46] D. Ravikumar, S. Peethamparan, and N. Neithalath, "Structure and strength of NaOH activated concretes containing fly ash or GGBFS as the sole binder," *Cement and Concrete Composites*, vol. 32, no. 6, pp. 399–410, 2010.
- [47] A. Fernandez-Jimenez, F. Puertas, and A. Arteaga, "Determination of kinetic equations of alkaline activation of blast furnace slag by means of calorimetric data," *Journal of Thermal Analysis and Calorimetry*, vol. 52, no. 3, pp. 945–955, 1998.
- [48] K. Pimraksa, P. Chindapasirt, A. Rungchet, K. Sagoe-Crentsil, and T. Sato, "Lightweight geopolymer made of highly porous siliceous materials with various $\text{Na}_2\text{O}/\text{Al}_2\text{O}_3$ and $\text{SiO}_2/\text{Al}_2\text{O}_3$ ratios," *Materials Science and Engineering A*, vol. 528, no. 21, pp. 6616–6623, 2011.
- [49] E. Altan and S. T. Erdogan, "Alkali activation of a slag at ambient and elevated temperatures," *Cement and Concrete Composites*, vol. 34, no. 2, pp. 131–139, 2012.
- [50] K. Sakr, "Effects of silica fume and rice husk ash on the properties of heavy weight concrete," *Journal of Materials in Civil Engineering*, vol. 18, no. 3, pp. 367–376, 2006.
- [51] N. B. Singh, V. D. Singh, S. Rai, and S. Chaturvedi, "Effect of lignosulfonate, calcium chloride and their mixture on the hydration of RHA-blended portland cement," *Cement and Concrete Research*, vol. 32, no. 3, pp. 387–392, 2002.
- [52] F. A. Miller and C. H. Wilkins, "Infrared spectra and characteristic frequencies of inorganic ions: their use in qualitative analysis," *Analytical Chemistry*, vol. 24, no. 8, pp. 1253–1294, 1952.

Research Article

Removal of Organic Dyes by Nanostructure ZnO-Bamboo Charcoal Composites with Photocatalysis Function

Xinliang Yu,¹ Aimiao Qin,¹ Lei Liao,² Rui Du,¹ Ning Tian,¹ Song Huang,¹ and Chun Wei¹

¹Key Lab New Processing Technology for Nonferrous Metals & Materials, Ministry of Education, College of Materials Science & Engineering, Guilin University of Technology, No. 12 Jiangan Road, Guilin 541004, China

²College of Environmental Science & Engineering, Guilin University of Technology, No. 12 Jiangan Road, Guilin 541004, China

Correspondence should be addressed to Aimiao Qin; 592491245@qq.com

Received 23 July 2014; Revised 19 December 2014; Accepted 8 January 2015

Academic Editor: Hao Wang

Copyright © 2015 Xinliang Yu et al. This is an open access article distributed under the Creative Commons Attribution License, which permits unrestricted use, distribution, and reproduction in any medium, provided the original work is properly cited.

Composites of nanostructure zinc oxide (nano-ZnO) and bamboo charcoal (BC) were successfully prepared via impregnation-precipitation method. The products were characterized by XRD, SEM, and EDS. Rhodamine B (RhB) and acid fuchsin (AF) were selected as the organic dyes of photocatalysis degradation under the irradiation of ultraviolet light (UV). The influence of particle size of BC, irradiation time, pH value of the solution, and additive amount of H₂O₂ on removal of the dyes has been studied. The results show that smaller particle size of BC in the composites has a better removal effect. The composites possess the highest removal capacity for RhB and AF under the conditions of pH = 2 and pH = 5.4, respectively. The optimum additive amount of H₂O₂ for 5 mL RhB and AF was 0.050 mL and 0.1 mL, with a removal rate of 93% and 99%, respectively.

1. Introduction

Nano-ZnO is considered to be one of the most promising highly active photochemical catalysts for its advantages such as high efficiency, energy saving, cleaning, nontoxicity, and no secondary pollution [1]. In the past few years, the study on its preparation method and catalytic performance has been one of the hot areas of research activities [2–4]. The photocatalysis mechanism is that, under irradiation of light, ZnO is emitted to produce a large number of electron-hole pairs in which the electrons have strong reducibility and the holes have strong oxidizability. Due to the oxidation of OH⁻ and H₂O molecules by the holes, highly active hydroxyl free radicals ([•]OH) with strong oxidizability generate. Subsequently, organics are oxidized by [•]OH and ultimately degraded into CO₂, H₂O, and other nontoxic inorganic small molecules [5]. At present, photocatalysis applications of ZnO concentrated on the sewage treatment and removal of interior organic contaminants [6, 7]. Most of the organics in the water can be oxidized and removed, including chloroform, carbon tetrachloride, and trichloroethylene, which are difficult to eliminate through traditional water treatment methods. In addition, heavy metal ions in the water can also be reduced

by the electrons in the conduction band without affecting the beneficial mineral elements for human beings [8–10]. However, actual applications of powdery nanometer oxide photocatalysts are limited due to some disadvantages such as low light utility efficiency, difficulties in separation, and recovery [11]. Further researches will focus on development of novel nano-ZnO material which is easier to commercially produce accompanied with lower energy consumption and higher photocatalytic activity.

Bamboo charcoal (BC) prepared from pyrolysis of bamboo presents a porous structure with a surface area of 360 m²/g and even 1000 m²/g if further treated, which is 2–5 times higher than that of the ordinary carbon [12]. Owing to the specific structure characteristics, BC exhibits strong adsorption performance to many kinds of contamination in air and water, and thus it can be applied in air purification, sewage filtering, and food preservation as a new functional material [13–15]. However, BC is unsuitable to be used alone as an adsorbent because of the secondary pollution caused by the incomplete removal of pollutants. Besides, its adsorption performance will decrease gradually as time goes on.

With synergistic reaction of absorption of BC and catalytic degradation of nanophotocatalysts, study of

nanomodified BC is believed to make good sense [16]. Chuang et al. [17], Zhou et al. [18], and Zhang et al. [19] have reported that nano-TiO₂ modified BC has a good photocatalysis performance to lots of organic pollutants. However, as one of the most common semiconductor photocatalysts as TiO₂, researches on nano-ZnO modified BC are very few. In fact, ZnO has a better photocatalysis performance than TiO₂ under specific conditions [20–22]. As an efficient photocatalyst, ZnO would likely replace TiO₂ in the future owing to the same band-gap energy, similar photocatalytic mechanism, and lower cost [23]. Our previous research showed that ZnO/BC composites prepared via impregnation-precipitation method have a good removal rate of methylene blue by more than 95% [24]. Rhodamine-B (RhB) and acid fuchsin (AF) are commonly used organic dyes in industry of spin printing and dyeing and biomedicine study. Due to the high concentration in the effluents and the higher stability of these modern synthetic dyes, the conventional biological treatment methods are ineffective for the complete removal and degradation, which are harmful to the environment and hazardous to human health. Therefore, the further study on the removal of another two basic organic dyes, RhB and AF, was carried out.

2. Materials and Experiments

2.1. Reagents and Materials. In this paper, the following chemicals were used: zinc oxide (ZnO, AR, ShanTou West Long Chemical Co., Ltd.); polyethylene glycol-6000 (PEG-6000, CP, Shantou West Long Chemical Co., Ltd.); sodium hydroxide (NaOH, AR, Guangdong Guanghua Chemical Factory Co., Ltd.); absolute ethyl alcohol (C₂H₅OH, AR, Tianjin Damao Chemical Reagent Factory); bamboo charcoal (BC, Jiangmen Jinrong Household Products Co., Ltd.); rhodamine B (RhB, AR, Tianjin Institute of Chemical Reagents); acid fuchsin (AR, Shanghai SSS Reagent Co., Ltd.); hydrochloric acid (HCl, 36–38%, AR, ShanTou West Long Chemical Co., Ltd.); and hydrogen peroxide (H₂O₂, 30%, AR, ShanTou West Long Chemical Co., Ltd.). Distilled water was used throughout the experiments.

2.2. Modification of BC by ZnO Nanoparticles. BC is modified by nano-ZnO via impregnation-precipitation method [25]. That is, BC as a carrier is soaked in soluble zinc salt solution for a period of time so that Zn²⁺ can be absorbed on the surface of BC adequately. Then NaOH as the precipitation agent is added into the solution to form precipitation with the absorbed Zn²⁺. Under the heating conditions, nano-ZnO generated and loaded on surface of BC.

In a typical experiment, BC was ground into powder and sieved to various particle sizes: 250–550 μm, 120–250 μm, 75–120 μm, and less than 75 μm. 0.5 g as-prepared BC powder was dispersed in 30 mL mixed solution containing 0.2 g PEG-6000 and 0.086 g ZnSO₄·7H₂O with distilled water as a solvent and stirred for 4 h. Then 20 mL NaOH (0.03 mol/L) was added dropwise into above mixture and kept on stirring for 8 h. Next, the mixture was kept at 80 °C for 50 min. After cooling, the products were filtered and washed repeatedly

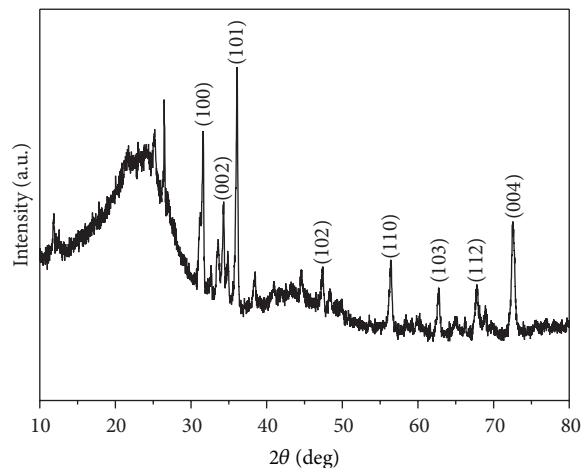


FIGURE 1: XRD pattern of the nano-ZnO/BC composites.

with distilled water until pH = 7. The final composites were obtained by drying at 80 °C for 12 h.

2.3. Characterizations. The XRD patterns were recorded via X-ray diffractometer (Netherlands PANalytical Company). The SEM images were acquired on JSM-6380LV scanning electron microscope (NEC Electronics Corporation). Elemental analysis was taken by an OIMS energy dispersive X-ray spectroscopy and UV-VIS was tested on UV-3600 ultraviolet-visible spectrophotometer (Shimadzu Corporation) at a range of 200 nm to 800 nm.

2.4. Removal of the Organic Dyes by Nano-ZnO/BC Composites. 2 mg/L RhB and 20 mg/L AF solution were prepared firstly. Then 0.1 g nano-ZnO/BC composites were added into 5 mL as-prepared organic dyes and the formed suspension system was irradiated by UV ($\lambda = 254$ nm). After specific time, the liquid phase was separated by centrifuging (10000 r/min) and the absorbance was detected by UV-VIS.

According to Lambert-Beer's law [26], the removal rate of the dyes is calculated by the following formula:

$$\text{Removal rate (\%)} = \frac{C_0 - C}{C_0} \times 100\% = \frac{A_0 - A}{A_0} \times 100\%. \quad (1)$$

In this formula, C_0 and C are defined as the initial concentration of the dyes and the concentration after photocatalysis reaction. A_0 and A are defined as the initial absorbance and the absorbance after photocatalysis reaction.

3. Results and Discussions

3.1. Structure Analysis. Figure 1 shows the XRD patterns of the ZnO/BC composites. Two broad peaks appearing around 24° and 43° indicate the typical peaks of amorphous carbon with noncrystalline structures. Typical characteristic peaks of ZnO can be observed on the diffraction patterns, which correspond to the (100), (002), (101), (102), (110), (103), (112),

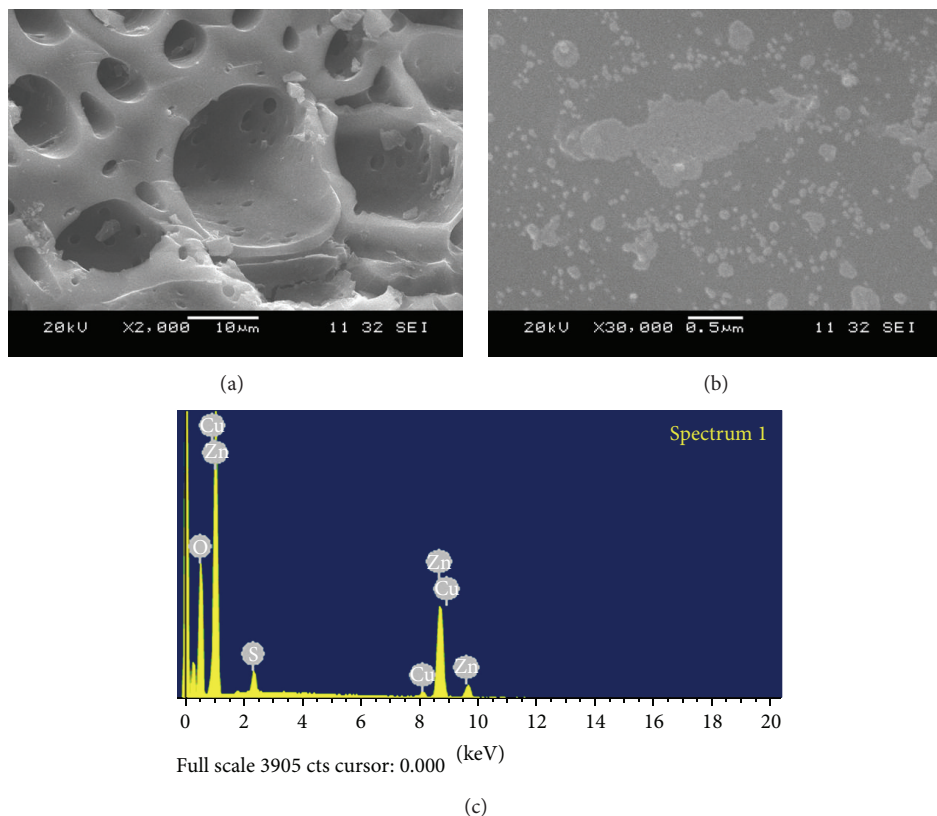


FIGURE 2: SEM images (a), (b) and EDS spectrum (c) of the nano-ZnO/BC composites.

and (004) planes in the reference PDF card (JCPDS 89-0511). The XRD result suggests that BC is a typical amorphous carbon and ZnO is assigned to hexagonal zincite structure.

3.2. Morphology and Component Analysis. The SEM images and the EDS analysis of the composites are shown in Figure 2. Figure 2(a) illustrates that BC presents a typical honeycomb structure with a large number of macropores with the diameter of 1–15 μm on the cross section. Figure 2(b) reveals that ZnO particles are mostly less than 50 nm in diameter and some are aggregated because of the high surface energy. The EDS result in Figure 2(c) shows that, besides Cu introduced by sample stage, O and Zn are mainly detected and the calculated atom ratio is close to 1:1. A small amount of S may derive from BC.

3.3. Photodegradation Studies of the Organic Dyes

3.3.1. Effect of Particle Size of BC. Table 1 presents the influence of particle size of BC on the removal of the organic dyes under UV for 15 min. The removal rates of RhB and AF increase by 41.49% and 25.20% when the particle size of BC decreases from 250–550 μm to ≤75 μm. The reason should be attributed to the stronger adsorption of the smaller particle with larger specific surface area. But if particle size is too small, preparation time will be longer and separation of the liquid-solid phase would be more difficult. So the particle size should be controlled to a specific region according to actual requirement.

TABLE 1: Influence of particle size of BC on removal of the organic dyes.

Particle size/μm	Removal rate of RhB/%	Removal rate of AF/%
250–550	43.46	61.60
120–250	54.32	73.76
75–120	55.79	81.56
≤75	84.95	86.80

3.3.2. Effect of Time. The influence of irradiation time of UV on the removal of the organic dyes is shown in Figure 3. It can be seen that the removal rate increases rapidly in the beginning and becomes stable after 60 min, which is because the concentration of the dyes falls down over time and the diffusion layer thickness surrounding the adsorbent particles decreases [27].

3.3.3. Effect of pH Value. Figure 4 shows the influence of the pH value of the solution on the removal of the organic dyes under UV for 15 min. The pH value was adjusted by HCl and NaOH. It is clear that the removal rate of two organic dyes is affected greatly by pH value. At lower pH value, the removal rate of RhB is higher than that under neutral and alkaline condition. It should be noted that when the pH value is 2.0, the removal rate reaches to 65% after only 15 min photocatalysis reaction. However, strong acid condition plays an opposite role in the removal of AF compared with RhB.

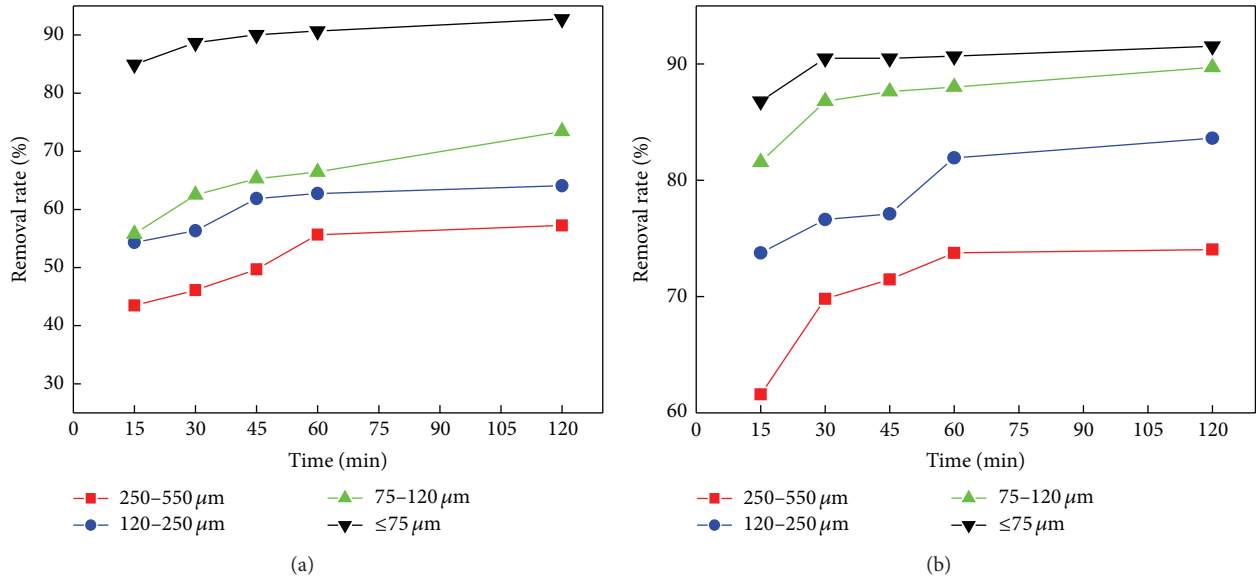


FIGURE 3: Influence of irradiation time of UV on the removal of the organic dyes by nano-ZnO/BC composites with different particle size of BC: (a) RhB, (b) AF.

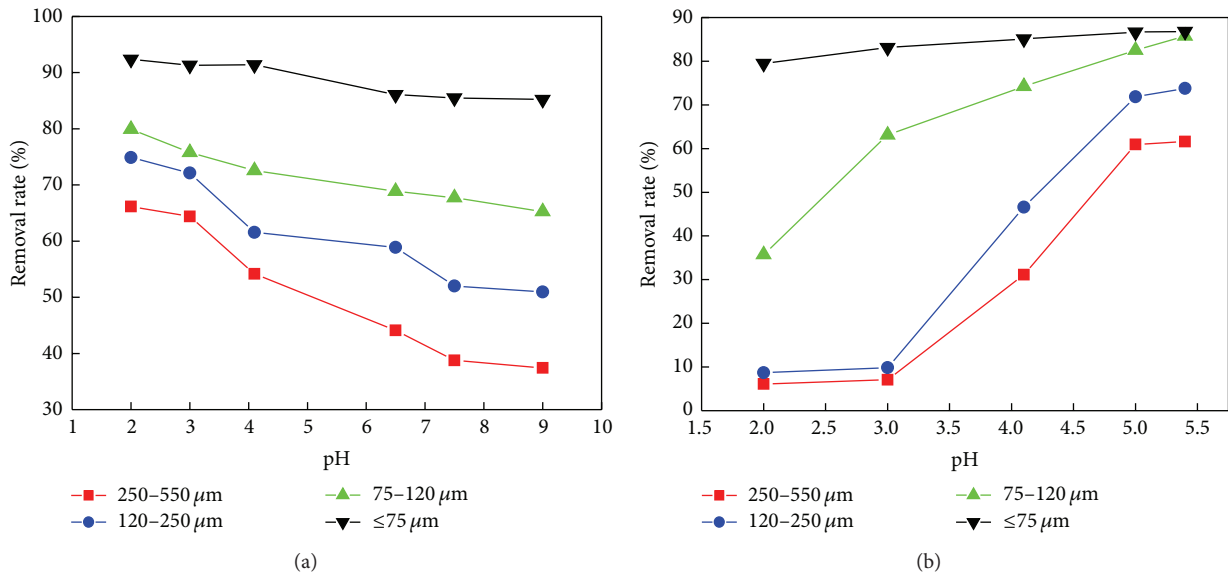


FIGURE 4: Influence of pH value on removal of the organic dyes by nano-ZnO/BC composites with different particle size of BC: (a) RhB, (b) AF.

The removal rate of AF improves much as the pH value increases. Therefore, pH value has different influences on removal of different organic dyes, for it affects not only the surface properties of ZnO but also the dissociation of dye molecules and the formation of hydroxyl radicals [28].

3.3.4. Effect of Additive Amount of H_2O_2 . Figure 5 shows the influence of additive amount of H_2O_2 on the removal of the organic dyes under UV for 15 min. A considerable improvement of the removal rate can be observed due to an increase of $\cdot OH$ in the solution after a small amount of H_2O_2 is added. For RhB, the removal rate reaches a relatively high level when the amount of H_2O_2 is 0.05 mL. However, as

concentration increases continuously, the removal rate begins to decrease. The reason may be that excess H_2O_2 acts as a hole or $\cdot OH$ scavenger or reacts with ZnO and forms peroxy compounds, which are detrimental to the photocatalysis action [29]. For AF, the removal rate increases significantly when the additive amount of H_2O_2 is less than 0.1 mL. It should be emphasized that when the particle size of BC is less than 75 μm, the removal rate of AF is close to 100% by the addition of only a little H_2O_2 solution. Therefore, more H_2O_2 is not necessarily better to assure a higher removal rate. To avoid waste, the optimum amount of H_2O_2 in this experiment is 0.05 mL and 0.1 mL for 5 mL RhB and 5 mL AF.

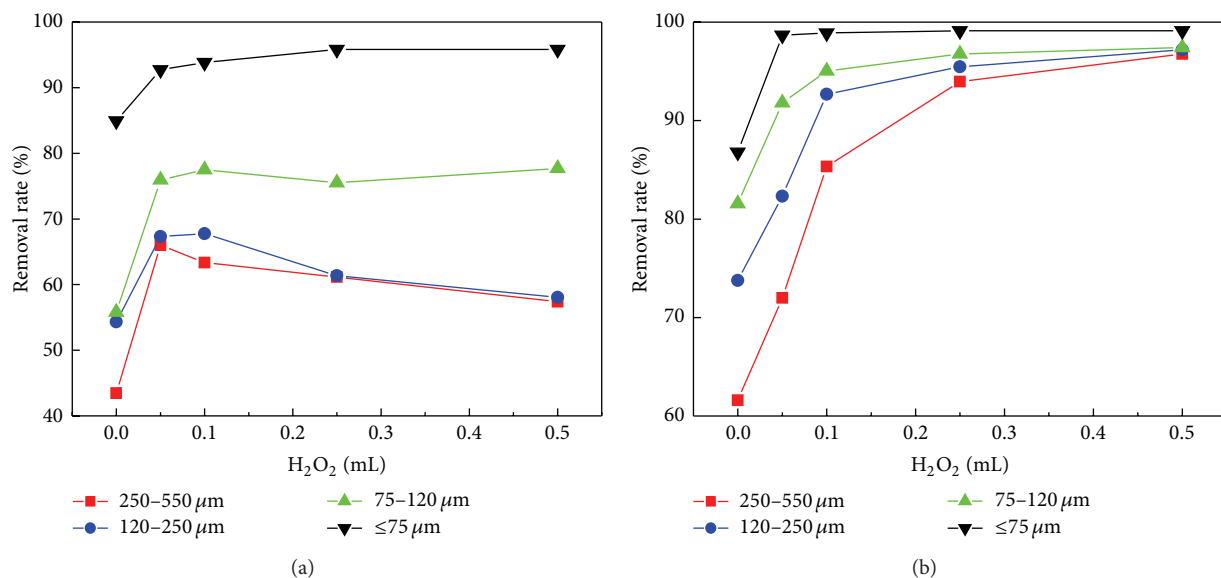


FIGURE 5: Influence of additive amount of H₂O₂ on removal of the organic dyes by nano-ZnO/BC composites with different particle size of BC: (a) RhB, (b) AF.

4. Conclusions

Nano-ZnO/BC composites were prepared via impregnation-precipitation method. The impact factors such as particle size of BC, irradiation time, pH value of solution, and additive amount of H₂O₂ on the photocatalysis properties of the composites are discussed. The results show that the as-prepared ZnO/BC composites are assigned to wurtzite of hexagonal crystal structure. Smaller particle size of BC shows better removal effect on the dyes. The removal rate of RhB is much higher under strong acid condition but it is better for removal of AF under weak acid condition. In addition, a certain amount of H₂O₂ contributes to the removal of the dyes for the enhanced oxidation of solution.

Conflict of Interests

The authors declare that there is no conflict of interests regarding the publication of this paper.

Acknowledgments

This work was supported by the National Science Foundation of China (under Grants nos: 21063005, 50968005, 21264005, and 51163003) and by the National Science Foundation of Guangxi Province (2014GXNSFAA118331 and 2010GXNSFC013007).

References

- [1] C. Tian, Q. Zhang, A. Wu et al., "Cost-effective large-scale synthesis of ZnO photocatalyst with excellent performance for dye photodegradation," *Chemical Communications*, vol. 48, no. 23, pp. 2858–2860, 2012.
- [2] Z. L. Wang, "Ten years' venturing in ZnO nanostructures: from discovery to scientific understanding and to technology applications," *Chinese Science Bulletin*, vol. 54, no. 22, pp. 4021–4034, 2009.
- [3] S. J. Pearton, D. P. Norton, K. Ip, Y. W. Heo, and T. Steiner, "Recent progress in processing and properties of ZnO," *Progress in Materials Science*, vol. 50, no. 3, pp. 293–340, 2005.
- [4] Z. Y. Fan and J. G. Lu, "Zinc oxide nanostructures: synthesis and properties," *Journal of Nanoscience and Nanotechnology*, vol. 5, no. 10, pp. 1561–1573, 2005.
- [5] D. Li and H. Haneda, "Morphologies of zinc oxide particles and their effects on photocatalysis," *Chemosphere*, vol. 51, no. 2, pp. 129–137, 2003.
- [6] J. Peral, X. Domènech, and D. F. Ollis, "Heterogeneous photocatalysis for purification, decontamination and deodorization of air," *Journal of Chemical Technology and Biotechnology*, vol. 70, no. 2, pp. 117–140, 1997.
- [7] S. Lathasree, A. N. Rao, B. Sivasankar, V. Sadasivam, and K. Rengaraj, "Heterogeneous photocatalytic mineralisation of phenols in aqueous solutions," *Journal of Molecular Catalysis A: Chemical*, vol. 223, no. 1-2, pp. 101–105, 2004.
- [8] A. A. Aal, S. A. Mahmoud, and A. K. Aboul-Gheit, "Nanocrystalline ZnO thin film for photocatalytic purification of water," *Materials Science and Engineering C*, vol. 29, no. 3, pp. 831–835, 2009.
- [9] C. Hariharan, "Photocatalytic degradation of organic contaminants in water by ZnO nanoparticles: revisited," *Applied Catalysis A: General*, vol. 304, pp. 55–61, 2006.
- [10] Z. Han, L. Liao, Y. Wu, H. Pan, S. Shen, and J. Chen, "Synthesis and photocatalytic application of oriented hierarchical ZnO flower-rod architectures," *Journal of Hazardous Materials*, vol. 217–218, pp. 100–106, 2012.
- [11] O. Legrini, E. Oliveros, and A. M. Braun, "Photochemical processes for water treatment," *Chemical Reviews*, vol. 93, no. 2, pp. 671–698, 1993.

- [12] Q. S. Zhang, "Playing great attention on bamboo chemical processing and exploiting bamboo charcoal applying technique," *Journal of Bamboo Research*, vol. 20, pp. 34–43, 2001 (Chinese).
- [13] S.-Y. Wang, M.-H. Tsai, S.-F. Lo, and M.-J. Tsai, "Effects of manufacturing conditions on the adsorption capacity of heavy metal ions by Makino bamboo charcoal," *Bioresource Technology*, vol. 99, no. 15, pp. 7027–7033, 2008.
- [14] M. Wang, Z.-H. Huang, G. Liu, and F. Kang, "Adsorption of dimethyl sulfide from aqueous solution by a cost-effective bamboo charcoal," *Journal of Hazardous Materials*, vol. 190, no. 1–3, pp. 1009–1015, 2011.
- [15] P. Liao, S. H. Yuan, W. J. Xie, W. Zhang, M. Tong, and K. Wang, "Adsorption of nitrogen-heterocyclic compounds on bamboo charcoal: kinetics, thermodynamics, and microwave regeneration," *Journal of Colloid and Interface Science*, vol. 390, no. 1, pp. 189–195, 2013.
- [16] C. M. Lu, "Photocatalytic oxidation of propoxur insecticide with titanium dioxide supported on activated carbon," *Journal of Environmental Science and Health Part B*, vol. 34, pp. 207–223, 1999.
- [17] C. S. Chuang, M.-K. Wang, C.-H. Ko, C.-C. Ou, and C.-H. Wu, "Removal of benzene and toluene by carbonized bamboo materials modified with TiO_2 ," *Bioresource Technology*, vol. 99, no. 5, pp. 954–958, 2008.
- [18] J. B. Zhou, C. J. Deng, J. H. Fu, and Q. S. Zhang, "Adsorption and degradation of toluene over TiO_2 supported on bamboo charcoal," *Carbon*, vol. 47, p. 2941, 2009.
- [19] J. Zhang, D. Zhao, J. Wang, and L. Yang, "Photocatalytic oxidation of dibenzothiophene using TiO_2 /bamboo charcoal," *Journal of Materials Science*, vol. 44, no. 12, pp. 3112–3117, 2009.
- [20] C. Lizama, J. Freer, J. Baeza, and H. D. Mansilla, "Optimized photodegradation of reactive blue 19 on TiO_2 and ZnO suspensions," *Catalysis Today*, vol. 76, no. 2–4, pp. 235–246, 2002.
- [21] A. A. Khodja, T. Sehili, J.-F. Pilichowski, and P. Boule, "Photocatalytic degradation of 2-phenylphenol on TiO_2 and ZnO in aqueous suspensions," *Journal of Photochemistry and Photobiology A: Chemistry*, vol. 141, no. 2-3, pp. 231–239, 2001.
- [22] H.-L. Liu and T. C.-K. Yang, "Photocatalytic inactivation of *Escherichia coli* and *Lactobacillus helveticus* by ZnO and TiO_2 activated with ultraviolet light," *Process Biochemistry*, vol. 39, no. 4, pp. 475–481, 2003.
- [23] N. Daneshvar, D. Salari, and A. R. Khataee, "Photocatalytic degradation of azo dye acid red 14 in water on ZnO as an alternative catalyst to TiO_2 ," *Journal of Photochemistry and Photobiology A: Chemistry*, vol. 162, no. 2-3, pp. 317–322, 2004.
- [24] A. M. Qin, H. N. Chen, and P. Tang, in *Proceedings of the 7th China Conference on Functional Materials and Applications*, 3rd Section, 2010.
- [25] H.-D. Zhuang, S.-F. Bai, X.-M. Liu, and Z.-F. Yan, "Structure and performance of Cu/ZrO₂ catalyst for the synthesis of methanol from CO₂ hydrogenation," *Journal of Fuel Chemistry and Technology*, vol. 38, no. 4, pp. 462–467, 2010.
- [26] J. D. Ingle and S. R. Crouch, *Spectrochemical Analysis*, Prentice Hall, Upper Saddle River, NJ, USA, 1988.
- [27] C. Namasivayam and R. T. Yamuna, "Removal of Rhodamine-B by biogas waste slurry from aqueous solution," *Water, Air, and Soil Pollution*, vol. 65, no. 1-2, pp. 101–109, 1992.
- [28] K. Byrappa, A. K. Subramani, S. Ananda, K. M. Lokanatha Rai, R. Dinesh, and M. Yoshimura, "Photocatalytic degradation of rhodamine B dye using hydrothermally synthesized ZnO," *Bulletin of Materials Science*, vol. 29, no. 5, pp. 433–438, 2006.
- [29] I. Poullos and I. Tsachpinis, "Photodegradation of the textile dye Reactive Black 5 in the presence of semiconducting oxides," *Journal of Chemical Technology and Biotechnology*, vol. 74, no. 4, pp. 349–357, 1999.

Research Article

Effect of Three Bioenzymes on Compaction, Consistency Limits, and Strength Characteristics of a Sedimentary Residual Soil

Tanveer Ahmed Khan¹ and Mohd Raihan Taha^{1,2}

¹Department of Civil and Structural Engineering, Universiti Kebangsaan Malaysia (UKM), 43600 Bangi, Selangor, Malaysia

²Institute for Environment and Development (LESTARI), Universiti Kebangsaan Malaysia (UKM), 43600 Bangi, Selangor, Malaysia

Correspondence should be addressed to Tanveer Ahmed Khan; takhan557@gmail.com

Received 30 October 2014; Accepted 1 March 2015

Academic Editor: Hao Wang

Copyright © 2015 T. A. Khan and M. R. Taha. This is an open access article distributed under the Creative Commons Attribution License, which permits unrestricted use, distribution, and reproduction in any medium, provided the original work is properly cited.

Bioenzymes are organic degradable materials, currently introduced as soil improvement additives. In this experimental study, three types of bioenzymes from three different countries were used to improve Universiti Kebangsaan Malaysia (UKM) soil. UKM soil has properties quite similar to soils recommended as suitable by bioenzyme suppliers. The effect of the three bioenzymes on Atterberg limits, compaction characteristics, and unconfined compressive strength was studied. Controlled untreated and treated samples for two dosages at curing times up to three months were prepared and tested after completion of the curing period. Some results showed little improvement in compaction characteristics, and unconfined compressive strength, but no notable improvement was noticed in Atterberg limits. X-ray diffraction (XRD), X-ray fluorescence (XRF), and field emission scanning electron microscopy (FESEM) tests were conducted for untreated and treated soil samples after two months of curing. XRD and XRF did not show any change in mineralogy and chemical composition between controlled untreated samples and samples treated with the three bioenzymes. However, the FESEM images revealed a denser packing of particles for soil samples treated with two of the bioenzymes.

1. Introduction

In the construction industry, maintaining a balance between performance and cost, while at the same time satisfying environmental regulations, has become a challenge for building material manufacturers, design engineers, and contractors. This challenge has led to identification and use of new construction materials and techniques. Geotechnical engineering projects are closely related to economic and environmental issues; therefore, improving sustainability of materials used in these projects may help in attaining overall sustainable development [1]. Unfortunately, planning and design phases of these projects are dictated by financial interests and are even more affected by lack of knowledge about the effect of the geotechnical process on the environment [2]. Manufacturing of readily used construction materials, such as cement and lime, has a deteriorating effect on the environment; the production of cement and lime is energy demanding, and production of only one ton of cement emits around one ton of CO₂ [3].

Recently, bioenzymes have been introduced for soil stabilization, especially in highway projects. They are organic materials, which are supplied as a concentrated liquid. It is claimed by bioenzyme manufacturers that their products are effective, environmentally friendly (nontoxic), cost-effective, and convenient to use. They are generally extracted by the fermentation of vegetables and sugar canes; thus they are degradable; that is, they easily break down and dissolve with time. They are supplied in liquid form and are easily soluble in water, which is used for soil compaction. This saves time and costs normally consumed by the mixing of traditional solid stabilizers with soil. Kestler [4] suggested that most of the information about enzymes is provided by enzyme suppliers, and, therefore, independent testing information is not readily available. Additionally, enzymes are often reformulated; all of these factors call for product-specific testing before the selection of an enzyme for a project.

Enzymes are biological catalysts present in all living organisms. They are obtained from plants and animals, including microorganisms, by extraction using suitable

solvent. Kestler [4] suggested that enzymes are proprietary of their supplier; unless they provide the composition, it is very difficult to determine the precise composition and stabilization mechanism. He also recommended that some commercial enzymes, for example, Bio Cat 300-1, EMC SQUARED, PermaZyme 11-X, TerraZyme, and UBIX No. 0010, should contain protein molecules which react with soil molecules to bind the soil particles together, thus decreasing the affection of soils for moisture.

Scholen [5] proposed that enzymes increase the rate of chemical reaction, which occurs at a much slower speed in the absence of enzymes, without becoming a component of the final product. Enzymes combine with big organic molecules to generate a reactant mediator, which swaps ions with the clay structure and breaks up the clay lattice. As a result, this produces a covering effect, which blocks further absorption of water and loss in density. This reaction regenerates the enzymes again, which sets out and reacts yet again. The enzymes are absorbed by the clay lattice and are afterwards freed upon exchange with metals cations. They have a significant role in the behaviour of the clay lattice, first causing them to get bigger and then to stiffen. Rauch et al. [6], through different chemical and physical tests, endorsed the hypothesis proposed by Scholen [5] that states that enzymes unite with the large organic molecules and adhere to clay surfaces, thus jamming potential cation exchange sites and preventing absorption of moisture and subsequent swelling. Resulting ionized water forms linkages among packed particles to provide a binding effect.

Enzyme manufacturers and suppliers claim that enzymes, when used in soil stabilization, can enhance the wetting and bonding properties of the soil particles. The enzymes make the soil more workable, which can be compacted more heavily. Furthermore, the enzymes enhance the chemical bonding of soil particles, which aids in combining them. Thus, a more durable soil structure is built that is more resistant to weathering, traffic, and water infiltration.

Strength tests have shown a considerable increase in strength for soils treated with bioenzymes [7, 8]. Lacuoture and Gonzalez [9] studied the effect of the TerraZyme soil stabilizer product on subbase and subgrade soils. Variation in properties and progressive improvement were observed, but no significant improvement was reported during the early days. Hitam et al. [10] also studied the effect of TerraZyme on plantation roads through field observations. He noticed that the roads, which had serious problems due to monsoons in the past, remained intact after two monsoon seasons.

Soil treated with PermaZyme 11-X showed very modest or no improvement in stiffness, freeze-thaw, leaching, and wet-dry tests [11]. Compaction, Atterberg limits, and strength tests revealed little or no improvement for the soils stabilized with PermaZyme 11-X and EarthZyme [12]. PermaZyme 11-X was also used to treat six single source and three blended soils to conduct Atterberg limits, density, strength, and *R*-value tests; the overall reduction in the plasticity index and increase in strength were recorded [13]. Rauch et al. [6] conducted experimental studies of three liquid stabilizers including one enzyme. Two natural soils and three reference clays, bentonite, illite, and kaolinite, were treated with this enzyme,

and different tests were conducted. Overall, no noticeable improvement was observed.

Soil investigation practices are sometimes criticized for the extensive time needed and high cost involved. However, larger losses can be saved, which may arise if proper soil investigation prior to field application is bypassed. If a stabilizer is not effective in controlled laboratory conditions, then it is likely that it cannot produce the desired results in the field. As discussed previously, the experimental studies conducted to evaluate enzyme's suitability as a soil stabilizer have revealed dissimilar results. Thus, this experimental study was aimed at evaluating the suitability of three commercial enzymes. The experimental studies conducted thus far used optimum moisture content (OMC) of untreated soil to prepare soil samples treated with enzymes. However, in this study, the effect of enzymes on compaction characteristics was examined. For this purpose, a revised protocol for sample preparation was adopted as recommended by Rauch et al. [6]. Samples were cured for an extended time period of 12 weeks to observe the progressive improvement due to enzyme activity. Instead of using one enzyme to check suitability against different types of soil, in this study, one suitable (presumably) soil was selected to evaluate the improvement by three different enzymes. This study was not restricted to mechanical testing of untreated and treated samples, but XRD and XRF tests were conducted to check any chemical reaction in the treated soil samples. FESEM images were taken to closely investigate the texture of untreated and treated soil samples. Untreated controlled samples were prepared and cured along with treated samples to account for gain in strength due to aging and moisture loss, if any.

2. Test Materials

2.1. Bioenzymes. Three types of bioenzymes, DZ-IX (Boron Innovations Pvt., Ltd., India), EarthZyme (Cypher Environmental Ltd., Canada), and TerraZyme (Nature Plus, Inc., USA), were selected for this study and designated as E-I, E-II, and E-III, respectively. EarthZyme and TerraZyme suppliers provided the material safety data sheet (MSDS), whereas the supplier of DZ-IX did not provide MSDS, though several requests were made. However, some of the properties of the DZ-IX enzyme were determined in the laboratory, and the information contained in MSDS for EarthZyme and TerraZyme is presented in Table 1. The main ingredients of two enzymes (E-II and E-III) are nonionic surfactant and carbohydrates. E-II contained carbohydrates (polysaccharides, oligosaccharides, disaccharides, and monosaccharides) and E-III consisted of fermented vegetable extract. Two dosages were used for all three enzymes: first, single dose (recommended by the supplier) and, second, double dose, that is, two times the recommended dosage, are denoted as D1 and D2, respectively.

Different suppliers often express the recommended application rates by using different terminology and units. However, it would be advantageous to define the following terms, which were suggested by Rauch et al. [14].

TABLE 1: Physical and chemical properties of enzymes.

Item	DZ-1X	EarthZyme	TerraZyme
Water	—	21.06%	>50%
Alcohols, C12–C16, ethoxylated	—	—	<30%
Fermented vegetable extract	—	—	<20%
Nonionic surfactants	—	55%	—
Polysaccharides	—	2%	—
Oligosaccharides	—	3%	—
Disaccharides	—	5%	—
Monosaccharide	—	8%	—
Lactic acid	—	3.5%	—
Potassium as the chloride	—	1.2%	—
Aluminum as the sulphate	—	0.04%	—
Magnesium as the sulphate	—	1.2%	—
Total	—	100%	—
Specific gravity	1.0	1.0 to 1.1	1.0 to 1.1
pH (neat) ¹	4.5	3 to 6	2.8 to 3.5
Boiling point	>100°C	>100°C	>100°C
Ultimate biodegradability	—	DOC ² reduction >90% after 28 days	—
Composition	—	A blend of fermented carbohydrates, inorganic salts, and surfactants	—

¹ Concentrated enzyme. ² Dissolved organic content.

TABLE 2: Recommended dosages, dilution ratios, and diluted application ratios of bioenzymes.

Stabilizer	E-I (DZ-1X)	E-II (EarthZyme)	E-III (TerraZyme)
Suppliers recommended dosage	1 liter per 4.2 m ³	1 liter per 33 m ³	1 liter per 25 m ³
Equivalent dilution mass ratio (DMR)	5/1000	1/1000	1/1000
Equivalent application mass ratio (AMR)*	1/7500	1/58900	1/44600
Diluted application ratios*	27 mL per kg of soil	17 mL per kg of soil	22 mL per kg of soil

* Maximum dry density of soil was taken for these calculations, that is, 1785 kg/m³.

(i) Dilution mass ratio (DMR) is the mass ratio of a concentrated chemical product to water, used to express the product dilution in water prior to soil application.

(ii) Application mass ratio (AMR) is the mass ratio of a concentrated chemical product to oven-dried material in the treated soil.

In addition, because the recommended doses by the suppliers were very low, the enzymes were diluted in water prior to their application. Suppliers recommended doses, DMR, AMR, and diluted application ratios are given in Table 2.

2.2. Test Soil. The selected soil was taken from within the campus of Universiti Kebangsaan Malaysia in Bangi, Selangor, Malaysia. Therefore, it is abbreviated as UKM soil. It is a residual soil classified as CL, using a plasticity chart. The soil for all the tests was collected at once to reduce the chances of heterogeneity while preparing soil samples.

3. Sample Preparation and Tests

Rauch et al. [6] developed a protocol to prepare soil samples treated with liquid stabilizers. They devised this protocol after consulting a number of industry representatives and

the Texas Department of Transportation. After the completion of their studies, this protocol was further modified to determine any change in compaction characteristics brought by liquid stabilizer. The thirteen-step, modified protocol was named “Revised Protocol for Preparing Soil Test Specimens” and is presented here in brief.

AMR was calculated from the dosage recommended by the product supplier, and concentrated stabilizer product was diluted to the recommended DMR. The soil was mixed with initial moisture content w_o :

$$w_o = \text{OWC} - \frac{\text{AMR}}{\text{DMR}} + 1\%. \quad (\text{i})$$

Next, the premoistened soil was allowed to mellow (standing time recommended by ASTM D698-7 to allow the moisture to be absorbed thoroughly by the soil particles) for the minimum of 16 h under sealed conditions. The diluted stabilizer required to attain the recommended AMR in the treated sample was then measured and mixed with the soil samples to achieve a homogeneous mixture. The mixture was allowed to stand for 1 h, again in a sealed condition. The soil was then compacted with the specified compaction method, and the compacted soil was extruded from the mould, sealed, and placed in a moist curing room. The compacted soil sample

was cured for the desired curing period, and the sample was then trimmed to the required size for testing; the moisture content was determined by means of sample trimmings or with the whole sample. Finally, if the moisture content was not within the permitted range, the sample was prepared again.

To explain the abovementioned procedure, consider the determination of MDD and OMC for E-I-D1 (sample prepared with a single dosage of enzyme DZ-IX). Four samples (2 kg each) of oven-dried soil were taken. Moisture loss during sample preparation was estimated as 1%; therefore, the first trial was made with a moisture content of 2% less than the OMC for untreated (UT) soil, that is, 15%. The volume of the diluted enzyme solution (5 mL in 1 litre of water) for a single dosage (D1) was calculated (54 mL for 2 kg). Thus, 246 mL ($0.15 \times 2000 \text{ mL} - 54 \text{ mL}$) was added in 2 kg of soil, and the soil was allowed to mellow for 16 h. After the mellowing period, 54 mL of diluted enzyme solution was added in the soil, and, again, the soil was mellowed for 1 h before compaction. Similarly, the other three samples were prepared with moisture contents of 16, 17, and 18%, and MDD and OMC were calculated for two dosages of all three enzymes.

Three geotechnical tests, that is, Atterberg limits, compaction, and unconfined compression strength (UCS), were conducted in this study. The Standard Test Methods for Laboratory Compaction Characteristics of Soil Using Standard Effort (ASTM D 698) was conducted to evaluate any changes brought by enzymes in compaction characteristics, that is, maximum dry density (MDD) and optimum moisture content. For UCS and Atterberg limits tests, initial curing periods of 7, 28, and 56 days were intended. However, it was later decided to cure the samples for 28, 56, and 84 days because no improvement was observed in UCS after 7 days for all of the enzymes and the two dosages used. For each curing time, one Proctor sample (dia. 101.6 mm, height 116.4 mm) was prepared, cured, and trimmed into three samples (dia. 38 mm, height 76–95 mm) just before the unconfined compressive strength test. Three samples were tested, and an average value of the three was recorded. After the test, the whole sample was used for moisture content determination. In total, three untreated (UT) and 18 treated (E series) samples were prepared. Atterberg limits (plastic limit and liquid limit) of the samples were determined after 56 days of curing.

4. Results and Discussion

4.1. UKM Soil Properties. The indices and other properties of UKM soil are shown in Table 3. Kabir and Taha [15] and M. R. Taha and O. M. E. Taha [16] used the residual soil from Universiti of Kebangsaan Malaysia in their experimental studies. The values of Kabir and Taha [15] were 18.8%, 23%, 15.8%, and 1.781 gm/cm^3 and those of M. R. Taha and O. M. E. Taha [16] were 16.96%, 18%, 14.29%, and 1.839 gm/cm^3 for the plasticity index, clay fraction, optimum moisture content, and maximum dry density (MDD), respectively. There were minor differences among these values, but, overall, the results are comparable.

TABLE 3: Characteristics of UKM soil.

Characteristics	Value/description
Plasticity index ¹ (PI)	19.5%
Liquid limit ¹ (LL)	42.3%
Clay fraction ²	29.6%
Soil classification ³	CL
Optimum moisture content (OMC) ⁴	16%
Maximum dry density (MDD) ⁴	1.785 gm/cm^3
pH	4.05

¹“Standard Test Methods for Liquid Limit, Plastic Limit, and Plasticity Index of Soils,” ASTM D 4318.

²“Standard Test Method for Particle-Size Analysis of Soils,” ASTM D 422.

³“Plasticity chart,” ASTM D 2487.

⁴“Standard Test Methods for Laboratory Compaction Characteristics of Soil Using Standard Effort,” ASTM D 698.

According to Kestler [4], enzymes may work suitably for soils containing 12–24% clay fraction with a plasticity index between 8 and 35. UKM soil almost falls into this category. Thus, it was assumed that the UKM soil is quite fitting for enzyme functioning.

4.2. Compaction Test. Compaction characteristics of UKM soil (untreated) were determined using the standard compaction effort (ASTM D698), and the same procedure was used to identify any change in compaction characteristics due to enzymes. During the preparation of untreated and treated soil samples, an increment of 1% moisture content was chosen so that precise compaction characteristics could be determined. Three important factors that affect the compaction of soil are moisture content, soil type, and compaction effort. For a given soil, as the compaction effort is improved, the MDD is increased and OMC is decreased. The bell-shaped curves with single peak, which were achieved in this study, are typical of clayey soils with liquid limits between 30 and 70 as observed by Lee and Suedkamp [17] in their studies of compaction curves of different soils. The compaction curves for untreated and treated samples for the two dosages are shown in Figures 1 and 2. The OMC and MDD for untreated soil were 16% and 1.785 gm/cm^3 , whereas those for samples treated with a single dose of three enzymes were 16.1% and 1.788 gm/cm^3 , 16% and 1.787 gm/cm^3 , and 16.2% and 1.786 gm/cm^3 for E-I, E-II, and E-III, respectively. Similarly, for double dosage, no reduction in OMC was observed, but modest improvement was noted in the increase of the maximum dry density.

The two enzymes E-II and E-III (chemical composition of DZ-IX was not provided by the supplier, but during the dilution of DZ-IX, foaming was formed, showing its surfactant-like behavior) contained nonionic surfactants, yet improvement in compaction was not observed. The reason for this performance could be a very low quantity dose of the enzymes. Therefore, all the treated samples were prepared with optimum moisture content of the control untreated soil samples. The average dry densities of all untreated and treated samples are given in Figure 3. The maximum increase in dry density was observed in samples treated with a double

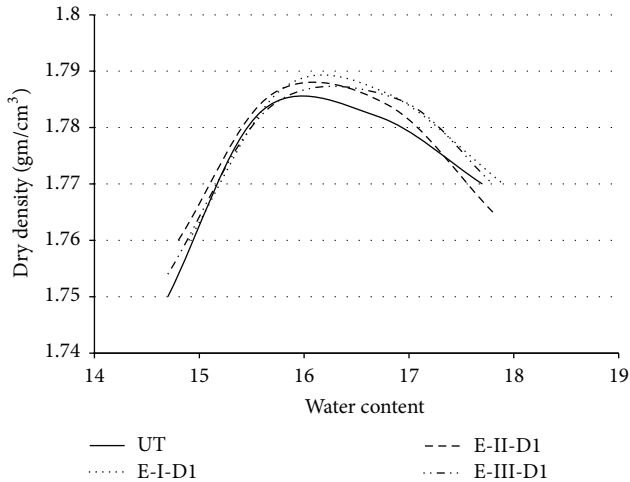


FIGURE 1: Compaction curves for untreated (UT) soil samples and soil treated with single dosage of the three different enzymes.

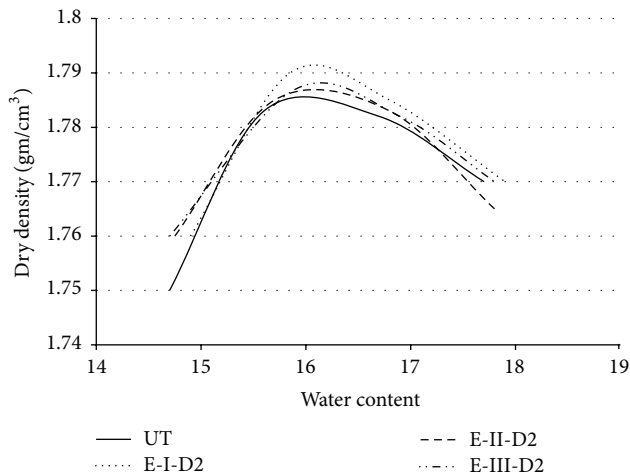


FIGURE 2: Compaction curves for untreated (UT) soil samples and soil treated with double dosage of the three different enzymes.

dose of enzyme E-I, and even this increase was only 3%. This increase can be attributed to the high application rate of enzyme E-I. In their study, Rauch et al. [14] examined the effect of the enzyme on compaction characteristics of three reference clays (kaolinite, illite, and montmorillonite) and two native Texas clays (from Bryan and Mesquite, Texas) but found no improvement in the dry density. They used the OMC of untreated soils to prepare soil samples treated with the enzyme. They then suggested that the compaction characteristics (OMC and MDD) for treated soils should be determined separately. Milburn and Parsons [11] conducted compaction tests on ML and SM soils. The moisture content for the treated soil samples was kept at 1% less than the optimum moisture content, but only 4% and 1% increases in dry density were found for ML and SM soils, respectively.

The moisture content determined at the time of compaction and moisture content at the time of testing (UCS) for all the prepared samples are given in Table 4. In moisture

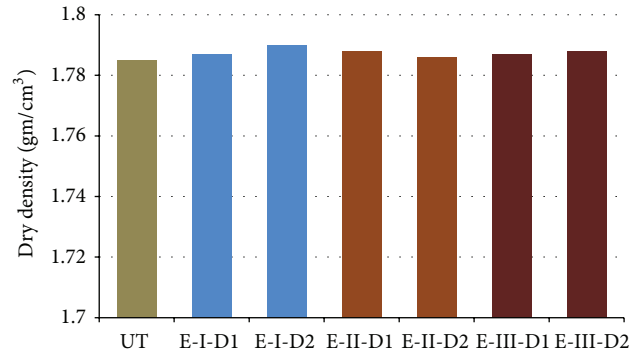


FIGURE 3: Average maximum dry density for untreated (UT) and treated (E series) samples.

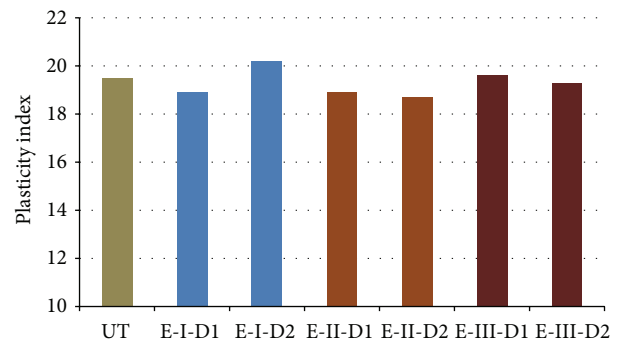


FIGURE 4: Plasticity indices for untreated (UT) and treated (E series) samples.

contents at the time of sample preparation and after, the curing was compared, and, in all samples, the difference remained within 1%. There could be two reasons for this moisture conservation: the samples were cured in a bigger sized and were trimmed to the required size at the time of testing and no chemical reaction took place that possibly could have changed the moisture content.

4.3. *Atterberg Limits Test.* Liquid limit and plastic limit were determined after 56 days of curing. Marasteanu et al. [8] recommended an extended period of curing up to four months. Additionally, considerable improvement in treated soil is generally required to be reflected consistently through Atterberg limits tests. Thus, curing periods of 56 days and 84 days were chosen. No noteworthy improvement was found after 56 days. Furthermore, the UCS results for the 84-day cured sample did not show substantial improvement; therefore, Atterberg limits for 84 days were not determined. The plasticity indices for untreated and treated samples for two doses are given in Figure 4. It showed marginal change from the untreated samples. It is indicated in the ASTM (1998) that determinations of plastic and liquid limits of a certain soil, even by a single operator, can vary by 2.6 and 2.4, respectively. Therefore, the difference in plasticity indices may be attributed to the routine inconsistency which is encountered in the laboratory.

TABLE 4: Moisture content of prepared samples.

Sr. number	Enzyme & dosage	One month		Two months		Three months	
		w_o ¹	w_f ²	w_o	w_f	w_o	w_f
1	UT	16.0	15.7	15.9	15.8	15.7	15.1
2	E-I-D1	15.3	15.2	16.2	16.0	15.9	15.9
3	E-I-D2	16.0	15.8	16.2	16.1	15.9	15.5
4	E-II-D1	16.5	16.1	16.1	15.9	16.3	16.2
5	E-II-D2	16.4	16.2	16.1	15.7	16.3	16.2
6	E-III-D1	15.7	15.6	16.1	15.9	16.4	16.0
7	E-III-D2	16.7	16.6	16.1	16.1	16.1	15.8

¹Moisture content in % at the time of compaction.

²Moisture content in % at the time of UCS test.

Mgangira [12] performed Atterberg limits tests on two soils treated with two enzymes (PermaZyme 11-X and Earth-Zyme) after 28 days of curing, and no significant improvement was observed. Similarly, Rauch et al. [14] also found no decrease in plasticity indices for the five soils they tested, as mentioned previously.

4.4. Unconfined Compressive Strength Test. The Standard Test Method for Unconfined Compressive Strength of Cohesive Soil (ASTM D 2166) was used to evaluate the ultimate compressive strength of untreated and treated soil samples. Untreated control samples were also prepared and cured for three curing periods. After the curing period, the sample was unsealed and trimmed into three samples of the required size, and all three samples were weighed before testing. The three samples were then tested on a strain controlled machine, and the average of the three ultimate compressive stresses was taken as the final value. The tested samples were then placed in an oven for moisture content determination.

The results are shown in Figures 5 and 6. The results of E-I for two doses showed no improvement, whereas, for enzymes E-II and E-III, there was little improvement. The maximum increase in strength was recorded for E-III-D2, which was 17%. It is evident that the results were generally moderate, or the improvement was, in individual cases, without any persistent pattern.

Controlled untreated samples were prepared to account for any strength gain due to thixotropy or aging. Some of the clayey soils were reported to reduce their unconfined compression strength when tested after remoulding without any change in moisture content. The main reason behind this loss was the destruction of clay particle structure, which developed from the original sedimentation process. However, when remoulded samples are held for some time, keeping the moisture content unchanged, they may gradually gain strength [18].

Unconfined compression tests on different soils treated with PermaZyme 11-X were also carried out by Peng et al. [19]. The treated samples were cured in two different conditions, that is, sealed and air-dry. No improvement was recorded for soil samples cured in a sealed condition, whereas a maximum of 10% gain in strength was observed for soil samples cured in an air-dry condition. However, Venkatasubramanian and

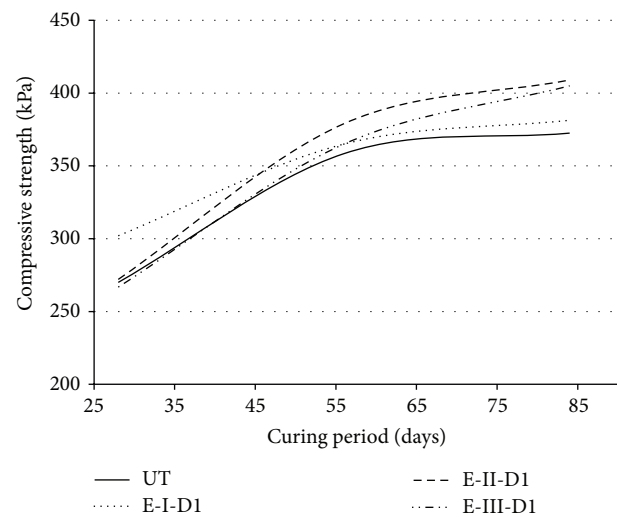


FIGURE 5: Variations in UCS for untreated (UT) and treated (single dosage) soil samples.

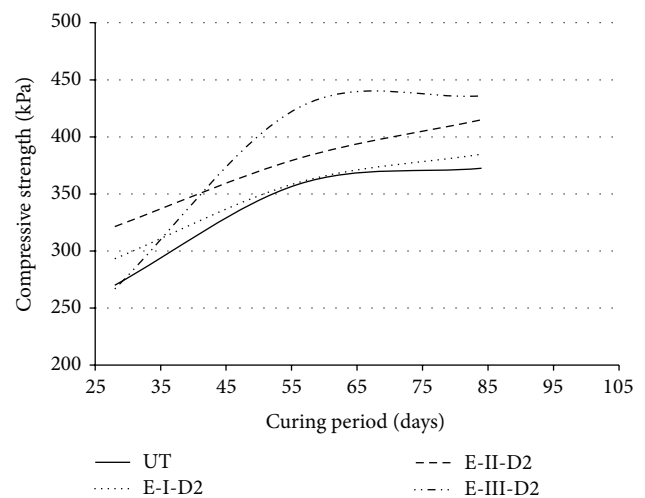


FIGURE 6: Variations in UCS for untreated (UT) and treated (double dosage) soil samples.

TABLE 5: Comparison of XRF results for untreated (UT) soil samples and soils treated with three enzymes.

Formula	UT	E-I-D2	E-II-D2	E-III-D2
	Concentration (%)	Concentration (%)	Concentration (%)	Concentration (%)
SiO ₂	49.07	51.42	46.17	48.74
Al ₂ O ₃	28.89	29.84	30.35	29.80
Fe ₂ O ₃	9.07	9.20	9.78	9.70
TiO ₂	1.59	1.55	1.60	1.61
K ₂ O	0.48	0.55	0.57	0.57
MgO	0.40	0.44	0.45	0.44
ZrO ₂	0.14	0.16	0.12	0.14
SO ₃	0.08	0.12	0.08	0.09
V ₂ O ₅	0.04	0.04	0.04	0.04
CaO	0.03	0.04	0.08	0.07
Cr ₂ O ₃	0.01	0.01	0.02	0.01

Dhinakaran [20] used three soils with clay content of 20, 12.5, and 8% with PIs of 6,5 and 6, respectively. Increases in unconfined compression strength went to 200% and 400% after 2 weeks and 4 weeks, respectively, and were recorded for the enzyme treated soils. A maximum increase of 450% in unconfined compression strength was recorded by Shankar et al. [21] when a lateritic soil (LL = 45 and PI = 10) was treated with 4 times the recommended dosage by the enzyme supplier TerraZyme. Part of this substantial improvement could have been due to moisture loss because the moisture content at the time of the sample preparation and testing was not mentioned in these two studies.

4.5. XRD, XRF, and FESEM. Willie and Norman [22] suggested that the XRD technique for identification of soil mineralogy is used a great deal and is considered one of the most dominant techniques used for mineral identification in soils and rocks. XRD, XRF, and FESEM tests were conducted for untreated (UT) and treated (E series) soil samples after 56 days of curing. The XRD results for the untreated (UT) soil and soil samples treated with three enzymes are given in Figure 7. The peaks were matched with different possible compounds present in the soil. The matching revealed SiO₂, Al₂O₃, and Fe₂O₃ as the three main ingredients (compounds) of UKM soil as verified by the chemical composition obtained from XRF test results for the untreated and the three treated soils as given in Table 5. The XRD results of the untreated and the three treated soil samples are stacked for comparison. It was evident that no chemical change took place to alter the chemical composition of the soil treated by any of the three enzymes. This conclusion is further verified by the XRF results, which showed no variation in chemical composition in any of the three treated soil samples. However, by looking at FESEM images in Figure 8, it can be observed that the particles for E-II-D2 and E-III-D2 samples were more closely packed and agglomerated than the untreated (UT) and E-I-D2 samples. The voids or pores can be seen as shadows in Figure 8 due to looseness of particles in untreated (UT) and treated samples (E-I-D1), with boundaries marked in lines. These results are consistent with the hypothesis suggested

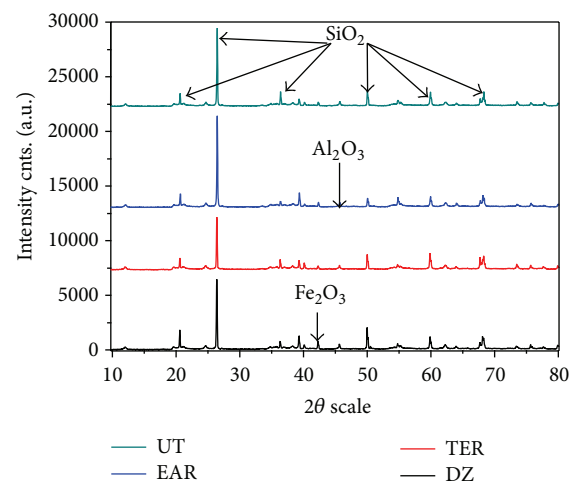


FIGURE 7: Comparison of XRD results for untreated (UT) soil samples and soils treated with three enzymes.

by Scholen [17] and Rauch et al. [16], which states that the enzymes combine with organic molecules, which then surround the clay minerals, nullifying the negative charge on the clay surface and lessening the clay's affinity for water.

5. Conclusions

In this experimental study, the effects of three enzymes on Atterberg limits, compaction characteristics, and unconfined compressive strength were evaluated. A Standard Proctor test was carried out to examine any change in optimum moisture content and maximum dry density with two doses of all three enzymes. The same test was conducted to prepare control untreated soil samples and soil samples treated with two doses of three enzymes for three curing periods (28, 56, and 84 days). The Atterberg limits test was carried out on untreated and treated soil samples after 56 days of curing. XRD, XRF, and FESEM were conducted to identify if any chemical change had occurred.

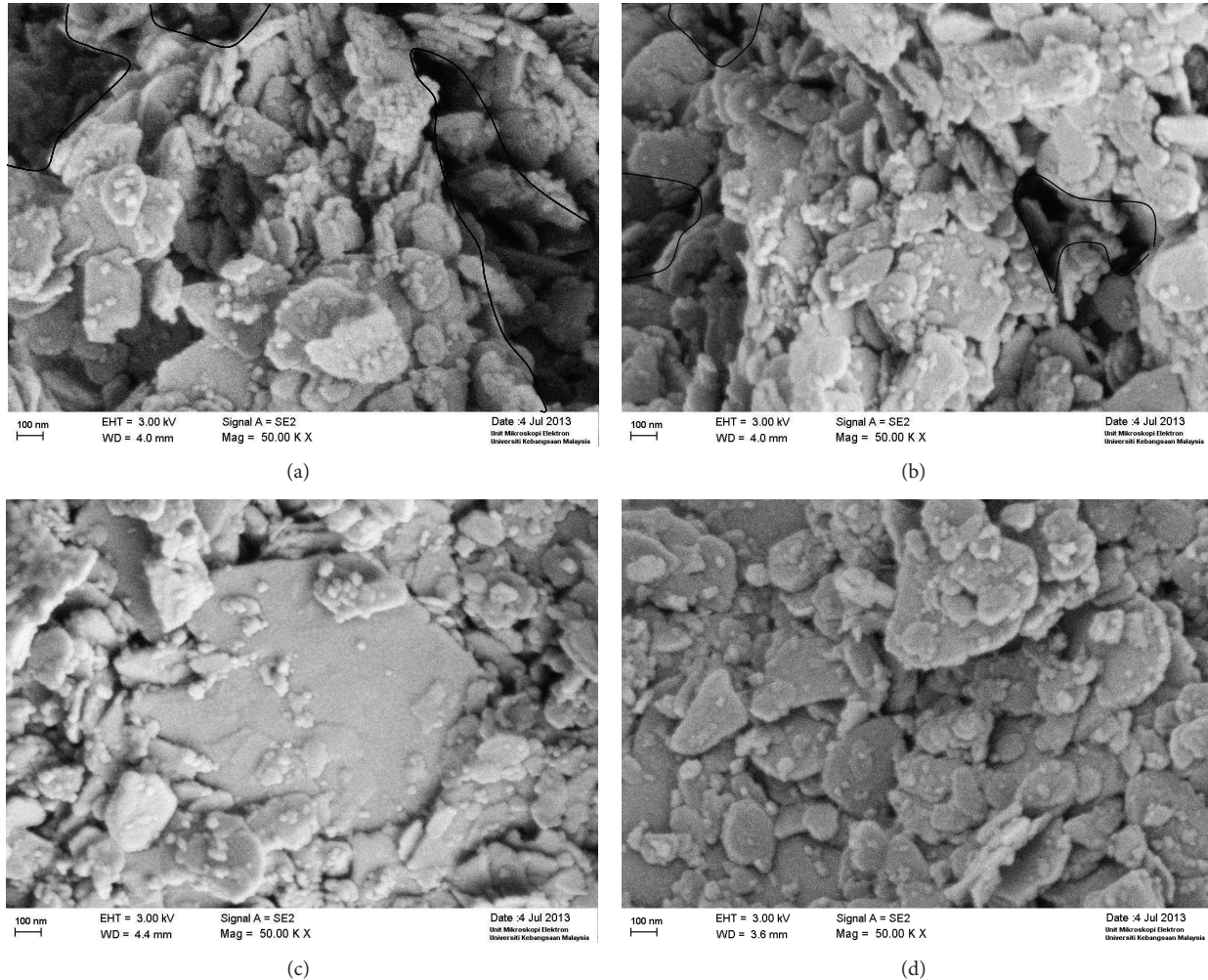


FIGURE 8: FESEM results: (a) UT, (b) E-I-D2, (c) E-II-D2, and (d) E-III-D2.

It was found that the three enzymes did not produce any comprehensible improvement in the three tests conducted, that is, Atterberg limits, compaction, and unconfined compression tests. Little improvement, in some cases, could be related to the hypothesis that the enzymes did not produce any chemical change, and they only prevented moisture absorption to bring the particles closer. Therefore, when selecting an invalidated stabilizer, it is imperative to check its suitability before using it on larger scale. It is hoped that this study will be beneficial for designers, contractors, and constructors when choosing bioenzymes as a soil stabilizer.

Conflict of Interests

The authors declare that there is no conflict of interests regarding the publication of this paper.

Acknowledgments

The authors gratefully acknowledge the support of the Ministry of Education, Malaysia, through Universiti Kebangsaan

Malaysia, which provided funding for the project under Code DPP-2014-047, and the Centre for Research & Instrumentation Management (CRIM) for XRD, XRF, and FESEM tests.

References

- [1] S. A. Jefferis, "Moving towards sustainability in geotechnical engineering," in *Proceedings of the Geoenvironment Annual Congress of the Geo-Institute of ASCE (GeoCongress '08)*, pp. 178–844, March 2008.
- [2] D. G. Abreu, I. Jefferson, P. A. Braithwaite, and D. N. Chapman, "Why is sustainability important in geotechnical engineering," in *Proceedings of the Geocongress, Geotechnical Special Publication no. 178 on Geosustainability and Geohazard Mitigation*, pp. 821–828, 2008.
- [3] J. Khedari, P. Watsanasathaporn, and J. Hirunlabh, "Development of fibre-based soil-cement block with low thermal conductivity," *Cement and Concrete Composites*, vol. 27, no. 1, pp. 111–116, 2005.
- [4] M. A. Kestler, *Stabilization Selection Guide for Aggregate and Native-Surfaced Low Volume Roads*, Forest Service, San Dimas

- Technology & Development Center USA, San Dimas, Calif, USA, 2009.
- [5] D. Scholen, "Non-standard stabilizers," Report FHWA-FLP-92-011, Department of Transportation, 1992.
- [6] A. F. Rauch, L. E. Katz, and H. M. Liljestrand, *An Analysis of the Mechanisms and Efficacy of Three Liquid Chemical Soil Stabilizers*, Center for Transportation Research, The University of Texas at Austin, 2003.
- [7] M. Shukla, S. Bose, and P. Sikdar, "Bio-enzyme for stabilization of soil in road construction a cost effective approach," in *Proceedings of the IRC Seminar Integrated Development of Rural and Arterial Road Networks for Socio-Economic Development*, New Delhi, India, 2003.
- [8] M. O. Marasteanu, R. Hozalski, T. R. Clyne, and R. Velasquez, "Preliminary laboratory investigation of enzyme solutions as a soil stabilizer," Tech. Rep., Department of Civil Engineering, University of Minnesota, Minneapolis, Minn, USA, 2005.
- [9] A. Lacuoture and H. Gonzalez, *Usage of Organic Enzymes for the Stabilization of Natural Base Soils and Sub-Bases in Bagota*, Faculty of Engineering, Pontificia Universidad Jevariana, 1995.
- [10] A. Hitam, A. Z. Yusof, and O. Samad, "Soil stabilizer for plantation road," in *Proceedings of the National Seminar on Mechanization in Oil Palm Plantation, Palm Oil Research Institute of Malaysia (PORIM '99)*, Bangi, Malaysia, 1999.
- [11] J. P. Milburn and R. Parsons, *Performance of Soil Stabilization Agents*, Kansas Department of Transportation, 2004.
- [12] M. Mgangira, "Evaluation of the effects of enzyme-based liquid chemical stabilizers on subgrade soils," in *Proceedings of the 28th Southern African Transport Conference*, Pretoria, South Africa, July 2009.
- [13] F. Bron, C. Ding, H. Gary, and R. Charles, *Permazyme Testing Volume I: Final Testing Summary Report*, California Pavement Preservation Center, 2010.
- [14] A. F. Rauch, J. S. Harmon, L. E. Katz, and H. M. Liljestrand, "Measured effects of liquid soil stabilizers on engineering properties of clay," *Transportation Research Record*, vol. 1787, no. 1, pp. 33–41, 2002.
- [15] M. H. Kabir and M. R. Taha, "Sedimentary residual soil as a waste containment barrier material," *Soil & Sediment Contamination*, vol. 13, no. 5, pp. 407–420, 2004.
- [16] M. R. Taha and O. M. E. Taha, "Influence of nano-material on the expansive and shrinkage soil behavior," *Journal of Nanoparticle Research*, vol. 14, article 1190, 2012.
- [17] P. Y. Lee and R. Suedkamp, "Characteristics of irregularly shaped compaction curves of soils," *Highway Research Record* 381, 1972.
- [18] B. M. Das, *Principles of Geotechnical Engineering*, Cengage Learning India Private Limited, 5th edition, 2001.
- [19] H. T. Peng, H. T. Su, X. P. Zhang, and J. Wang, "An experimental comparison of compressive strengths of soils stabilized with enzyme and ground quicklime," *Advanced Materials Research*, vol. 280, pp. 9–12, 2011.
- [20] C. Venkatasubramanian and G. Dhinakaran, "Effect of bio-enzymatic soil stabilisation on unconfined compressive strength and California Bearing Ratio," *Journal of Engineering and Applied Sciences*, vol. 6, no. 5, pp. 295–298, 2011.
- [21] A. Shankar, H. K. Rai, and R. Mithanthaya, "Bio-enzyme stabilized lateritic soil as a highway material," *Indian Roads Congress Journal*, vol. 70, no. 2, 2009.
- [22] H. Willie and W. Norman, *Methods of Soil Analysis. Part 5. Mineralogical Methods*, SSSA Book Series, No. 5, Soil Science Society of America, Madison, Wis, USA, 2007, edited by L. R. Drees, A. L. Ulery.

Research Article

Effect of Fiber Waviness on Tensile Strength of a Flax-Sliver-Reinforced Composite Material

Taweesak Piyatuchsananon,¹ Akira Furuya,¹ Baosheng Ren,² and Koichi Goda³

¹Graduate School of Science and Engineering, Yamaguchi University, Tokiwadai, Ube 755-8611, Japan

²School of Material Science and Engineering, University of Jinan, Jinan, Shandong 250022, China

³Department of Mechanical Engineering, Yamaguchi University, Ube 755-8611, Japan

Correspondence should be addressed to Koichi Goda; goda@yamaguchi-u.ac.jp

Received 11 January 2015; Accepted 2 March 2015

Academic Editor: P. J. Schubel

Copyright © 2015 Taweesak Piyatuchsananon et al. This is an open access article distributed under the Creative Commons Attribution License, which permits unrestricted use, distribution, and reproduction in any medium, provided the original work is properly cited.

Recently, a composite material made from natural fibers and biodegradable resin, “green composite,” is attracting attention as an alternative composite material for the replacement of glass fiber-reinforced plastics. Plant-based natural fibers such as kenaf and flax have already been used as composite reinforcement materials because they are more environmentally friendly and costless fibers than artificial fibers. A problem of using natural fibers is the fiber waviness, which affects the tensile properties. Fiber waviness is fluctuation in the fiber orientation that is inherent in the sliver morphology of plant-based natural fibers. This study was conducted to clarify the relation between quantified parameters of fiber waviness and a composite’s tensile strength. First, the fiber orientation angles on a flax-sliver-reinforced composite were measured. Then the angle distribution was quantified through spatial autocorrelation analysis methods: Local Moran’s I and Local Geary’s c . Finally, the relation between the resultant tensile strength and quantified parameters was discussed.

1. Introduction

Strong demand for the use of composite materials is increasing today because high strength and stiffness, as well as low density, are needed to reduce energy consumption in aviation and automotive transport industries. The use of artificial fiber-reinforced composite materials, such as glass fiber-reinforced plastics (GFRP) and carbon fiber-reinforced plastics (CFRP), is effective to meet these demands, but disposal difficulties that arise after their use have surfaced as an environmental problem. Therefore, many researchers have strived to develop biodegradable renewable composite materials and various production methods for the materials that will widen their practical availability [1–5]. Plant-based natural fibers, such as flax, hemp, ramie, jute, kenaf, curaua, and bamboo, are expected for use as the composite reinforcement materials, but these are often used as short fibers, as seen in injection-molded products. Long fibers are generally known to exhibit load-bearing potential in a matrix material as compared to short fibers. Before spinning process, plant-based

natural fibers are often supplied as long fibers called “slivers.” When this form is successfully prepared with resin, slivers can be applied as a semifinished composite material in prepregs [5, 6]. One of the problems in preparing slivers is their fiber waviness, which is fluctuation in the fiber orientation inherent in plant-based natural fibers as well as synthetic fibers. Such waviness often engenders a decrease in the mechanical properties of the composites. It was pointed out in the model proposed by Hsiao and Daniel [7] that the decrease in elastic properties of a unidirectional carbon/epoxy composite resulted from the fiber waviness. Karami and Garnich [8] used a finite element micromechanical model to predict the effects of periodic and localized fiber waviness on carbon fiber reinforcement. In these papers, however, the fiber waviness was assumed as a deterministic shape such as a sine curve. In order to take the stochastic wavy effect of sliver into account, Ren et al. [9, 10] quantified the fibre orientation fluctuation in curaua-sliver- and flax-sliver-reinforced composite through one-dimensional and two-dimensional



FIGURE 1: Flax sliver.

autocorrelations between fiber orientation angles on the composite surface. The quantified parameter expressing the degree of the fluctuation, called the “area ratio,” was correlated with the composite tensile strength. However, the use of autocorrelations was intended to evaluate the quality of fiber orientation but not to express the degree of local disorder in fiber orientation. In general, stiffness is insensible for structural defects, but strength is sensible. Therefore, the local disorder in fiber orientation is of great interest for quantification through some statistical or stochastic analytical method. It is also expected that the quantified parameter shall play a role as a key indicator during quality inspection for produced prepregs.

Thus, the purpose of this study is to examine the effects of the fiber waviness on the tensile strength of a flax-sliver-reinforced composite (in-plane tensile modulus). Resin-pasted flax slivers were first compression molded, and then fiber orientation angles were measured on the surfaces of the resultant composite laminates. To quantify the degree of the disorder in fiber orientation, the measurement results were analyzed by Local Moran’s I and Local Geary’s c [11], which are measures of the representative spatial autocorrelation analyses. Quantification by the “area ratio” was optimized by seeking an appropriate threshold level of the measures, correlated closely with tensile strength data.

2. Experimental

2.1. Summary of Experimental Method. Since the present experimental results are based on the previous paper [10], in this section the experimental method is briefly introduced as follows.

Materials. Flax slivers, one of the representative natural fibers, were used as reinforcement as shown in Figure 1. The slivers were supplied from Teikoku Sen-i Co., Ltd., Japan. Biodegradable thermoplastic resin was used as the matrix, which was supplied from Miyoshi Oil and Fat Co., Ltd., Japan (product name: Randy PL-1000). The resin was supplied in a water emulsion containing microorder fine particles of approximately $5.0\ \mu\text{m}$ diameter. The Randy PL-1000 is made from plant-derived biodegradable resins. In this sense,



FIGURE 2: Resin-pasted sliver (preform).

the resultant composite is a “fully green composite.” Typical physical and mechanical properties of these constituents are shown in Table 1.

Molding Process. First, the fibers on the front side were closed with resin and dried for 24 hours. Subsequently, another side (back side) was done with the same process as the front side. The thickness was 0.4 to 0.6 mm, of which the range was enough to exhibit nearly the same fiber orientation at the surface and inside. Such resin-pasted slivers are called preforms or prepregs. Figure 2 shows the photograph of the preform. At each process, the weight was measured for calculation of the fiber content. After finishing preparation of the preforms, we cut them to $100\ \text{mm} \times 100\ \text{mm}$ and put two pieces into the mold. The mold was set at 150°C for 40 min, and then the hydraulic press was set at 3 MPa pressure. The temperature was reduced to room temperature at pressure of 3 MPa for 24 hours. The fiber volume fractions V_f of all fabricated composites were calculated using the following equation:

$$V_f = 1 - \frac{W - W_f}{\rho_m V}, \quad (1)$$

where W is the fabricated composite weight, W_f is the flax fibre weight in the composite, V is the fabricated composite volume, and ρ_m is the biodegradable resin density.

Two methods were used to fabricate the composites: sheet lamination method (SLM) and direct method (DM). In DM, the resin was pasted directly for the as-supplied slivers. This method is more appropriate for mass production than SLM, but products fabricated using DM include numerous disordered parts in the fiber orientation. In SLM, the sliver was combed carefully to form unidirectionally oriented fibers before resin pasting.

Tensile Tests. Tensile specimens were cut to 15 mm width from DM and SLM composite laminates of $100\ \text{mm} \times 100\ \text{mm}$ square, and then aluminum plates ($15\ \text{mm} \times 15\ \text{mm}$) were attached with epoxy adhesive to both ends of all composite specimens for tensile testing. To prevent stress concentration near aluminum plates during tensile testing, their edges were shaved to 45° . A strain gage was attached on the center of

TABLE 1: Properties of the fibers and matrix [12, 13].

Material	Density (Mg/m ³)	Fiber width (μm)	Tensile strength (MPa)	Fracture strain (%)	Young's modulus (GPa)
Randy PL-1000	1.20	—	32.5	—	3.8
Flax fiber	1.50	10–30	600–1100	1.5–2.4	40–100

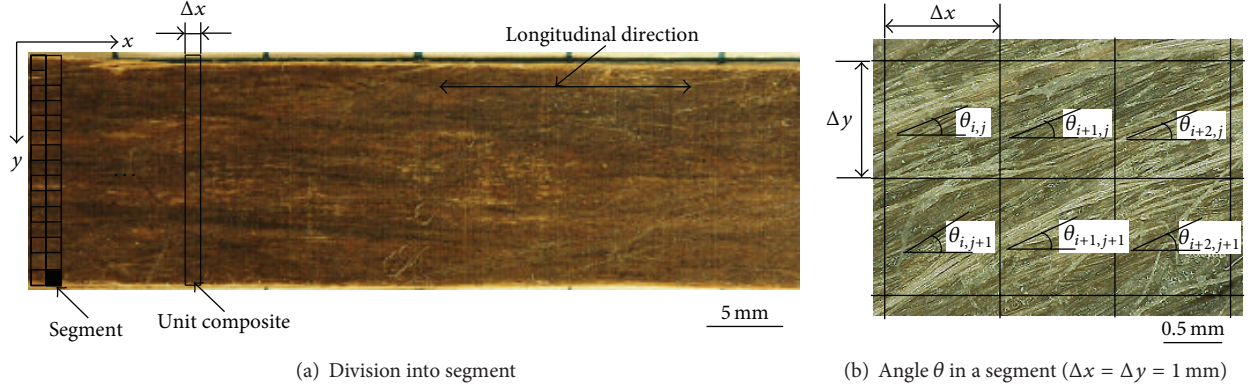


FIGURE 3: Measurement of fiber orientation angles on a flax-silver-reinforced composite laminate.

specimens to measure uniaxial strain. Tensile tests were carried out using an Instron-type testing machine (Autograph IS-500; Shimadzu Corp.) with cross-head speed of 1 mm/min.

Angle Measurements. Fiber orientation angles are important data for determining the strength and stiffness of a composite with fiber waviness. In this measurement, the x -axis is the longitudinal direction and y -axis is the transverse direction. Specimens were divided into a small size as 1 mm for Δx and Δy , which consist of 50 unit composites along the x -axis and one unit composite divided into 15 segments along the y -axis, as shown in Figure 3(a). The fiber orientation angle to the x -axis was measured in each segment of both sides, as shown in Figure 3(b). The total segments were 750 for each side. Image analysis software (Asahi Kasei Corp., Japan) was used for angle measurements.

2.2. Spatial Autocorrelation Analysis. In this study, two representative spatial autocorrelation analyses, Local Moran's I and Local Geary's c [11], were used to define the degree of local disorder of fiber orientation on tensile strength.

2.2.1. Local Moran's I . Moran's I was created by Moran [11] as a typical tool of spatial autocorrelation to analyze the deviation from the average. Local Moran's I is given as

$$I(\theta_i) = \frac{(\theta_i - \bar{\theta})}{(1/n) \sum_{i=1}^n (\theta_i - \bar{\theta})^2} \sum_{j=1, j \neq i}^n w_{ij}(d) (\theta_j - \bar{\theta}), \quad (2)$$

where $w_{ij}(d)$ is the weight function of the pair samples in distance d between the pair points, i th and j th locations, given as

$$w_{ij}(d) = \left\{ (x_i - x_j)^2 + (y_i - y_j)^2 \right\}^{-1/2}, \quad (3)$$

where x_i is i th position of the x -axis and the range is 1–50 mm. Also, y_i is the i th position of the y -axis, and the range is 1–15 mm. θ_i and θ_j are the angle data at the i th and j th positions, respectively. $\bar{\theta}$ is the average angle. Hereinafter, Local Moran's I is denoted as LM- I . LM- I varies between -1 and $+1$. If LM- I approaches $+1$, then the angle at this location is more largely far from the average, but similar to the neighbor's angles in their deviation from the average. On the other hand, if LM- I tends to approach -1 , then the angle at this location is also higher or lower than the average. But, the sign is different from the neighbor angles. When LM- I tends to approach 0 , the angle at this location is similar to the average. Theoretically, when LM- I is either much higher or lower than 0 , then the fiber orientation angle is significantly different from the average. Consequently, such LM- I points, if gathered locally, could form a large disordered area in fiber orientation.

2.2.2. Local Geary's c . Local Geary's c is another typical spatial autocorrelation to analyze a deviation from the surroundings. Local Geary's c is shown as

$$c(\theta_i) = \frac{1}{(1/n) \sum_{i=1}^n (\theta_i - \bar{\theta})^2} \sum_{j=1, j \neq i}^n w_{ij}(d) (\theta_i - \theta_j)^2. \quad (4)$$

Local Geary's c is hereinafter denoted as LG- c . LG- c varies between 0 and 1 . When LG- c tends to approach 0 , the angle at this location is similar to the neighbor angles. In contrast, when LG- c tends to approach 1 , the angle at this location differs from the sign of neighbor angles or is much higher than the neighbor's angles in absolute value. Consequently, such points can be disordered parts in fiber orientation.

2.3. Calculation of Area Ratio. To quantify the degree of local disorder in fiber orientation, we defined the "area ratio" which can be obtained from the contour maps of LM- I and LG- c .

TABLE 2: Fiber orientation angles and mechanical properties of flax-sliver-reinforced green composites [10].

Production method	Sample number	Fiber volume fraction	Specimens				Tensile strength and (standard deviation) (MPa)	Young's modulus (GPa)
			Side A (lower angle)		Side B (higher angle)			
			Avg. angle (°)	S.D. of angles (°)	Avg. angle (°)	S.D. of angles (°)		
SLM	—	0.72	0	—	0	—	238	40.5
	<1>	0.55	1.99	3.54	3.30	4.28	132	22.7
	<2>	0.55	2.62	5.22	4.19	4.03	224	26.7
	<3>	0.55	5.14	4.06	5.55	3.18	158	29.6
	<4>	0.55	3.05	3.22	8.76	4.18	211	27.6
	<5>	0.65	1.74	3.73	2.85	2.66	158	23.3
DM	<6>	0.65	2.10	2.62	3.07	3.48	203	26.4
	<7>	0.65	1.61	2.33	2.20	2.32	153	27.5
	<8>	0.65	2.08	3.47	3.76	2.95	170	28.0
	<9>	0.65	1.45	3.72	5.26	4.77	173	26.8
	<10>	0.65	0.76	3.50	4.55	3.90	168	28.8
	Avg.	0.61	2.35	3.50	4.35	3.60	175 (28.81)	26.8

The number of SLM specimens was seven. Avg.: Average, S.D.: Standard deviation.

In this quantification, we used two image analysis programs; first “Graph R221” was used for replotting the above contour maps to binary images (black and white areas), and next “Azo R235” was used to calculate the area ratios of the black (risky areas) and white (nonrisky areas). The meaning of “risky area” is described in the next section.

3. Results and Discussion

3.1. Tensile Properties and Fiber Orientation Angle. Table 2 shows results of tensile tests. The fiber volume fraction of DM specimens is lower than that of SLM specimens because of the fiber waviness. It was confirmed from the angle measurement that DM specimens scattered in a wide range from positive twenty degrees to negative twenty degrees. Typical contour maps of fiber orientation angles are shown in Figures 4(a) and 4(b), in which the standard deviations are largely different. The former specimen has a relatively large positive angle distribution in the upper left-side part. On the other hand, the latter shows a uniform angle distribution. As known from Table 2, any tensile strength and Young's modulus of DM specimens are lower than those of SLM specimens. It is considered that such degradation is caused by the fiber waviness, as well as the lower fiber volume fraction.

As described in earlier papers [9, 10], the Young's modulus was well correlated with the average fiber orientation angle, which is recognized as an average property of fiber waviness. On the other hand, tensile strength was not correlated with it, because tensile strength is a mechanical property sensitive to local structural defects. It was concluded in the paper [10], however, that the degree of increase in tensile strength was correlated with the area ratio of well-oriented fibers, which was analyzed from two-dimensional autocorrelation between two arbitrary regions of 7×15 segments. When the area ratio was larger, the tensile strength tended to be higher. But this area ratio did not express the degree of local disorder

in fiber orientation. In the next section, thus, we focus on quantification of the degree of local disorder.

3.2. Spatial Analysis. The contour maps of LM-I and LG-c are shown in Figures 5 and 6, in which the specimens are the same as those of Figure 4. In Figure 5, the large positive value segments are in nearly the same positions with the high angle distribution in absolute value in Figure 4. In comparison with the fractured specimens, we confirmed that the crack line tended to pass the positions of high coefficient of two methods. Thus, we call such positions the “risky area.” In many specimens, the risky areas of both LM-I and LG-c included one part of the crack line.

The segments with larger LM-I in absolute value would be loaded in shear and would suffer from premature damage, because many average angles in the specimens are relatively close to 0° , which are loaded in tension. If such premature damage is accumulated in the specimen, then it would cause premature tensile fracture, leading to low tensile strength. Therefore, the aggregate of such segments is risky from the viewpoint of materials reliability engineering. As shown in Figure 5, the scale of positive LM-I is large and that of negative LM-I is small. This is because a bunch of wavy fibers is larger in scale than the segment size, and its angles are measured as the same sign on the segments next to each other. In contrast, the segments with opposite signs in neighbors, which show negative LM-I, are only a few and are not major in scale. The scale of high LG-c values in Figure 6 is also small, as compared to that of positive LM-I values in Figure 5. One reason is the same as the cause of negative value scale in LM-I. Another is considered such that, even if the neighbors have the same sign, then LG-c can approach unity on the condition that there is a large difference between their angles. But, the scale could not extend more than a single segment size, because of a wavy flow structure of sliver. In this case, also, the segment with larger angle in absolute value would be loaded in shear. Thus, although there is a difference in scale, the areas

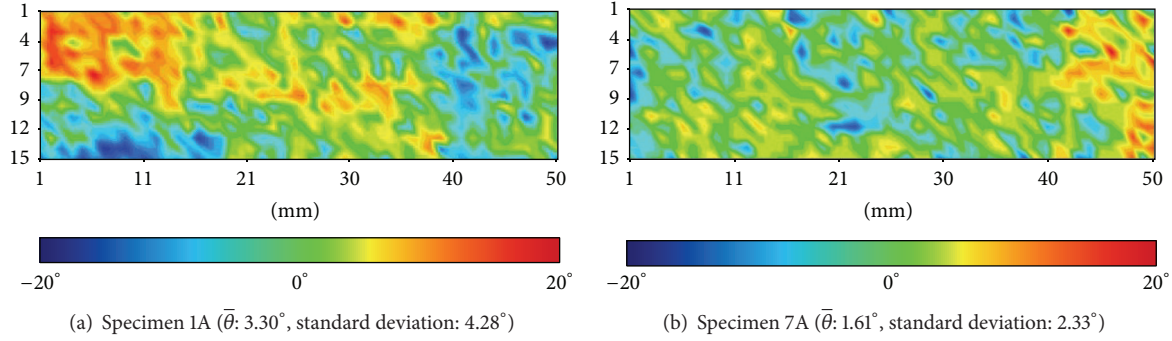


FIGURE 4: Contour map of fiber orientation angle distribution.

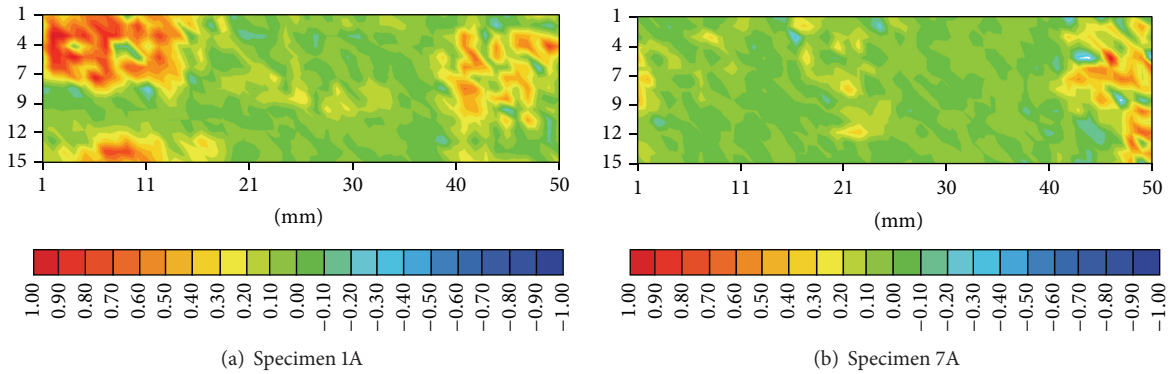


FIGURE 5: Contour maps of Local Moran's *I* distribution.

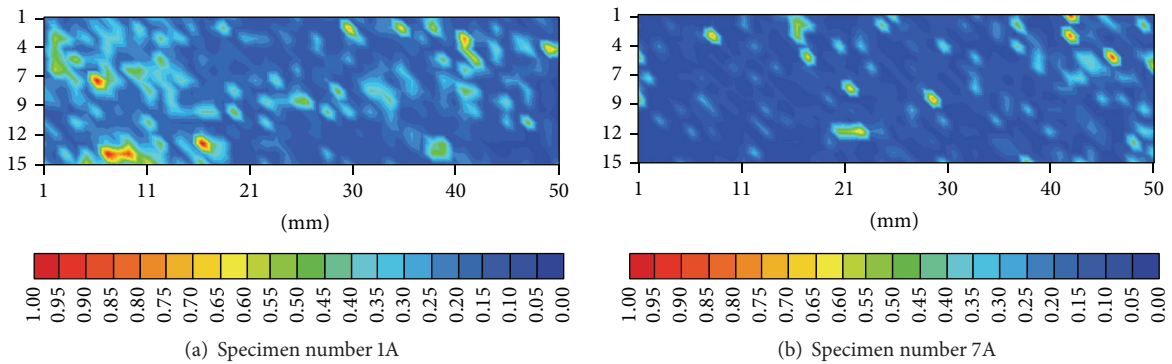


FIGURE 6: Contour maps of Local Geary's *c* distribution.

with large positive LM-*I*, negative LM-*I*, and large LG-*c* are equivalent to disordered parts in fiber orientation and may be correlated with tensile strength.

3.3. Area Ratio. Figure 7 shows LM-*I* binary images of specimens 1A and 7A, in which the areas consisting of LM-*I* higher than 0.65 or lower than -0.15 were temporarily selected. The numerical values, 0.65 and -0.15, are so-called threshold levels, which divide the areas into white and black. In Figure 7, the percentage of black area ratio was 6.80% (positive side = 4.80%, negative side = 2.00%) for specimen 1A and 3.47% (positive side = 0.67%, negative side = 2.80%) for specimen 7A. In these samples, the range of negative values

was designated more widely than that of positive value, because the segments with negative LM-*I* values are not so major but present the possibility of causing premature damage in shear, as mentioned in Section 3.2. Thus, wide range negative values and high positive values correspond to risky areas.

Regarding binary images of LG-*c*, the same samples as Figure 7 are shown in Figure 8. For these images, LG-*c* areas higher than 0.35 were selected. The value of 0.35 is a temporal threshold level. The percentages of black area ratio were 12.80% for specimen 1A and 5.33% for specimen 7A, respectively. As is easily known, when the threshold levels of LM-*I* and LG-*c* are changed, the area ratios accordingly

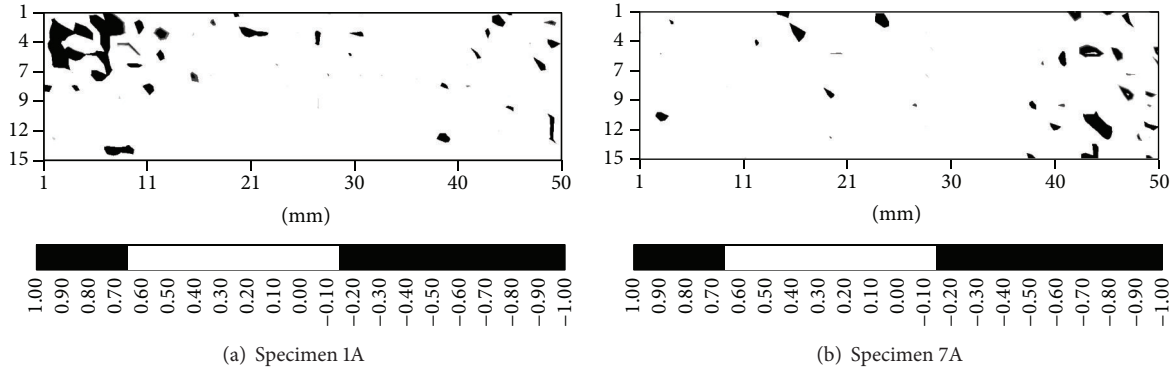


FIGURE 7: Binary images of Local Moran's I distribution (threshold levels: positive $LM-I = 0.65$ and negative $LM-I = -0.15$).

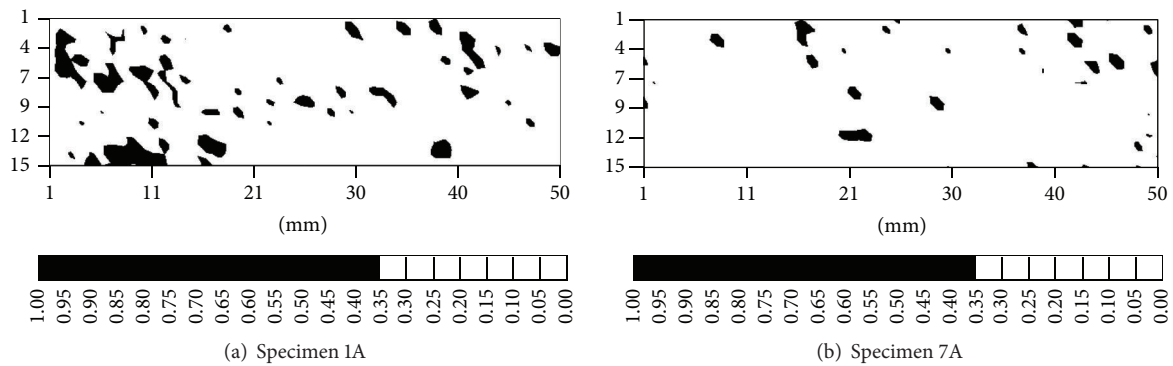


FIGURE 8: Binary images of Local Geary's c distribution (threshold level: $LG-c = 0.35$).

change. We consider that, if appropriate threshold level(s) are given, then some optimal area ratio correlated with tensile strength exists for each specimen. This is because the ratio of segments suffering from shear damages during tensile loading should be related closely with the area ratio. In the next section, thus, the relation between area ratio and tensile strength is investigated.

3.4. Relation between Area Ratio and Tensile Strength. To investigate the correlation between the area ratio and tensile strength, normalized tensile strength data were plotted as a function of area ratio, as shown in Figures 9 and 10, where each tensile strength value was normalized at the same fiber volume fraction. That is to say, the tensile strengths were normalized by dividing the measured strength by the fiber volume fraction V_f and then multiplying it by 0.72, corresponding to V_f of SLM specimen. In Figure 9, it appears that the normalized strength is correlated with the area ratio. The correlation coefficient in Figure 9 was calculated as -0.618 when setting the threshold levels at 0.65 (positive $LM-I$) and -0.15 (negative $LM-I$). The value of -0.618 is not so strong but presents an intermediate strong correlation. This means that if many segments in a specimen are distributed with $LM-I$ values higher or lower than the above threshold levels, its tensile strength tends to be lowered. It also means that a rough value of tensile strength can be estimated through the least-squares regression line between area ratio and tensile

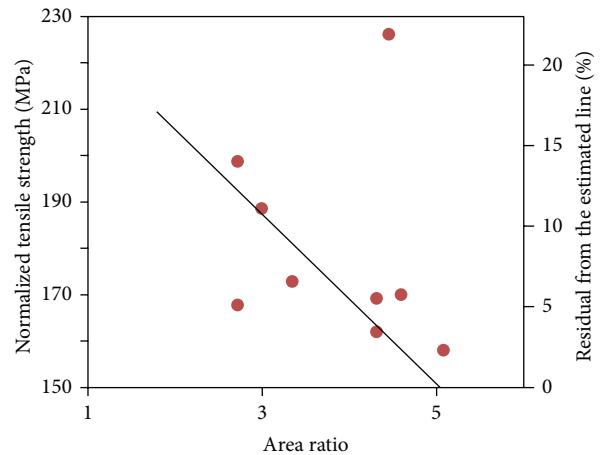


FIGURE 9: Area ratio dependence on normalized tensile strength (threshold levels: positive $LM-I = 0.65$ and negative $LM-I = -0.15$).

strength. In contrast, the correlation coefficient between the area ratio and tensile strength in Figure 10 was only -0.117 , when choosing 0.35 as a threshold level. The value of -0.117 signifies weak correlation. This result implies that 0.35 is not appropriate as a threshold level or that Local Geary's c does not match correlation with tensile strength. To find the optimal threshold levels of $LM-I$ and $LG-c$, the negative

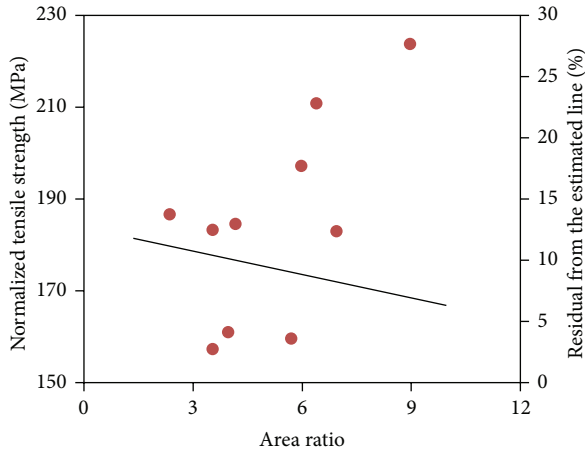


FIGURE 10: Area ratio dependence on normalized tensile strength (threshold level: LG- $c = 0.35$).

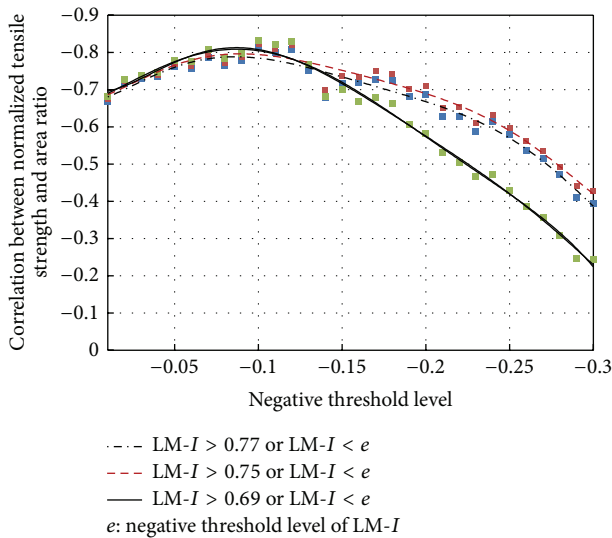


FIGURE 11: Correlation coefficients between LM- I area ratio and normalized tensile strength versus negative threshold level.

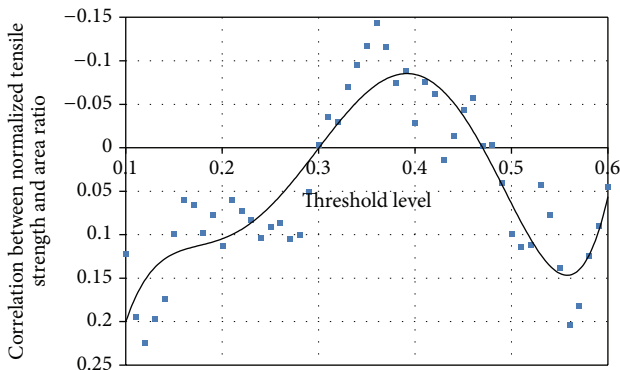


FIGURE 12: Correlation coefficients between LG- c area ratio and normalized tensile strength versus threshold level.

threshold level of LM- I was assigned in the range of -0.01 to -0.3 , and the threshold level of LG- c was in the range of 0.1 to 0.60 . For LM- I , the positive threshold level was also chosen as 0.69 , 0.75 , or 0.77 .

The results are shown in Figures 11 and 12. Figure 11 shows that the optimal threshold levels of LM- I are 0.69 at the positive level and -0.10 at the negative level, and that of LG- c is 0.36 . At the former optimal threshold levels, the correlation coefficient between the area ratio and tensile strength was -0.832 . On the other hand, the highest correlation coefficient in Figure 12 was only -0.14 even at the optimal threshold level. The value of -0.832 denotes a strong negative correlation between the area ratio and tensile strength. In other words, tensile strength can be estimated to some degree using the least-squares regression line when setting the optimal threshold levels of LM- I . It is also expected that the present procedure is applied as an effective screening method for extracting low-quality prepreps at quality inspection.

4. Conclusions

This study clarified the effect of fiber waviness on the tensile strength of a flax-sliver-reinforced biodegradable resin matrix composite material. The fiber waviness was quantified using Local Moran's I and Local Geary's c , each of which can express the degree of disorder in fiber orientation. Results show that Local Moran's I is correlated well with tensile strength of the composite specimens when appropriate threshold levels are selected. On the other hand, Local Geary's c is not well correlated with tensile strength exists for each specimen. Normally, finite element analysis is a well-known as a method for elucidating the mechanical behavior of composite materials, such as stress and strain distributions. Furthermore, finite element analysis is often extended to the fracture process simulation to predict strength properties. However, the method needs to use several math models to ascertain the solution that takes time and the advanced knowledge for understanding. However, this study using the spatial autocorrelation analysis has fewer equations and does not take a long time for the program code development. Thus, we conclude that the method proposed in this study is an effective tool for rough prediction of the tensile strength of natural-fiber-sliver-based composite materials.

Conflict of Interests

The authors declare that there is no conflict of interests regarding the publication of this paper.

References

- [1] L. Liu, J. Yu, L. Cheng, and X. Yang, "Biodegradability of poly(butylene succinate) (PBS) composite reinforced with jute fibre," *Polymer Degradation and Stability*, vol. 94, no. 1, pp. 90–94, 2009.
- [2] S. Alix, S. Marais, C. Morvan, and L. Lebrun, "Biocomposite materials from flax plants: preparation and properties," *Composites Part A: Applied Science and Manufacturing*, vol. 39, no. 12, pp. 1793–1801, 2008.

- [3] P. Lodha and A. N. Netravali, "Characterization of stearic acid modified soy protein isolate resin and ramie fiber reinforced 'green' composites," *Composites Science and Technology*, vol. 65, no. 7-8, pp. 1211-1225, 2005.
- [4] S. Serizawa, K. Inoue, and M. Iji, "Kenaf-fiber-reinforced poly(lactic acid) used for electronic products," *Journal of Applied Polymer Science*, vol. 100, no. 1, pp. 618-624, 2006.
- [5] A. Gomes, T. Matsuo, K. Goda, and J. Ohgi, "Development and effect of alkali treatment on tensile properties of curaua fiber green composites," *Composites Part A: Applied Science and Manufacturing*, vol. 38, no. 8, pp. 1811-1820, 2007.
- [6] LINEO FLAXTAPE, <http://www.lineo.eu/#!products>.
- [7] H. M. Hsiao and I. M. Daniel, *Elastic Properties of Composite with Fiber Waviness*, Elsevier Science, 1996.
- [8] G. Karami and M. Garnich, "Effective moduli and failure considerations for composites with periodic fiber waviness," *Composite Structures*, vol. 67, no. 4, pp. 461-475, 2005.
- [9] B. Ren, K. Goda, and J. Noda, "Effects of fiber orientation angles and fluctuation on the stiffness and strength of sliver-based green composites," *Journal of the Society of Materials Science, Japan*, vol. 59, no. 7, pp. 567-574, 2010.
- [10] B. Ren, T. Mizue, K. Goda, and J. Noda, "Effects of fluctuation of fibre orientation on tensile properties of flax sliver-reinforced green composites," *Composite Structures*, vol. 94, no. 12, pp. 3457-3464, 2012.
- [11] M.-J. Fortin and M. Dale, *Spatial Analysis*, Cambridge University Press, 2014.
- [12] Flax slivers, Teikoku Sen-I, Tokyo, Japan, <http://www.teisen.co.jp>.
- [13] Miyoshi Oil & Fat, *Randy PL-1000*, Miyoshi Oil & Fat, Tokyo, Japan, 2012, <http://www.miyoshi-yushi.co.jp>.

Research Article

Ground Hemp Fibers as Filler/Reinforcement for Thermoplastic Biocomposites

Amir Etaati,¹ Selvan Pather,² Moloud Rahman,³ and Hao Wang¹

¹Centre of Excellence in Engineered Fibre Composite, Faculty of Health, Engineering and Sciences, University of Southern Queensland, Toowoomba, QLD 4350, Australia

²Faculty of Science, Health, Engineering and Education, University of the Sunshine Coast, Sunshine Coast, QLD 4558, Australia

³University of Southern Queensland, Toowoomba, QLD 4350, Australia

Correspondence should be addressed to Hao Wang; hao.wang@usq.edu.au

Received 9 January 2015; Accepted 5 May 2015

Academic Editor: Pavel Lejcek

Copyright © 2015 Amir Etaati et al. This is an open access article distributed under the Creative Commons Attribution License, which permits unrestricted use, distribution, and reproduction in any medium, provided the original work is properly cited.

Mechanical properties (tensile, flexural, and impact) of ground hemp fibre polypropylene composites were investigated. Ground alkali-treated hemp fibre and noil hemp fibres with various initial fibre lengths were utilized to reinforce polypropylene matrix. Firstly, the microstructural and tensile characterizations of the two types of fibres were characterized using scanning electron microscope (SEM), Fourier transform infrared analysis (FTIR), and Dynamic Mechanical Analyser (DMA). Then, the fibres were ground into different lengths of 0.2, 0.5, 1, and 2 mm; composites containing 40 wt% short hemp fibre and 5 wt% maleic anhydride grafted polypropylene (MAPP) were fabricated by means of a twin screw extruder and an injection moulding machine. Finally, influence of hemp fibre type and initial hemp fibre length on tensile property of the composites were investigated. The results revealed that addition of either noil hemp fibre or normal treated hemp fibre into the pure polypropylene matrix increased the tensile strength almost twice and stiffness of the composites more than three times. Although noil hemp fibre composite indicated slightly lower mechanical properties than the normal alkali-treated fibre composites, the difference was not significant. The analysis of the results provided the optimum initial fibre length (powder) of 0.2 mm hemp polypropylene composite. The results can be extended to different types of natural fibres.

1. Introduction

Biocomposites refer to composites that combine natural fibres, such as kenaf, jute, hemp, and sisal, with either biodegradable or nonbiodegradable polymers. Investigations on the use of natural fibres as reinforcement have introduced further applications for fibre reinforced thermoplastics in automotive and construction industries. Hemp fibre is a sustainable resource and also has shown a promising specific tensile strength to be used as reinforcement in composites for many applications [1].

Many attempts have been carried out to investigate the influence of fibre content on tensile strength and modulus of elasticity of different natural fibre reinforced polymer composites [1–3]. In general, the increase in fibre content improves tensile strengths and modulus of elasticity of

the natural fibre reinforced polymer composites up to a peak value, which then decrease rapidly [1]. However, the tensile strength of the composites might be far below their potential values due to the poor interfacial adhesion between hydrophilic lignocellulosic fibres and the hydrophobic polymer matrix. A strong fibre/matrix bonding is essential for transferring the stress from the matrix to the fibres, thus taking full advantage of the natural fibres as load bearing reinforcements in the composite.

Over the past decades, many researchers have studied the effect of various compatibilizers to improve the fibre adhesion and dispersion in the composites such as maleic anhydride grafted polyolefins [4], isocyanates [5] and silanes [5, 6], and maleic anhydride grafted polyethylene octene elastomer (MAGPOE) [4, 7]. Compatibilizers can modify the interface by interacting with both the fibre and the matrix,

forming a bridge between the components and consequently enhancing the interface bonding. Among the studied compatibilizers, maleic anhydride grafted polypropylene (MAPP) is the most commonly used coupling agent to strengthen the natural fibre/matrix interfacial adhesion. Referring to the literature, the optimum tensile properties were observed after adding 3–5 wt% of MAPP to the natural fibre reinforced plastic composites [1, 4].

Injection moulding can be used to produce high quality complex parts, which is evident from the mass of plastic parts with complex shapes used in the construction, furniture, appliance, and automotive industries. Short fibres are normally used in injection moulding. Noil hemp fibre is a by-product of textile hemp fibre industries. In comparison with the hemp fibres, noil fibres are more thermally resistant because they are highly degummed and they have lower pectin content. They will be referred as noil fibre in this paper to recognise it from normal hemp fibre. They are too short to be used for fabric production but have the potential to be used as the reinforcements in injection-moulded thermoplastic composites [8].

Fibre length strongly affects mechanical properties of the composite. Surface area, which is a factor of fibre length and diameter, provides the interface to transmit the stresses from the matrix to the fibres under an applied load [9]. However, during the processing of the short fibre plastic composites, the natural fibres undergo breakage and also fibre agglomeration which reduce the reinforcing efficiency of the fibres. Our previous work revealed that hemp fibre with an average length of 1.5 cm is shortened to less than 200 μm after fabrication of composite [10–12]. Thus, the current project attempted to use the powdered fibres, which might reduce the fibre agglomeration and might result in higher tensile properties of hemp fibre composites ultimately. Also, this paper aimed to assess whether noil hemp fibre is suitable alternative for the normal hemp fibre or not.

2. Experimental

2.1. Raw Materials. Noil fibres and normal hemp fibres (Figure 1) were supplied by China-Hemp Industrial Investments and Holding Co. Ltd. A M800E polypropylene (Sinopec Shanghai petrochemical Co. Ltd., China) with melt flow index of 8.0 ± 1.5 g/10 min being used as the matrix. MAPP with MA content of 1.0 wt% (Bondyram1001, Polyram Ram-On Industries, Israel) was used as the compatibilizer to the resin mix.

2.2. Fibre Treatments. Only normal hemp fibres were immersed in hydroxide solutions with concentration of 5 wt% at ambient temperature holding for 3 hours. After treatment, fibres were washed several times with 40°C water until its PH reached to 7. Then they were oven-dried for 24 hours at 80°C.

2.3. Fibre Characterizations Methods. Surfaces of untreated and treated normal hemp fibre and also noil fibres were examined by scanning electron microscope (JEOL 7800F SEM) operated at 5 kV. Samples were mounted onto aluminium

stubs with carbon tape and then sputter coated with platinum in 120 seconds to make them conductive prior to SEM observation.

Fourier transform infrared analysis was examined using Thermo Nicolet FTIR Spectrometer model Nexus which uses a Perking-Elmer spectrometer and the standard KBr pellet technique. Approximately 3 mg hemp fibres was crushed into fine particles and mixed with about 15 mg KBr and then pressed into a pellet for FTIR measurement. Effects of fibre treatment on chemical composition of hemp fibres were investigated.

A DMA Q800 V5.1 Dynamic Mechanical Analyser was used at ambient temperature to investigate the tensile properties of noil hemp fibres according to ASTM D 3822-01. Noil hemp fibres were separated and then mounted on cardboards with 7, 12, and 20 mm holes as gauge lengths.

Fibres were observed under a MOTIC SMZ-168 series stereo zoom microscope equipped with a CC12 Soft Imaging System to measure diameter of the fibres (average of 5 randomly measured diameters). The mounted fibres were then placed in the holders of the DMA Q800 V5.1 Dynamic Mechanical Analyser testing machine and the supporting sides of the mounting cards were cut. The fibres were then tensile tested to failure at rate of 10 mm/min.

2.4. Composite Fabrication. Then both noil fibres and treated normal hemp fibres were ground into 0.2, 0.5, 1, and 2 mm and dried at 80°C for 24 h. In order to make hemp fibre powder, hemp fibres were first chopped into snippets by a cutter mill (Pulverisette 15), and then variable-speed rotor mill (Pulverisette 14) was applied to further ground the fibrous materials into powder. The powder size was controlled by the passing times of hemp fibres through the rotor mill.

The 40 wt% ground fibre, 5 wt% MAPP, and polypropylene were compounded in a EuroLab 16XL twin-screw extruder operated at 100 revolutions per minute (rpm). The extruder barrel consisted of six heating zones, which were set at 180°C. After cooling in air, the extruded composite material was granulated in an industrial granulator to produce composite pellets with a length around 5 mm. The composite pellets were then dried at 80°C for 3 h before being injection moulded into tensile test specimens.

2.5. Composite Tensile Testing. The tensile strength of the specimens were evaluated using a MTS RT/10 (10 KN Capacity) according to the ASTM D638-91 standard at the specified loading rate of 10 mm/min. The composite specimens were tested to failure and the average value of 10 tensile-tested specimens was reported for each sample.

2.6. Composite Flexural Testing. Three-point flexural testing of the pure polypropylene and normal hemp fibre polypropylene composites were carried out by means of the 10 KN MTS testing machine according to the ISO 178 at a loading rate of 5 mm/min. The average of 5 specimens with cross sections of 4 mm \times 10 mm was reported for each sample. The span set at approximately 16 times of the thickness.



FIGURE 1: (a) As-received noil hemp bundles, (b) ground noil hemp fibres, (c) untreated normal hemp fibre, and (d) ground treated hemp fibres.

2.7. Composite Impact Testing. To investigate the impact performance of the composites, an unnotched Charpy impact strength test was carried out according to ASTM-D256, using an Instron Dynatup impact tester. Impact test was used to characterize the impact performance of composites with varying original fibre length. Sample dimensions were 160 mm × 10 mm × 4 mm for impact testing. A total of 5 specimens were used to determine the impact properties of the composites.

3. Results and Discussion

3.1. Chemical Structure of the Fibres. FTIR allows studying the influence of chemical treatment on variations of hemp fibre composition. Infrared spectrums of untreated and treated hemp and noil hemp fibres are plotted in Figure 2. Table 1 also summarizes the major peaks observed in the FTIR spectrums along with their possible sources.

As can be seen in Figure 2, one of the most noticeable changes generated by alkali treatment is the disappearance of the peak at 1732 cm⁻¹. Referring to [13, 14], this can be attributed to the C=O carbonyl stretching in carboxylic groups that mostly occur in the branched chain hemicelluloses and also in esterified and carboxylic groups in pectin. Therefore, disappearance of the mentioned peak indicates to removal of pectin and hemicellulose from surface of the fibre.

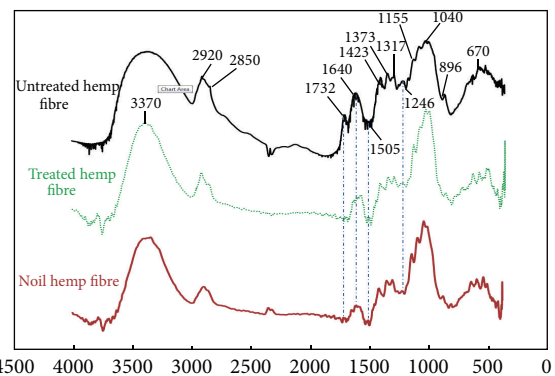


FIGURE 2: Infrared spectrums of untreated and treated hemp and noil hemp fibres.

The peak located at 1505 cm⁻¹ which is originated from lignin can be seen in the spectrums before and after alkali treatment. Nevertheless, another peak associated to the lignin (peak at 1246 cm⁻¹) was broadened after alkali treatment. It seems that alkali can remove the lignin partially from the hemp fibre's surface.

There is a blunt peak in the FTIR spectrums of the untreated fibre in the region of 3250–3550 cm⁻¹. This peak is

TABLE 1: The major peaks observed in the FTIR spectrums and their possible source [18–21].

Wave number (cm ⁻¹)	Vibration	Sources
670	C–OH out-of-plane bending	Cellulose
896	COC, CCO, and CCH deformation and stretching	Cellulose
1040	C–C, C–OH, C–H ring, and side group vibrations	Cellulose and hemicellulose
1155	C–O–C asymmetrical stretching	Cellulose and hemicellulose
1246	C–O aryl group	Lignin
1317	CH ₂ rocking vibration	Cellulose
1373	In-the-plane CH bending	Cellulose and hemicellulose
1423	HCH and OCH in-plane bending vibration	Pectin, lignin, hemicelluloses, and calcium pectates
1505	C=C aromatic symmetrical stretching	Lignin
1640	OH bending of absorbed water	Water
1732	C=O stretching Esterified and carboxylic groups	Xylans (hemicelluloses) Pectin
2850	CH ₂ symmetrical stretching	Wax
2920	C–H symmetrical stretching	Cellulose
3370	O–H linked shearing	Polysaccharides

associated to the stretching vibration of hydrogen bonding of the hydroxyl group. It is not sharp due to interfering contributions from a variety of stretching modes in the amorphous regions [14]. However, after removal of amorphous materials (hemicellulose, pectin, and lignin), the peak becomes sharp at 3370 cm⁻¹. Besides, there is another sharp peak in the FTIR spectrum of the untreated fibres around 1640 cm⁻¹, which is associated to the OH bending of absorbed water. This peak broadened after alkali treatment. Thus, treating the fibres reduced the moisture absorbance of the fibres by removal of hydrophilic lignocellulosic materials which include accessible hydroxyl groups.

It is worth mentioning that FTIR spectrum of the noil hemp fibre is so much similar to that of the treated fibre. Noil hemp fibre contains almost the same type of chemical components as the treated hemp fibres. Noil fibres can be used as reinforcement in the short fibre composites without applying further treatments to remove the lignocellulosic amorphous materials.

3.2. Fibre Morphology Analysis. The morphology of the fibres was studied by scanning electron microscope (SEM). SEM micrographs of the fibre surfaces can be seen from Figure 3 to Figure 6. Figure 3 reveals the SEM micrographs of an untreated hemp bundle whose surface is covered by the gummy polysaccharides of lignin, pectin, and hemicellulose. These materials are completely/partially removed after alkali treatment as seen in Figure 4. Removal of the lignin, pectin, and hemicellulose alters the morphology of the hemp fibre. The fibres can partially/completely be separated to elementary fibres after alkali treatment. The separation lines which show bundles of continuous elementary fibre can be viewed in Figure 4. In comparison with the untreated fibre, the treated fibres are clean but rough. The roughness enhances mechanical interlocking bonding mechanisms between fibre and the

matrix, and the clean surfaces are supposed to create stronger bonding between OH groups of the fibre and the matrix. This observation clearly indicated that alkali treatments could remove the hemicellulose and lignin coverings from the fibre surfaces. Figure 5 shows the SEM micrographs of the noil hemp fibre and Figure 6 presents the kink band observed in noil hemp fibres.

As can be seen in Figures 5 and 6, the fibre surfaces are completely clean of gummy polysaccharides. Its cleanness implies that the noil hemp fibres are already separated to elementary fibres (microfibres) during degumming processes in textile industry. Thus, in correlation with FTIR analysis, it does not require to remove the noncellulosic materials (pectin, lignin, and hemicellulose).

Two main types of defects, which are naturally expected to be found in the cell walls of the natural fibres, are known as kink bands and microcracks. Figure 6 shows the kink band observed in SEM micrographs of noil hemp fibres. At the kink band regions, the angle of the microfibrils relative to the fibre axis differs from the angle of the surround cell wall, which corresponds to the change of crystalline orientation. It has been reported that the kink bands result in a lower strength and they are the most likely area to break during tensile tests of fibres [15, 16].

Figure 7 shows SEM micrographs of noil hemp fibres including microcracks in fibre cell wall along the fibre length. Microcracks lead to stress concentrations when fibres are loaded as reinforcements in composites. Not only do these defects cause variability in fibre properties but they also considerably reduce fibre strength. More defects (microcracks) are observed in noil fibres. Thus, it is expected that noil hemp fibres have a lower tensile strength than normal hemp fibres.

3.3. Strength of the Fibres. The tensile properties of single hemp fibres were evaluated for all investigating fibres.

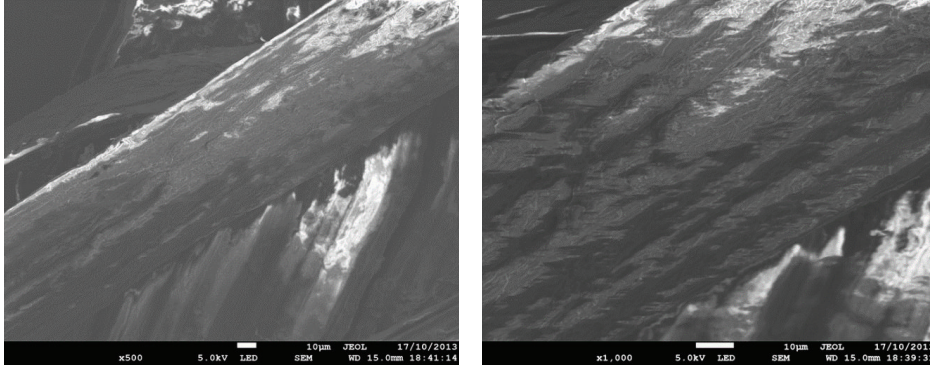


FIGURE 3: SEM micrographs of an untreated hemp bundle (the surface is covered by the gummy polysaccharides).

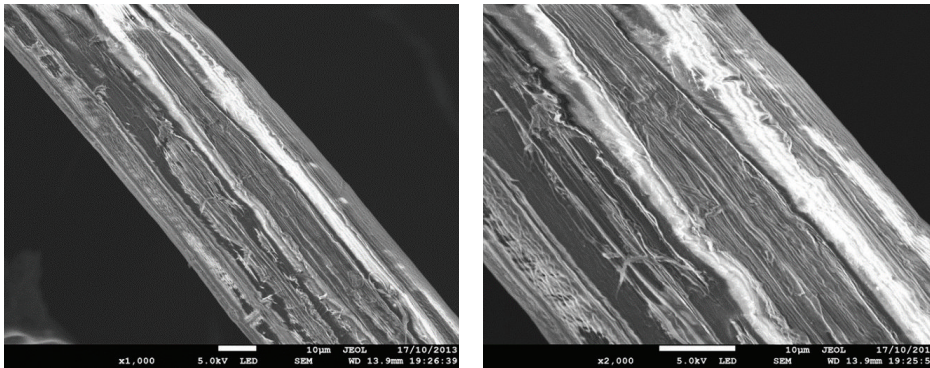


FIGURE 4: SEM micrographs of a treated hemp fibre.

Figures 8(a) and 8(b) represent the typical stress-strain curves of single noil hemp fibre and the average tensile strength values of untreated, treated, and noil hemp fibres, respectively. It can be seen that the stress versus strain curves were almost linear until fracture of the fibre. Figure 8(b) shows that the tensile strength of the 5 wt% alkali treated fibre is almost 40% higher than that of the untreated fibre. The increase in tensile strength of treated fibre was due to removal of cementing materials which resulted in lower cross section of fibres in single fibre tensile testing. On the other hand, the noil hemp fibres introduced 33% lower tensile strength compared with the alkali treated fibre. The transversal cross section of hemp is not cylindrical and there are many defects that exist along fibres length. Thus, this massive deviation is inevitable in studying characteristics of hemp fibres. Although standard deviation of the data is high, it can be concluded that tensile strength of noil hemp fibres are significantly lower than those of normal hemp fibres. It is believed that stress concentrations around microcracks can act as the sites for the initiation of fibre matrix debonding, for the formation of microcracks in the matrix or for fracture of the hemp fibre.

3.4. Tensile Properties. The tensile strengths of the pure polypropylene and their composites with 40 wt% fibre content with various initial fibre length are illustrated in Figure 9 and Table 2. It can be seen that the addition of 40 wt% noil hemp fibre with initial length of 0.2 mm into the pure PP

increased the tensile strength of the samples from 16.9 MPa to 32.8 MPa.

In addition, it can be noted in Figure 9 that as the initial fibre length increased, the tensile strength of the samples decreased gradually. However, the difference between composites with 0.2 mm and 0.5 mm is insignificant. It implies the fact that feeding of longer fibres in compounding and injection moulding machines cannot only improve the tensile properties of the composites but also can degrade the properties, probably due to the formation of fibre agglomerations and consequently heterogeneous dispersion of the fibres.

Young's modulus (GPa) of the samples followed the same trend (Figure 10). It increased from 1 GPa for pure PP to 3.6 for GPa composite with 0.2 mm long fibres. Then it decreased gradually as the fibre length increased.

Referring to Figure 8, the average tensile strength of the noil hemp fibre was approximately 175 MPa lower than that of the treated normal hemp fibres. However, there is no significant difference in tensile strength values between treated hemp and noil fibres composites.

3.5. Flexural Properties. Typical flexural stress-strain curves for noil hemp fibre composites are presented in Figure 11. It can be seen that the curves show initially linear portion, followed by a nonlinear region prior to the maximum flexural stress. Once the maximum stress is reached, the stress decreases just slightly until the fracture happens.

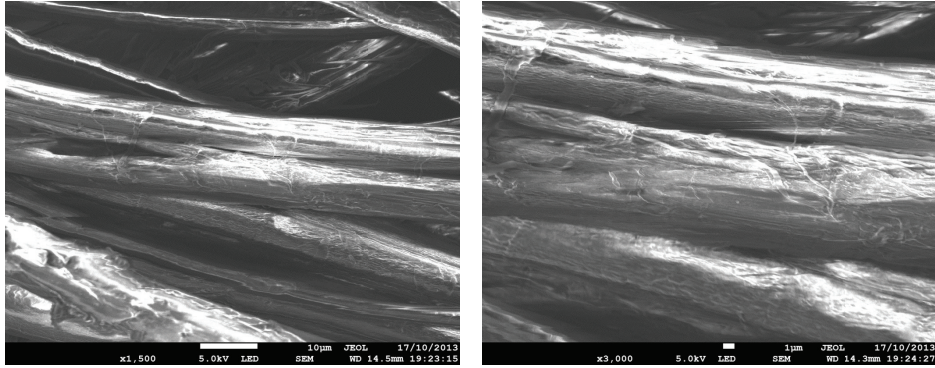


FIGURE 5: SEM micrographs of the noil hemp fibre (elementary fibres are already separated).

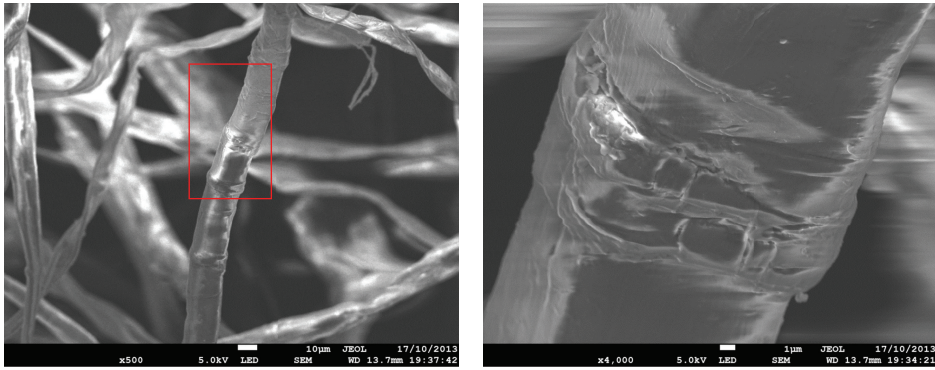


FIGURE 6: SEM micrographs of noil hemp fibres presenting the kink band clearly observed in noil hemp fibres.

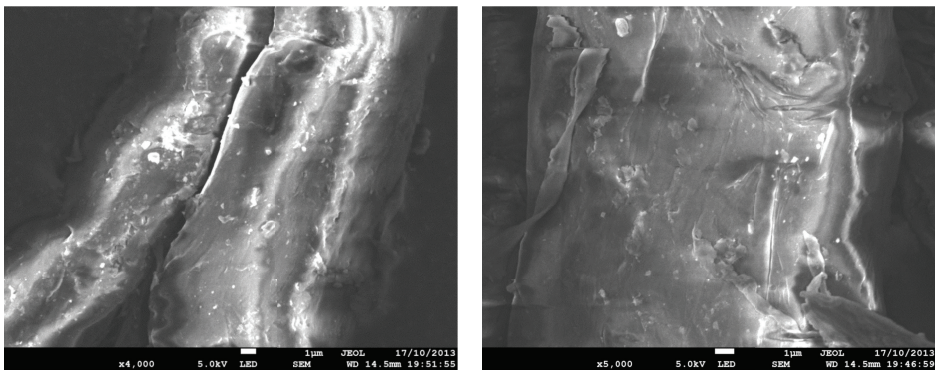


FIGURE 7: SEM micrographs of noil hemp fibres presenting the microcracks.

TABLE 2: Tensile properties of the noil hemp fibre and hemp fibre composites with varying initial fibre lengths.

Fibre length (mm)	Noil hemp fibre		Hemp fibre	
	Tensile strength (MPa)	Young's modulus (GPa)	Tensile strength (MPa)	Young's modulus (GPa)
0.20	32.85 ± 0.67	3.57 ± 0.29	33.61 ± 1.35	3.77 ± 0.31
0.50	31.83 ± 1.96	3.29 ± 0.29	32.86 ± 0.36	3.38 ± 0.67
1.00	27.90 ± 2.76	3.03 ± 0.07	31.53 ± 2.23	3.55 ± 0.88
2.00	31.18 ± 2.47	3.32 ± 0.30	29.64 ± 1.78	3.03 ± 0.52

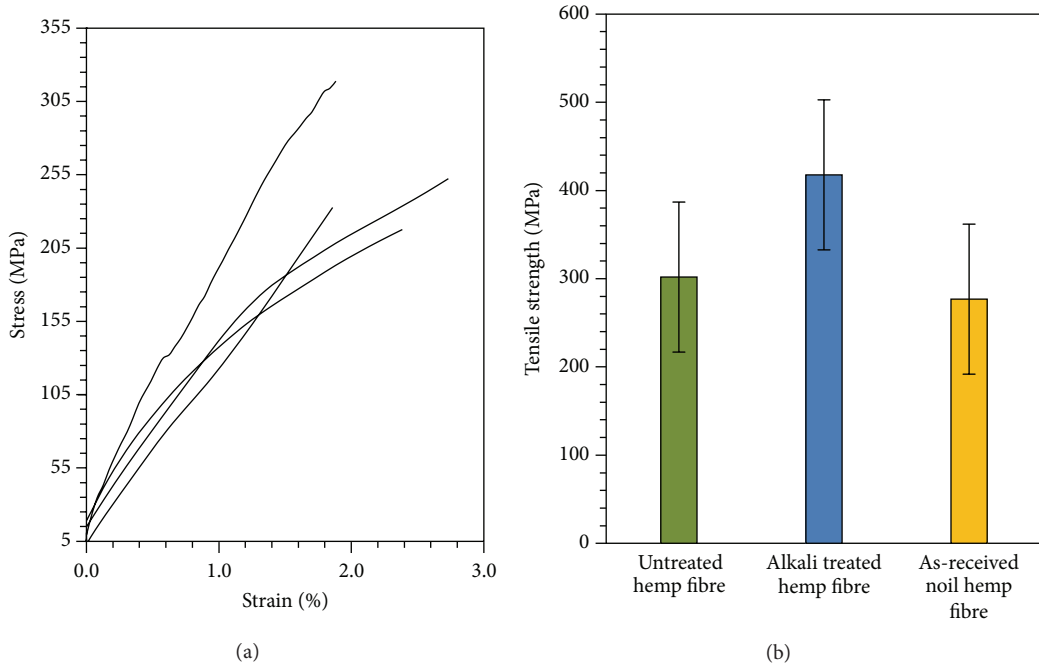


FIGURE 8: (a) Typical stress-strain curves of single noil hemp fibre at gauge length of 12 mm and (b) tensile strength of the untreated, alkali treated, and noil hemp fibres at the same gauge length.

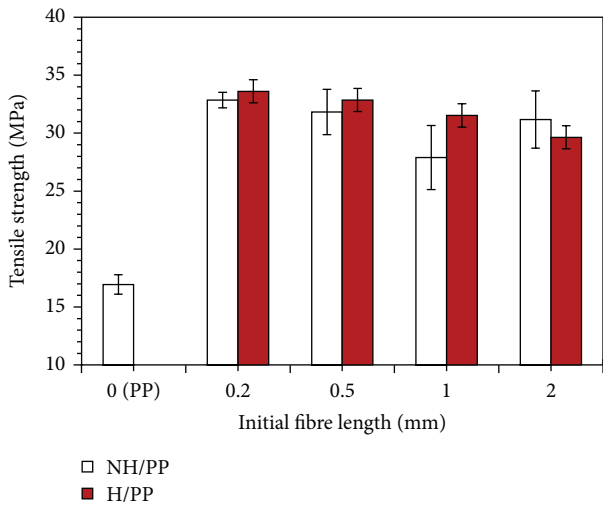


FIGURE 9: The influence of the initial fibre length on tensile strength of the noil (white) and treated hemp (red) fibre reinforced polypropylene composites.

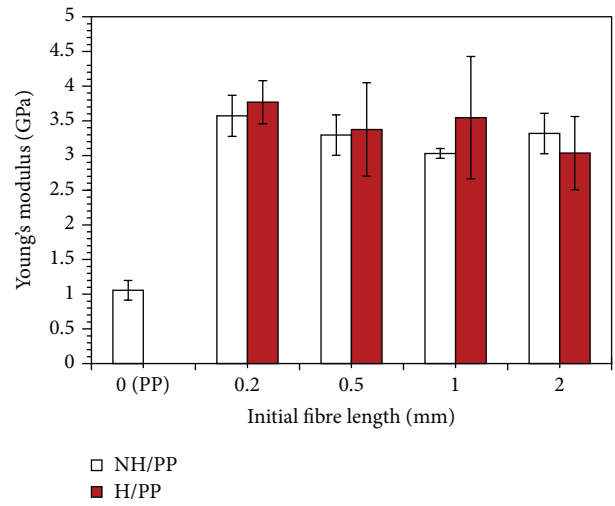


FIGURE 10: The influence of the initial fibre length on Young's modulus of the noil (white) and treated hemp (red) fibre reinforced polypropylene composites.

The average flexural strength and flexural modulus of the noil hemp fibre polypropylene (NH/PP) and hemp fibre polypropylene (H/PP) composites as a function of initial fibre length are shown and presented in Table 3 and Figures 12 and 13. As can be seen in Figure 12, the flexural strength increased with addition of 40 wt% short fibres into the pure polypropylene. The average flexural strength increased with addition of 0.2 mm short fibres from 12.4 for pure polypropylene to 55.65 for NH/PP and 51.19 for H/PP. Likewise, the flexural modulus

of the composites raised from approximately 0.5 GPa for polypropylene to higher than 3 GPa for the composites with fibre length of 0.2 mm (Figure 13). Similar to tensile strength and Young's modulus findings, the flexural strength and flexural modulus of both composites were declined as fibres longer than 0.2 mm were used to fabricate the composites.

3.6. Impact Strength. It has been concluded so far that reinforcing fibres with initial length of 0.2 mm can provide

TABLE 3: Flexural properties of composites with different fibre lengths.

Fibre length (mm)	Noil hemp fibre composite		Hemp fibre composite	
	Flexural strength (MPa)	Flexural modulus (GPa)	Flexural strength (MPa)	Flexural modulus (GPa)
0.20	55.65 ± 0.98	3.31 ± 0.14	51.19 ± 4.21	3.11 ± 0.22
0.50	53.25 ± 4.11	3.04 ± 0.07	51.18 ± 5.01	3.06 ± 0.13
1.00	44.05 ± 4.00	2.76 ± 0.37	39.63 ± 0.95	1.95 ± 0.16
2.00	39.91 ± 6.77	2.14 ± 0.43	40.26 ± 4.01	2.32 ± 0.27

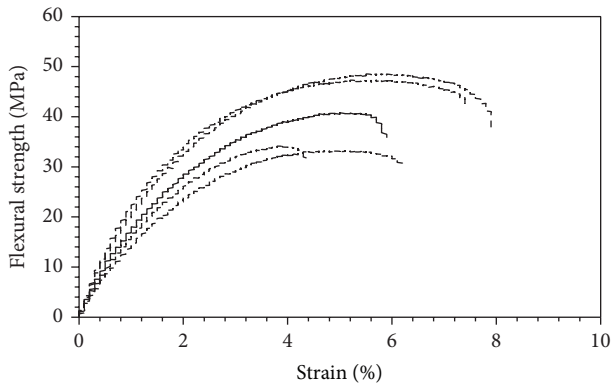


FIGURE 11: Flexural stress-strain curves for 40 wt% noil hemp fibre composite with initial fibre length of 2 mm.

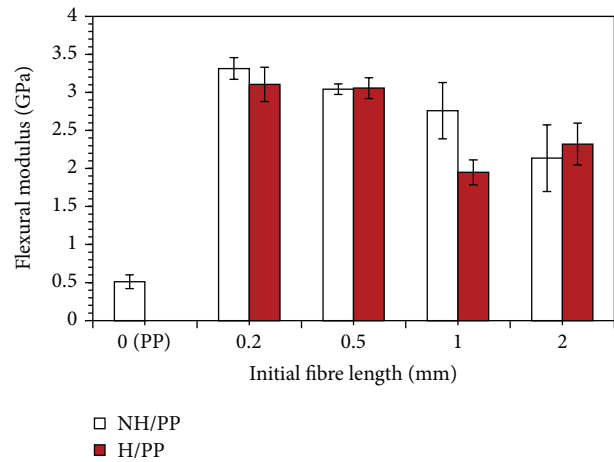


FIGURE 13: The influence of the initial fibre length on flexural modulus of the noil (white) and treated hemp (red) fibre reinforced polypropylene composites.

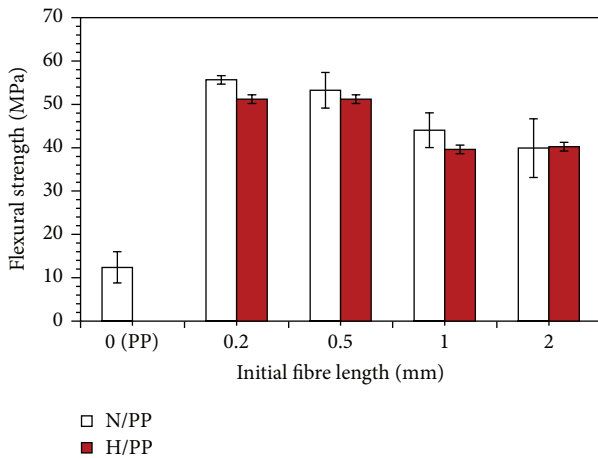


FIGURE 12: The influence of the initial fibre length on flexural strength of the noil (white) and treated hemp (red) fibre reinforced polypropylene composites.

the optimum tensile and flexural properties among all composites. To extend the results, the effect of fibre lengths on impact toughness of the composite samples has been also investigated using impact tests. The impact toughness of a composite is the amount of energy it can absorb through plastic deformation before fracture. Therefore, study on impact properties of the composites can be of great importance when the reinforcing fibres are very short, as short fibres create stress concentration sites in the matrix, which might reduce impact toughness of the materials.

Typical impact force-time and impact energy-time curves are shown in Figure 14. The Energy-time curve, shown in Figure 14, was plotted using the calculation of the total area under the force-time curve. Then, the amount of total energy requires to damage the composite can be extracted using the energy-time curve. Belingardi et al. [17] introduced the damage degree (DD) to account for damage accumulation. It was defined as the ratio between the absorbed energy E_a and the impact energy E_i (E_a/E_i).

Once the impact energy (E_i) is high enough, the composite failure eventually can happen. In a case, the specimen does not completely fail; the projectile bounces back from the specimen. The energy created when the projectile bounces back is known as rebounded energy (E_r). When the specimen completely fails, the projectile is not rebound and the rebound energy (E_r) is zero. In this case, complete failure of the specimen happens and DD value becomes 1. The impact force (F_m), maximum impact energy (E_m), absorbed energy (E_a), and rebounded energy (E_r) of the specimens were extracted from corresponding impact force-time and impact energy-time curves of the composites and then summarised in Tables 4 and 5. Moreover, the changes in peak load, rebounded energy, and damage degree as function of initial fibre length are presented in Figures 15 and 16.

A comparison between the pure PP sample and the composites shows that the E_r and DD of the pure PP is higher and lower, respectively. In other words, addition of

TABLE 4: Impact properties of polypropylene sample.

	F_m (N)	E_m (J)	E_a (J)	E_r (J)	DD
PP sample	118.50 ± 0.75	3.05 ± 0.43	2.41 ± 0.52	0.64 ± 0.12	0.79 ± 0.08

TABLE 5: Impact properties of composites with different fibre lengths.

Fibre length (mm)	Noil hemp fibre composite					Hemp fibre composite				
	F_m (N)	E_m (J)	E_a (J)	E_r (J)	DD	F_m (N)	E_m (J)	E_a (J)	E_r (J)	DD
0.2	191.70 ± 8.6	2.99 ± 0.22	2.57 ± 0.21	0.42 ± 0.02	0.86 ± 0.01	175.50 ± 2.20	2.71 ± 0.01	2.25 ± 0.04	0.46 ± 0.04	0.83 ± 0.01
0.5	177.24 ± 3.16	2.80 ± 0.17	2.43 ± 0.12	0.37 ± 0.01	0.87 ± 0.01	173.30 ± 3.12	2.64 ± 0.08	2.24 ± 0.07	0.40 ± 0.01	0.85 ± 0.01
1	164.40 ± 2.31	2.64 ± 0.25	2.32 ± 0.26	0.32 ± 0.08	0.88 ± 0.02	173.67 ± 3.83	2.75 ± 0.13	2.37 ± 0.12	0.38 ± 0.01	0.86 ± 0.00
2	150.00 ± 5.65	2.45 ± 0.63	2.30 ± 0.51	0.15 ± 0.06	0.94 ± 0.01	159.65 ± 4.55	2.38 ± 0.06	2.11 ± 0.18	0.34 ± 0.06	0.86 ± 0.02

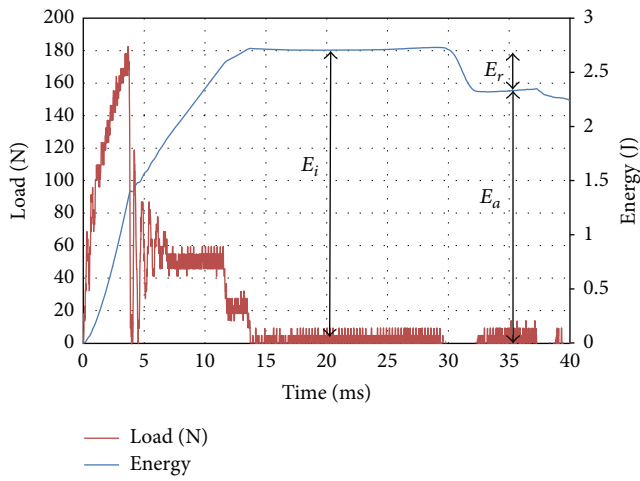


FIGURE 14: Load and energy history curves of a Noil hemp fibre polypropylene composite specimen reinforced with 0.2 mm Noil fibres.

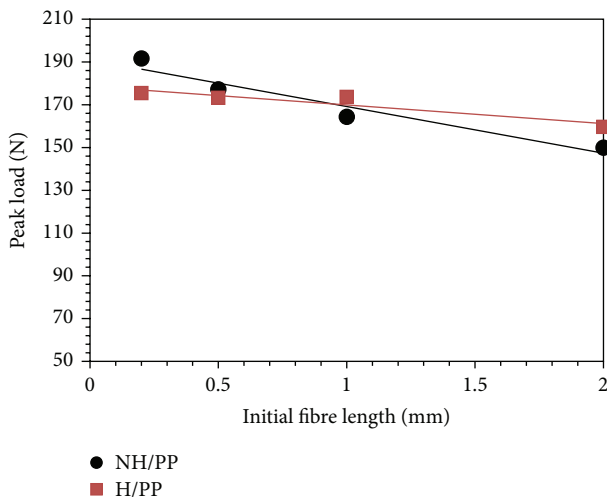


FIGURE 15: Effect of initial fibre length on peak load of noil hemp fibre and treated hemp fibre composites.

fibres/fillers in the pure reduces the impact properties as expected.

From Figure 15, it can be observed that as fibre length increased the peak load of the composites reduced. Peak load, also known as impact Load, corresponds to the onset of material damage or complete failure. Therefore, the composite with 0.2 mm initial fibre showed better impact resistance among all other samples.

During impact, compressive, shear, and tensile loadings are applied on the composite samples simultaneously. As aforementioned, fibre agglomerations are more likely to form in composites with longer fibres. Then fibres are not properly wet up in agglomeration sites and crack can be initiated from fibre/matrix interface in the agglomeration sites. As a result, poor dispersion of fibres reduces composite impact resistance during compression, shear, and tensile by reduction of interface bonding between the fibre and matrix in agglomeration sites.

Likewise, Figure 16(a) shows the higher E_r values for composites with shorter initial fibres. It indicates that better fibre dispersion and subsequently strong interfaces in the composites with shorter fibres prevented the impactor from penetrating the samples and thus more rebounded energy was observed. Also, the lower DD values as shown in Figure 16(b) indicated that the extent of impact damage was less on composites with shorter fibres. Both noil hemp fibre composites and hemp fibre composites provided almost the same values of impact energy at different initial fibre length. However, as Figure 16(b) shows, the damage degree (DD) values of the noil hemp fibres composites are significantly higher than those of normal hemp fibre due to the fibre weakness (defects/cracks) caused by the degumming process. The impact results gained here are in correlation with their tensile and flexural properties as discussed earlier.

To summarize, the impact test results show that increase in initial fibre length of the composites decreases the maximum load and rebounded energy but increases the damage degree (DD) of the composites. In addition, noil hemp fibres composite represents lower impact properties than hemp fibre composites.

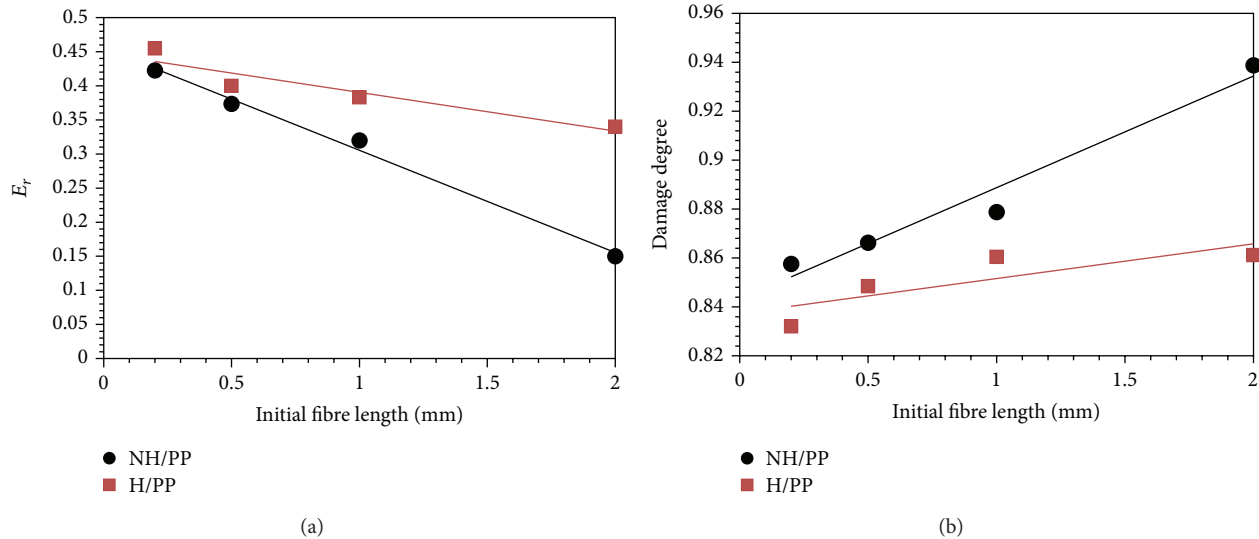


FIGURE 16: Effect of initial fibre length on impact properties of noil hemp fibre and treated hemp fibre composites (a) impact energy and (b) damage degree.

4. Conclusion

In this paper, noil fibre and normal treated and untreated hemp fibre were characterized. Also, the influence of initial fibre length on mechanical properties of ground fibre polypropylene composites was studied. The following can be concluded.

Alkali treatment of normal hemp fibres could remove cementing materials (pectin, hemicellulose, and lignin) partial/completely from surface of the fibres.

Noil hemp fibre contains almost the same type of chemical components and morphology as 5 wt% alkali treated hemp fibres contain. Therefore, noil hemp fibres do not require any chemical treatments to remove the lignocellulosic amorphous materials.

The noil hemp fibres delivered lower tensile properties than treated hemp fibres due to the cellulose degradations (fibre defects) because of overdegumming happens in textile processing. The ground fibres are still capable of reinforcing the polypropylene matrices.

Hemp and noil hemp powder (fillers) with original length of 0.2 mm resulted in highest tensile, flexural, and impact properties of the composites due to better dispersion of the fillers and more homogenous structure of the composites. However, as the initial fibre length increased, the tensile, flexural, and impact strength of the samples decreased slightly.

Conflict of Interests

The authors declare that there is no conflict of interests regarding the publication of this paper.

References

- [1] H. Ku, H. Wang, N. Pattarachaiyakoop, and M. Trada, "A review on the tensile properties of natural fiber reinforced polymer composites," *Composites Part B: Engineering*, vol. 42, no. 4, pp. 856–873, 2011.
- [2] Z.-Y. Sun, H.-S. Han, and G.-C. Dai, "Mechanical properties of injection-molded natural fiber-reinforced polypropylene composites: formulation and compounding processes," *Journal of Reinforced Plastics and Composites*, vol. 29, no. 5, pp. 637–650, 2010.
- [3] R. Gosselin, D. Rodrigue, and B. Riedl, "Injection molding of postconsumer wood-plastic composites II: mechanical properties," *Journal of Thermoplastic Composite Materials*, vol. 19, no. 6, pp. 659–669, 2006.
- [4] P. Niu, B. Liu, X. Wei, X. Wang, and J. Yang, "Study on mechanical properties and thermal stability of polypropylene/hemp fiber composites," *Journal of Reinforced Plastics and Composites*, vol. 30, no. 1, pp. 36–44, 2011.
- [5] M. Bengtsson, M. L. Baillif, and K. Oksman, "Extrusion and mechanical properties of highly filled cellulose fibre-polypropylene composites," *Composites Part A: Applied Science and Manufacturing*, vol. 38, no. 8, pp. 1922–1931, 2007.
- [6] D. Maldas, B. V. Kokta, and C. Daneault, "Influence of coupling agents and treatments on the mechanical-properties of cellulose fiber-polystyrene composites," *Journal of Applied Polymer Science*, vol. 37, no. 3, pp. 751–775, 1989.
- [7] A. Etaati, S. A. Mehdizadeh, H. Wang, and S. Pather, "Vibration damping characteristics of short hemp fibre thermoplastic composites," *Journal of Reinforced Plastics and Composites*, vol. 33, no. 4, pp. 330–341, 2014.
- [8] Z. L. Yan, H. Wang, K. T. Lau et al., "Reinforcement of polypropylene with hemp fibres," *Composites Part B: Engineering*, vol. 46, pp. 221–226, 2013.
- [9] G. Zhang and M. R. Thompson, "Reduced fibre breakage in a glass-fibre reinforced thermoplastic through foaming," *Composites Science and Technology*, vol. 65, no. 14, pp. 2240–2249, 2005.
- [10] A. Etaati, H. Wang, S. Pather, Z. Yan, and S. Abdanan Mehdizadeh, "3D X-ray microtomography study on fibre breakage in noil hemp fibre reinforced polypropylene composites," *Composites Part B: Engineering*, vol. 50, pp. 239–246, 2013.

- [11] A. Etaati, S. Pather, Z. Fang, and H. Wang, "The study of fibre/matrix bond strength in short hemp polypropylene composites from dynamic mechanical analysis," *Composites Part B: Engineering*, vol. 62, pp. 19–28, 2014.
- [12] A. Etaati, S. Pather, F. Cardona, and H. Wang, "Injection molded noil hemp fiber composites: Interfacial shear strength, fiber strength, and aspect ratio," *Polymer Composites*, 2014.
- [13] S. Korte and M. P. Staiger, "Effect of processing route on the composition and properties of hemp fibre," *Fibers and Polymers*, vol. 9, no. 5, pp. 593–603, 2008.
- [14] A. Sonia and K. Priya Dasan, "Chemical, morphology and thermal evaluation of cellulose microfibrils obtained from *Hibiscus sabdariffa*," *Carbohydrate Polymers*, vol. 92, no. 1, pp. 668–674, 2013.
- [15] C. Baley, "Influence of kink bands on the tensile strength of flax fibers," *Journal of Materials Science*, vol. 39, no. 1, pp. 331–334, 2004.
- [16] M. Symington, W. M. Banks, J. L. Thomason, R. A. Pethrick, and O. David-West, "Kink bands in flax and hemp polyester composites," in *Proceedings of the 18th International Conference on Composites Materials (ICCM '11)*, Jeju Island, Republic of Korea, August 2011.
- [17] G. Belingardi, F. Grasso, and R. Vadori, "Energy absorption and damage degree in impact testing of composite materials," in *Experimental Mechanics, Vols 1 and 2: Advances in Design, Testing and Analysis*, I. M. Allison, Ed., pp. 279–285, 1998.
- [18] D. Dai and M. Fan, "Characteristic and performance of elementary hemp fibre," *Materials Sciences and Applications*, vol. 1, no. 6, pp. 336–342, 2010.
- [19] H. L. Liu, L. L. You, H. B. Jin, and W. D. Yu, "Influence of alkali treatment on the structure and properties of hemp fibers," *Fibers and Polymers*, vol. 14, no. 3, pp. 389–395, 2013.
- [20] D. Sedan, C. Pagnoux, T. Chotard et al., "Effect of calcium rich and alkaline solutions on the chemical behaviour of hemp fibres," *Journal of Materials Science*, vol. 42, no. 22, pp. 9336–9342, 2007.
- [21] M. Le Troëdec, C. S. Peyratout, A. Smith, and T. Chotard, "Influence of various chemical treatments on the interactions between hemp fibres and a lime matrix," *Journal of the European Ceramic Society*, vol. 29, no. 10, pp. 1861–1868, 2009.

Research Article

Role of Metals Content in Spinach in Enhancing the Conductivity and Optical Band Gap of Chitosan Films

Irwana Nainggolan,¹ Devi Shantini,¹ Tulus Ikhsan Nasution,² and Mohd Nazree Derman¹

¹*School of Materials Engineering, Universiti Malaysia Perlis, 01000 Kangar, Perlis, Malaysia*

²*Physics Department, Faculty of Mathematic and Natural Science, University of Sumatera Utara, Medan, Sumatera Utara 20155, Indonesia*

Correspondence should be addressed to Irwana Nainggolan; jasminee.24@yahoo.com

Received 19 October 2014; Accepted 26 February 2015

Academic Editor: Yiping Qiu

Copyright © 2015 Irwana Nainggolan et al. This is an open access article distributed under the Creative Commons Attribution License, which permits unrestricted use, distribution, and reproduction in any medium, provided the original work is properly cited.

Blend of chitosan and spinach extract has been successfully prepared using acetic acid as a solvent medium to produce chitosan-spinach films. The conductivity measurements showed that chitosan-spinach films for all ratios of 95 : 5, 90 : 10, 85 : 15, and 80 : 20 had better conductivity than the chitosan film. The optical band gap reduced with the addition of the spinach extract into chitosan. Chitosan-spinach film with the ratio of 85 : 15 gave the best electrical properties in this work with the conductivity of 3.41×10^{-6} S/m and optical band gap of 2.839 eV. SEM-EDX spectra showed the existence of potassium, phosphorus, sulphur, iron, and oxygen in chitosan-spinach films. AFM image showed that the surface morphology of the films became rougher as the spinach incorporated into chitosan. The minerals which exist in spinach extract play a role in enhancing electrical properties of chitosan film.

1. Introduction

Chitosan, a linear β -linked polysaccharide, has long been marked as one of the most promising biopolymers. This biopolymer exhibits excellent characteristics including good chemical inertness, high mechanical strength, biodegradability, biocompatibility, high-quality film forming properties, and low cost [1]. Chitosan has been widely studied in various fields which include sensors, biomedical, food processing industries, and more. The broad application of chitosan biopolymer becomes one of the main reasons for the intensive investigation and development of these materials [1–4]. Chitosan is a unique material that is well suited for biological microdevices due to its ability to be selectively deposited and its high density of amine groups, which provide active bonding sites [5], and it has the ability to retain its natural properties even after being processed into film [6]. However, the chitosan itself has a low conductivity value which limits its electronic applications. Therefore, composites or blends have been attempted by incorporating a conducting material into chitosan to combine the good process ability of the chitosan

matrix and electrical conductivity of the conductive materials [1].

The chitosan-spinach films were expected to have better conductivity than the chitosan film because spinach contains minerals such as potassium, phosphorus, and iron (ferredoxin) [7]. Potassium (K) plays a critical role in adjusting the electronic properties of conductive materials [8]. Phosphorus (P) has been mostly used for doping. It has been reported that there is a proportionality relation between the conductivity and the doping concentration of phosphorus [9]. Spinach also contains ferredoxin which was represented as $[2\text{Fe}-2\text{S}]^{2+}$. Ferredoxin is iron-sulfur proteins that function as electron carriers in many metabolic processes. The Fe (III) ions in $[2\text{Fe}-2\text{S}]^{2+}$ are bridged by two sulfides and the tetrahedral coordination of each iron completed by cysteine residues. One electron reduction of the $[2\text{Fe}-2\text{S}]^{2+}$ cluster occurs at one of the iron atoms to give the reduced $[2\text{Fe}-2\text{S}]^{2+}$ cluster. In the oxidized state, both iron atoms are in a similar chemical state, which appears from the chemical shift and quadrupole splitting to be high-spin Fe^{3+} . In the reduced state

the iron atoms are different and the molecule appears to contain one high-spin Fe^{2+} and one high-spin Fe^{3+} [10]. It was believed that the incorporation of spinach into chitosan matrix is able to improve the electrical properties of chitosan films by reducing the band gap of the films since the amine group in chitosan has the ability to bind cationic and anionic forms of noble and transition metal ions [11]. As far as we know, there is no reported study on the electrical conductivity, optical band gap, and microstructure of chitosan-spinach films. Therefore, the success of using the spinach to improve the chitosan film characteristics in this study has made spinach able to function as a novel conductive additive with several advantages including being nontoxic, environmentally friendly, reproducible resource, abundant in nature, and cheap.

In this study, chitosan-spinach solution was prepared and coated on the glass substrate by spin coating. Chitosan-spinach films were fabricated to study the conductivity, band gap energy, and microstructure of the films. Two-point probe method was used to test the conductivity and UV-visible spectrometer was utilized to determine the band gap energy, while Fourier transform infrared spectroscopy (FTIR), scanning electron microscopy (SEM), and atomic force microscopy (AFM) were employed to characterize the prepared films.

2. Experimental

2.1. Materials. Chitosan from crab shell (degree of deacetylation 75–85%, medium molecular weight) and methanol with purity of 99.98% were purchased from Sigma Aldrich Ltd. Meanwhile, acetic acid with purity of 99% purchased from Merck was used in this research. Red spinach was chosen as a biomaterial to be blended with chitosan. The red spinach was cleaned, cut, dried, and squeezed for spinach preparation purpose. Then, methanol, acetic acid, and distilled water were used for spinach extraction.

2.2. Preparation of Chitosan-Spinach Films. A solution gel of 1.75 wt.% chitosan was prepared by dissolving chitosan into 2% acetic acid solution with rotation speed of 300 rpm for 24 h. After being cleaned, cut, dried, and squeezed, red spinach juice was poured into the mixture solution of methanol, acetic acid, and deionised water with the ratio 10 : 4 : 1 : 5 followed by magnetic stirring with rotation speed of 350 rpm for 1 h. Then, the chitosan solution was mixed with spinach extract and stirred for 2 h. There are five distinct concentration solutions which were prepared using chitosan and spinach extract. One solution was made of pure chitosan as control, while the other four solutions were blends of chitosan and spinach extract with the spinach extract to chitosan ratios of 5/95, 10/90, 15/85, and 20/80, respectively. The chitosan and chitosan-spinach films were fabricated by using spin coating technique. In this work, rotation speed of 100 rpm and spin time of 30 seconds were used to coat the chitosan and chitosan-spinach films on the glass substrate. Finally the films were annealed at 105°C to remove the excessive water molecules in the films.

2.3. Characterizations. There were several instruments that have been used in this research. Spin coater (WS-650 Mz-23 NPP Laurell) was used to coat the chitosan and chitosan-spinach solution onto the glass substrate. Vacuum oven was used for annealing purpose. Meanwhile the thickness of the films was measured using 3D-Profilor (Pemtron Hawk 3D). FTIR spectra measurements were conducted by a Perkin Elmer RX1 FTIR spectrometer. The surface morphology of chitosan and chitosan-spinach films was examined by using a Jeol JSM-6460LA scanning electron microscopy (SEM) at an accelerating voltage of 5 kV. The surface roughness of the films was investigated by atomic force microscopy (AFM) (Nanoscope IV/Multimode, Digital Instruments) equipped with a $100\ \mu\text{m}$ scanner operated in tapping mode. Conductivity of the chitosan and chitosan-spinach films was determined using the two-point probe method. The output current (I) was measured for different input voltage (V) ranging from 0 V to 20 V with the increment of 1 V. The resistance (R) and the conductance (G) were obtained by using Ohm's Law [12]:

$$R = \frac{\Delta V}{\Delta I}, \quad (1)$$

$$G = \frac{1}{R}.$$

Thus, the resistivity of the films was calculated by using

$$\rho = R \times \frac{a}{t}, \quad (2)$$

where ρ is the resistivity ($\Omega\cdot\text{m}$) of the film, R is the resistance of the film (Ω), a is the surface area of the film (m^2), and t is the thickness of the film (m). Finally, after the value of the resistivity is obtained, the conductivity of the sample can be calculated using (3) where σ is the conductivity:

$$\sigma = \frac{1}{\rho}. \quad (3)$$

The optical band gap was studied using UV-Vis spectrometer (Perkin Elmer UV-Vis spectrometer Lambda 35). Generally, the band gap energy (E_g) in the semiconductor is determined by the Tauc equation [12] as described in

$$[\alpha h\nu]^{2/n} = K (h\nu - E_g), \quad (4)$$

where n represent the nature of transition, K is constant, and $h\nu$ is the energy of photon. Meanwhile, the energy of photon can be calculated using

$$h\nu = \frac{hc}{\lambda}, \quad (5)$$

where h is the plank constant ($6.626 \times 10^{-34}\ \text{m}^2\ \text{kg/s}$), c is the speed of light ($3 \times 10^8\ \text{m/s}$), and λ is the wavelength (m).

The absorption coefficient $\alpha(\nu)$ at various wavelength was calculated from absorbance (A) and thickness (t) of the sample using

$$\alpha(\nu) = \frac{2.303 \times A(\nu)}{t}. \quad (6)$$

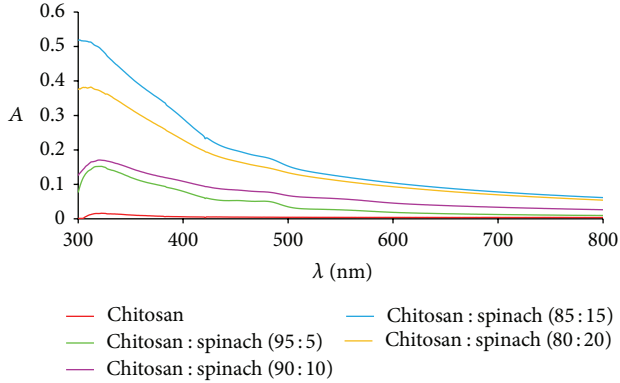


FIGURE 1: UV-Vis spectra of chitosan and chitosan-spinach blend films.

3. Results and Discussion

3.1. Optical Band Gap and Conductivity of Chitosan-Spinach Films. Figure 1 illustrates the UV-Vis spectra of chitosan film and chitosan-spinach film. The lower wavelength band is associated with the $\pi \pi^*$ transition of the conjugated ring systems [1, 13]. Basically, the interaction is said to be strong if the wavelength is lower [13]. In this work, the absorptions occurred at the band with lower wavelength ranging from 350 nm to 300 nm that indicated there was a strong interaction between chitosan and spinach. It was found that the absorption (A) of the film increased with increasing spinach content. However, the absorption decreased with the addition of 20% of spinach in chitosan. This result is in line with the data of SEM-EDX that, in general, the minerals content in spinach started to decrease when 20% of spinach is blended with the chitosan. It is because, at that concentration, the minerals have tendency to agglomerate and hence increase the particle-particle interaction of minerals. The agglomeration of the film is the factor that contributes to increment in band gap energy (reduction on the absorption) [11]. Thus, it can be concluded that the threshold or the optimum ratio of chitosan and spinach which shows the strongest interaction is 85 : 15. The absorption value (A) was used to calculate the optical band gap energy using Tauc equation (4).

Table 1 shows electrical conductivity values of chitosan film and chitosan-spinach blend film. In general, the chitosan-spinach films have higher conductivity than chitosan film. The chitosan-spinach film with the ratio 15 : 85 has the highest conductivity of 3.41×10^{-6} S/m. However, the conductivity value reduced to 3.25×10^{-6} S/m when 20% of spinach was blended with the chitosan due to agglomeration. The band gap energy became smaller prior to addition of spinach into chitosan as shown in Table 1. The chitosan-spinach film with the ratio 15 : 85 has the smallest band gap energy which is 2.839 eV. However, the band gap energy seems to be increased to 3.807 eV when 20% of spinach was incorporated into chitosan. Thus it can be concluded that the optimum ratio of spinach that can be incorporated into chitosan is 15%.

The changes in the electrical properties of chitosan-spinach films are attributed to the electron movement

TABLE 1: Thickness, conductivity, and band gap energy of chitosan and chitosan-spinach blend films.

Chitosan : spinach ratio	Thickness (μm)	Conductivity (S/m)	Band gap (eV)
100 : 0	48.954	4.2×10^{-7}	4.133
95 : 5	48.821	1.76×10^{-6}	4.125
90 : 10	49.045	2.54×10^{-6}	4.118
85 : 15	48.630	3.41×10^{-6}	2.839
80 : 20	49.023	3.25×10^{-6}	3.807

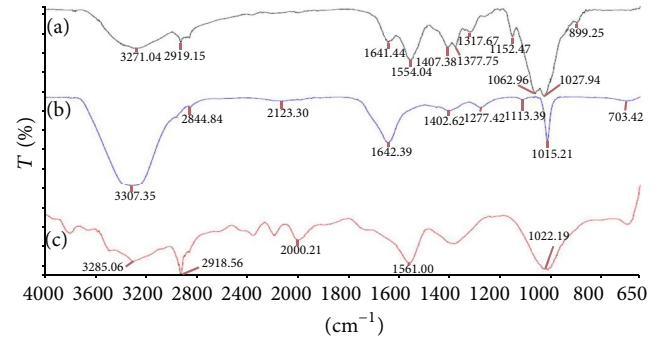


FIGURE 2: Infrared spectra of (a) chitosan film, (b) spinach extract, and (c) chitosan-spinach blend film.

within the chitosan-spinach films. Chitosan has amino (NH_2) and hydroxyl (OH) groups. These functional groups provide active bonding sites to interact with the metals complexes [14]. SEM-EDX micrographs of chitosan-spinach films (Figure 3) show the existence of potassium, phosphorus, iron, sulphur, and oxygen in these films. The existence of potassium, phosphorus, and ferredoxin contributes to the enhancement in output voltage or current because the ions create extra free electrons and pathway for electron transfer. The potassium ion is necessary for redox reaction of electron carrier. Potassium ion also has a rapid electron transfer rate and, as a dopant, it has a tendency to enhance the conductivity of the host materials [15]. As a dopant, phosphorus can increase surface electronic density and enhance the ability of adsorbed oxygen. Phosphorus is able to reduce the resistance of host materials [16]. One electron reduction of the ferredoxin cluster occurs at one of the iron atoms to give the reduced $[2\text{Fe}-2\text{S}]^+$. The reduced electrons then become the free electrons that move randomly in chitosan-spinach film under the certain supplied voltage. Therefore, the higher percentage of spinach extract in the blend films caused the presence of free electrons much more and, in turn, enhanced the conductivity of the blend films.

3.2. Fourier Transform Infrared Spectroscopy (FTIR). The FTIR spectrum of the chitosan film is shown in Figure 2(a). In the spectrum of chitosan, the band at 3271 cm^{-1} is due to $-\text{OH}$ vibration [17]. This band is quite broad and has covered characteristic $-\text{NH}$ band for chitosan at 1641 cm^{-1} and band at 1554 cm^{-1} belonging to $-\text{NH}_2$ bending. The band occurring at 1377 cm^{-1} is ascribed to the $\text{C}-\text{OH}$ vibration of the alcohol

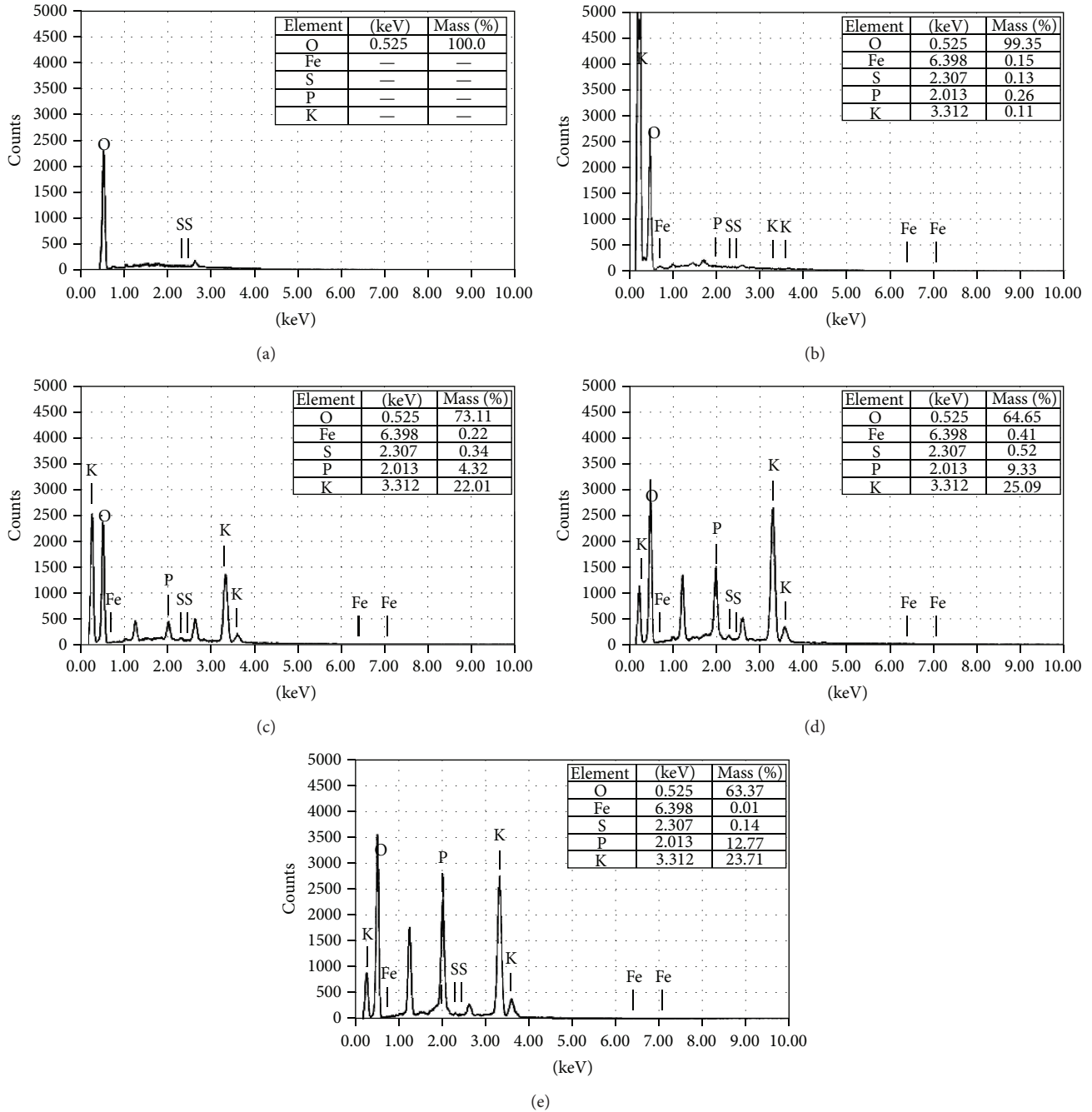


FIGURE 3: SEM (EDX) micrographs of (a) chitosan film, (b) chitosan-spinach blend film (95:5), (c) chitosan-spinach blend film (90:10), (d) chitosan-spinach blend film (85:15), and (e) chitosan-spinach blend film (80:20).

groups in the chitosan and the band around 2919 cm^{-1} is ascribed to the C–H stretching mode in the chitosan [18]. The absorption band at 1152 cm^{-1} due to antisymmetric stretching of C–O–C bridge and the 1062 cm^{-1} skeletal vibration involving the C–O stretching is characteristic of its saccharide structure [19].

The FTIR spectra of spinach can be seen in Figure 2(b). In the spectrum of spinach, the iron sulphides do not provide clear absorption bands at lower wavenumber in

the infrared spectrum. The presence of asymmetric stretching of carboxylate $(\text{C}=\text{O})_2$ at 1642 cm^{-1} is typical of amino acid, a weak band at 1402 cm^{-1} characteristic of ammonium ion NH_4^+ , and band at 1113 cm^{-1} indicating the presence of sulfate. The band occurring at 2123 cm^{-1} is ascribed to the existence of ferredoxin [Fe–S] [20]. The band occurring at 3307 cm^{-1} is due to –OH vibration and the band around 2844 cm^{-1} is ascribed to the C–H stretching mode in the spinach.

It can be seen from the FTIR spectra (Figure 2(c)) that the blend film has the characteristic bands of both chitosan and spinach ferredoxin. The 3285 cm^{-1} , 2918 cm^{-1} , 1561 cm^{-1} , and 1022 cm^{-1} bands are characteristics of the -OH vibration, C-H stretching, -NH_2 bending, and skeletal vibration involving the C-O stretching present in chitosan. The spectrum of the NH_2 group overlapped with the O-H group was shifted from 3271 cm^{-1} (chitosan film) to 3285 cm^{-1} (chitosan-spinach film). Besides that, the free amine group observed at 1641 cm^{-1} (chitosan film) disappears. These two phenomena indicate that NH_2 and OH groups take part in complex formation with ferredoxin [21, 22]. The band occurring at 2000 cm^{-1} is ascribed to the existence of ferredoxin $[\text{Fe-S}]$ in the blend. The Fe-S stretching is seen around 2123 cm^{-1} in the spectra of spinach. However, the band has shifted to lower wavenumber in the blend, that is, 2000 cm^{-1} . This result indicates larger interaction between spinach ferredoxin and chitosan. Theoretically, chitosan has a free amine group in its molecular structure. On the other hand, ferredoxin which is linked with sulfur consists of Fe^{3+} where it can reduce to Fe^{2+} by interacting with the free amine group in chitosan [23]. The complex formation induces the increment of conductivity since it creates an extra pathway for the electrons to flow, which is consistent with data of conductivity and band gap as depicted in Table 1.

3.3. Scanning Electron Microscope (SEM). The SEM-EDX micrographs obtained from chitosan film and chitosan-spinach film are presented in Figure 3. The SEM-EDX micrograph of the chitosan film (Figure 3(a)) shows the existence of oxygen whereas SEM-EDX micrographs of chitosan-spinach films (Figures 3(b)–3(e)) show the existence of potassium, phosphorus, iron, sulphur, and oxygen. The potassium, phosphorus, iron, and sulphur contents increase as the amount of spinach increases as shown in Figures 3(b), 3(c), and 3(d). The mass of potassium is 0.11%, 22.01%, and 25.09% for spinach contents of 5%, 10%, and 15%, respectively; however the mass of potassium decreased to 23.71 when 20% of spinach content was blended with the chitosan. The mass of phosphorus is 0.26%, 4.32%, 9.33%, and 12.77% for spinach content of 5%, 10%, 15%, and 20%, respectively. The iron mass increment is almost the same with the potassium; the mass increased up to 15% and decreased when 20% of spinach content was blended with the chitosan. Meanwhile, the sulphur content also increased as the spinach content increased. The amount of sulphur in percentage is 0.13%, 0.34%, and 0.52% for spinach content of 5%, 10%, and 15%, respectively. However the amount of this component reduced at spinach content of 20% (Figure 3(e)) where the sulphur content drops to 0.14%. In general, the minerals content started to decrease when 20% of spinach is blended with the chitosan because, at that concentration, the minerals have tendency to agglomerate and hence increase the particle-particle interaction of minerals as we can see in Figure 4(e).

Figure 4 describes the morphology of the chitosan film and chitosan-spinach blend film. It appears that morphology has some influence on the electrical conductivity of the films [1]. Chitosan as in Figure 4(a) shows a homogenous surface.

This result is consistent with the previous work which has been done before [17]. The presence of a nonhomogeneous structure in Figures 4(b), 4(c), 4(d), and 4(e) serves as an evidence for the interaction between chitosan and spinach extract which indicates that chitosan and metals content in spinach form complexes. The compact surface of the films affects the electrical properties of the films since the compact surface enhances the pathways for electron transfer. Besides that, the compact surface indicated that the films were well deposited onto the substrate. The strong bond of the films and substrate is very important to avoid swelling of the films; besides the suitable annealing temperature (105°C) is important parameter to remove the water molecules which exist in the films and to make the films surface compact. The uneven surface of blend films is because the interaction between the chitosan and metals content in spinach forms complexes. There are no significant changes in the surface morphology when 5% of spinach was incorporated in chitosan (Figure 4(b)). The morphology of the film started to change via addition of 10% of spinach where it becomes rougher as shown in Figure 4(c). Figure 4(d) shows the chitosan and spinach extract form almost uniform surface when 15% of spinach was blended with chitosan. It indicates that spinach extract disperses well within the chitosan and they have good interaction. However, the chitosan-spinach film started to agglomerate when 20% spinach extract was blended with chitosan as shown in Figure 4(e). The agglomeration of the film is the factor that contributes to increment in band gap energy and reduction in the conductivity value [24]. Thus, it can be concluded that the optimum ratio of spinach that can be incorporated into chitosan is 15%.

3.4. Atomic Force Microscope (AFM). The surfaces of the films were mapped by atomic force microscopy (AFM) with the aim of observing the differences in the film surface associated with the interaction between spinach extract and chitosan. The roughness of the films was determined by the value of RMS and Ra value from AFM data where higher RMS and Ra value indicate that the film surface is getting rougher [25]. Figure 5 shows 3D image of chitosan and chitosan-spinach films. The chitosan film presents a flat homogeneous surface exhibiting a very low dispersion in the roughness profile which is 0.372 nm. It is consistent with the result from previous work done by Li [26, 27]. It can be observed that the chitosan-spinach films display a rough surface in Figures 4(b), 4(c), 4(d), and 4(e). The roughness of the films increases with increasing spinach extract content as indicated by the RMS values starting from 1.413 nm, 4.848 nm, 12.980 nm, and 36.250 nm for spinach extract content of 5%, 10%, 15%, and 20%, respectively, as listed in Table 2. The roughness of the films can be explained through the difference between the minimum and maximum peaks on AFM image of the film surface. The axis in Figure 5 clearly illustrates that the height of peaks increases with the increasing of spinach extract concentration. This can be associated with the interaction between the chitosan and spinach extract which indicates that chitosan and metals content in spinach form complexes.

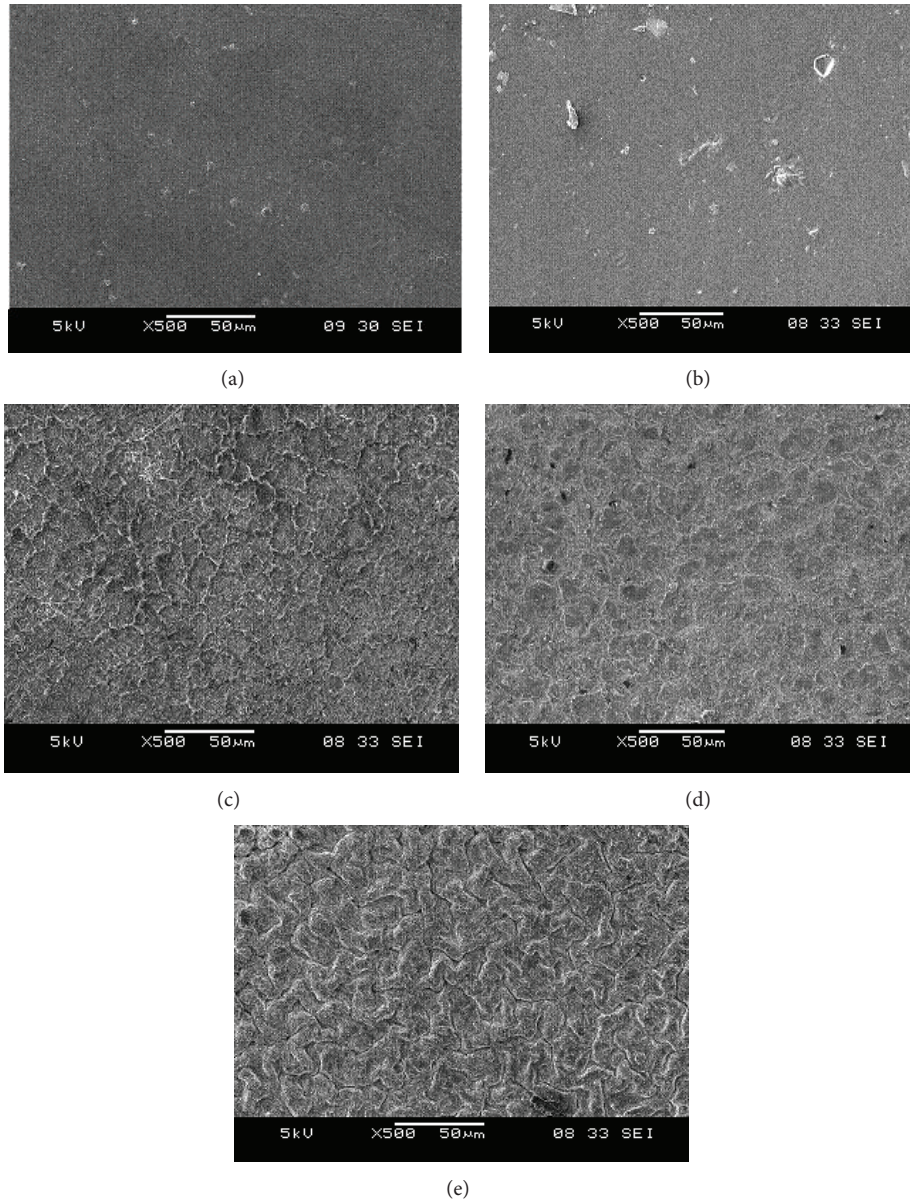


FIGURE 4: SEM images of (a) chitosan film, (b) chitosan-spinach blend film (95 : 5), (c) chitosan-spinach blend film (90 : 10), (d) chitosan-spinach blend film (85 : 15), and (e) chitosan-spinach blend film (80 : 20).

TABLE 2: Surface analysis data of the chitosan film and chitosan-spinach blend film.

Chitosan : spinach	100 : 0	95 : 5	90 : 10	85 : 15	80 : 20
Rms (nm)	0.372	1.413	4.848	12.980	36.250
Ra (nm)	0.235	1.022	3.747	10.200	20.391

4. Conclusion

The chitosan film properties have been successfully improved by blending chitosan with spinach extract. The existence of potassium, phosphorus, and ferredoxin in spinach resulted

in the optical band gap of chitosan-spinach films becoming narrower than chitosan film. As a result, the electrical conductivity of chitosan-spinach films was higher compared to chitosan film. Besides that, the presence of a nonhomogeneous structure served as an evidence for the interaction between chitosan and spinach which indicates that chitosan and metals content in spinach form complexes. Therefore, spinach has been proven as a new effective conductive additive for the purpose of improving the electrical properties of chitosan film wherein the chitosan-spinach film with the ratio of 85 : 15 has been found as the best ratio to fabricate the blend films.

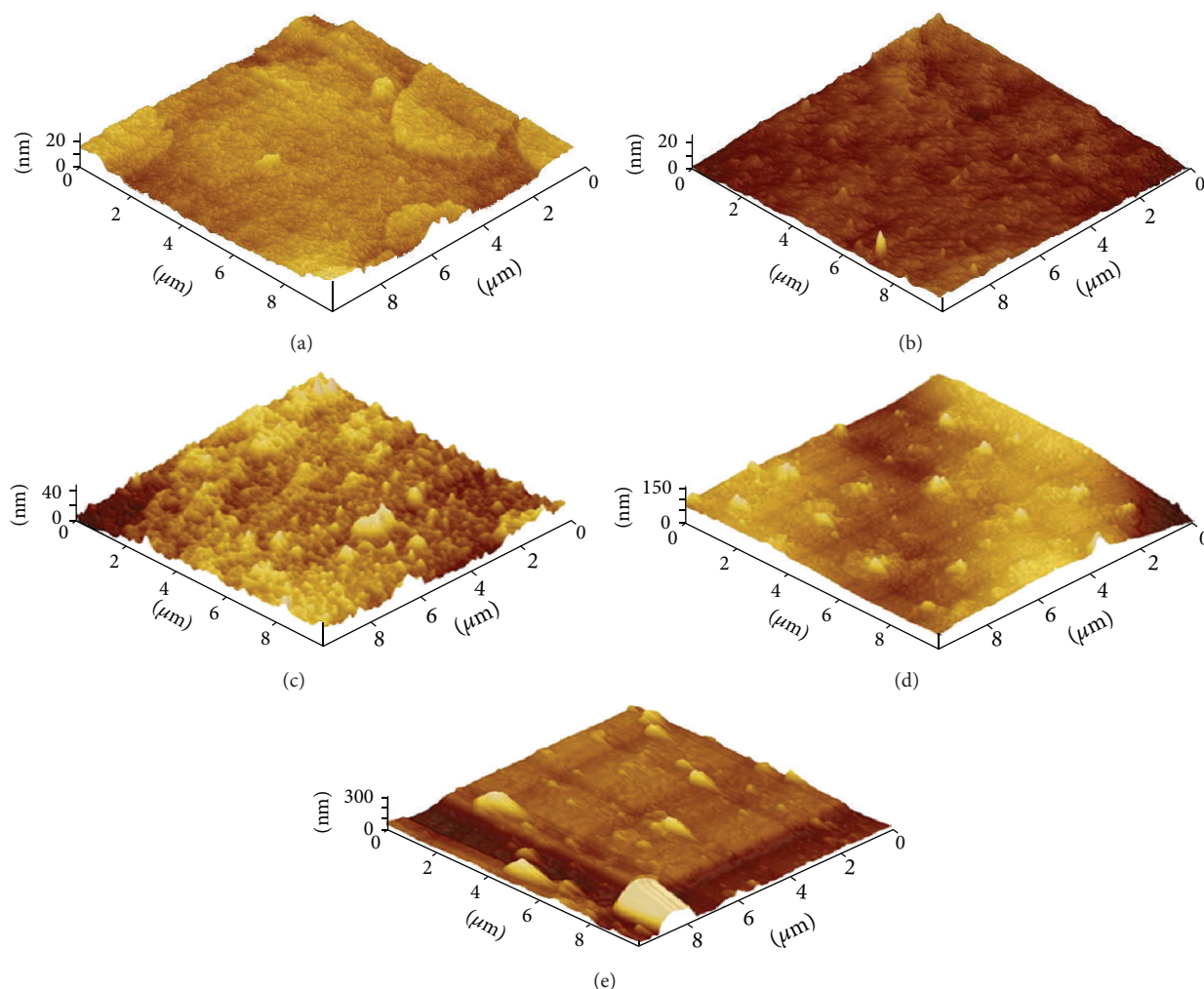


FIGURE 5: AFM (3D) images of (a) chitosan film, (b) chitosan-spinach blend film (95 : 5), (c) chitosan-spinach blend film (90 : 10), (d) chitosan-spinach blend film (85 : 15), and (e) chitosan-spinach blend film (80 : 20).

Conflict of Interests

The authors declare that there is no conflict of interests regarding the publication of this paper.

Acknowledgments

This work was financially supported by FRGS research grant (Project no. 9003-00436). The authors thank School of Materials Engineering, UniMAP, for other supports.

References

- [1] A. G. Yavuz, A. Uygun, and V. R. Bhethanabotla, "Substituted polyaniline/chitosan composites: synthesis and characterization," *Carbohydrate Polymers*, vol. 75, no. 3, pp. 448–453, 2009.
- [2] N. K. Mathur and C. K. Narang, "Chitin and chitosan, versatile polysaccharides from marine animals," *Journal of Chemical Education*, vol. 67, no. 11, pp. 938–942, 1990.
- [3] M. N. V. R. Kumar, "A review of chitin and chitosan applications," *Reactive and Functional Polymers*, vol. 46, no. 1, pp. 1–27, 2000.
- [4] C. Stefanescu, W. H. Daly, and I. I. Negulescu, "Biocomposite films prepared from ionic liquid solutions of chitosan and cellulose," *Carbohydrate Polymers*, vol. 87, no. 1, pp. 435–443, 2012.
- [5] P. Dykstra, J. Hao, S. T. Koev, G. F. Payne, L. Yu, and R. Ghodssi, "An optical MEMS sensor utilizing a chitosan film for catechol detection," *Sensors and Actuators, B: Chemical*, vol. 138, no. 1, pp. 64–70, 2009.
- [6] D. Du, J. Ding, J. Cai, and A. Zhang, "One-step electrochemically deposited interface of chitosan-gold nanoparticles for acetylcholinesterase biosensor design," *Journal of Electroanalytical Chemistry*, vol. 605, no. 1, pp. 53–60, 2007.
- [7] S. Smoleń and W. Sady, "Influence of iodine form and application method on the effectiveness of iodine biofortification, nitrogen metabolism as well as the content of mineral nutrients and heavy metals in spinach plants (*Spinacia oleracea* L.)," *Scientia Horticulturae*, vol. 143, pp. 176–183, 2012.
- [8] X.-R. Li, J. Liu, F.-Y. Kong, X.-C. Liu, J.-J. Xu, and H.-Y. Chen, "Potassium-doped graphene for simultaneous determination of nitrite and sulfite in polluted water," *Electrochemistry Communications*, vol. 20, no. 1, pp. 109–112, 2012.

- [9] A. Bakry and A. M. El-Naggar, "Correlation between phosphorus concentration and opto-electrical properties of doped a-Si:H films," *Optik*, vol. 124, no. 24, pp. 6501–6505, 2013.
- [10] K. K. Rao, R. Cammack, D. O. Hall, and C. E. Johnson, "Mössbauer effect in Scenedesmus and spinach ferredoxins. The mechanism of electron transfer in plant-type iron-sulphur proteins," *Biochemical Journal*, vol. 122, no. 3, pp. 257–265, 1971.
- [11] A. Mironenko, E. Modin, A. Sergeev, S. Voznesenskiy, and S. Bratskaya, "Fabrication and optical properties of chitosan/Ag nanoparticles thin film composites," *Chemical Engineering Journal*, vol. 244, pp. 457–463, 2014.
- [12] M. M. Abdi, H. N. M. E. Mahmud, L. C. Abdullah, A. Kassim, M. Z. A. Rahman, and J. L. Y. Chyi, "Optical band gap and conductivity measurements of polypyrrole-chitosan composite thin films," *Chinese Journal of Polymer Science*, vol. 30, no. 1, pp. 93–100, 2012.
- [13] P. Kannusamy and T. Sivalingam, "Chitosan-ZnO/polyaniline hybrid composites: polymerization of aniline with chitosan-ZnO for better thermal and electrical property," *Polymer Degradation and Stability*, vol. 98, no. 5, pp. 988–996, 2013.
- [14] X. H. Wang, Y. Du, and H. Liu, "Preparation, characterization and antimicrobial activity of chitosan-Zn complex," *Carbohydrate Polymers*, vol. 56, no. 1, pp. 21–26, 2004.
- [15] Y. Mishima, J. Motonaka, K. Maruyama, and S. Ikeda, "Determination of hydrogen peroxide using a potassium hexacyanoferrate(III) modified titanium dioxide electrode," *Analytica Chimica Acta*, vol. 358, no. 3, pp. 291–296, 1998.
- [16] Z. Han, J. Wang, L. Liao, H. Pan, S. Shen, and J. Chen, "Phosphorus doped TiO₂ as oxygen sensor with low operating temperature and sensing mechanism," *Applied Surface Science*, vol. 273, pp. 349–356, 2013.
- [17] S. Yalçinkaya, C. Demetgül, M. Timur, and N. Çolak, "Electrochemical synthesis and characterization of polypyrrole/chitosan composite on platinum electrode: its electrochemical and thermal behaviors," *Carbohydrate Polymers*, vol. 79, no. 4, pp. 908–913, 2010.
- [18] Y. A. Ismail, S. R. Shin, K. M. Shin et al., "Electrochemical actuation in chitosan/polyaniline microfibers for artificial muscles fabricated using an in situ polymerization," *Sensors and Actuators, B: Chemical*, vol. 129, no. 2, pp. 834–840, 2008.
- [19] S. J. Kim, S. R. Shin, S. M. Lee, I. Y. Kim, and S. I. Kim, "Electromechanical properties of hydrogels based on chitosan and poly(hydroxyethyl methacrylate) in NaCl solution," *Smart Materials and Structures*, vol. 13, no. 5, pp. 1036–1039, 2004.
- [20] M. R. M. Chaves, K. T. Valsaraj, R. D. DeLaune, R. P. Gambrell, and P. M. Buchler, "Modification of mackinawite with L-cysteine: synthesis, characterization, and implications to mercury immobilization in sediment," in *Sediment Transport*, chapter 16, University of Sao Paulo, Sao Paulo, Brazil, 2008.
- [21] X. Wang, Y. Du, L. Fan, H. Liu, and Y. Hu, "Chitosan-metal complexes as antimicrobial agent: Synthesis, characterization and Structure-activity study," *Polymer Bulletin*, vol. 55, no. 1-2, pp. 105–113, 2005.
- [22] H. T. Boey, W. L. Tan, N. H. H. A. Bakar, M. A. Bakar, and J. Ismail, "Formation and morphology of colloidal chitosan-stabilized copper sulphides," *Journal of Physical Science*, vol. 18, no. 1, pp. 87–101, 2007.
- [23] S. Gao, J. Fan, S. Sun et al., "Di/mono-nuclear iron(i)/(ii) complexes as functional models for the 2Fe₂S subunit and distal Fe moiety of the active site of [FeFe] hydrogenases: protonations, molecular structures and electrochemical properties," *Dalton Transactions*, vol. 41, no. 39, pp. 12064–12074, 2012.
- [24] N. N. Mobarak, A. Ahmad, M. P. Abdullah, N. Ramli, and M. Y. A. Rahman, "Conductivity enhancement via chemical modification of chitosan based green polymer electrolyte," *Electrochimica Acta*, vol. 92, pp. 161–167, 2013.
- [25] A. P. P. Praxedes, A. J. C. da Silva, R. C. da Silva et al., "Effects of UV irradiation on the wettability of chitosan films containing dansyl derivatives," *Journal of Colloid and Interface Science*, vol. 376, no. 1, pp. 255–261, 2012.
- [26] J. Li, S. Zivanovic, P. M. Davidson, and K. Kit, "Production and characterization of thick, thin and ultra-thin chitosan/PEO films," *Carbohydrate Polymers*, vol. 83, no. 2, pp. 375–382, 2011.
- [27] W. H. Nosal, D. W. Thompson, L. Yan, S. Sarkar, A. Subramanian, and J. A. Woollam, "Infrared optical properties and AFM of spin-cast chitosan films chemically modified with 1,2 Epoxy-3-phenoxy-propane," *Colloids and Surfaces B: Biointerfaces*, vol. 46, no. 1, pp. 26–31, 2005.

Research Article

Composites Based Green Poly(L-Lactic Acid) and Dioctyl Phthalate: Preparation and Performance

Yan-Hua Cai,^{1,2} Li-Sha Zhao,¹ and Yan-Hua Zhang¹

¹Chongqing Key Laboratory of Environmental Materials & Remediation Technologies, Chongqing University of Arts and Sciences, Chongqing 402160, China

²School of Materials and Chemical Engineering, Chongqing University of Arts and Sciences, Yongchuan, Chongqing 402160, China

Correspondence should be addressed to Yan-Hua Cai; caiyh651@aliyun.com

Received 12 October 2014; Revised 30 January 2015; Accepted 6 February 2015

Academic Editor: P. J. Schubel

Copyright © 2015 Yan-Hua Cai et al. This is an open access article distributed under the Creative Commons Attribution License, which permits unrestricted use, distribution, and reproduction in any medium, provided the original work is properly cited.

The effects of dioctyl phthalate (DOP) on performances of poly(L-lactic acid) (PLLA) were investigated in detail using optical depolarizer, X-ray diffraction, melt index instrument, and electronic tensile tester. Crystallization performance showed that the half time of overall PLLA crystallization $t_{1/2}$ decreased with increasing of crystallization temperature (80°C to 105°C), but the $t_{1/2}$ of PLLA/DOP composites firstly decreased and then increased, and $t_{1/2}$ of PLLA/DOP exhibited minimum value at 85°C. Compared to neat PLLA, 20%DOP made the $t_{1/2}$ decrease from 7258.3 s to 265.4 s. X-ray diffraction experiment further confirmed that DOP could accelerate the crystallization of PLLA. The fluidity of PLLA/DOP composites indicated that the melt mass flow rate firstly decreased and then greatly increased with increasing of DOP content. The mechanical performance showed that DOP could improve the general mechanical performance, and the elongation at break of PLLA/25%DOP was about 30 times longer than that of neat PLLA.

1. Introduction

Dioctyl phthalate (DOP) as a conventional additive in the world has obtained broader attention due to its cheaper cost and more advanced plasticization ability. Thus, viscous DOP was widely used to improve the plasticization ability for polymer materials [1–3]. In addition, the presence of DOP also influences the crystallization and stability of the polymers [4, 5]. Some literatures reported that the addition of DOP could decrease the degree of crystallization of the polymers, resulting from the increasing of macromolecule moving ability. For examples, Baltieri et al. [6] reported the influence of DOP on thermal properties of poly(3-hydroxybutyrate). Experiment dates analysis indicated that DOP exhibited a good effect on the thermal properties of poly(3-hydroxybutyrate), and DOP made the glass transition temperature, melt point, and the degree of crystallinity decrease. Similarly, the results from Huang and his colleagues also confirmed that addition of DOP could make the degree of crystallization of PVC decrease [7].

Compared to other thermoplastic polymers, poly(L-lactic acid) (PLLA) produced from renewable sources has become the most important biomass thermoplastic polymers materials, because of its excellent lower energy consumption, biodegradation ability, processability, and biocompatibility [8, 9]. Nowadays, PLLA and its composites have been applied to more and more fields to be as substitution of the traditional polymer such PP, PE, and PVC. However, it is necessary to further improve the performance of materials based PLLA to wide application., PLLA still has especially some disadvantages such as slow crystallization rate and poor dimensional stability to restrict the wider range application in daily life. Thus, many technologies and methods were used by researcher to improve the performance of PLLA. Fan et al. [10] reported that a novel organic compound *N, N'*-bis(benzoyl)sebacic acid dihydrazide was synthesized to be as a nucleating agent for PLLA to improve the degree of crystallinity, the experiment results showed that *N, N'*-bis(benzoyl)sebacic acid dihydrazide could enhance the crystallization rate and thermal

stability of PLLA. 1.5% *N,N'*-bis(benzoyl)sebacic acid dihydrazide made the half time of overall PLLA crystallization decrease from 33.76 min to 2.36 min at 110°C. Similarly, Wang and his colleagues [11] also synthesized a series of 1,3,5-trialkyl-benzenetricarboxylamides to use as nucleating agents of PLA, and compared to the neat PLLA, 1,3,5-trialkyl-benzenetricarboxylamides made PLA exhibit a very short half time of overall crystallization in a wide region from 90°C to 130°C.

PLLA and DOP including ester group may improve the miscibility of PLLA and DOP. On the other hand, it is fact that DOP was used mainly for PVC plasticization [1, 12]. Thus, the investigations are of very importance to investigate the effect of DOP on PLLA. In this paper, DOP was introduced into PLLA matrix to fabricate composites, and the crystallization behavior, fluidity, and mechanical performance were investigated in detail.

2. Experiment

2.1. Materials. PLLA (2002D) was purchased from Nature Works LLC (USA). DOP (analytical grade) was purchased from Beijing Chemical Reagents Company (Beijing, China).

2.2. Preparation of PLLA/DOP Composites. Firstly, PLLA was dried overnight at 35°C under vacuum, then the blending of PLLA and DOP was carried out using a counter-rotating mixer, and the similar operation process was reported in our previous work [13].

2.3. Test

2.3.1. X-Ray Diffraction (XRD). XRD of PLLA/DOP composites with different heating treatment was performed on a diffractometer using Cu K_{α} radiation (wavelength, 1.54 Å) in the range of $2\theta = 10\text{--}60^{\circ}$ with scanning rate of $2^{\circ}/\text{min}$.

2.3.2. Crystallization Measurement. Crystallization behavior of PLLA/DOP composites was investigated by optical depolarizer from 80°C to 105°C.

2.3.3. Melt Index. The fluidity of melting PLLA/DOP composites was measured by melt index instrument, and the measurement temperature was 180°C; load is 10 Kg.

2.3.4. Mechanical Performance Measurement. Mechanical performance measurement was performed on a M-4010 electronic tensile tester at the speed of 50 mm/min at room temperature.

3. Results and Discussion

3.1. Isothermal Crystallization Behavior. Usually, the different crystallization behavior of PLLA with additive would directly affect the physical performance of PLLA, and the reason is that slow crystallization rate of the neat PLLA makes the molding process of materials based on PLLA become

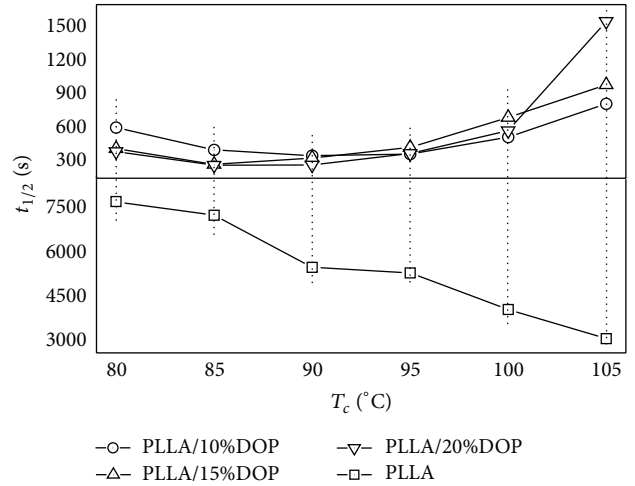


FIGURE 1: The $t_{1/2}$ of PLLA and PLLA/DOP with the crystallization temperature T_c .

difficult. On the other hand, the addition of the additive often can improve the crystallization properties of PLLA. In this study, we firstly investigate the effect of DOP on crystallization behavior of PLLA using optical depolarizer and XRD.

Figure 1 shows the effect of crystallization temperature and DOP content on crystallization of PLLA. As shown in Figure 1, the half time of overall PLLA crystallization $t_{1/2}$ is very long in the region from 80°C to 105°C; the reason is that low crystallization temperature makes the movement ability of PLLA become difficulty, though low crystallization temperature easily makes PLLA aggregate to be nucleation, resulting in PLLA molecular chain not achieving regular arrangement. However, it is very clear that DOP significantly affects the crystallization of PLLA, and the addition of DOP can accelerate the crystallization of PLLA and makes the $t_{1/2}$ decrease. On the other hand, the $t_{1/2}$ of PLLA continuously decreases with increasing of crystallization temperature, which indicates that crystallization temperature is also one of the most important factors for crystallization of PLLA. However, the trend of PLLA/DOP composites is different from neat PLLA. With increasing of crystallization temperature, the $t_{1/2}$ of PLLA/DOP composites firstly decreases and then increases. And the $t_{1/2}$ has the minimum value at 85°C. In addition, the $t_{1/2}$ of PLLA/DOP composites decreases in the region from 80°C to 90°C with increasing of DOP content. In contrast, the $t_{1/2}$ increases in the region from 95°C to 105°C, indicating very complicated effect of DOP on crystallization of PLLA. Compared to neat PLLA, 20%DOP makes the $t_{1/2}$ have the minimum value in 85°C, and the $t_{1/2}$ decreases from 7258.3 s to 265.4 s. That is to say, the $t_{1/2}$ for neat PLLA is about 27 times longer than that of PLLA with 20%DOP.

XRD analysis of PLLA/DOP samples was carried out to further confirm the enhancement of DOP on crystallization of PLLA. Figure 2 shows the XRD curves of PLLA/DOP without heat treatment. It is observed that the diffraction peaks of PLLA and PLLA/DOP samples are very wide, which

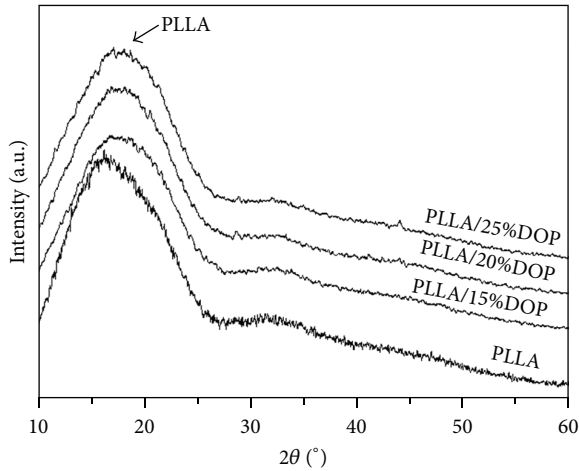


FIGURE 2: XRD curves of PLLA and PLLA/DOP samples.

indicates the most of PLLA matrix is noncrystal. Moreover, the diffraction peak of neat PLLA is sharper than that of PLLA/DOP; the possible reason is that the addition of DOP increases the plasticity of PLLA and makes PLLA form more noncrystal.

However, the XRD curve of PLLA/DOP samples after heat treatment is completely different from that of PLLA at room temperature. Figure 3 is the XRD curves of neat PLLA and PLLA/DOP samples after heat treatment. It is observed from Figure 3 that the diffraction peak of neat PLLA is still very wide after isothermal crystallization for 4 min at 85°C, indicating the poor crystallization ability of neat PLLA. And the PLLA/DOP samples exhibit very strong diffraction peaks after the same heat treatment, resulting from forming more PLLA crystal. This result further confirms that DOP can accelerate the crystallization of PLLA; on the other hand, this result is consistent with the aforementioned isothermal crystallization results. As seen in Figure 3, the strongest diffraction peak of PLLA/DOP samples at $2\theta = 16.6^\circ$ due to diffraction from (110) planes and other peaks at $2\theta = 14.7^\circ$, 19.0° , and 22.2° occurring from the (010) plane, (203) plane, and (205) plane, respectively [14]. In addition, the intensity of diffraction peak increases with increase of DOP content, but 25%DOP makes the intensity of diffraction peak slightly decrease; this result also indicates effect of DOP on crystallization of PLLA is very complicated.

With increasing of crystallization time, as to the neat PLLA, the diffraction peak appears and the intensity of diffraction peak is very weak (see Figure 4). But the intensity of diffraction peak of PLLA/DOP samples is very strong, what is more, the intensity of diffraction peak of PLLA/DOP hardly change except for PLLA/15%DOP, indicating the PLLA/20%DOP and PLLA/25%DOP exhibit the maximum degree of crystallization after heat treatment for 8 min at 85°C. And the intensity of diffraction peak of PLLA/15%DOP also achieves the maximum after further increasing crystallization time (see Figure 5). However, the intensity of diffraction peak of neat PLLA still increases, resulting from

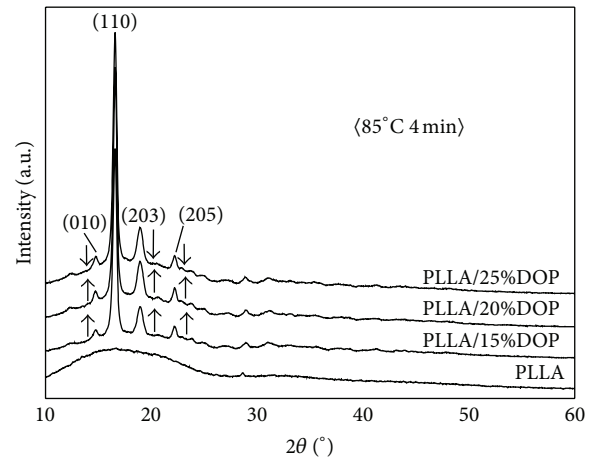


FIGURE 3: XRD curves of PLLA and PLLA/DOP samples for 4 min at 85°C.

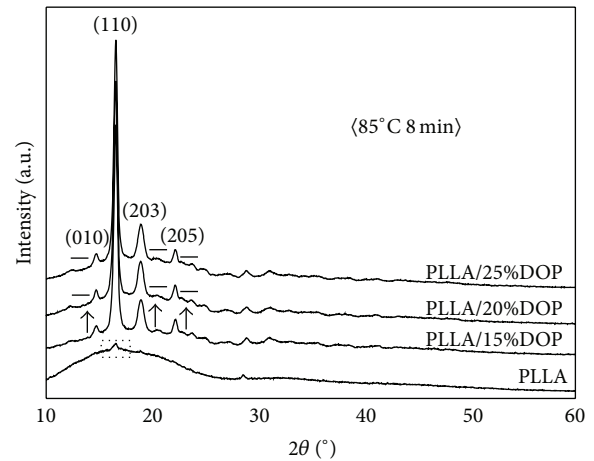


FIGURE 4: XRD curves of PLLA and PLLA/DOP samples for 8 min at 85°C.

increasing crystal of neat PLLA, which also further confirms that the crystallization ability of neat PLLA is very poor.

3.2. Fluidity and Mechanical Performance. As mentioned above, the addition of DOP would change the movement ability of PLLA molecular chain. Thus, there is no doubt that the addition of DOP also would affect the fluidity of PLLA. Figure 6 shows the effect of DOP on the melt mass flow rate (MFR) of PLLA. With increasing of DOP content, the MFR firstly decreases and then greatly increases. The reason may be that a small amount of DOP only slightly improves the movement ability of PLLA molecular chain, resulting in twine of macromolecule segment and affecting the fluidity of PLLA. However, upon a large load DOP, the movement ability and the plasticization ability of macromolecule segment significantly increase and the MFR also increases during process of PLLA. Overall, the addition of DOP can effectively improve the fluidity of PLLA.

Mechanical performance is the most important index to measure plasticization ability of additive. Table 1 shows the

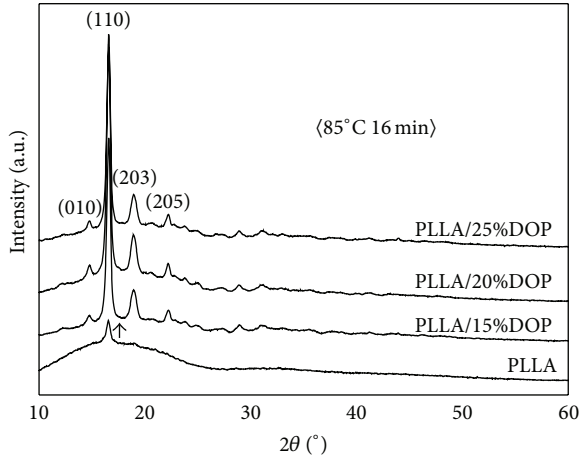


FIGURE 5: XRD curves of PLLA and PLLA/DOP samples for 16 min at 85°C.

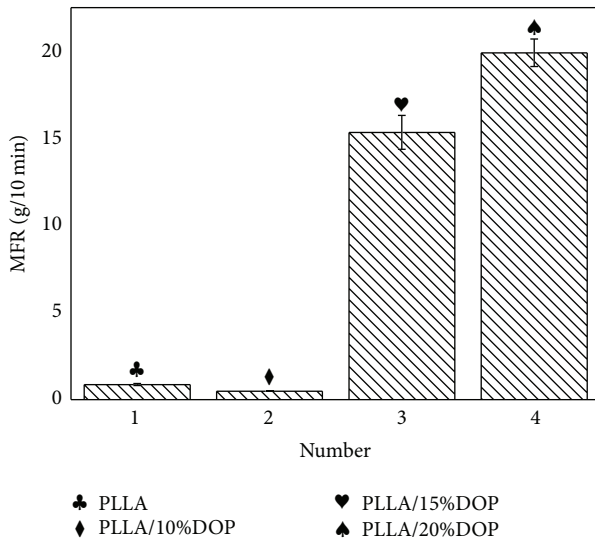


FIGURE 6: The effect of DOP content on MFR of PLLA.

influence of DOP on the mechanical performance of PLLA. With increasing of DOP content, the tensile strength of PLLA decreases, and the elongation at break of PLLA increases; the results are similar to the effect of DOP on mechanical properties of other thermoplastic polymers [3]. It is obvious from Table 1 that the tensile strength of PLLA is about 2 times than that of PLLA/25%DOP, and the elongation at break of PLLA/25%DOP is about 30 times than that of PLLA. In a word, to some extent plasticizer DOP can improve the general mechanical performance.

4. Conclusion

PLLA/DOP composites were fabricated by melt blending technology, and the physical performances of PLLA/DOP composites were investigated. The crystallization behavior indicated that the introduction of DOP could significantly increase the crystallization rate of PLLA through optical

TABLE 1: Mechanical properties of PLLA and PLLA/DOP samples.

Sample	Tensile strength (MPa)	Elongation at break (%)
PLLA	47.6 ± 2.4	5.2 ± 0.63
PLLA/10%DOP	40.6 ± 1.1	6.98 ± 0.56
PLLA/15%DOP	35 ± 1.9	12.18 ± 0.81
PLLA/20%DOP	27.4 ± 0.9	38.99 ± 0.85
PLLA/25%DOP	20.8 ± 1.5	155.98 ± 1.75

depolarizer and XRD. The melt index and mechanical experiment showed DOP can effectively improve the fluidity and the general mechanical performance of PLLA. In a word, the PLLA/DOP composites may be a promising application polymer material.

Conflict of Interests

The authors declare that there is no conflict of interests regarding the publication of this paper.

Acknowledgments

This work was supported by National Natural Science Foundation of China (Project no. 51403027), China Post-doctoral Science Foundation (Project no. 2013M531937), Natural Science Foundation Project of CQ CSTC (Project no. cstc2012jjA50001), Foundation of Chongqing Municipal Education Commission (Project no. KJ131202), and Chongqing University of Arts and Sciences (Project no. R2013CH11).

References

- [1] G. Szarka and B. Iván, "Thermal properties, degradation and stability of poly(vinyl chloride) predegraded thermooxidatively in the presence of dioctyl phthalate plasticizer," *Journal of Macromolecular Science, Part A: Pure and Applied Chemistry*, vol. 50, no. 2, pp. 208–214, 2013.
- [2] Y.-T. Shieh and C.-M. Liu, "Influences of contents and molecular weights of LDPE on DOP plasticization of PVC," *Journal of Applied Polymer Science*, vol. 83, no. 12, pp. 2548–2555, 2002.
- [3] M.-S. Zhou, Z.-J. Sun, D.-J. Yang, J.-H. Huang, and X.-Q. Qiu, "The effect of plasticizer on the properties of alkali lignin/HDPE composites," *Acta Polymerica Sinica*, vol. 2, pp. 210–217, 2014.
- [4] G. Szarka and B. Iván, "Degradative transformation of poly(vinyl chloride) under mild oxidative conditions," *ACS Symposium Series*, vol. 1004, pp. 219–226, 2009.
- [5] S.-L. Yang, Z.-H. Wu, B. Meng, and W. Yang, "The effects of dioctyl phthalate plasticization on the morphology and thermal, mechanical, and rheological properties of chemical crosslinked polylactide," *Journal of Polymer Science, Part B: Polymer Physics*, vol. 47, no. 12, pp. 1136–1145, 2009.
- [6] R. C. Baltieri, L. H. I. Mei, and J. Bartoli, "Study of the influence of plasticizers on the thermal and mechanical properties of poly(3-hydroxybutyrate) compounds," *Macromolecular Symposia*, vol. 197, pp. 33–44, 2003.
- [7] Z.-M. Huang, Y.-Z. Bao, Z.-X. Weng, and Z.-R. Pan, "Study on crystallization behavior of poly(vinyl chloride)," *Polymer Materials Science and Engineering*, vol. 14, no. 4, pp. 78–81, 1998.

- [8] Y.-H. Cai, "Synthesis and nucleating effect of *N, N'*-bis(benzoyl) terephthalic acid dihydrazide," *Journal of the Chemical Society of Pakistan*, vol. 34, no. 3, pp. 709–712, 2012.
- [9] J. Tuominen, J. Kylmä, A. Kapanen, O. Venelampi, M. Itävaara, and J. Seppälä, "Biodegradation of lactic acid based polymers under controlled composting conditions and evaluation of the ecotoxicological impact," *Biomacromolecules*, vol. 3, no. 3, pp. 445–455, 2002.
- [10] Y. Fan, Z. Yu, Y. Cai et al., "Crystallization behavior and crystallite morphology control of poly(L-lactic acid) through *N, N'*-bis(benzoyl)sebacic acid dihydrazide," *Polymer International*, vol. 62, no. 4, pp. 647–657, 2013.
- [11] T. Wang, Y. Yang, C. Zhang, Z. Tang, H. Na, and J. Zhu, "Effect of 1,3,5-trialkyl-benzenetricarboxylamide on the crystallization of poly(lactic acid)," *Journal of Applied Polymer Science*, vol. 130, no. 2, pp. 1328–1336, 2013.
- [12] A. E. A. Toubal, N. Fertikh, S. Ali-Mokhnache, and D. Messadi, "Evaluation of a mathematical model of dioctyl phthalate plasticizer migration from PVC discs into colza oil," *Iranian Polymer Journal*, vol. 14, no. 8, pp. 721–728, 2005.
- [13] Y.-H. Cai, "Nucleation, melting behaviour and mechanical properties of poly(L-lactic acid) affected by the addition of *N, N'*-bis(benzoyl) suberic acid dihydrazide," *South African Journal of Chemistry*, vol. 64, pp. 115–119, 2011.
- [14] W.-D. Hergeth, W. Lebek, E. Stettin, K. Witkowski, and K. Schmutzler, "Particle formation in emulsion polymerization, 2. Aggregation of primary particles," *Die Makromolekulare Chemie*, vol. 193, no. 7, pp. 1607–1621, 1992.

Research Article

Preparation of PAN Spinning Solution with Fine Dispersion of Cellulose Microparticles

Jee-Woo Yang, Jong Sung Won, Da Young Jin, Ji Eun Lee, Won Ho Park, and Seung Goo Lee

Department of Advanced Organic Materials and Textile System Engineering, Chungnam National University, Daejeon, Republic of Korea

Correspondence should be addressed to Won Ho Park; parkwh@cnu.ac.kr and Seung Goo Lee; lsgoo@cnu.ac.kr

Received 12 November 2014; Accepted 25 March 2015

Academic Editor: Jin Zhu

Copyright © 2015 Jee-Woo Yang et al. This is an open access article distributed under the Creative Commons Attribution License, which permits unrestricted use, distribution, and reproduction in any medium, provided the original work is properly cited.

This study suggested the optimum conditions for the stable dispersion of cellulose microparticles in PAN spinning dope, which was prepared for spinning the fiber. Many research studies have investigated methods for preparing a variety of carbon fiber precursors in an attempt to control their characteristics according to the applications. In order to prepare PAN fiber that contains fine cellulose particles, it is important to create a uniformly dispersed spinning dope. Minimization of the cellulose particle size was subjected to heat treatment at various temperatures in order to reduce the cohesive force from the hydrogen bonds between the cellulose molecules. Carbonized cellulose microparticles were obtained for efficient dispersion using the physical method and the sedimentation method. Several instrumental analyses were conducted to study the characteristics of the particles and solutions with SEM, FT-IR, XRD, and a particle size analyzer. From the results, the dispersion of the PAN spinning dope with a chemical treatment was superior to the milling method followed by heat treatment. In this study, heat-treating cellulose microparticles at 400°C was found to be the most effective method.

1. Introduction

A carbon fiber is a type of fiber that contains over 90% carbon and it can be prepared by heat treatment of an organic fiber as a precursor. Carbon fiber applications are extended to the aerospace, defense, energy, ship-building, vehicle-manufacturing, sports, and leisure fields because of the material's excellent properties, including specific strength, specific modulus, and thermal stability. Recently, emerging energy saving and global warming issues have led to the acceleration of the application of lightweight materials, such as carbon fiber. Use of this fiber is especially promising in the aircraft industry because it is lightweight, has less volume change, and is stable under high temperatures and chemical attacks while retaining high strength and high modulus.

Carbon fiber is categorized into three groups based on the starting material: rayon-based carbon fiber, pitch-based carbon fiber, and PAN-based carbon fiber [1–4]. Rayon-based carbon fiber has good thermal properties and high modulus. The processing costs for pitch-based carbon fiber are affordable, which makes its use advantageous to manufacturers.

PAN-based carbon fiber is used in many kinds of composites, due to its high strength. Process development studies have been widely conducted because high performance carbon fiber can be obtained via stabilization and the carbonization process [5–7]. After the carbonization process of the well-controlled stabilization of PAN-based carbon fiber, that material's tensile and shear strength would be improved so that it can be applied to the composite material.

Due to the need for materials having excellent mechanical and thermal properties, various researches have been consistently developed into hybrid technology of carbon fiber materials. For example, carbon fiber, which has relatively high thermal conductivity and low thermal insulation, had limitations for use in rocket engine nozzle and nuclear reactor applications. These applications require materials that simultaneously feature high strength, lightweight, and insulation properties. To address these points, there is a need to develop a new type of carbon fiber. Recently, a high performance carbon fiber composite with inorganic nanofibers and cellulose nanoparticles has been reported [8]. Based on the results of thermal conductivities of carbon fiber

with various precursors, the thermal conductivity of rayon-based carbon fiber, heat-treated at 1500 K, was 20.5% lower than that of PAN-based carbon fiber heat-treated at 1600 K. The thermal conductivity of rayon-based carbon fiber, heat-treated at 2500 K, was also found to be 16.7% lower than that of pitch-based carbon fiber, heat-treated at 2700 K [9]. Using this result, a study on lowering the thermal conductivity using a composite of PAN-based carbon fiber and microcellulose particles has been conducted [10].

In this study, the preparation, including dispersion of the cellulose particles, was investigated for PAN-based carbon composite fiber with cellulose particles in order to reduce the thermal conductivity of the composite fiber without decreasing its elasticity. The most important process for manufacturing a composite fiber is the dispersion of fine cellulose particles in the PAN dough. In this current study, the chemical method and the physical method were applied to enhance the dispersion. In the physical method, the size of the cellulose particles is reduced by heat treatment and mechanical milling. Finally, a PAN-based composite carbon fiber with cellulose particles can be produced. This result reveals the possibility of composite fiber preparation that will yield tailor-made properties. Further researches related to the analysis of the thermal properties and mechanical properties of composite carbon fiber are needed, and these will be conducted through ongoing research studies.

2. Experimental Methods

2.1. Materials. The polyacrylonitrile (PAN) precursor used as raw material for the carbon fiber was provided by Bluestar Fibres Co., Ltd., China, as 12 K fits, Single Tow uncrimped carbon fiber. Commercial-grade dimethylsulphoxide (DMSO) with a purity of 99% was used as the solvent for making the PAN dope. It was obtained from Samcheon Co., Ltd., a local supplier. Cellulose microcrystalline particles with an average Mw. of ~80,000 and bulk density of 0.6 g/mL at 25°C were purchased from Sigma Aldrich Co., Ltd., USA.

2.2. Preparation of Cellulose Particles for Dispersion. Due to the large aspect ratio of the cellulose particles and the hydrogen bond between the molecules, it was difficult to disperse them in the PAN dope. To improve this dispersion and to increase its stability, the chemical treatment method and the physical treatment method were applied.

2.2.1. Chemical Treatment. Chemical treatment was performed using the following steps. Cellulose microcrystalline particles were added by 10 wt% into the DMSO solution containing 0.5 wt% LiCl. After stirring and swelling for 12 h at 70°C, bonding could be eliminated by sonication. The samples were washed with deionized water several times and then dried for 12 h at 100°C in the vacuum dry oven.

2.2.2. Physical Treatment. The cellulose particles for dispersion were prepared by mechanical milling after heat treatment. The heat treatment conditions were 300°C, 350°C, 400°C, and 1,200°C. Detailed heat treatment conditions are

TABLE 1: Heat treatment conditions of the cellulose particles.

Sample	Condition	Heating rate	Soaking	Atmosphere
<i>Cel 00</i>	Chemical treatment			
<i>Cel 30</i>	300°C	300°C/3 hr	4 hr	Air
<i>Cel 35</i>	350°C	350°C/3 hr 30 min	4 hr	Air
<i>Cel 40</i>	400°C	400°C/4 hr	4 hr	Air
<i>Cel 40/120</i>	1,200°C	400°C/4 hr → 1,200°C/4 hr	4 hr, 2 hr	Air, N ₂

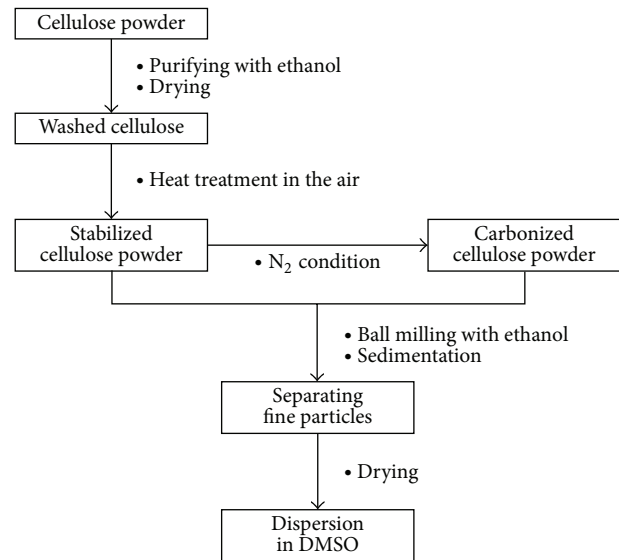


FIGURE 1: Preparation of the cellulose dispersed PAN dope.

shown in Table 1. In the case of heat treatment at 1,200°C, the cellulose particles heat-treated at 400°C were used for the 2nd heat treatment at 1,200°C in N₂. The manufacturing process for the PAN dope that contained cellulose particles consisted of three steps. In the first step, the cellulose particles underwent heat treatment. In the second step, the particles were dispersed. In the final step the stable DMSO solution was made. The detailed process used to prepare the PAN dope containing the dispersed cellulose particles is shown in Figure 1.

The heat-treated cellulose particles were ball milled with zirconia balls (3 mm in diameter) in a jar with ethanol for 48 h. Before and after the milling, the size of the heat-treated particles was checked. The shape of the particles in the carbon fiber was determined by examining the fibers that were flattened by high pressure (more than 10-ton load) using an optical microscope (Optiphot 150, Nikon, Japan).

2.3. Preparation of the PAN-Carbon Fiber Having Cellulose Microparticles. In order to prepare a PAN dope containing heat-treated cellulose particles for spinning, the dispersion of cellulose particles should be stabilized in the dope by size reduction, a process that includes milling the particles and selecting microparticles by collecting 30% of the cellulose

TABLE 2: PAN-DMSO dope containing heat-treated cellulose particles.

Sample	PAN (wt%)	DMSO (wt%)	Cellulose condition	Additional contents (wt%)
<i>Cel 30 (1.0)</i>	17.82	82	Heat-treated at 300°C	0.18 (1.0 wt% based on PAN)
<i>Cel 35 (1.0)</i>	17.82	82	Heat-treated at 350°C	0.18 (1.0 wt% based on PAN)
<i>Cel 40 (1.0)</i>	17.82	82	Heat-treated at 400°C	0.18 (1.0 wt% based on PAN)
<i>Cel 40 (1.5)</i>	17.73	82	Heat-treated at 400°C	0.27 (1.5 wt% based on PAN)
<i>Cel 40 (2.0)</i>	17.64	82	Heat-treated at 400°C	0.36 (2.0 wt% based on PAN)
<i>Cel 40/120 (1.0)</i>	17.82	82	Heat-treated at 1,200°C	0.18 (1.0 wt% based on PAN)
<i>Cel 40/120 (1.5)</i>	17.73	82	Heat-treated at 1,200°C	0.27 (1.5 wt% based on PAN)
<i>Cel 40/120 (2.0)</i>	17.64	82	Heat-treated at 1,200°C	0.36 (2.0 wt% based on PAN)

particles from supernatant fluid of the settled dope. Average particle size was measured using the particle size analyzer.

The spinning dope was prepared using various process parameters, such as cellulose heat treatment conditions and the amount of cellulose in the composite fiber. Detailed conditions for the dope are shown in Table 2. Slurry, which includes ground cellulose particles, was dried in the dry oven for 24 h at 90°C. These dried particles were dispersed in the DMSO with a homogenizer for 2 h. To classify the small particles, floating particles in the mass cylinder were selected in the equivalent sedimentation condition for the samples. The net weight of the cellulose that was used could be calculated from the remaining cellulose particles, which were found at the bottom of the cylinder. The final spinning dope, mixed with carbonized cellulose, DMSO, and PAN, was prepared as shown in Figure 2.

2.4. Characterizations

2.4.1. Thermal Analysis. The starting and ending point of the thermal decomposition of the cellulose due to heat treatment conditions were confirmed by the TG/DTA results (TA, TGA/SDTA 851e, Mettler-Toledo) with N₂ atmosphere.

2.4.2. Morphology Observation. The microstructure of the cellulose particles was observed by a scanning electron microscope (SEM) (FE-SEM, XL30, Philips). The size and morphology changes could be compared with the treatment conditions.

2.4.3. Chemical Structure Analysis. The chemical structure of the heat-treated cellulose particles was examined by Fourier transformation infrared spectroscopy (FT-IR) (Magna IR550, Scinco). The spectra could be obtained from proper molecular vibrations in the range of 500 cm⁻¹–4000 cm⁻¹.

2.4.4. Crystal Structure Analysis. The crystal structures of the carbonized cellulose were observed using an X-ray diffractometer (XRD) (D8 Discovery, Bruker) with the variations of the heat treatment temperature. The measurement was conducted in the range of $2\theta = 10^\circ\text{C} - 60^\circ\text{C}$.

2.4.5. Particle Size Analysis. The particle size of the carbonized cellulose was obtained by particle size analyzer (LS 13 320, Beckman Coulter, Inc., USA).

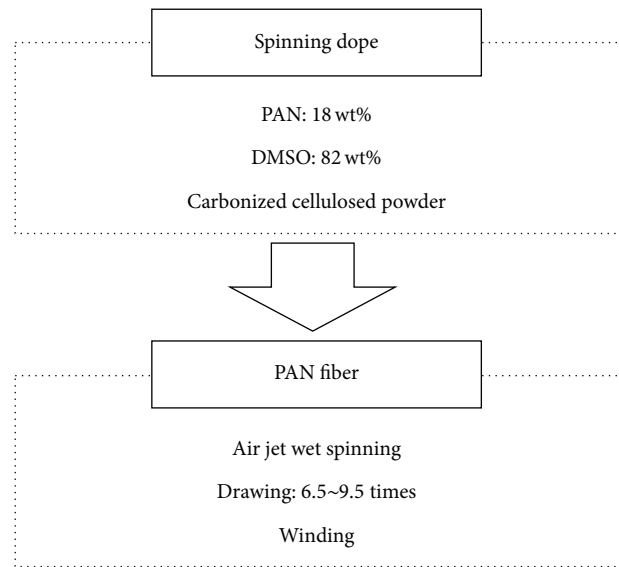


FIGURE 2: Preparation process of the PAN fiber containing carbonized cellulose particles.

3. Results and Discussion

3.1. Cellulose Particles. Heat treatment was conducted in order to comprehend the thermal properties of the cellulose and to investigate the optimum treatment condition for the cellulose particles. The first step of this study involved preparing the dope with proper cellulose particles to spin the PAN fiber with stable dispersion. Because the stabilization and carbonization process is essential for preparing PAN-based carbon fiber [11, 12], the heat-treating temperatures were chosen from the range of the stabilization temperatures for carbon fiber. The range for the optimum heat treatment condition was established based on the following thermal analysis results.

The results of the thermal decomposition of the cellulose examined by TG/DTA are shown in Figure 3. The weight loss of 5-6% until 100°C, which was shown in region “a,” was attributed to the evaporation of the physisorbed water. The main weight loss of the cellulose occurred in temperature range “b,” about 260–350°C, due to the breakdown of the anhydrous glucose bond by the pyrolysis. It arose from the evaporation of water vapor, tar, OH, CO, and CO₂ in

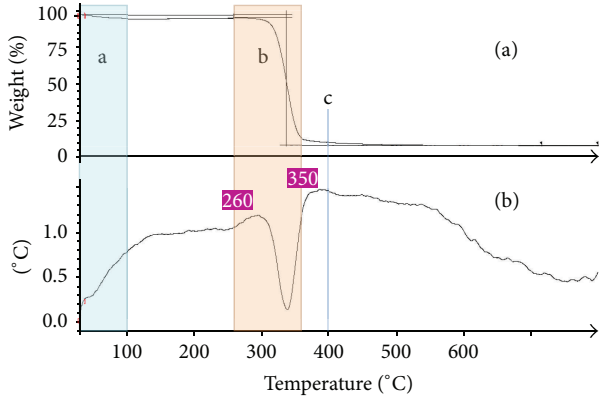


FIGURE 3: TG and DTA curves of the cellulose particles.

the decomposition process of levoglucosan from the debonding of the glycosidic unit. The weight loss occurred continuously, via the breakdown of anhydrous cellulose, with elevating temperature until the temperature reached 400°C. This result was similar to the results reported by Brunner [13] and Fengel and Wegener [14]. By way of explanation, the thermal decomposition of cellulose occurred because the side groups (H, OH) were removed and were disintegrated as small molecules of the carbonyl compound by chain scission from the ring opening reaction as the temperature increased [15]. The maximum rate of decomposition was found at 335°C, via the DTA results. After that temperature, the decomposition rate was decreased linearly. In this experiment, the final weight loss was 87%. Even though the weight decreased continuously as the temperature reached 400°C, the rate of loss was lower. These phenomena could be explained by the thermal decomposition of additives as the result of FT-IR experiments. The final product of cellulose through heat treatment was amorphous carbon.

3.2. Morphology of Cellulose

3.2.1. Particle Size and Distribution. In order to spin the PAN dope containing the cellulose particles, the size of the cellulose particle should be reduced by ball milling in order to enable the particles to pass through the spinning nozzle (50 μm in diameter). Moreover, the cellulose particle size should be smaller than the final fiber diameter of the PAN, in the range of 4–15 μm . The particle size and size distribution were decided by the results of the particle size analysis, as shown in Figure 4. The measured data are shown in Table 3 where the average particle size and the distribution of the *Cel 40* particle sample were 4.71 μm and 3.88 μm , respectively, showing the smallest value in this study. As shown in Figure 3, the cellulose particles were initially decomposed in the range of 260°C–350°C. When the temperature exceeded 400°C, the thermal decomposition was terminated and most of the hydrogen bonded organic substance was removed. Finally, the cellulose particles were converted to amorphous carbon with a weak bond, making it easier for the particles to be ground due to the highest milling efficiency at a condition of *Cel 40*.

TABLE 3: Particle size analysis of the cellulose particles after heat treatment and milling.

Sample	Mean size (μm)	Standard deviation (μm)	Maximum size at interest region (μm)
<i>Cel 30</i>	14.52	12.02	2.80
<i>Cel 35</i>	11.41	9.25	2.70
<i>Cel 40</i>	4.71	3.88	2.50
<i>Cel 40/120</i>	5.14	7.10	2.10

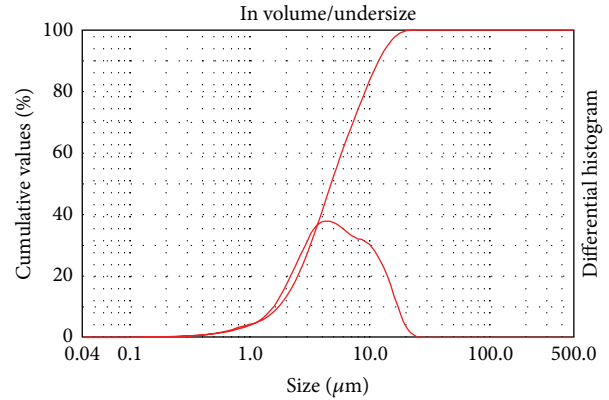


FIGURE 4: Typical result of the particle size analysis (*Cel 40*).

This explanation could be supported by the FT-IR results, which revealed that *Cel 40* was the intermediate product of the carbon structure. The average particle size of *Cel 40/120* sample, which was the *Cel 40* cellulose sample treated at 1,200°C, was 5.14 μm . During the carbonization process at 1,200°C, the carbon structure was formed with weight loss and the bonding force was simultaneously increased.

As previously mentioned, in this experiment the fine cellulose particles were obtained by the sedimentation method. Although the settling rate of the particles in the dope was different between the samples, the average particle size of the acquired cellulose particles, which are identified as the “maximum size at interest region” in Table 3, showed a similar size ranging from 2.8 μm to 2.1 μm .

3.2.2. Morphologies of the Cellulose Particles. The study examining the dispersion of cellulose particles in the dope was conducted using chemical treatment and physical treatment methods. At first, the chemical method using LiCl as an additive could be expected to result in cellulose swelling and dissolving [16]. Figure 5 shows the morphologies of (a) the original cellulose particles and (b) the chemically treated cellulose particles. The shape of the cellulose is a linear chain made of D-glucose, which is related to its structure depending on $(\text{C}_6\text{H}_{10}\text{O}_5)_n$ where n is the number ranging from 100 to 10,000. Chemical treatments, which consisted of ultrasonic treatments followed by surface treatment using LiCl, removed the binding substance between the microfibrils by dissolving the glycosidic bond. The acidic-hydrolysis reaction would affect the dissolution. There seemed to be some limitations in

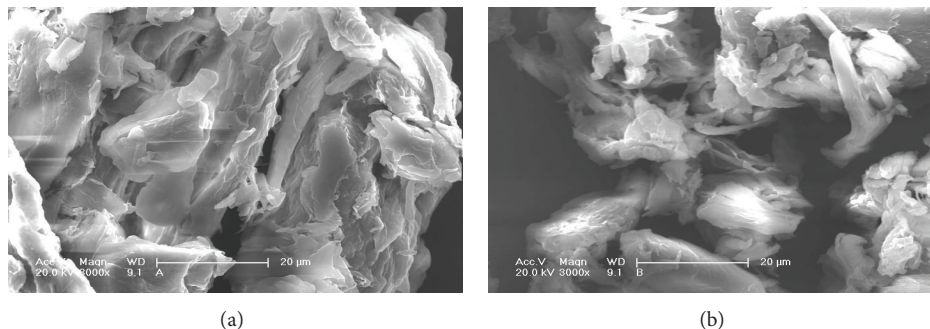


FIGURE 5: SEM micrographs ($\times 5,000$) of the cellulose powders with chemical treatment. (a) Untreated cellulose powders. (b) Dispersed cellulose powders with LiCl.

size reduction for the chemical method because of the linkage between the microfibril chains due to the hydrogen bonding that took place during the washing process with the water that was used to eliminate the Li^+ ions. This made it difficult to separate the particles from each other when the sample was dried in the air. Finally, the cellulose particles treated chemically were too large to spin through the nozzle when they were mixed in the spinning dope.

The second method used for the dispersion of cellulose particles was a milling process after heat treatment. The heat-treated and milled cellulose particles were added as an additive before preparing the spinning dope. Temperatures of 300°C , 350°C , 400°C , and $1,200^\circ\text{C}$ were selected as the heat treatment conditions for achieving the optimum condition of dispersion.

After heat treatment, morphological changes could be observed in the microstructure, as shown in Figure 6. From the SEM photographs it can be seen that the content of the microdebris was reduced and the overall size became smaller as the heat treatment temperature increased. The size reduction of the cellulose particles was caused by the breakdown of anhydrous glucose bonding due to pyrolysis over 240°C (until the temperature reached 400°C).

It could be suspected that the moisture was physically absorbed and the fine fibrils at the surface were thermally decomposed in the course of the heat treatment for temperatures up to 300°C . For *Cel 40* and *Cel 35*, most of the particles under $10\ \mu\text{m}$ in diameter could be compared to the particle size of *Cel 30*, which showed a diameter of about $20\ \mu\text{m}$. In the range of 260°C – 350°C , which was described in Section 3.1, a decrease in the particle size was consistent with the results of thermal gravimetric analysis, which showed a weight reduction because the anhydrous glucose ring was destroyed.

Even though the particle sizes of the *Cel 40* sample and the *Cel 35* sample were similar, there were differences in the surface shape. The surface of the *Cel 40* sample was uneven, whereas the surface of the *Cel 35* sample was relatively smooth. This could be explained by the fact that the organic substance that was left in a small amount until the temperature reached 350°C was removed when the temperature was around 400°C , due to thermal decomposition. For *Cel 40/120*, the particle size increased. The growth in the layered structure

of the carbon residue, which had been formed in the previous step, was thought to be due to the aromatization when the temperature was over 400°C .

3.2.3. Dispersion of Cellulose Particles. Figure 7 represents the flattened shape of the spun PAN fibers that contained carbonized cellulose observed by the optical microscope. The black spots, which are the carbonized cellulose particles, could be observed when the spun fiber flattened at a pressure of 20,000 psi on a mirror-like polished metal plate. This was closely related to the morphology and properties of the carbonized cellulose particle size shown in Figure 6 and Table 3, but cellulose microparticles under the micrometer level could not be observed due to the limitations of the optical microscope. The carbonized cellulose at a temperature over 400°C could be observed in black; however, the cellulose particles were represented by particles that were slightly dark brown when the heat treatment temperature was lower, as shown in Figures 7(a) and 7(b).

The dispersion with the heat treatment of 400°C and $400^\circ\text{C}/1,200^\circ\text{C}$ indicated a small difference in the fiber; thus, it can be concluded that excellent dispersion was achieved at those conditions. Figures 7(a) and 7(b) show that the particles were agglomerated slightly. Therefore, the dispersion of the cellulose particles in the dope was better when the heat treatment temperature was higher. These results came from the decomposition of the organic substance in the cellulose at a high temperature, which leads to weak binding of the cellulose particles, enabling them to break easily.

3.3. Chemical Structure of Cellulose. The changes in the chemical structure of cellulose with the heat treatment were analyzed by FT-IR spectra, as shown in Figure 8. All the samples revealed the O-H stretching absorbing band in $3,400\ \text{cm}^{-1}$. For the *Cel 00* sample, the absorbing band related to the C-H stretching of the cellulose could be observed at $2,900\ \text{cm}^{-1}$. Many absorbing bands related to cellulose were found, such as a C=O vibration band at $1,635\ \text{cm}^{-1}$, a CH_2 bending band at $1,426\ \text{cm}^{-1}$ [17], and a stretch band of C-O-C asymmetry at $1,106\ \text{cm}^{-1}$ [18]. The result of the C-O-C stretching band at $898\ \text{cm}^{-1}$ in this sample meant that there was a small amorphous form in the cellulose structure [17].

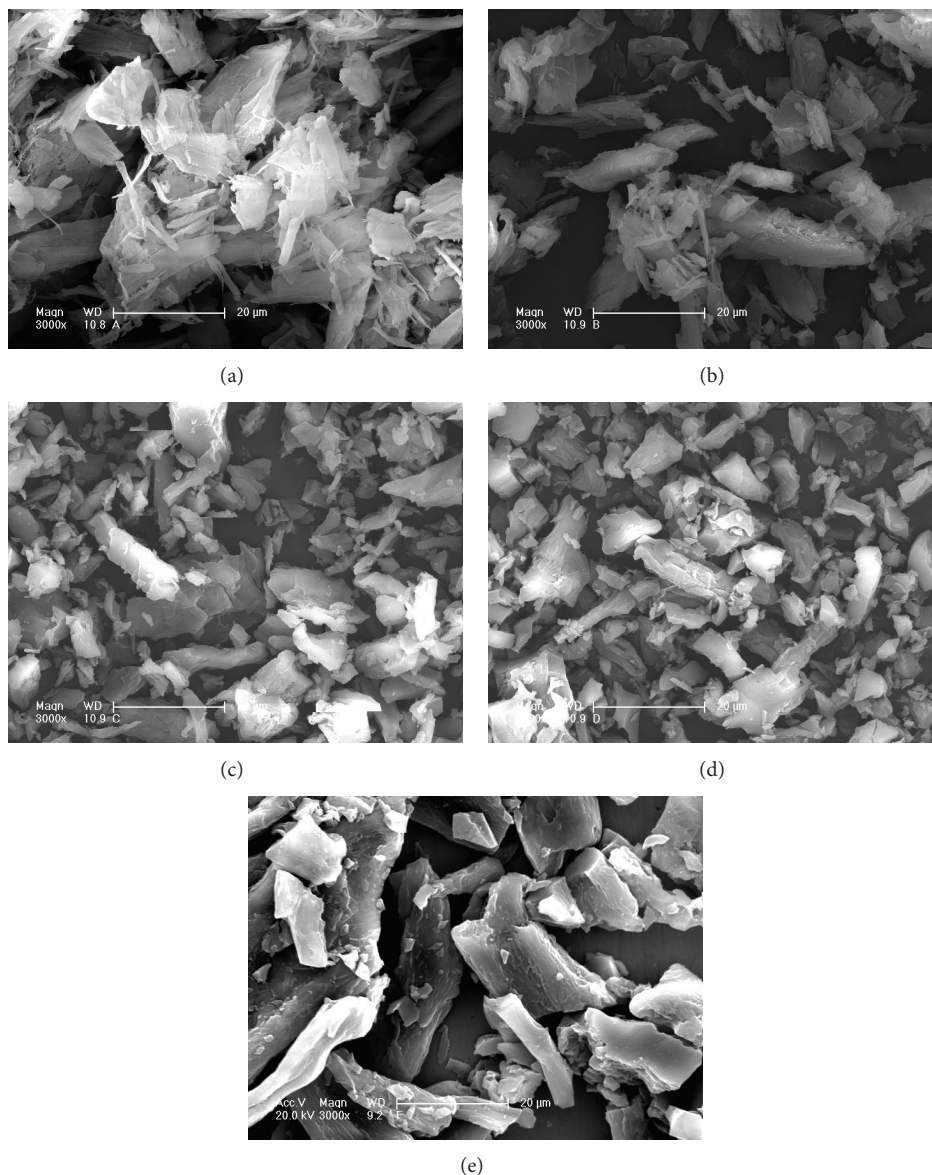


FIGURE 6: SEM micrographs ($\times 3,000$) of the heat-treated cellulose particles. (a) *Cel 00*. (b) *Cel 30*. (c) *Cel 35*. (d) *Cel 40*. (e) *Cel 40/120*.

In the case of the *Cel 35* sample, the characteristic cellulose peaks, such as $2,900\text{ cm}^{-1}$ and 890 cm^{-1} – $1,500\text{ cm}^{-1}$, disappeared and the sample showed the absorbing of levoglucosan [19]. The final heat-treated sample of *Cel 40* revealed the disappearance of the cellulose peaks and the levoglucosan peak, and the sample showed only a weak peak at $1,635\text{ cm}^{-1}$ related to C=O vibration.

3.4. Crystal Structure of Cellulose. The crystal structure changes of the cellulose particles based on heat treatment condition are displayed in Figure 9. As shown, the results of the untreated cellulose particles agreed with crystal structure of JCPDS 03-0289 (natural cellulose). A maximum peak of (002) appeared at $2\theta = 22.8$, similar to other results reported by Wang et al. [20]. As the heat treatment temperature increased over 350°C (*Cel 40*), the characteristic peaks of

cellulose disappeared and then the structure showed an amorphous state. This result could be explained by the decomposition reaction of the side group, as shown in Figure 3. When the temperature increased up to 400°C , broad peaks could be observed over $2\theta = 20$ – 25 and $2\theta = 40$ – 45 in *Cel 40/120*, related to the graphite crystal structure. The result was coincident with the FT-IR results (Figure 8) and the TGA results (Figure 3).

4. Conclusions

The effects of cellulose particles on PAN dope have been studied. In order to achieve a stable and fine-dispersed state for PAN dope, chemical treatment and physical treatment were performed on the cellulose particles. The physical treatment included a milling process followed by a heat

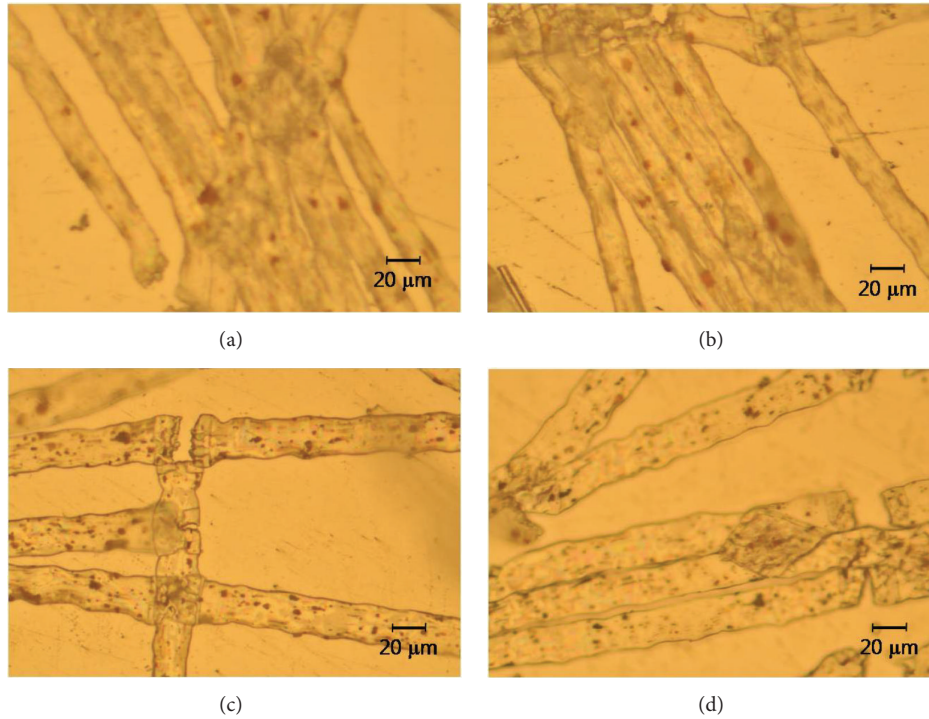


FIGURE 7: Optical micrographs ($\times 400$) of the spun fiber with cellulose particles at various heat treatment conditions. (a) *Cel 30* particles. (b) *Cel 35* particles. (c) *Cel 40* particles. (d) *Cel 40/120* particles.

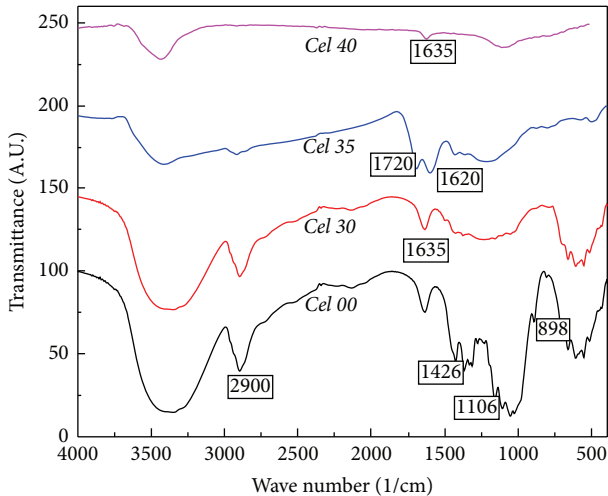


FIGURE 8: The FT-IR spectra of the heat-treated cellulose particles.

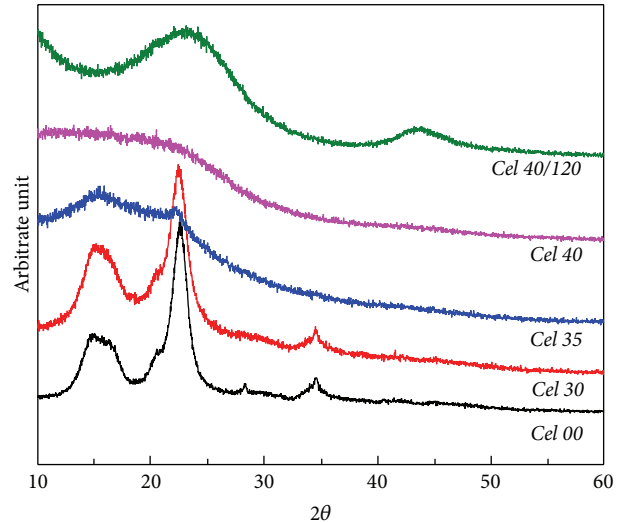


FIGURE 9: The XRD curves of the cellulose particles based on the heat treatment conditions.

treatment process for carbonization of the cellulose. Finally, the following conclusions were obtained.

- (1) Thermal/mechanical process has a better effect for preparing fine cellulose particles than the chemical treatment process in this study.
- (2) The condition of heat treatment at 400°C in the air revealed the best properties for particle size (average $4.71\ \mu\text{m}$) and size distribution ($3.88\ \mu\text{m}$). The final

particle size was selected in the range of $2.1\ \mu\text{m}$ – $2.8\ \mu\text{m}$ using the sedimentation method.

- (3) Based on the results obtained from examining the dispersion characteristics of spun fiber with carbonized cellulose, the condition of carbonization at 400°C revealed relatively good dispersion of the cellulose particles in the dope.

Conflict of Interests

The authors declare that there is no conflict of interests regarding the publication of this paper.

Acknowledgments

This research was financially supported by the “Fundamental R&D Program for Technology of the Graduate Student Education Program for Research of Hybrid and Super Fiber Materials” through the Ministry of Trade, Industry & Energy (MOTIE) and the Korea Institute for Advancement of Technology (KIAT) (N0000993).

References

- [1] K. Morita, Y. Murata, A. Ishitani, K. Murayama, and A. Nakajima, “Characterization of commercially available PAN-based carbon fiber,” *Pure and Applied Chemistry*, vol. 58, no. 3, pp. 455–468, 1986.
- [2] I. Mochida, S.-H. Yoon, N. Takano, F. Fortin, Y. Korai, and K. Yokogawa, “Microstructure of mesophase pitch-based carbon fiber and its control,” *Carbon*, vol. 34, no. 8, pp. 941–956, 1996.
- [3] H. M. Hawthorne, C. Baker, R. H. Bentall, and K. R. Linger, “High strength, high modulus graphite fibres from pitch,” *Nature*, vol. 227, no. 5261, pp. 946–947, 1970.
- [4] M. Endo, “Grow carbon fibers in the vapor phase,” *ChemTech*, vol. 18, no. 9, pp. 568–576, 1988.
- [5] A. G. Fazlitdinova, V. A. Tyumentsev, S. A. Podkopayev, and G. P. Shveikin, “Changes of polyacrylonitrile fiber fine structure during thermal stabilization,” *Journal of Materials Science*, vol. 45, no. 15, pp. 3998–4005, 2010.
- [6] Y. Xue, J. Liu, and J. Liang, “Kinetic study of the dehydrogenation reaction in polyacrylonitrile-based carbon fiber precursors during thermal stabilization,” *Journal of Applied Polymer Science*, vol. 127, no. 1, pp. 237–245, 2013.
- [7] J. Ding, X. Huang, G. Zhu, S. Chen, and G. Wang, “Mechanical performance evaluation of concrete beams strengthened with carbon fiber materials,” *Advances in Materials Science and Engineering*, vol. 2013, Article ID 572151, 9 pages, 2013.
- [8] J. Yang, J. J. Yoo, H. J. Jang, D. K. Yong, J. S. Won, and S. G. Lee, “Preparation and characterization of PAN-based carbon fibers having zirconia nanofibers,” *Textile Science and Engineering*, vol. 49, no. 5, pp. 307–313, 2012.
- [9] C. Pradere, J. C. Batsale, J. M. Goyh  n  che, R. Pailler, and S. Dilhaire, “Thermal properties of carbon fibers at very high temperature,” *Carbon*, vol. 47, no. 3, pp. 737–743, 2009.
- [10] J.-W. Yang, H. N. Choi, Y. S. Chung, S. H. Kim, and S. G. Lee, “Preparation and properties of PAN-based carbon fibers having nano-cellulose,” in *Proceedings of the Asian Textile Conference*, Daegu, Republic of Korea, 2011.
- [11] A. Takaku and J. Shimizu, “Volume contraction and its significance in structural formation during the thermal stabilization of acrylic fibers,” *Journal of Applied Polymer Science*, vol. 29, no. 4, pp. 1319–1326, 1984.
- [12] J. D. Brooks and G. H. Taylor, *Chemistry and Physics of Carbon*, Marcel Dekker, New York, NY, USA, 1968.
- [13] P. H. Brunner, “Beitrag zur pyrolyse von cellulose fur Herstellung von Aktivkohlen aus Abfallstoffen,” Ph.D. Dissertation no. 5705, Swiss Federal Institute of Technology, Z  rich, Switzerland, 1976.
- [14] D. Fengel and G. Wegener, *Wood*, De Gruyter, 1983.
- [15] K. W. Kim, *Analysis of natural fiber using pyrolysis [M.S. thesis]*, Chungnam National University, 2011.
- [16] P. Navard and C. Cuissinat, “Cellulose swelling and dissolution as a tool to study the fiber structure,” in *Proceedings of the 7th International Symposium on Alternative Cellulose : Manufacturing, Forming, Properties*, HAL ID: hal-00579326, Rudolstadt, Germany, 2006.
- [17] D. Ciolacu, F. Ciolacu, and V. I. Popa, “Amorphous cellulose—structure and characterization,” *Cellulose Chemistry and Technology*, vol. 45, no. 1-2, pp. 13–21, 2011.
- [18] S. Ates, M. H. Akyildiz, and H. Ozdemir, “Effects of heat treatment on *Calabrian pine (Pinus brutia Ten.)* wood,” *BioResources*, vol. 4, no. 3, pp. 1032–1043, 2009.
- [19] K. Pielichowski and J. Njuguna, *Thermal Degradation of Polymeric Materials*, Rapra Technology Limited, 2005.
- [20] B. Wang, M. Sain, and K. Oksman, “Study of structural morphology of hemp fiber from the micro to the nanoscale,” *Applied Composite Materials*, vol. 14, no. 2, pp. 89–103, 2007.

Research Article

Effects of Low Volume Fraction of Polyvinyl Alcohol Fibers on the Mechanical Properties of Oil Palm Shell Lightweight Concrete

Ming Kun Yew,¹ Hilmi Bin Mahmud,¹ Bee Chin Ang,² and Ming Chian Yew¹

¹Department of Civil Engineering, Faculty of Engineering, University of Malaya, Lembah Pantai, 50603 Kuala Lumpur, Malaysia

²Center of Advanced Materials, Department of Mechanical Engineering, Faculty of Engineering, University of Malaya, 50603 Kuala Lumpur, Malaysia

Correspondence should be addressed to Ming Kun Yew; davidyew1983@gmail.com

Received 9 August 2014; Revised 24 November 2014; Accepted 24 November 2014

Academic Editor: Hao Wang

Copyright © 2015 Ming Kun Yew et al. This is an open access article distributed under the Creative Commons Attribution License, which permits unrestricted use, distribution, and reproduction in any medium, provided the original work is properly cited.

This paper presents the effects of low volume fraction (V_f) of polyvinyl alcohol (PVA) fibers on the mechanical properties of oil palm shell (OPS) high strength lightweight concrete mixtures. The slump, density, compressive strength, splitting tensile strength, flexural strength, and modulus of elasticity under various curing conditions have been measured and evaluated. The results indicate that an increase in PVA fibers decreases the workability of the concrete and decreases the density slightly. The 28-day compressive strength of oil palm shell fiber-reinforced concrete (OPSFRC) high strength lightweight concrete (HSLWC) subject to continuous moist curing was within the range of 43–49 MPa. The average modulus of elasticity (E) value is found to be 16.1 GPa for all mixes, which is higher than that reported in previous studies and is within the range of normal weight concrete. Hence, the findings of this study revealed that the PVA fibers can be used as an alternative material to enhance the properties of OPS HSLWC for building and construction applications.

1. Introduction

Concrete is the most widely used construction material in civil engineering projects worldwide. Huge quantities of different types of concrete have been produced annually. From the various kinds of concrete, lightweight concrete (LWC) is one of the most interesting subjects for researchers. LWC is used extensively by the building construction industry as nonstructural wall panels, partitions, light tiles, bricks, and architectural exterior finishing. Since their mechanical properties are considerably lower than those for normal weight concrete, the structural use of LWC is limited as load-bearing structural members. In order to use LWC for structural purposes, the material must be engineered to provide adequate strength, ductility, or a combination of both. Hence, the amount of lightweight aggregate concrete (LWAC) is increasing, and research and development are ongoing worldwide to develop new techniques and materials as well

as investigating the engineering properties of such materials. Recently, a high strength lightweight aggregate concrete (HSLWAC) achieved a compressive strength in the range of 40–100 MPa by using several types of LWAs [1–4]. However, an increase in concrete strength results in brittleness of the concrete during compression and tension [5–7], specifically in the case of LWAC [6]. By advancement in fiber-reinforced cementitious composites, lightweight cement composites reinforced with a small amount of discontinuous (steel, polypropylene, and nylon) fibers may prove themselves as favourable construction materials. However, the main disadvantage of adding steel fibers into OPSLWC in a fresh state is its significant reduction in slump value and increased density [8]. Chen and Liu [7] have intensively studied the effect by using 1% of volume content of polypropylene fibers (length: 15 mm, aspect ratio: 150) on LWC. Based on their findings, the addition of polypropylene fibers into LWC mixtures using expanded clay resulted in a reduction of slump values of

about 20.8%. Furthermore, the addition of polypropylene and nylon insignificantly increased the mechanical properties of OPS concrete, particularly for the tensile strength [9]. A new method that can be adopted to resolve the brittle texture of LWAC is to combine the PVA fibers with heat-treated OPS concrete to enhance its mechanical properties.

The most popular method of LWC production is through the use of LWAs [10], which may be either natural or manufactured. The LWA can be natural aggregates such as pumice, scoria, and those of volcanic origin whereas artificial aggregates include expanded blast-furnace slag, vermiculite, and clinker aggregates [11]. Another type of natural LWA is agricultural resource OPS. It has known that there are large amounts of agricultural residue in countries where the oil palm industry is dominant such as Malaysia, Indonesia, and Nigeria. Malaysia is one of the world leaders in the production and export of palm oil [12]. The production of OPS has estimated that over 4 million tonnes are produced annually in this country alone [13]. The densities of OPS are within the range of most typical structural LWAs [14–16]. Structural LWC is typically defined as concrete with an oven-dry density less than 2000 kg/m^3 [17, 18]. The 28-day oven-dry density for the crushed OPS mixes range between $1871\text{--}1876 \text{ kg/m}^3$ [4]. It has reported that the mechanical properties of OPS concrete are lower than other types of LWAC [10]. Recently, Yew et al. [4] reported that the different species and age categories of OPS coarse aggregates show the most significant impact on the performance of HSLWC compared to previous studies.

Most of the research on OPS lightweight concrete has focused on the investigation of their engineering properties as there is inadequate information concerning the enhancement of its low mechanical properties. Despite there have many advantages of incorporating steel fibers into OPS LWC. However, steel fibers pose several drawbacks; in particular, the workability of fresh concrete is reduced, and the dead load of the composite is increased [8]. To the authors' knowledge, no studies have been conducted regarding the properties of OPS concrete that incorporate PVA fibers. Therefore, this study focuses on investigating the effects of various low V_f of polyvinyl alcohol (PVA) fibers on the mechanical properties of LWAC subject to different curing conditions.

2. Materials and Methods

2.1. Materials

2.1.1. Cement. The cement used in this study is ASTM type I ordinary Portland cement (OPC) [19] with a specific gravity of 3.14 g/cm^3 . The Blaine's specific surface area for this cement is $3510 \text{ cm}^2/\text{g}$. The chemical compositions and physical properties of OPC are tabulated in Table 1.

2.1.2. Water and Superplasticizer (SP). Potable water is used for all mixes. The SP used in this study is polycarboxylic ether (PCE) supplied by BASF, which complies with ASTM C494/C494 M-13. The amount of SP for all mixes is kept constant, with a value 1.5% of cement weight in order to facilitate workability of the concrete.

TABLE 1: Chemical composition and physical properties of OPC.

Chemical composition (%)	
SiO ₂	21.28
Fe ₂ O ₃	3.36
CaO	64.64
MgO	2.06
Al ₂ O ₃	5.60
SO ₃	2.14
Physical properties	
LOI	0.64
Specific gravity	3.14
Blain specific surface area (cm ² /g)	3510

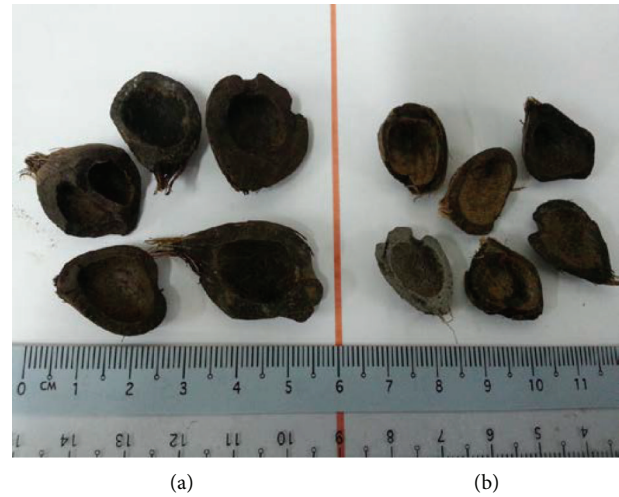


FIGURE 1: Original *dura* (a) and *tenera* (b) OPS aggregates.

2.1.3. Aggregates. Local mining sand is used as fine aggregates, having a specific gravity, fineness modulus, water absorption, and maximum grain size of 2.67 g/cm^3 , 2.71, 0.95%, and 4.75 mm, respectively.

Figure 1 shows the different species of original *dura* and *tenera* OPS waste from a local crude palm oil producing mill. In this study, the OPS aggregates used are *dura* species. The original *dura* OPS was washed and sieved using a 12.5 mm sieve. The OPS aggregates retained in the sieve were collected and then crushed using a stone-crushing machine in the laboratory as shown in Figure 2. The crushed OPS aggregates were sieved using a 9.5 mm sieve to remove OPS aggregates with sizes greater than 9.5 mm (Figure 3). It has been reported that the maximum size of OPS changes from original (12.5 mm) to crushed (9.5 mm). The broken edges of *dura* OPS are rough and spiky improved the physical bond between the aggregates and hydrated cement paste and yields higher compressive strength [4]. Furthermore, the OPS aggregates were heat treated at 60°C over a period of 0.5 h using a temperature-controlled laboratory oven. Once cooled to room temperature, they were weighed under dry room conditions and immersed in water for 24 h. Yew et al. [20] found that OPS aggregates were subjected to heat treatment at



FIGURE 2: Stone-crushing machine for OPS aggregates.

this temperature setting and duration of the period improved the performance of OPS properties without compromising the strength of the OPSC. Due to the high water absorption of OPS, it was subsequently air dried in the laboratory to attain a saturated surface dry (SSD) condition before mixing. The difference in quality of the crushed OPS surface between heat treatment and without heat treatment condition was reported by Yew et al. [20] and shown in Figure 4. The physical properties of the OPS used are shown in Table 2.

2.1.4. Fibers. A photograph of the polyvinyl alcohol (PVA) fibers is shown in Figure 5 and their physical properties are listed in Table 3.

2.2. Mix Proportions. The mix proportions used in this study have been shown in Table 4. The amount of volume fraction (V_f) of fibers added to the concrete mix typically ranges between 0.1 and 3.0% [21]. However, fibers with an extremely high V_f tend to “ball” in the mix and create workability problems. Hence, a low volume fraction ($\leq 0.5\%$) for the PVA fibers is used in this study. The volume fractions of PVA fibers in the OPS concrete are 0, 0.125, 0.25, 0.375, and 0.5%. The dosages of water and superplasticizer are kept constant for all mixes.

2.3. Test Methods and Curing Regimes. The procedure adopted for mixing the fiber-reinforced concrete involves the following steps. The sand and OPS are first poured into a concrete mixer and dry mixed for 1 min. Following this, the cement is spread and dry mixed for 1 min, after which the specified amount of fibers is distributed and mixed for 3 min in the mix. This is followed by the addition of water and superplasticizer with a mixing time of 5 min. Slump test is carried out on the mixture prior to sample casting. The concrete specimens are cast onto oiled moulds and a poker vibrator is used to eliminate the amount of air bubbles in the mix. For each mixture, 18 cubes ($100 \times 100 \times 100$ mm)

TABLE 2: Physical properties of crushed-heat treatment *dura* OPS aggregates.

Physical property	OPS	OPS*
Maximum size (mm)	9.5	9.5
Specific gravity (saturated surface dry)	1.35	1.31
Compacted bulk density (kg/m^3)	632	628
Water absorption (24 h) (%)	23.8	21.0
Aggregate impact value (%)	2.38	2.36

* Dried OPS.

TABLE 3: Physical properties of polyvinyl alcohol fibers.

Parameter	Polyvinyl alcohol
Length	30 mm
Filament diameter	660 microns
Specific gravity	1.3
Tensile strength	800 MPa
Flexural strength	23 GPa
Melting point	225°C
Colour	Yellow
Water absorption	<1% by weight
Alkali resistance	Excellent

TABLE 4: Mix proportions (kg/m^3).

Mix code	Cement	Water	Sand	OPS	Fiber volume (%)
V0	530	155	920	340	0
V0.125	530	155	920	340	0.125
V0.250	530	155	920	340	0.250
V0.375	530	155	920	340	0.375
V0.500	530	155	920	340	0.500

are used to determine the compressive strength at 1, 3, 7, 28, and 90 days. In addition, two cylinders (diameter: 150 mm, height: 300 mm), three cylinders (diameter: 100 mm, height: 200 mm), and three prisms ($100 \text{ mm} \times 100 \text{ mm} \times 500 \text{ mm}$) are used to determine the modulus of elasticity, indirect tensile strength, and flexural strength, respectively, on the 28th day. The specimens are demoulded approximately 24 hours after casting.

The specimens are cured under three types of curing conditions in order to determine the effects of curing environment on the 28-day compressive strength of OPS concrete, as listed below.

CC: the specimens are cured in water at $23 \pm 3^\circ\text{C}$ until the time of testing.

14C: the specimens are cured in water for 13 days after demoulding and then being air-cured in laboratory environment with a relative humidity (RH %) of 60 ± 15 and a temperature of $28 \pm 3^\circ\text{C}$.



FIGURE 3: Crushed *dura* (a) and *tenera* (b) OPS coarse aggregates.

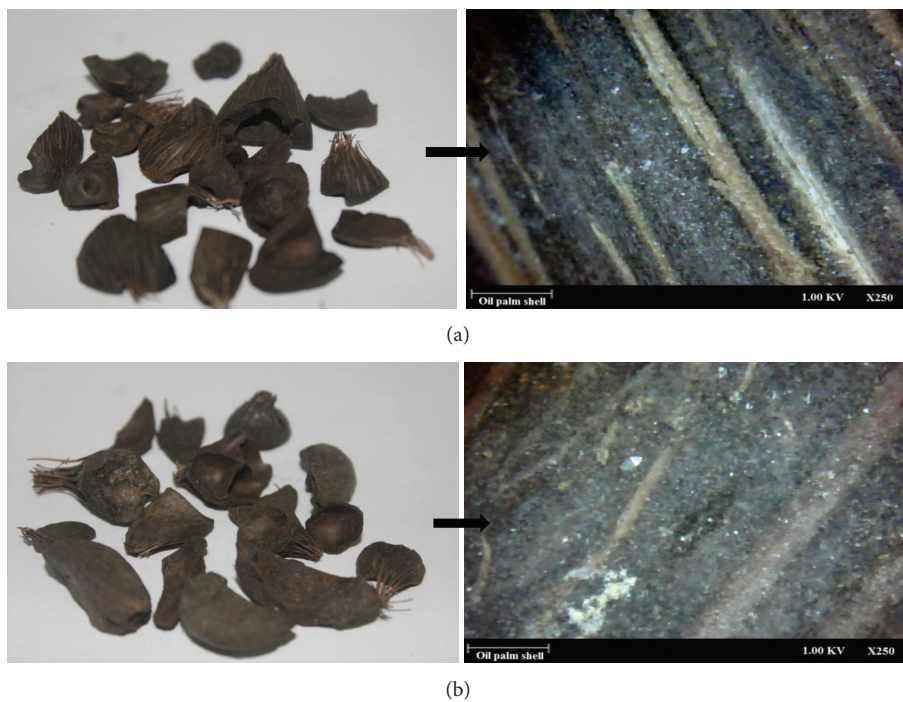


FIGURE 4: Images (left) and microscopic images (right) of crushed OPS aggregates: (a) with heat treatment and (b) without heat treatment.



FIGURE 5: Photograph of polyvinyl alcohol fibers.

AC: the specimens are stored under laboratory environment after demoulding.

3. Results and Discussion

3.1. Workability and Slump of Fiber-Reinforced Concrete. Slump tests are carried out to determine the consistency of fresh concrete. The use of fibers is well known to influence the workability and flow ability of plain concrete intrinsically [21, 22]. The slump of fresh OPS concrete decreases due to an increase in volume fraction of the PVA fibers. The quantity of water and SP is kept constant for all mixes in this study. The addition of fibers into the mixtures from 0 to 0.125, 0.25, 0.375, and 0.5% decreases the workability by 5.0, 7.5, 22.5, and 40.0%, respectively. Noushini et al. [23] reported that the addition of monofilament PVA fibers into the mixtures from 0 to 0.5% reduced the slump at about 20%. Figure 6 shows that there is a linear relationship between the PVA fiber volume fraction and slump for OPS concrete.

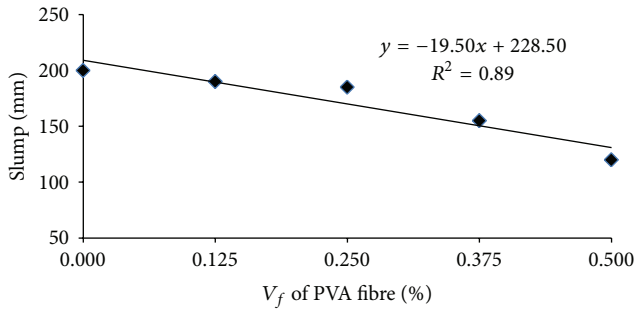


FIGURE 6: Relationship between PVA fiber volume fraction and slump.

The declining trend in slump value is attributed to the fact that the addition of fibers creates a network structure in the concrete, which restrains the mixture from segregation and flow. It can be ascertained that the fibers will absorb more of the cement paste in order to “wrap around.” This phenomenon is due to the high content and large surface area of the fibers, and an increase in viscosity of the mixture promotes a decrease in slump [24]. However, a number of studies have attempted to overcome the segregation problem by adding superplasticizers and using optimum proportions of aggregates and sand into the concrete mixtures to achieve high workability and flow ability [25–28]. Campione et al. [29] reported that good workability has been achieved for pumice and expanded clay LWAC reinforced with steel fibers by adding 1.5% superplasticizer of the cement weight. In general, the use of a low dosage of fibers is recommended to ensure good workability for fiber-reinforced concrete [30].

3.2. Hardened Density. Steel fibers are the most commonly used fibers for improving the mechanical properties of LWAC amongst the various types of fibers [31]. The relationship between steel fiber volume fraction and density of Shafiq et al. [8] shows that the density increases with an increase in fiber volume fraction. However, the low specific gravity of PVA fibers provides a lower density fiber-reinforced LWC with higher strength.

Three types of densities, namely, demoulded density, 28-day air-dry density, and oven-dry density, are measured for all mixes. The density of the concrete mixes decreases slightly with an increase in fiber volume fraction, which is attributed to the low specific gravity of the PVA fibers [32]. The 28-day air-dry density of the V0.5 mix is found to be approximately 1939 kg/m³, which indicates that the density falls within the range of those for structural lightweight concrete even though the volume fraction of PVA fibers is only 0.5%. The relationship between the demoulded, air-dry and oven-dry densities with respect to the volume fraction of PVA fibers is illustrated in Figure 7. The 28-days air-dry and oven-dry densities range from 1939 to 1970 kg/m³ and 1914 to 1941 kg/m³, respectively, for various volume fractions. It is found that increasing the volume fraction from 0 to 0.125, 0.25, 0.375, and 0.5% decreases the demoulded density, air dry density, and oven-dry density slightly by 0.2, 0.6, 1.0, and

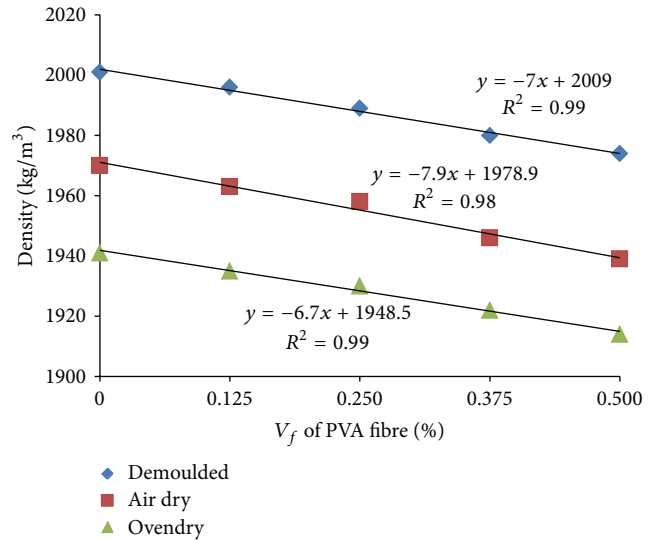


FIGURE 7: Relationship between PVA fiber volume fraction and densities.

1.3% at 1-day age, 0.4, 0.6, 1.2, and 1.6% at 28-days age and 0.3, 0.6, 1.0, and 1.4% at 28-days age, respectively. Although the addition of the very low specific gravity PVA into heat-treated OPS concrete produced an insignificant change in density. However, their contribution to the density cannot be ignored. It might be attributed to PVA tend to displace mortar in concrete as the diameter of PVA is 0.66 mm. Furthermore, it has been reported that there is a marginal reduction in density without alterations in mechanical properties when polypropylene (PP) fibers are added into OPSFRC [9, 33]. Hence, there is substantial cost savings by providing less dead load for LWC in this study.

3.3. Compressive Strength

3.3.1. Continuous Moist Curing. The effects of PP fibers ($L = 15$ mm and $D = 0.10$ mm) on the properties of LWAC have been much researched amongst the various types of fibers. It has been reported that PP fibers result in a decrease in compressive strength of LWAC [24]. It can be seen that the compressive strength of concrete increases for all ages with an increase in PVA fiber volume fraction (Table 5). Increasing the PVA fiber volume fraction from 0 to 0.125, 0.25, 0.375, and 0.50% increases the compressive strength by roughly 0.9, 6.2, 8.7, and 13.1% at 28-days age and 0.6, 8.0, 10.0, and 18.9% at 90-days age, respectively. Comparison between the compressive strength of the fiber-reinforced concrete during the former and latter ages indicates that the rate of compressive strength development increases from the former to latter ages and is particularly more pronounced for concrete mixes with higher PVA fiber content. This trend can be clearly observed from the percentages of the 28-day compressive strength (shown within the parentheses) for each age in Table 5. It can be seen that the percentage of compressive strength at 3 days and 7 days decreases with an increase in PVA fiber volume fraction whereas the value increases at 90-day age. This trend is attributed to the higher rate of compressive strength gained at

TABLE 5: Development of compressive strength of lightweight OPS FRC under continuous moist curing.

Mix code	Compressive strength (MPa) ^a				
	1 d	3 d	7 d	28 d	90 d
V0	29.32 (68%) (0.61)	33.04 (77%) (0.33)	39.48 (92%) (0.48)	42.89 (0.49)	43.29 (101%) (0.67)
V0.125	28.81 (67%) (0.83)	32.61 (75%) (0.97)	39.70 (91%) (0.62)	43.29 (0.73)	43.54 (101%) (0.89)
V0.250	28.95 (64%) (0.90)	34.60 (76%) (0.97)	39.92 (88%) (0.81)	45.56 (0.86)	46.77 (103%) (0.78)
V0.375	29.65 (64%) (0.83)	35.88 (77%) (0.95)	41.95 (90%) (0.75)	46.62 (0.87)	47.60 (102%) (0.95)
V0.500	30.66 (63%) (0.88)	37.58 (77%) (0.80)	43.75 (90%) (0.81)	48.51 (1.22)	51.48 (106%) (0.66)

^aThe data in parentheses are percentages of 28-day compressive strength.

Note: the standard deviations (in MPa) of the corresponding mechanical properties are shown in the bracket (below).

latter ages, and the rate is particularly significant for the 0.5% PVA fiber volume fraction. The relative strength between the control and PVA fiber volume fraction from 0 to 0.125, 0.25, 0.375, and 0.50% increases the compressive strength at about 0.9, 0.6, 2.7, 2.1, and 6.1% at 90-day age as compared to 28-day age. It is apparent that PVA fiber volume fraction up to 0.25%, the performance of PVA fibers in the OPS concrete increases at latter ages, which is possibly due to the improvement of PVA fiber-mortar interfaces [34].

Shafiqh et al. [8] have shown the possibility of producing grade 40 strength OPS concrete at the age of 28 days. Based on the findings of this study, it can be deduced that the production of grade 40 OPS concrete with lower cement content is possible [35], even with a low volume fraction of PVA fibers, relative to previous studies. In practical applications of concrete, the early-age compressive strength test can be used in replacement of the 28 days or other latter ages for the purpose of routine quality control. In this study, two equations are generated to predict the performance of the concrete in latter ages. By using new (1) at the early age compressive strength test, changes in concrete properties can be detected at an early stage and the appropriate corrective actions can be taken to improve concrete quality [36]:

$$\begin{aligned}
 F_{28} &= 1.35F_7 - 9.94, \\
 F_{90} &= 1.40F_{28} - 16.9.
 \end{aligned}
 \tag{1}$$

3.3.2. Effect of Curing Condition. Figure 8 illustrates the 28-days compressive strength of specimens subject to three curing conditions, namely, continuous curing (CC), 14-days moist curing (14C) and no curing in the laboratory environment (AC). It can be seen that the order of strength for the concrete is $CC > 14C > AC$. The loss in 28-day compressive strength of the specimens consisting of 0, 0.125, 0.25, 0.375, and 0.5% PVA fiber volume fraction is 14.9, 14.7, 13.7, 10.8, and 9.6%, respectively, under AC curing. The values decrease to 5.4, 6.4, 6.8, 8.3, and 5.4%, respectively, when the specimens are cured over a short period (14C).

The results show that the behaviour of OPS concrete containing PVA fibers up to 0.5% by volume under no curing

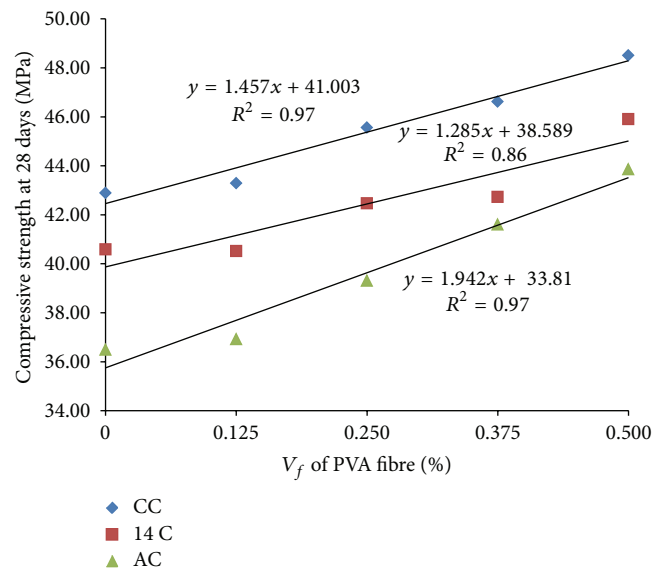


FIGURE 8: Relationship between PVA fiber volume fraction and compressive strength under different curing conditions on the 28th day.

regimes is almost similar to that of OPS concrete under CC condition. However, OPS concrete with a PVA fiber volume fraction exceeding 0.375% exhibits lower strength loss under AC curing as compared to CC and 14C. This observation shows that although the strength of OPS concrete appears to be sensitive to poor curing [8], the sensitivity of compressive strength loss decreases by incorporating PVA fibers with a volume fraction exceeding 0.375%. This is due to the possibility that when the PVA fiber content is high (particularly a volume fraction of 0.5%), the fibers arrest the development and number of original shrinkage cracks. Therefore, it can be deduced PVA fibers offer an additional benefit, whereby the sensitivity of OPS concrete is reduced under poor curing environments. Furthermore, it can be observed from Figure 7 that the 28-day compressive strength of OPS concrete increases linearly with an increase in PVA

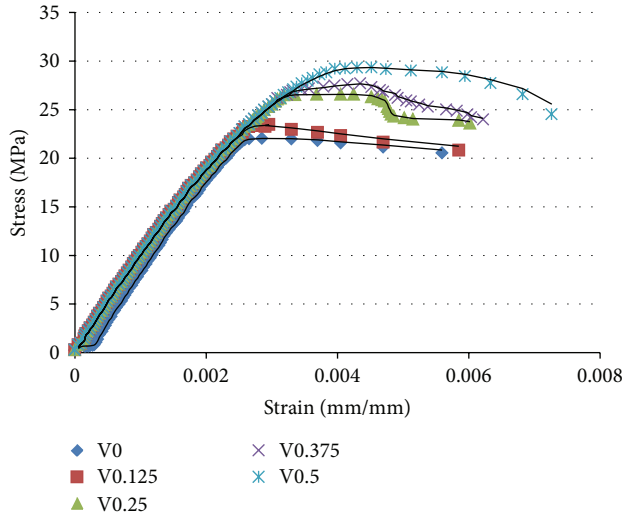


FIGURE 9: Typical stress-strain relationship.

fibers volume fraction. A prominent feature of this figure is that the slope of the straight line for AC specimens is the steepest (slope = 1.942), whereas the slope for CC and 14C specimens is nearly equal with a value of 1.457 and 1.285, respectively. This shows the positive effect of incorporating PVA fibers into OPS concrete even in poor curing conditions.

3.3.3. Strain at Peak Stress. Figure 9 shows the stress-strain curves of sample at 28-day continuously moist curing for V0, V0.125, V0.25, V0.375, and V0.5 mixes under compression. The stress-strain curves of most LWACs for both normal and high strength levels are typically linear to levels approaching 90% or higher of the failure strength [31, 37, 38]. It is usually 30 to 45% for a normal weight concrete (NWC) [31]. This shows that LWACs are more brittle than NWCs, which causes its explosive fracture after peak load [39]. One of the disadvantages that prevented its use in concrete structures is due to the brittle nature of LWC. Therefore, the possible solution is to use PVA fibers to enhance the brittleness of LWC.

From the results, the strain at peak stress (ϵ) of the V0, V0.125, V0.25, V0.375, and V0.5 mixes measured in this study varies from 0.0029 to 0.0045. The ϵ value of the V0 and V0.125 mixes is of similar value of approximately 0.0030. However, when the inclusion of PVA fiber is up to 0.25–0.5%, the ϵ value increased about 41, 52, and 55%, which is significant. It could be noted that the PVA fiber up to 0.25% reinforced OPSLWA shows different behavior to plain OPSC. This phenomenon might be attributed to arresting of cracks by PVA fibers which contribute to very large deformations before total uncontrollable collapse. It has been shown that, in contrast to many types of structural lightweight aggregate concretes, plain OPS concrete is a ductile material [40]. In addition, it was found that the addition of steel fiber into OPS concrete increases the strain capacity and improves its ductility performance [8]. However, the main disadvantage of adding steel fibers into OPSLWC is its significant increment in density compared with PVA fibers. Such improvement in the ductility performance of OPS concrete can be observed in

OPS concrete containing PVA. It is clear that by adding PVA to the OPS concrete the strain of the concrete corresponding to the peak stress increases significantly. Increasing in the strain capacity of concrete results in an increase in the area of the stress-strain diagram and energy absorption capacity and also changed the concrete into a more ductile material. The stress-strain relationship for uniaxial compression of OPSC and PVA fiber-reinforced OPSC is shown in Figure 9. It has been reported that the improvement in resistance to cracking due to restrained shrinkage is of the advantages of greater strain capacity of a concrete [41]. Furthermore, it should be noted that the ϵ value of NWC with normal strength is in the range of 0.0015 to 0.002 [42]. Shafiqh et al. had shown that when 0.5 and 1% volume fraction of the steel fiber is added to an OPS concrete, its ϵ value increases about 20 and 35%, respectively [8].

3.4. Splitting Tensile Strength. Fiber-reinforced concrete and polymer concrete have been developed over the years in order to improve the tensile strength of concrete [43]. It has been reported that the addition of fibers provides a significant increase in splitting tensile strength of LWAC and semi-LWAC concrete [43–45]. Figure 10 shows the 28-day splitting tensile strength increases from 2.88 to 3.74 MPa when the fiber content is increased from 0 to 0.5%. The rate of increase for V0.125, V0.25, V0.375, and V0.5 mixes is determined to be 9.4, 11.1, 19.8, and 29.9%, respectively, which indicates a considerable improvement in the splitting tensile strength of the OPS concrete, even in the presence of low fiber content.

It has also been reported that the 28-days splitting tensile strength of OPS concrete under moist curing is within the range of 1.9–2.41 MPa [46, 47], which is approximately 6–10% of the corresponding cube compressive strength. Chen and Liu [24] investigated the effect of three types of fibers on the properties of expanded clay HSLWAC, in which the amount of each type of fibers is 1%. They reported that PP fibers result in a slight reduction in splitting tensile strength of about 2%. In this study, the splitting tensile strength for OPS concrete is determined to be 6.7%, which falls within the range of 6.7–7.7%, of the compressive strength. This shows that the PVA fibers obviously enhance the tensile to compressive strength ratio. Figure 10 shows the relationship between the splitting tensile strength and PVA fiber volume fraction. It is clear that the splitting tensile strength increases with an increase in PVA fiber content. The relationship between the two parameters is found to be parabolic, whereby $F_t = (0.0171)V_f^2 + (0.0991)V_f + 2.798$ and the R^2 value is 0.97. F_t and V_f represent the splitting tensile strength (MPa) and fiber volume fraction (%), respectively. Furthermore, Figure 11 shows a parabolic correlation with a strong correlation ($R^2 = 0.97$) between fiber volume (%) and the splitting tensile strength to compressive strength.

An equation has been proposed to correlate splitting tensile strength of OPSFRC by Yap et al. [9] by incorporating PP and nylon fibers as shown in

$$f_t = 0.52\sqrt{f_{cu}}, \quad (2)$$

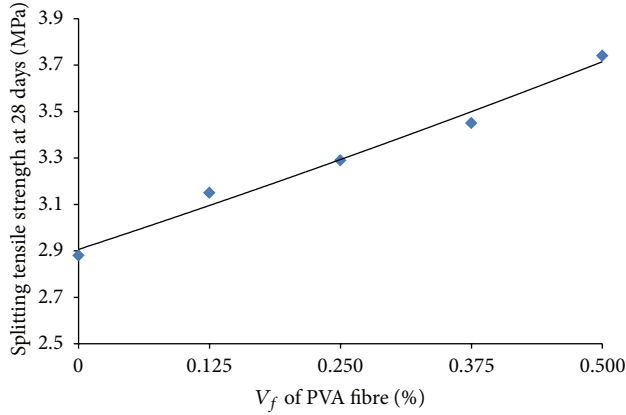


FIGURE 10: Relationship between PVA fiber volume fraction and splitting tensile strength.

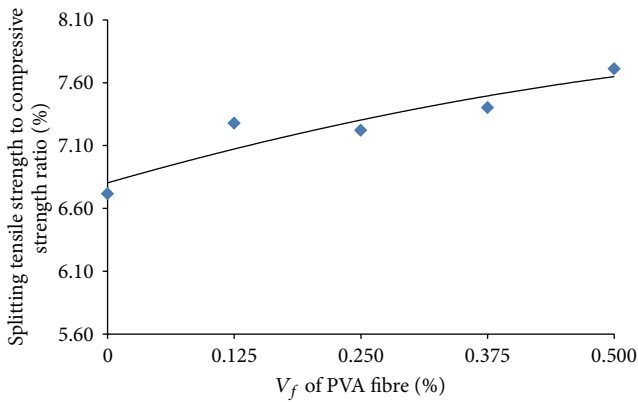


FIGURE 11: Relationship between PVA fiber volume fraction and the splitting tensile strength to compressive strength ratio.

where f_t and f_{cu} represent the splitting tensile and cube compressive strengths in MPa, respectively.

A new equation to correlate splitting tensile strength and compressive strength of OPSFRC is proposed in (3), whereby a higher coefficient of correlation is produced (accuracy = $\pm 10\%$). An accurate prediction of tensile strength of the concrete imperative in mitigating cracking problems minimizes the failure of concrete in tension and increases shear strength prediction as shown below

$$f_t = 0.49 \sqrt{f_{cu}}. \quad (3)$$

3.5. Flexural Strength. The relationship between PVA volume fraction and flexural strength is shown in Figure 12. It can be seen that the 28-day flexural strength increases from 4.17 to 5.49 MPa, ranging from 9.7 to 11.3% of the 28-day compressive strength when the fiber content is increased from 0 to 0.5%. This range is higher than the findings of previous studies which focused on OPS LWAC [46, 48] and expanded clay LWA [49].

In comparison to mix V0, the rate of increase of flexural strength is obtained to be 9, 26, 28, and 32% for V0.125, V0.25, V0.375, and V0.5 mixes, respectively. These rates indicate that

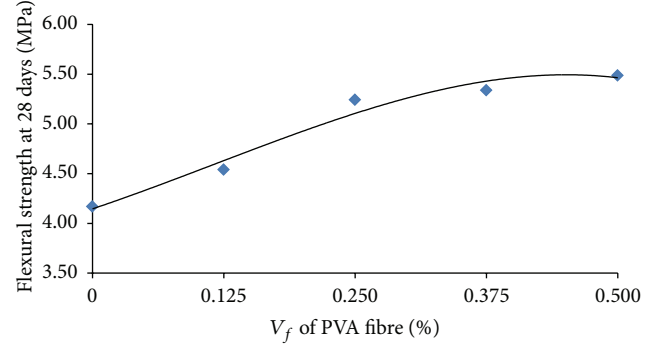


FIGURE 12: Relationship between PVA fiber volume fraction and flexural strength.

an increase in the PVA fiber volume fraction up to 0.25% exhibits a nearly similar effect on the increase in flexural strength (Figure 12). This phenomenon might be attributed to fiber clogging within the 0.25% volume fraction which causes more pores resulting in the similar effect on the increase in flexural strength. However, a significant increase in flexural strength is attained with a higher fiber volume fraction of 0.5% as compared to OPS concrete. Shi et al. [50] discovered that the addition of a small amount of fibers does not influence the flexural strength of lightweight concrete; however, the ductility is significantly improved. They believed that this may be due to the lower tensile strength of PP fibers as well as the weaker bonds between PP fibers and the cement matrix compared to PVA fibers.

A relationship between the flexural strength and cube compressive strength for OPS concrete has been proposed by Alengaram et al. [46], as given by the following equation:

$$f_r = 0.3 \sqrt[3]{f_{cu}^2}. \quad (4)$$

Lo et al. [49] proposed the following equation for LWAC made with expanded clay aggregates:

$$f_r = 0.69 \sqrt{f_{cu}}. \quad (5)$$

Furthermore, the equation for LWAC made with a combination of expanded shale and clay aggregate, for cube strengths, ranging from 20 to 60 MPa [51] is follows:

$$f_r = 0.46 \sqrt[3]{f_{cu}^2}. \quad (6)$$

A new equation has also been proposed to correlate flexural strength to compressive strength of OPSLWAC in this study. Equation (7) is suggested for OPSFRC with different volume fraction of PVA fibers to predict the flexural strength within $\pm 14\%$:

$$f_r = 0.39 \sqrt[3]{f_{cu}^2}, \quad (7)$$

where f_r , f_t , and f_{cu} represent the flexural, splitting tensile, and cube compressive strength, respectively, with units in MPa.

TABLE 6: Measured and estimated flexural strength.

Mix code	28-day compressive strength (MPa)	Measured flexural strength (MPa)	Equation (5) by Alengaram et al. [46]	Estimated flexural strength (MPa)		
				Equation (6) by Lo et al. [49]	Equation (7) by CEB/FIP [51]	Equation (7) in this study
V0	42.89	4.17	3.47	4.33	5.32	4.78
V0.125	43.29	4.54	3.61	4.46	5.54	4.81
V0.250	45.56	5.24	3.63	4.47	5.56	4.97
V0.375	46.62	5.34	3.79	4.62	5.81	5.05
V0.500	48.51	5.49	3.79	4.63	5.82	5.19

Table 6 shows the estimated flexural strength using the four (2)–(5) as given. From the estimated flexural strength values, it can be seen that (7) is generally acceptable to predict the flexural strength of OPS concrete. It can be deduced from the results that the flexural strength of OPS concrete with and without fibers is comparable to artificial LWA with expanded shale and clay aggregates.

3.6. Modulus of Elasticity. In this study, the value of static modulus of elasticity (E) is 15.3, 15.6, 16.3, 16.4, and 16.9 GPa for mixes V0, V0.125, V0.25, V0.375, and V0.5, respectively. These values indicate that the addition of PVA to OPS concrete has a significant effect on the (E) value. This phenomenon might be attributed to the heat treatment on OPS enhancing the dimensional stability and surface quality of OPS which improve the adhesion between the aggregate and the cement matrix. In addition, the MOE of OPSFRC was found to be dependent on the fiber volume. It might be due to the fact the addition of fibers contributed to crack bridging which enhances the MOE of OPSFRC. Yap et al. [9] reported that the combined effect of both silica fume and fibers (PP and nylon) enhanced the MOE of OPSFRC, even higher compared to OPSC with crushed OPS. However, in the present study, the combined effect of both heat-treated crushed *dura* OPS and PVA fibers reduced the strain induced under compression loadings and eventually improved the MOE of OPSFRC significantly compared to previous studies.

In a previous study, the (E) value of OPS concrete with total cementitious materials (cement/fly ash/silica fume) is reported to be 11 GPa, whereas the compressive strength is approximately 38 MPa [35]. The (E) value of mix V0 is roughly 39% higher than this value. The use of *dura* OPS with heat-treated and PVA fibers has a significant effect on the compressive strength due to the enhanced adhesion between the OPS and PVA fibers with the cement matrix. Hence, it can be deduced that it is possible to attain a higher average (E) value of 16.1 GPa for OPSFRC.

It has been reported by CEB/FIP that the (E) value of structural lightweight concrete ranges between 10 and 24 GPa [51]. Swamy and Lambert [52] reported (E) values within the range of 15–22 GPa for LWAC made with pulverized fuel ash (PFA) aggregates. Mehta and Monteiro [53] reported that the (E) value is 10 and 14 GPa for 20 and 40 MPa compressive strength LWC containing expanded clay aggregates, respectively. For normal weight concrete, the (E) values range

from 14 to 41 GPa [54]. Thus, it can be deduced that the (E) value measured for the concrete in this study falls within the range of normal weight and artificial lightweight aggregate concrete.

4. Conclusion

Based on the experimental results of this study, it can be found that the addition of PVA fibers enhanced the mechanical properties of concrete. The workability of fiber-reinforced concrete decreases by increasing the volume fraction of PVA fibers. A maximum reduction of 40% has been determined for OPS concrete with 0.5% PVA fiber content. Furthermore, the addition of PVA fibers with low specific gravity to the OPS mixtures reduces the density of the concrete. However, PVA fibers that contribute to the marginal reduction in density cannot be ignored. The compressive strength of OPS concrete has increased for all ages with an increase in PVA fibers. The effect of PVA on compressive strength of lightweight concrete has been shown more prominent at latter ages due to better fiber/matrix interface adhesion. The 28-day compressive strength of PVA fiber-reinforced OPS concrete is found to be within 43–49 MPa. The addition of PVA fiber up to 0.375% had a positive effect on the compressive strength loss under no curing (AC) condition. Therefore, it can be deduced that PVA fibers can be used to reduce the sensitivity of OPS concrete in poor curing environments. The inclusion of PVA fiber to OPS concrete increases the strain capacity corresponding to peak stress, which causes OPS concrete to become more ductile. The addition of PVA fibers also enhances the splitting tensile and flexural strengths significantly up to 30 and 32%, respectively, compared to the control concrete. The inclusion of PVA fibers into OPS concrete has a significant effect on the modulus of elasticity. The (E) value measured in this study is 16.1 GPa, which is higher compared to previous studies. Hence, it can be concluded that PVA fiber-reinforced OPS LWC showed the possibility and accepted performance for potential application in producing green composite concrete structures.

Conflict of Interests

The authors declare that there is no conflict of interests regarding the publication of this paper.

Acknowledgment

The authors wish to extend their greatest appreciation to the University of Malaya for providing the financial support for this work under the University of Malaya Research Grant (UMRG), Grant no. RP018/2012C.

References

- [1] O. Kayali, M. N. Haque, and B. Zhu, "Some characteristics of high strength fiber reinforced lightweight aggregate concrete," *Cement and Concrete Composites*, vol. 25, no. 2, pp. 207–213, 2003.
- [2] M. H. Zhang, L. Li, and P. Paramasivam, "Flexural toughness and impact resistance of steel-fibre-reinforced lightweight concrete," *Magazine of Concrete Research*, vol. 56, no. 5, pp. 251–262, 2004.
- [3] H. Costa, E. Júlio, and J. Loureno, "New approach for shrinkage prediction of high-strength lightweight aggregate concrete," *Construction and Building Materials*, vol. 35, pp. 84–91, 2012.
- [4] M. K. Yew, H. Mahmud, B. C. Ang, and M. C. Yew, "Effects of oil palm shell coarse aggregate species on high strength lightweight concrete," *The Scientific World Journal*, vol. 2014, Article ID 387647, 12 pages, 2014.
- [5] V. C. Li, "Large volume, high-performance applications of fibers in civil engineering," *Journal of Applied Polymer Science*, vol. 83, no. 3, pp. 660–686, 2001.
- [6] A. R. Khaloo and M. Sharifian, "Experimental investigation of low to high-strength steel fiber reinforced lightweight concrete under pure torsion," *Asian Journal of Civil Engineering*, vol. 6, no. 6, pp. 533–547, 2005.
- [7] B. Chen and J. Liu, "Contribution of hybrid fibers on the properties of the high-strength lightweight concrete having good workability," *Cement and Concrete Research*, vol. 35, no. 5, pp. 913–917, 2005.
- [8] P. Shafigh, H. Mahmud, and M. Z. Jumaat, "Effect of steel fiber on the mechanical properties of oil palm shell lightweight concrete," *Materials and Design*, vol. 32, no. 7, pp. 3926–3932, 2011.
- [9] S. P. Yap, U. J. Alengaram, and M. Z. Jumaat, "Enhancement of mechanical properties in polypropylene- and nylon-fibre reinforced oil palm shell concrete," *Materials & Design*, vol. 49, pp. 1034–1041, 2013.
- [10] R. Polat, R. Demirboğa, M. B. Karakoç, and I. Türkmen, "The influence of lightweight aggregate on the physico-mechanical properties of concrete exposed to freeze-thaw cycles," *Cold Regions Science and Technology*, vol. 60, no. 1, pp. 51–56, 2010.
- [11] A. M. Neville and J. J. Brooks, *Concrete Technology*, Pearson Education Asia Pte, Kuala Lumpur, Malaysia, 2008.
- [12] V. Subramaniam, A. N. Ma, Y. M. Choo, and N. M. N. Sulaiman, "Environmental performance of the milling process of Malaysian palm oil using the life cycle assessment approach," *American Journal of Environmental Sciences*, vol. 4, no. 4, pp. 310–315, 2008.
- [13] D. C. L. Teo, M. A. Mannan, and J. V. Kurian, "Flexural behaviour of reinforced lightweight concrete beams made with oil palm shell (OPS)," *Journal of Advanced Concrete Technology*, vol. 4, no. 3, pp. 459–468, 2006.
- [14] D. C. Okpala, "Palm kernel shell as a lightweight aggregate in concrete," *Building and Environment*, vol. 25, no. 4, pp. 291–296, 1990.
- [15] F. O. Okafor, "Palm kernel shell as a lightweight aggregate for concrete," *Cement and Concrete Research*, vol. 18, no. 6, pp. 901–910, 1988.
- [16] P. Shafigh, M. Z. Jumaat, and H. Mahmud, "Oil palm shell as a lightweight aggregate for production high strength lightweight concrete," *Construction and Building Materials*, vol. 25, no. 4, pp. 1848–1853, 2011.
- [17] J. Newman and P. Owens, *Properties of Lightweight Concrete, Advanced Concrete Technology Set*, Butterworth-Heinemann, Oxford, UK, 2003.
- [18] Z. Li, *Advanced Concrete Technology*, John Wiley & Sons, 2011.
- [19] ASTM C192-90a, "Standard test method of making and curing concrete test specimens in the laboratory," in *Annual Book of ASTM Standards*, 1990.
- [20] M. K. Yew, H. B. Mahmud, B. C. Ang, and M. C. Yew, "Effects of heat treatment on oil palm shell coarse aggregates for high strength lightweight concrete," *Materials and Design*, vol. 54, pp. 702–707, 2014.
- [21] M. K. Yew, I. Othman, M. C. Yew, S. H. Yeo, and H. B. Mahmud, "Strength properties of hybrid nylon-steel and polypropylene-steel fibre-reinforced high strength concrete at low volume fraction," *International Journal of Physical Sciences*, vol. 6, no. 33, pp. 7584–7588, 2011.
- [22] N. A. Memon, S. R. Sumadi, and M. Ramli, "Performance of high workability slag-cement mortar for ferrocement," *Building and Environment*, vol. 42, no. 7, pp. 2710–2717, 2007.
- [23] A. Noushini, K. Vessalas, G. Arabian, and B. Samali, "Drying shrinkage behaviour of fiber reinforced concrete incorporating polyvinyl alcohol fibers and fly ash," *Advances in Civil Engineering*, vol. 2014, Article ID 836173, 10 pages, 2014.
- [24] C. Qian and P. Stroeven, "Fracture properties of concrete reinforced with steel-polypropylene hybrid fibres," *Cement and Concrete Composites*, vol. 22, no. 5, pp. 343–351, 2000.
- [25] E. T. Dawood and M. Ramli, "Flowable high-strength system as repair material," *Structural Concrete*, vol. 11, no. 4, pp. 199–209, 2010.
- [26] G. Lu, K. Wang, and T. J. Rudolph, "Modeling rheological behavior of highly flowable mortar using concepts of particle and fluid mechanics," *Cement and Concrete Composites*, vol. 30, no. 1, pp. 1–12, 2008.
- [27] H. Okamura and M. Ouchi, "Self compacting concrete," *Journal of Advanced Concrete Technology*, vol. 1, pp. 5–15, 2003.
- [28] M. K. Yew and I. Othman, "Mechanical properties of hybrid nylon-steel- and steel-fibre-reinforced high strength concrete at low fibre volume fraction," *Advanced Materials Research*, vol. 168–170, pp. 1704–1707, 2011.
- [29] G. Campione, N. Miraglia, and M. Papia, "Mechanical properties of steel fibre reinforced lightweight concrete with pumice stone or expanded clay aggregates," *Materials and Structures*, vol. 34, no. 238, pp. 201–210, 2001.
- [30] A. Sivakumar, "Influence of hybrid fibers on the post crack performance of high strength concrete: part I experimental investigations," *Journal of Civil Engineering Construction Technology*, vol. 2, no. 7, pp. 147–159, 2011.
- [31] L. Domagala, "Modification of properties of structural lightweight concrete with steel fibres," *Journal of Civil Engineering and Management*, vol. 17, no. 1, pp. 36–44, 2011.
- [32] B. Arisoy and H.-C. Wu, "Material characteristics of high performance lightweight concrete reinforced with PVA," *Construction and Building Materials*, vol. 22, no. 4, pp. 635–645, 2008.

- [33] M. K. Yew, H. Mahmud, B. C. Ang, and M. C. Yew, "Enhancement of mechanical properties in polypropylene twisted bundle fiber-reinforced oil palm shell high-strength lightweight concrete," in *Proceedings of the 8th International Conference on Engineering and Technology Research*, Novotel World Trade Centre, Dubai, UAE, 2014.
- [34] M. A. Mannan, J. Alexander, C. Ganapathy, and D. C. L. Teo, "Quality improvement of oil palm shell (OPS) as coarse aggregate in lightweight concrete," *Building and Environment*, vol. 41, no. 9, pp. 1239–1242, 2006.
- [35] U. J. Alengaram, H. Mahmud, and M. Z. Jumaat, "Enhancement and prediction of modulus of elasticity of palm kernel shell concrete," *Materials and Design*, vol. 32, no. 4, pp. 2143–2148, 2011.
- [36] J. Newman and B. S. Choo, *Advanced Concrete Technology: Testing and Quality*, Butterworth-Heinemann, Oxford, UK, 2003.
- [37] S. Chandra and L. Berntsson, *Lightweight Aggregate Concrete: Science, Technology, and Applications*, Noyes/William A, New York, NY, USA, 2002.
- [38] I. B. Topçu and T. Uygunoğlu, "Effect of aggregate type on properties of hardened self-consolidating lightweight concrete (SCLC)," *Construction and Building Materials*, vol. 24, no. 7, pp. 1286–1295, 2010.
- [39] R. V. Balendran, F. P. Zhou, A. Nadeem, and A. Y. T. Leung, "Influence of steel fibres on strength and ductility of normal and lightweight high strength concrete," *Building and Environment*, vol. 37, no. 12, pp. 1361–1367, 2002.
- [40] P. Shafiq, H. B. Mahmud, and M. Z. Jumaat, "Oil palm shell lightweight concrete as a ductile material," *Materials and Design*, vol. 36, pp. 650–654, 2012.
- [41] A. Turatsinze and M. Garros, "On the modulus of elasticity and strain capacity of self-compacting concrete incorporating rubber aggregates," *Resources, Conservation and Recycling*, vol. 52, no. 10, pp. 1209–1215, 2008.
- [42] H. Akbar, *Design of Reinforced Concrete Structures*, vol. 1, Basic topics, Simay Danesh, Tehran, Iran, 2008.
- [43] Z. Li, *Advanced Concrete Technology*, John Wiley & Sons, New York, NY, USA, 2011.
- [44] P. Balaguru and A. Foden, "Properties of fiber reinforced structural lightweight concrete," *ACI Structural Journal*, vol. 93, no. 1, pp. 62–78, 1996.
- [45] P. Balaguru and M. G. Dipsia, "Properties of fiber reinforced high-strength semilightweight concrete," *ACI Materials Journal*, vol. 90, no. 5, pp. 399–405, 1993.
- [46] U. J. Alengaram, M. Z. Jumaat, and H. Mahmud, "Influence of sand content and silica fume on mechanical properties of palm kernel shell concrete," in *Proceedings of the International Conference on Construction and Building Technology (ICCBT '08)*, pp. 251–262, 2008.
- [47] M. A. Mannan and C. Ganapathy, "Engineering properties of concrete with oil palm shell as coarse aggregate," *Construction and Building Materials*, vol. 16, no. 1, pp. 29–34, 2002.
- [48] U. J. Alengaram, M. Z. Jumaat, and H. Mahmud, "Ductility behaviour of reinforced palm kernel shell concrete beams," *European Journal of Scientific Research*, vol. 23, no. 3, pp. 406–420, 2008.
- [49] T. Y. Lo, H. Z. Cui, and Z. G. Li, "Influence of aggregate pre-wetting and fly ash on mechanical properties of lightweight concrete," *Waste Management*, vol. 24, no. 4, pp. 333–338, 2004.
- [50] C. Shi, Y. Wu, and M. Riefler, "Properties of fiber-reinforced lightweight concrete," *ACI Special Publication*, vol. 226, pp. 123–134, 2005.
- [51] *CEB/FIP Manual of Design and Technology*, Lightweight Aggregate Concrete, 1997.
- [52] R. N. Swamy and G. H. Lambert, "Mix design and properties of concrete made from PFA coarse aggregates and sand," *International Journal of Cement Composites and Lightweight Concrete*, vol. 5, no. 4, pp. 263–275, 1983.
- [53] P. K. Mehta and P. J. M. Monteiro, *Concrete: Microstructure, Properties, and Materials*, McGraw-Hill, New York, NY, USA, 3rd edition, 2006.
- [54] H. Mazaheripour, S. Ghanbarpour, S. H. Mirmoradi, and I. Hosseinpour, "The effect of polypropylene fibers on the properties of fresh and hardened lightweight self-compacting concrete," *Construction and Building Materials*, vol. 25, no. 1, pp. 351–358, 2011.

Research Article

Influence of Molarity and Chemical Composition on the Development of Compressive Strength in POFA Based Geopolymer Mortar

S. M. Alamgir Kabir, U. Johnson Alengaram, Mohd Zamin Jumaat, Afia Sharmin, and Azizul Islam

Department of Civil Engineering, Faculty of Engineering, University of Malaya, 50603 Kuala Lumpur, Malaysia

Correspondence should be addressed to U. Johnson Alengaram; ujohnrose@yahoo.com

Received 23 September 2014; Revised 3 January 2015; Accepted 8 January 2015

Academic Editor: Hao Wang

Copyright © 2015 S. M. Alamgir Kabir et al. This is an open access article distributed under the Creative Commons Attribution License, which permits unrestricted use, distribution, and reproduction in any medium, provided the original work is properly cited.

The investigation concerns the use of the optimum mix proportion of two locally available pozzolanic waste materials, namely, ground granulated blast furnace slag (GGBS) and palm oil fuel ash (POFA), together with metakaolin (MK) as binders. In addition, another local waste material, manufactured sand (M-sand), was used as a replacement for conventional sand in the development of green geopolymer mortar. Twenty-four mortar mixtures were designed with varying binder contents and alkaline activators. The oven dry curing was also kept consistent for all the mix proportions at a temperature of 65°C for 24 hours. The highest 28-day compressive strength of about 48 MPa was obtained for the mortar containing 20% of MK, 35% of GGBS, and 45% of POFA. The increment of MK beyond 20% leads to reduction of the compressive strength. The GGBS replacement beyond 35% also reduced the compressive strength. The entire specimen achieved average 80% of the 28-day strength at the age of 3 days. The density decreased with the increase of POFA percentage. The finding of this research by using the combination of MK, GGBS, and POFA as binders to wholly replace conventional ordinary Portland cement would lead to alternate eco-friendly geopolymer matrix.

1. Introduction

The utilization of waste materials or industrial by-products, such as fly ash (FA), metakaolin (MK), silica fume (SF), ground granulated blast furnace slag (GGBS), rich husk ash (RHA), and palm oil fuel ash (POFA), as binders in the development of geopolymer concrete is gaining momentum [1–3] due to the overuse of virgin materials in the production of ordinary Portland cement (OPC). The use of OPC has resulted in a high volume of carbon dioxide (CO₂) emissions, as the construction industries cannot replace the use of OPC entirely with the other cementitious materials due to the huge demand for concrete. The extraction of natural deposits in the production of cement and concrete has led to an ecological imbalance due to the continuous depletion of natural resources. The present annual consumption of 2.9 billion tons of cement globally could increase to 4 billion

tons by 2020 [4]. The estimated value of CO₂ emission in the production of 1 ton OPC is about 0.6 tons [5]. The cement industry is responsible for approximately 5% of global CO₂ emissions and it is likely to reach 6% annually by 2015 [6].

The ratio of clinker to cement is the main fact upon which the CO₂ emissions per ton of cement depend. Normally this ratio varies from 0.5 to 0.95 [7]. The CaO share in clinker amounts to 64–67%. The rest consists of silicon oxides, iron oxides, and aluminium oxides. On the other hand, the production of industrial by-products and other waste materials, such as FA, GGBS, RHA, SF, POFA, and MK, continues to rise and the waste disposal of these materials in an environmentally friendly manner is becoming a challenge. The use of these waste materials in the production of concrete could reduce the greenhouse gas emissions [8]. Geopolymers are usually reported to be much more sustainable than Portland cement, in terms of reduced production energy

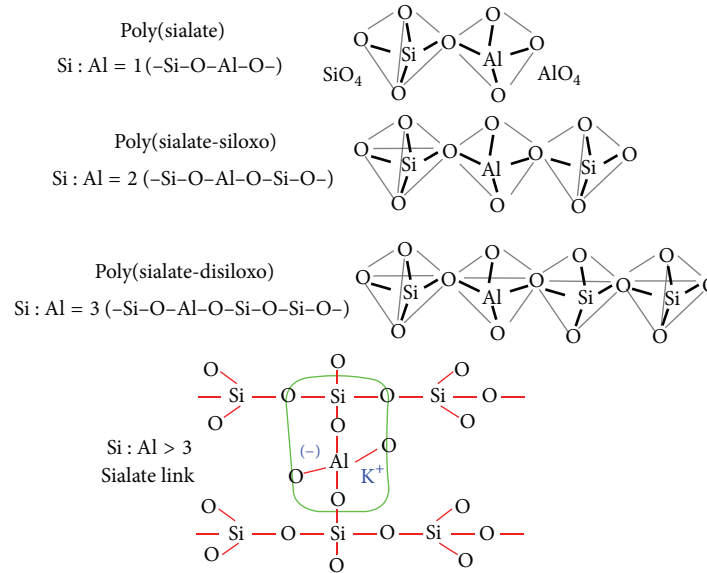


FIGURE 1: Geopolymer terminology [11].

necessity, lower CO₂ emissions comparing with the OPC concrete; Turner and Collins (2013) [9] have pointed out only 9% less CO₂ emission from geopolymer concrete production considering curing as well as FA, sodium silicate, and sodium hydroxide production. The emission of CO₂ from geopolymer concrete may control considering emissions during curing as well as production of FA, sodium silicate, and sodium hydroxide. Geopolymers are a class of synthetic alkali-activated alumina silicate inorganic polymers (AIPs) featuring a predominantly X-ray amorphous three-dimensional network [10]. Glukhovskiy carried out the maiden work on alkali-activated alumina silicate materials in the 1950s, which consisted of mixed alkalis with a burnt mixture of kaolinite, limestone, and dolomite. Later, binders other than cement could be produced by the reaction between alkaline solution and source materials that are rich in silica (SiO₂) and alumina (Al₂O₃). Davidovits was the pioneer in introducing the term known as geopolymer and [11] further categorized the geopolymer structure based on the ratio of Si/Al (Figure 1).

Duxson et al. [12] proposed another model for the mechanism of geopolymerisation (Figure 2), which consisted of (a) dissolution, (b) speciation equilibrium, (c) gelation, (d) reorganization, and (e) polymerization and hardening. The type of alkaline activator plays an important role in the geopolymerisation process and has a significant effect on the mechanical strength of the geopolymer.

Provis and van Deventer (2009) pointed out the reality of the geopolymer gel structure and the Davidovits sialate nomenclature implies certain aspects of the geopolymer gel structure which do not correspond to reality [14]. Provis (2014) has recently presented latest definition of the geopolymer structure. Provis [15] reported that geopolymers are produced through the reaction of an aluminosilicate, normally supplied in powder form as an industrial by-product or other inexpensive material, with an alkaline activator, which is

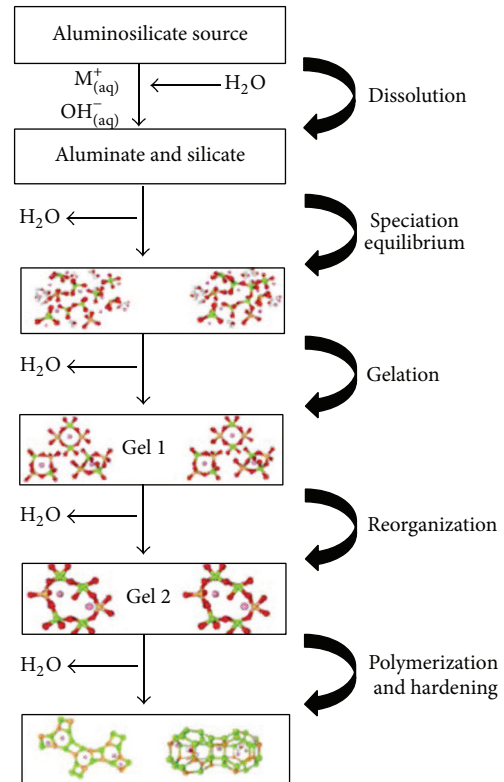


FIGURE 2: Geopolymerisation-conceptual model [12].

usually a concentrated aqueous solution of alkali hydroxide, silicate, carbonate, or sulfate.

The commonly used alkaline activators in current times are combinations of sodium hydroxide solution (NaOH)

and sodium silicate solution (Na_2SiO_3) with different $\text{Na}_2\text{SiO}_3/\text{NaOH}$ mass ratios [16]. Geopolymers can be progressed through a series of several distinct reaction processes from initial pozzolanic activation to final microstructure development, which is very similar to zeolites. The rate of strength development and the chemical reaction of geopolymer concrete are influenced by several factors based on the chemical composition of the source materials, alkaline activators, and curing conditions [17].

Due to the pure alumina silicate content of metakaolin (MK), it was used in the early development of geopolymers and has continued to be used as a raw material. MK is obtained by the calcination of kaolinitic clay at a temperature ranging between 500°C and 800°C , and, of course, it is a pozzolanic material. The comparison between OPC and MK shows that the latter is environmentally friendly as its production requires a much lower calcining temperature and emits 80–90% less CO_2 than the former [18]. MK is a good source of Al_2O_3 and SiO_2 and is highly reactive with alkaline activators and produces a higher degree of geopolymerization. MK is a better material for geopolymers because it has a higher amorphous phase content and smaller sized particles, the compressive strength of MK-based geopolymers increases with an increase of alumina content by up to 20% [19]. Islam et al. [13] reported that with the increase of GGBS content in the matrix containing FA and POFA the compressive strength of geopolymer mortar could be increased. The addition of calcium from other sources in geopolymer based on metakaolin improved its mechanical strength [20]. Depolymerised siliceous structures with raw materials, such as GGBS, exhibit higher dissolution rates under high alkalinity conditions compared with raw materials composed of laminar structures such as MK. Therefore, blending these components can contribute to an improvement in the stability of the system, and, potentially, also to the durability, when compared to the binders prepared from a single raw material.

Malaysia is one of the largest producers of POFA. There are nearly 200 palm oil mills operating in Malaysia, which produce about 100 tons of POFA annually. In addition, although due to the increased plantation of palm oil trees this production rate is likely to increase [21], this material has no market value and is simply dumped into ponds/lagoons [22], which causes environmental pollution. However, recent research [23, 24] has paved the way for the development of sustainable material using POFA and related waste materials from the palm oil industry. Such development has become more significant as a number of studies have identified it as being rich in silica. Alengaram et al. [23] reported that the compressive strength of concrete can improve with the increase in sand content coupled with a reduction in OPS content. POFA is a cementitious material that could be used with recycled aggregate concrete that could result in a higher compressive strength than that of recycled aggregate concrete without POFA [25].

For centuries, river or mining sand was used as fine aggregate even though river sand is a nonrenewable natural resource. The exploitation of river sand endangers the stability of riverbanks and creates environmental problems, such

as flooding and the reduction of ground water level. Thus, the urgency to find an alternate to natural sand is vital. Cai [26] suggested the use of alternative materials for river sand, such as manufactured sand (M-sand), industrial by-products (some forms of slag, bottom ash), and recycled aggregates. Among these, the use of manufactured sand is gaining momentum [26]. M-sand, which is a by-product of quarry dust (QD), is obtained by centrifuging it using a technology known as the vertical shaft impact (VSI). QD, which is the by-product of rock crushing, contains angular and flaky edged particles. Hence, the process of VSI technology produces particle sizes with greater integrity and a more isometric shape. M-sand fines contribute to an increase in paste volume [27] and the shape and texture of M-sand lead to improved strength due to better interlocking between the particles.

During the last two decades, there have been a number of researchers who focused their efforts to utilize geopolymer concrete due to the wide range of potential applications [8, 9, 15]. The effect of single and binary combination of binders among MK, GGBS, and POFA has been reported by previous researchers [28–30]. Islam et al. [13] reported the highest compressive strength of about 66 MPa by using 70% GGBS with 30% POFA. However, the use of large amount of GGBS leads to workability and setting time problems. Sahana [31] reported that the inclusion of GGBS at different replacement levels below 40% increases the setting time of mortar, but beyond this level, the setting time decreases and this could lead to loss of workability and casting of concrete; Deb et al. [32] described that the workability decreased with the high content of GGBS due to accelerated reaction of the calcium and the angular shape of GGBS. Islam et al. [13] also used 12-molarity sodium hydroxide solution to obtain the maximum compressive strength; however the effect of higher molarity was not investigated.

Thus these research questions, such as the loss of workability and early setting due to high GGBS content, have to be addressed. In order to address this issue, an attempt has been made through this research work to minimize the use of GGBS content within 20–45%; and at the same time to ensure the required compressive strength, POFA and MK were used along with GGBS. Therefore, the research focus of this work is to utilize ternary binders and at the same time to optimize the local waste material, POFA as binder. Utilization of 45% of POFA along with 35% and 20% of GGBS and MK, respectively, was experimented and the main flaw of low workability was investigated. The use of hydroxide solution with 12 and 14 molarities on the compressive strength was also carried out.

The variables investigated in the research are different percentages of binder, sand, and two molarities of alkali activators to obtain maximum compressive strength. In this study M-sand was used as fine aggregate for the replacement of conventional mining sand. The other parameters, such as M-sand and water contents, were kept constant. The flow ability, oven dry density, and compressive strength at different ages of cube specimens were tested and reported in this investigation. A total of 24 mixes were prepared to obtain the optimum mix that could be used for further works.

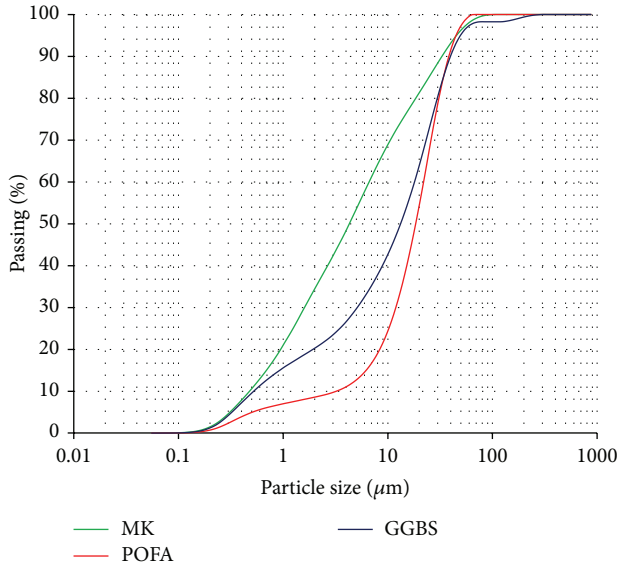


FIGURE 3: MK, GGBS, and POFA's particle size distribution (log scale).

2. Experimental Programme

2.1. Materials

2.1.1. Metakaolin. Metakaolin (MK) is an industrial by-product material, it has significant potential in the development of concrete composites, and it is a highly reactive pozzolanic admixture. MK is manufactured from a natural geological mineral that often contains impurities and inconsistent Si:Al atomic ratios. The chemical composition of MK and the physical properties are given in Tables 1 and 2, respectively. It can be seen from the chemical composition that MK contains 90% silica and alumina. The physical properties show that MK has a specific gravity and specific surface area of 2.5 and 2.16 m²/gm, respectively. The particle size distribution of MK is shown in Figure 3, which shows that MK is much finer than GGBS or POFA.

2.1.2. Ground Granulated Blast Furnace Slag. Ground granulated blast furnace slag (GGBS) was used as one of the source materials to produce a cementless binder. GGBS was collected from YTL Cement Marketing Sdn Bhd, Malaysia. GGBS has both cementitious and pozzolanic properties and is different from other supplementary cementitious materials. GGBS develops its own hydraulic reaction when mixed with water. GGBS is off-white in colour. The combination of calcium, silicates, and alumina comprising about 90% of GGBS shows that it satisfies the requirements of a pozzolanic material. Table 1 shows the chemical composition of GGBS, and its physical properties are given in Table 2. The specific gravity is 2.89 g/cm³ and specific surface area is 2.36 m²/gm. The particle size distribution of GGBS is shown in Figure 3.

2.1.3. Palm Oil Fuel Ash. Palm oil fuel ash (POFA) is a waste material; it is obtained from palm oil mill boilers by

TABLE 1: The raw materials (MK, GGBS, and POFA) chemical composition (wt %).

Chemical composition	MK	GGBS	POFA
CaO	0.04	45.83	4.34
SiO ₂	52.68	32.52	63.41
Al ₂ O ₃	42.42	13.7	5.55
MgO	0.12	3.27	3.74
Na ₂ O	0.07	0.25	0.16
SO ₃	0.05	1.8	0.91
P ₂ O ₅	0.4	0.04	3.78
K ₂ O	0.34	0.48	6.33
TiO ₂	1.46	0.73	0.33
MnO	0.08	0.35	0.17
Fe ₂ O ₃	2.01	0.76	4.19
SrO	0.03	0.08	0.02
Cl	—	0.02	0.45
CuO	—	—	6.54
LOI	—	0.6	6.2

TABLE 2: Materials physical properties.

Properties	Materials			
	MK	GGBS	POFA	M-sand
Specific gravity	2.5	2.89	2.2	2.78
Specific surface area (m ² /gm)	2.16	2.36	1.65	—
Colour	Off-white	Off-white	Dark	—

the burning of palm oil husk and shell as fuel. However, this ash has pozzolanic properties that play an active role in making strong and durable concrete by the replacement of cement. Raw POFA was collected from the local palm oil industry, Malaysia. The incompletely combusted fibres and kernel shells were separated by using a 300 μm sieve. Before that, they were dried in an oven for at least 24 h at 100°C to remove the moisture. The POFA was then ground in a ball mill to obtain particle sizes of about 10 μm. Forty mild steel rods of 10 mm diameter and 400 mm length were placed in the rotating drum to grind approximately 10 kg of POFA one time before being sieved through 300 μm. To obtain the desired level of fineness (>66%), the grinding of POFA was carried out for 30,000 cycles over 16 h. The mass of natural pozzolan passing a 45 μm wet sieve should be at least 86% based on ASTM: C618-12a. The POFA was greyish in colour. The physical properties of POFA are shown in Table 2. Its particle size distribution is shown in Figure 3. The fineness of POFA was found to be 88.7%. Table 1 shows the chemical analysis of POFA. The chemical analysis suggests that, in general, this POFA satisfies the requirement to be considered pozzolanic and may be grouped between Class C and Class F pozzolana, as specified in ASTM C618-92a.1. Figure 4 shows the palm fruits and the raw POFA in factory.



FIGURE 4: Palm fruits (left) and raw palm oil fuel ash (right).

2.1.4. Manufactured Sand (M-Sand). M-sand was collected from the local industry in Malaysia. The shape and texture of M-sand particles could lead to improvements in the strength of concrete due to better interlocking between particles. The physical properties of M-sand are shown in Table 2. The fine aggregate is separated into three grades based on the percentage passing through standard sieves according to BS 882-1992. M-sand falls into the category of grade C sand. The packing ability of M-sand's finer particles enables the mortar to achieve higher packing density, which could enhance the durability of the concrete. Figure 6 shows that the M-sand has a wide range of particles (metakaolin (MK), palm oil fuel ash (POFA), ground granulated blast furnace slag (GGBS), and manufactured sand (M-sand) are shown in Figure 5).

2.1.5. Alkaline Activators. Sodium hydroxide, silicate, carbonate, and sulphate are the commonly used activators and one of the most common and effective activators are sodium silicate. For the development of geopolymerisation in geopolymer materials, the main contribution of silicate ions is through alkali activation. An activator's efficiency depends on certain factors, such as the type of activator, dosage, ambient temperature, and water to FA (W/FA) ratio. The NaOH was of commercial grade in pellet form (5 mm), with a specific gravity of 2.13 and 97% purity. Na_2SiO_3 in liquid form with a density of about 1.5 gm/mL at 20°C, a modulus ratio of 2.5 ($\text{SiO}_2/\text{Na}_2\text{O}$, $\text{SiO}_2 = 30\%$ and $\text{Na}_2\text{O} = 12\%$, water = 57% by mass), and specific gravity of 1.5 was used along with NaOH as an alkali activator according to [33]. Two different molarities (namely, 12 M and 14 M) were used by using sodium hydroxide solution to obtain the optimum strength. For instance, NaOH solution with a concentration of 12 M consists of $12 \times 40 = 480$ g of NaOH solids per litre of the solution, where 40 is the molecular weight of NaOH. The mass of NaOH solids was measured as 361 g per kg of NaOH solution of 12 M concentration [34]. The reaction was exothermic, so the solution was made to cool down before use. The ratio of $\text{Na}_2\text{SiO}_3\text{aq}/\text{NaOH}$ was kept constant at 2.5 for all the mixtures.

2.1.6. Water. Potable water with a pH value of 6 and free from impurities and chemical contaminants was used in all

the mixes. The water to binder ratio of 0.25 was used for all the mixes.

2.2. Specimen Preparation and Curing

2.2.1. Mixing Procedure and Casting. A total of 24 mixes were prepared. The mix proportions of all the concrete mixes are shown in Tables 3 and 7. By varying the MK, POFA, GGBS, and activator contents, the mixtures were prepared. To investigate the effect of the binders, the M-sand and water contents were kept constant. The ratio of binder to sand content was kept at 1:2 in all the mixes. In order to mix the ternary binders of MK, POFA, and GGBS along with sand, these materials were mixed in dry condition in a bowl mixer at a low rate of speed for about 5 min. The alkali activator solution was then slowly added into the mix for another 5 min and the mode of speed was then changed from slow to high. Then, additional water was added to the mix to increase the workability and homogeneity of the mortar. The mortar was then cast in 50 mm cube moulds and poured in three phases with appropriate compaction. A total of 12 specimens were cast for each mix proportion. To remove the entrained air and bubbles the samples were vibrated with standard compaction using a rod and vibrating table. A comparison between Islam et al. [13] and the present research work on mixing and casting time shows that the former required finishing the casting within 7 min, while the duration could be extended to 10 min in the present research. Another salient point in the comparison is the total binder content; the present research has total binder content of about 760 kg/m^3 compared to 460 kg/m^3 used by Islam et al. [13]. Thus, the use of such high volume of binder with large quantity of GGBS would have reduced the setting time drastically [31]. Hence, the proposed mixing time with different speed of mixer is crucial in balancing the mix and workability.

2.2.2. Curing Regime. Immediately after casting, the specimens along with the moulds were covered using plastic film to reduce water loss during curing in an oven for 24 h at 65°C. Subsequently, the specimens were taken out of the oven and kept at ambient condition with an average temperature and humidity of 28°C and 70%, respectively,



FIGURE 5: (a) Metakaolin (MK), (b) palm oil fuel ash (POFA), (c) ground granulated blast furnace slag (GGBS), and (d) manufactured sand (M-sand).

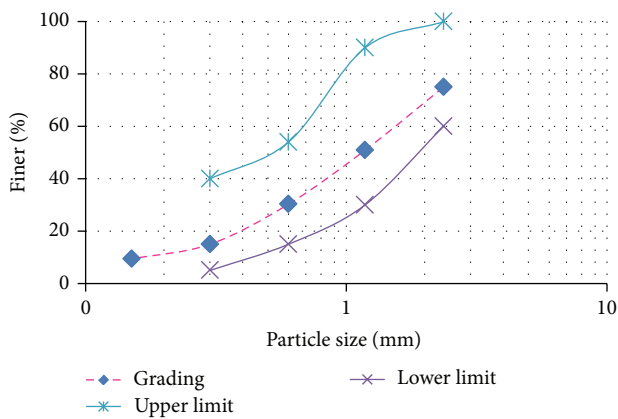


FIGURE 6: The particle size distribution of M-sand [13].

until testing day. This procedure was adopted from the method suggested by Hardjito and Rangan [34]. To gain high early strength geopolymers with acceptable physical and mechanical properties, the optimum geopolymer oven curing temperature was between 60°C and 65°C [35]. Therefore,

the selection of 65°C was justified as the 50 mm cubes have high surface to volume ratio and are more susceptible to curing heat and to moisture loss.

2.2.3. *Compressive Strength.* The compressive strength test was done using an ELE Auto Compressive Testing Machine in accordance with ASTM: C109/C109M-13. The compressive strength of the specimens was tested after 3, 7, 14, and 28 days. Each day's compressive strength value was determined as the average of three specimens. The compressive strength of the specimen was determined by dividing the maximum load carried by the specimen during the test by the average cross-sectional area. The failure mode of the specimens is shown in Figure 7(a) and that was found satisfactory as specified in BS EN 12390-3:2002 (Figure 7(b)). Compressive strength = Failure load/Cross-sectional area.

2.2.4. *Flow Test.* The flow test was done according to the ASTM C230 standard [36]. The used apparatus comprised a flow table, flow mould, tamper, trowel, and measuring tape. The flow test can give an indication as to the consistency, filling ability, and workability of the mortar.

TABLE 3: Mix design for development of compressive strength of geopolymer mortar.

Mortar designation	Mix proportion (%) MK/GGBS/POFA	MK content (kg/m ³)	GGBS content (kg/m ³)	POFA content (kg/m ³)	Compressive strength (MPa)	
					3-day	28-day
M1	5/35/60	38.3	268.3	460	18.88	23.5
M2	10/30/1960	76.7	230	460	33.89	39.2
M3	10/35/55	76.7	268.3	421.7	21.91	30.34
M4	10/45/45	76.7	345	345	36.59	40.85
M5	15/20/65	115	153.3	498.3	31.01	38.57
M6	15/35/50	115	268.3	383.3	22.14	32.47
M7	15/40/45	115	306.7	345	35.51	40.24
M8	20/20/60	153.3	153.3	460	25.18	33.65
M9	20/25/55	153.3	191.7	421.7	37.15	41.05
M10	20/28/52	153.3	214.7	398.7	32.92	37.78
M11	20/30/50	153.3	230	383.3	36.46	42.19
M12	20/35/45	153.3	268.3	345	43.2	48
M13	20/40/40	153.3	306.7	306.7	34.93	41.62
M14	20/45/35	153.3	345	268.3	33.85	40.92
M15	25/30/45	191.7	230	345	35.86	41.43
M16	25/35/40	191.7	268.3	306.7	33.45	37.23
M17	30/40/30	230	306.7	230	33.5	39.6
M18	30/35/35	230	268.3	268.3	32.95	40.73

Note: MK: metakaolin; GGBS: ground granulated blast furnace slag; POFA: palm oil fuel ash.



FIGURE 7: (a) Failure mode of cubes. (b) Satisfactory failures of BSEN 12390-3:2002.

3. Results and Discussion

3.1. Flow. The flow of mortar is shown in Figure 8, while the flow values are shown in Table 4. A lower flow ability of the mortar was observed for mix M5, which could be due to the higher percentage of POFA. POFA decreases the flow tendency because of the porous and spongy nature of the microstructure (Figure 9) [2] of these materials and an increased fineness or surface area. Figure 11 and Table 4 show that the flow percentage increased in mixes M16, M17, and M18, which could be attributed to a decrease in the percentage of POFA (Table 3) in the mortars. It is also observed in Figure 11 that the flow percentage increased with the increase in the MK percentage in the mortars because MK has a much finer particle size than POFA and GGBS and requires less water to obtain a flow [37]. Workability in geopolymer depends on the viscous properties of the binder matrix. Si plays major role in producing viscosity [13]. The percentage of SiO₂ is not so much different between mixes M1 and M18; that

is why the flow has no significant differences between each of the mixtures.

3.2. Oven Dry Density (ODD). The oven dry density (ODD) was taken for all specimens after oven-drying at a temperature of 65°C for a period of 24-h. Figure 10 and Table 4 show the 3-day oven dry density (ODD) of the specimens with different replacement levels of MK, GGBS, and POFA. The ODD of the mortar varied between 1639 kg/m³ and 2181 kg/m³. The spherical particles of all the materials, compared to the crushed particles in a wet state, could produce a higher packing density, resulting in lower water retention in the spherical case, and, consequently, lower water demand [38]. Thus, the use of a high percentage of GGBS with spherical particles produced the highest ODD of 2181 kg/m³ among all the mixes. The POFA, due to its agglomerated and crushed shape and increasing interparticle friction particles, cannot easily roll over one another. Therefore, this highlights

TABLE 4: Flow of mortar and 3-day average oven dry density (ODD) (kg/m^3) of mortar for all mixes.

	Mix number																	
	M1	M2	M3	M4	M5	M6	M7	M8	M9	M10	M11	M12	M13	M14	M15	M16	M17	M18
Flow (%)	61	62	64	67	60	67	67	68	69	72	71	72	70	73	75	76	79	78
Density (kg/m^3)	1874	1789	1870	2115	1639	1896	2007	1691	1739	1756	1821	1914	2067	2181	1833	1943	2089	1961



FIGURE 8: Flow of mortar.

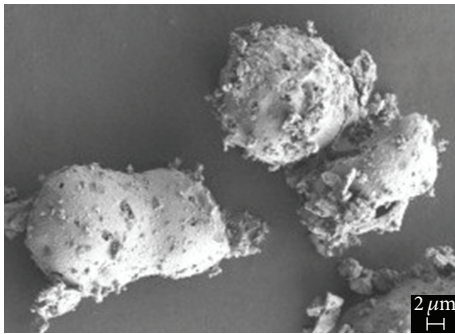


FIGURE 9: Field emission scanning electron microscopy (FESEM) images of POFA [2].

the need for more evaporable water in mixes with high POFA content in order to obtain a workable mix. Hence, the use of a higher dosage of POFA decreases the specimen density [2]. The use of 65% of POFA in mix 5 shows the lowest ODD of 1639 kg/m^3 . Another factor that influences the density is the ability of finer particles to fill the voids within the mortar. Figure 3 shows that POFA has relatively coarser particles within a narrow range compared to that of GGBS and MK. Thus, a high percentage of GGBS (mix 14) with finer particles enhances its density by about 25% compared to mortar with a high percentage of POFA (mix 5). Khatib and Wild [39] reported that the threshold value for pastes decreased with the increase in MK content. The ODD of the mortar decreased slightly by about 2.2% in the first few weeks but remained almost constant thereafter. Figure 11 shows the reduction in density for all mixes (mix 14).

3.3. *Compressive Strength Development.* The development of the compressive strength of hardened geopolymer mortar

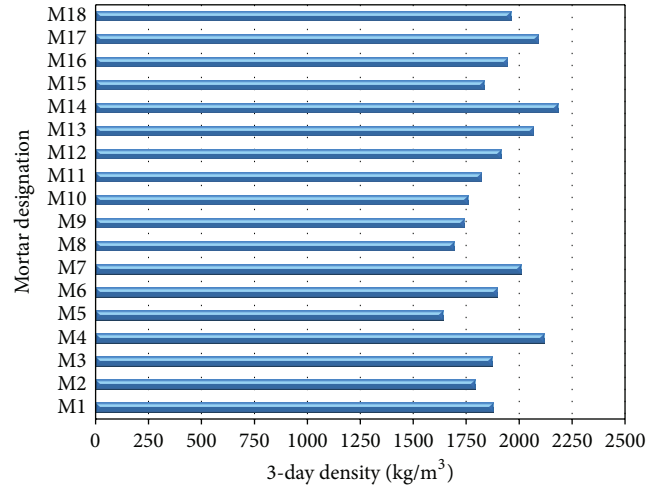


FIGURE 10: 3-day average density (kg/m^3) for all mixes.

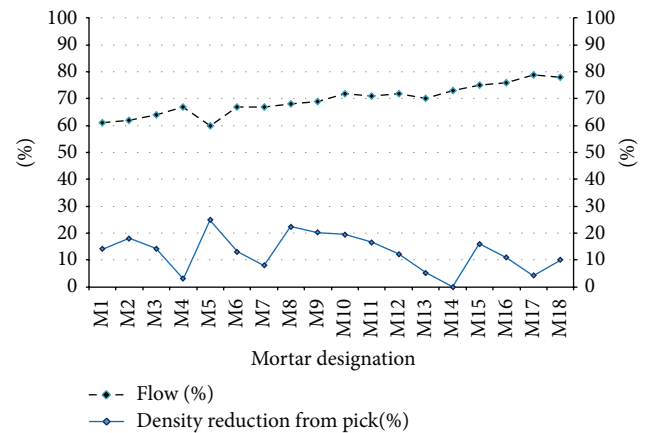


FIGURE 11: Density (kg/m^3) reduction for all mixes from the peak of density and the percentage of flow of mortar.

is the basic indicator of the performance of alternative source materials, since it provides a fundamental description concerning the quality of geopolymerization products. The development of compressive strength at the ages of 3, 7, 14, and 28 days is shown in Figure 12. As indicated in the methodology, the specimens were cured at 65°C for 24-h. Curing at an elevated temperature allows a reduction in the time of heat treatment to achieve high strength [40]. It can be observed from Figure 12 that mix M1, which contained 5% MK, 35% GGBS, and 60% POFA and was cured at 65°C for 24-h, produced the lowest compressive strength. However, an increase in the MK from 5% to 10% and

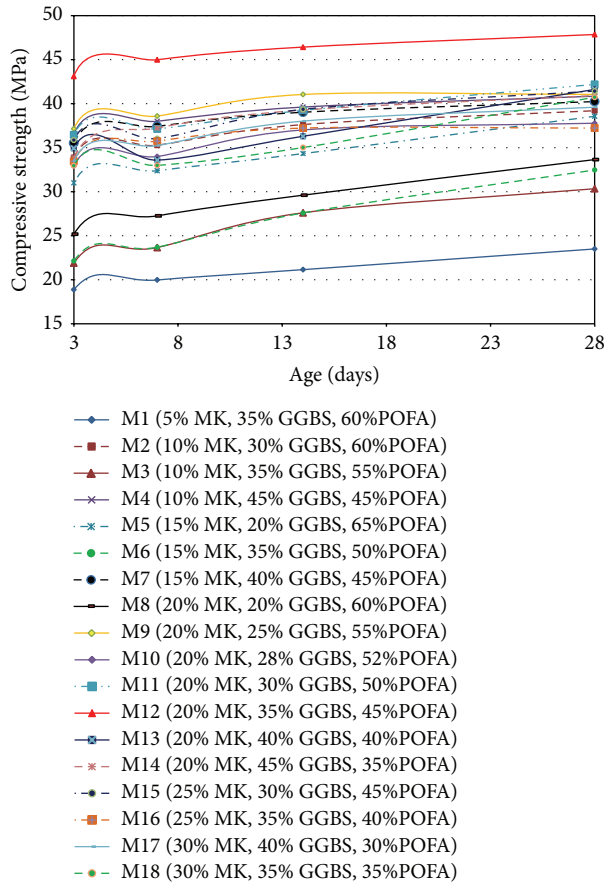


FIGURE 12: Compressive strength development of mortar at different ages with varying binder content ratios.

subsequent decrease in POFA in mix M3 showed an increase in the compressive strength. It can be seen that this trend continued until the MK was increased to 20%. It was observed that with up to 20% replacement of MK by POFA the highest compressive strength of about 48 MPa could be obtained. With any further increase in the MK content beyond 20%, the strength decreased, as seen from the mixes M16 and M18, which had 25% and 30% of MK, respectively. A similar trend was observed for mixes with an increase in both the GGBS and POFA contents. Thus, it can be concluded that mix M12 with 20% MK, 35% GGBS, and 45% POFA with high SiO₂ and Al₂O₃ contents produced the highest compressive strength. It is evident that POFA contained fewer amounts of Al₂O₃ and Ca, when mixed with GGBS, which enhanced the compressive strength. From the results, it is also observed that up to 45% of the binders could be replaced by POFA to achieve a compressive strength of 48 MPa. However, an increase of POFA beyond 45% had a negative effect on the compressive strength. Thus, the amount of Ca and Al₂O₃ had a significant influence on the compressive strength of the mortar [41]. From Figure 12, it can also be seen that the compressive strength curve is steep at the age of 3 days with a slight drop at 7 days, which may be because the Si/Al ratio varies during the geopolymerization process [42]. Table 5

TABLE 5: The percentage (%) increase in the compressive strength at 3, 7, and 14 days compared with the 28-day strength.

Mortar designation	Increase of compressive strength (%)		
	3-day (%)	7-day (%)	14-day (%)
M1	80	85	90
M2	87	90	96
M3	72	78	91
M4	90	93	97
M5	80	84	89
M6	68	73	85
M7	88	93	97
M8	75	81	88
M9	91	94	100
M10	87	90	98
M11	86	88	93
M12	90	94	97
M13	84	87	94
M14	83	91	96
M15	87	87	95
M16	90	96	100
M17	85	89	96
M18	81	81	86

shows the increase in the compressive strength at 3, 7, and 14 days compared to 28 days expressed as a percentage. It can be seen from a comparison of the 3-day test results with the 28-day strength that most of the specimens achieved about 80% of the 28-day strength. Correspondingly, the 7-day and 14-day strengths were 87% and 94%, respectively, of the 28-day strength (Figure 15).

3.4. Analysis of Chemical Composition on the Development of Strength. The parameters, such as curing temperature, water content, alkali concentration, initial solids content, silicate and aluminate ratio, pH, and the type of activators used, influence the rate of polymerization [13]. The comparison of the major oxide composition of the three materials, that is, MK, GGBS, and POFA, is shown in Table 6. As explained in Section 3.3, the mixes M1 and M12 produced the lowest and the highest compressive strengths, respectively. It can be seen from Table that the SiO₂ content was found to be higher in mix M12 compared to the other mixes, for which the ratio of Si/Al for mix M12 was 3.26. In contrast, the Si/Al ratio for M1 was found to be 5.12. The initial Si/Al ratio will not be constant all the way through the geopolymerization process. During different stages of geopolymerization the Si/Al ratio increases [42]. The trend of compressive strength development is affected by the change in the Si/Al ratio in the original particles, the reactive ones, and the reacted product during the reaction process [43]. Geopolymerization was almost complete after 7 days and that the strength gain beyond this period was found to be insignificant. Lime (CaO) plays a very important role as it controls the strength and soundness, whereas excess CaO

TABLE 6: The major chemical components of mortar.

Chemical components	Mortar designation																	
	M1	M2	M3	M4	M5	M6	M7	M8	M9	M10	M11	M12	M13	M14	M15	M16	M17	M18
CaO	18.68	16.42	18.5	22.65	12.09	18.32	20.39	11.91	13.99	15.23	16.06	18.14	20.21	22.28	15.88	17.95	19.85	17.77
SiO ₂	52.01	52.97	51.43	48.34	55.48	50.84	49.3	54.89	53.35	52.42	51.8	50.26	48.71	47.17	51.22	49.67	47.54	49.09
Al ₂ O ₃	10.16	11.5	11.91	12.73	12.44	13.66	14.07	14.19	14.6	14.84	15.01	15.42	15.82	16.23	16.76	17.17	19.33	18.92
MgO	3.44	3.32	3.3	3.25	3.23	3.16	3.14	3.09	3.07	3.05	3.04	3.02	3	2.97	2.9	2.88	2.72	2.74
Fe ₂ O ₃	2.81	2.81	2.63	2.29	2.97	2.46	2.29	2.79	2.62	2.52	2.45	2.28	2.11	1.94	2.27	2.1	1.75	1.92
Na ₂ O	0.2	0.2	0.21	0.22	0.2	0.21	0.22	0.21	0.21	0.22	0.22	0.22	0.23	0.23	0.22	0.23	0.24	0.24
K ₂ O	4.07	4.14	3.85	3.26	4.51	3.63	3.34	4.29	4	3.83	3.71	3.42	3.12	2.83	3.49	3.2	2.69	2.98
SiO ₂ /Al ₂ O ₃	5.12	4.61	4.32	3.8	4.46	3.72	3.5	3.87	3.65	3.53	3.45	3.26	3.08	2.91	3.06	2.89	2.46	2.59

content makes the material unsound and causes expansion and disintegration. An excessive quantity of lime (CaO) is considered for the hardening mechanism of mortar [44]. Mix M4 contained the highest percentage of CaO among all the mixes but produced the lowest compressive strength of about 37 MPa. The formation of Ca compounds in geopolymers is greatly dependent on the pH and Si/Al ratio. The SiO₂ content provides greater strength, but, at the same time, it extends the setting time [13]. Although mix M5 contained the highest percentage of SiO₂ among all the mixes, the Si/Al ratio was quite high (4.45). Further, mixes M5 and M1 contained high percentages of K₂O and MgO, respectively, which are harmful ingredients in cement. Mixes M17 and M1 contained the highest percentage of Na₂O and MgO. If the amount of Na₂O and K₂O exceeds 1%, it leads to the failure of concrete and if the content of MgO exceeds 5%, it causes cracks in the hardened concrete. Further, the Al component tends to dissolve easier than the Si components, which enables a higher rate of condensation between the silicate and aluminate species than the condensation between just the silicate species [45].

3.5. Effect of Metakaolin on the Compressive Strength. In general, MK is a poorly crystallized white powder with a specific surface of 12,000 m²/kg (Table 2) and an average particle size between 1.5 and 2.5 μm [46]. MK is effective at reducing the rate of diffusion of the Cl⁻ and Na⁺ ions in mortar and also the rate of water absorption [47]. The effect of MK content on the compressive strength is shown in Figure 13. The results of Wild et al. [48] derived the maximum compressive strength possible at the different percentage replacements of MK. The use of 20% MK with 45% of POFA and 35% of GGBS in mix M12 produced the highest strength of about 48 MPa. The mixes M1, M3, and M6 that contained 5%, 10%, and 15% MK with 35% GGBS and different amounts of POFA produced about 51%, 37%, and 32% lower compressive strength than mix M12. This is because M12 contained more Al₂O₃ compared to the other mixes. Al plays an important role, as, to a large degree, it controls the properties of geopolymers, and the

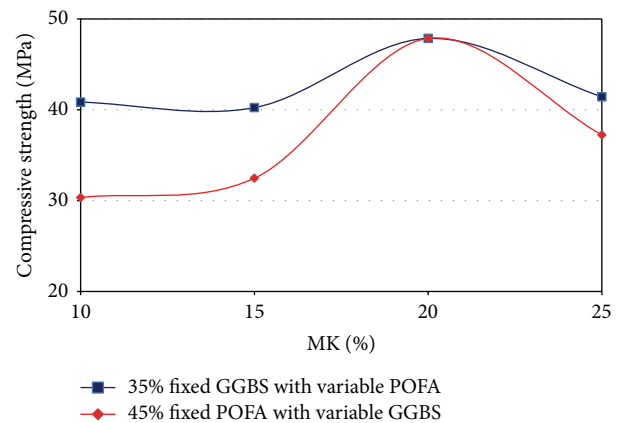


FIGURE 13: Effect of MK on compressive strength mixed with 45% POFA and 35% GGBS.

absolute amount of available Al throughout the reaction affects the final compressive strength [49]. Similarly, for mixes M7 and M14, which contained 15% MK, 40% GGBS, and 45% POFA and 20% MK, 45% GGBS, and 35% POFA, respectively, the compressive strength decreased by 16% and 15% compared to mix M12. MK grains are not fully dissolved during the geopolymerization process as the reaction takes place on the surface layer of the solid particles [50]. The reaction rate is then mainly controlled by diffusion of the hydroxide and silicate ions through the primary geopolymer gel, which is mainly affected by the curing temperature at the early stage of the reaction. In the case of increasing the percentage of MK, the compressive strength also reduced compared to mix M12. The inclusion of a small amount of MK in GGBS-rich alkali silicate-activated binders produces stable Al-substituted calcium silicate hydrate (C-S-H) gels and promotes enhanced workability. A low activator content does not provide sufficient alkalinity to promote the dissolution of MK to produce a highly stable coexisting geopolymer gel. Therefore, a large proportion of MK needs activator content with very high concentration that will affect the

rate of polymerization. Thus, the inclusion of MK after 20% reduces the compressive strength. Mixes M16 and M18, which contained 25% MK, 35% GGBS, and 40% POFA and 30% MK, 35% GGBS, and 35% POFA, showed a reduction in the compressive strength by about 22% and 15% compared to M12. According to Austell [51] the rate of water absorption of mortar is halved by replacing 20% of MK. So, mix M12 with 20% MK, 35% GGBS, and 45% POFA produced the highest compressive strength and is considered the optimum mix to develop geopolymer mortar with a compressive cube strength of 40 MPa. Wild et al. [52] reported that increasing the specific surface of MK from 12,000 to 15,000 m²/kg reduces the age at which the maximum strength enhancement occurs in MK mortar. The effect of MK on the compressive strength at 28 days with 35% GGBS and 45% POFA is shown in Figure 13. One of the reasons for mixing MK with GGBS in this study is to provide better control of the setting time. GGBS binders have a tendency to set extremely rapidly and the addition of a small amount of MK can retard setting to provide a more convenient period of workability.

3.6. Effect of GGBS on the Compressive Strength. GGBS plays an important role for compressive strength development. A higher concentration of GGBS results in a higher compressive strength of geopolymer concrete [53]. GGBS contains higher CaO, and, as a result, it is a good potential source of soluble Ca in the mixture. The compressive strength of mortar is shown in Figure 12. Mix number M12, with 35% GGBS, produced the highest strength, while a further decrease in the GGBS content reduced the compressive strength. M11 (30% GGBS with 20% MK, 50% POFA) and M9 (25% GGBS with 20% MK, 55% POFA) showed a decrease in strength of about 12% and 14% with respect to M12. Yunsheng et al. [54] also reported that the addition of GGBS leads to a considerable increase in the compressive strength but only when the GGBS replacement percentage exceeds 30%. GGBS is a latent hydraulic product, which can be activated by suitable activators, and, without activation, the development of the strength of the GGBS is extremely slow and the development of the slag necessitates a pHP12 [44]. Mix M13 contained 40% GGBS with 20% MK, 40% POFA, while mix M12 contained 35% GGBS with 20% MK, 45% POFA. A comparison between mixes M12 and M13 showed that the former with 40% GGBS produced 13% lower compressive strength compared to the mix with 35% GGBS and that mix M14 with 45% GGBS showed that the reduction is 15%. Therefore, if the percentage of GGBS exceeds 35%, then the compressive strength also reduces. This might be because the GGBS undergoes a slower hydration process; therefore at higher GGBS replacement levels, the hydration process becomes increasingly slower, which leads to a reduction in the compressive strength [55]. Another reason is that the quantity of soluble Ca depends on the volume of GGBS present in the mixture, which has a direct effect on the compressive strength. Figure 14 shows the effect of GGBS on the compressive strength with POFA and 20% MK.

3.7. Effect of POFA on the Compressive Strength. POFA, which is also a by-product from thermal power plants, contains

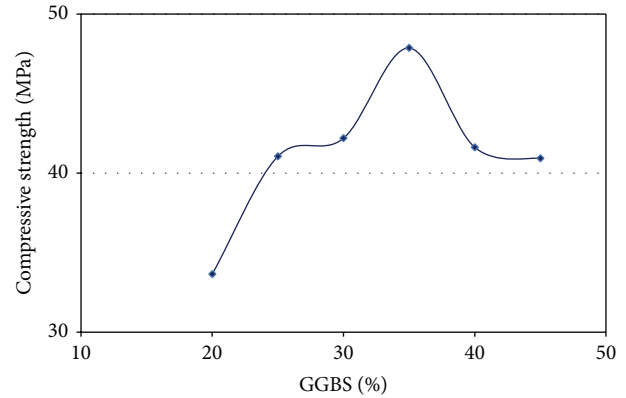


FIGURE 14: Effect of GGBS on compressive strength mixed with POFA and 20% fixed MK.

high amounts of Si and Al oxides in the amorphous state and is considered to be a pozzolanic material [56]. The high fineness of POFA produces a greater pozzolanic reaction and acts as a filler in the voids and thus increases the compressive strength of the concrete [21]. Figure 16 shows the effect of varying POFA contents on the compressive strength with MK varying from 5% to 30% with nonvarying GGBS at 35%. The compressive strengths of mixes M1 and M3, which contained 60% POFA and 55% POFA, respectively, produced about 51% and 37% lower compressive strength than mix M12. Mix M12 with 45% of POFA, 35% of GGBS, and 20% MK produced the highest strength of 48 MPa. Ariffin et al. [57] opined that due to its low content of Al₂O₃, it produces low compressive strength; the use of high POFA content could be attributed to the incomplete geopolymerization, because Al₂O₃ tends to dissolve at a higher rate during the early stage of geopolymerization. The comparison between mixes M12 and M13 showed that the former with 40% POFA produced 13% lower compressive strength compared to the mix with 45% POFA. Then, from the comparison between mixes M12 and M14 (35% POFA), the strength reduced by about 15% for the latter.

The particles of the POFA with cohesive characteristics could not be mixed properly, and, hence, the strength development was poor. Tonnyayopas et al. [58] explained that the low early compressive strength is due to the slow pozzolanic activity of POFA. Figure 14 shows the 28 days' compressive strength of all mixes.

3.8. Effect of Curing. All the specimens were covered with plastic wrapping and cured in an oven at 65°C for 24 h, as stated in the methodology; the results for the compressive strengths are shown in Figure 12. The average difference between the 14- and 28-day compressive strength for the mixes was about 10%, and, between the 7- and 14-day strengths, it was 8%. This shows that the rate of the geopolymerization is accelerated by elevated temperature at the early stage [59]. Kusbiantoro et al. [60] reported that compared to the other curing methods—ambient and external exposure—the oven-cured geopolymer concrete at 65°C exhibited superior mechanical properties. They reasoned that this could

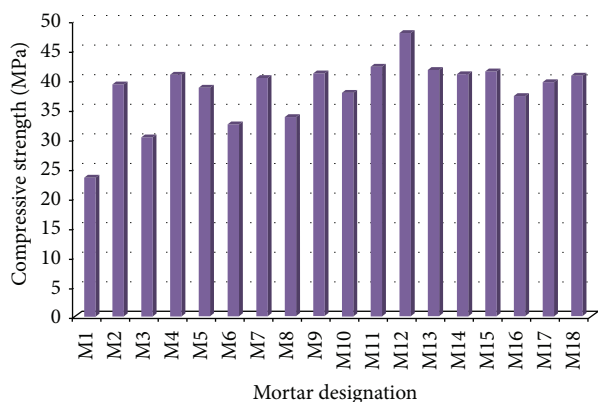


FIGURE 15: 28-day compressive strength of different mixes.

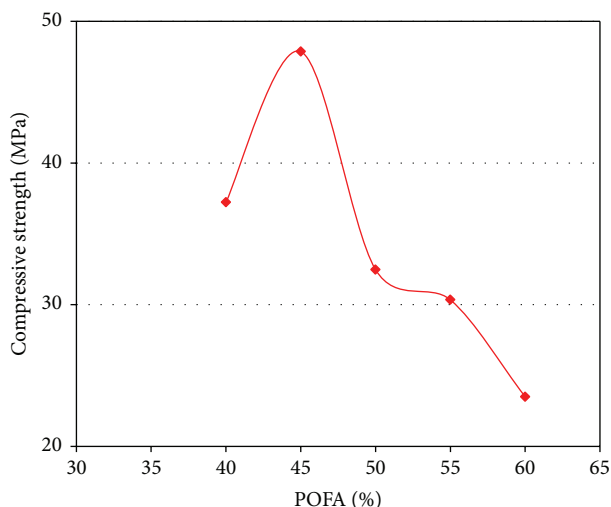


FIGURE 16: Effect of POFA on compressive strength mixed with MK and 35% fixed GGBS.

be attributed to the oven curing as the suitable condition to accelerate the dissolution and polycondensation of alumina silicate gel in the geopolymer framework. Furthermore, geopolymer concrete could achieve high early compressive strength when oven-cured, instead of undergoing ambient curing [61]. Hence, all the mixes, M1 to M18, gathered maximum strength within 3 days, as shown in Table 5.

3.9. Alkaline Solution to Binder Ratio by Mass on Compressive Strength Analysis. The solution to binder ratio was kept constant at 0.5 for all the mixtures, as stated in Table 4. Abdullah et al. [62] reported that the ratio of S/B of 0.5 by mass produces higher compressive strength compared to the ratio of 0.67. Sathonsaowaphak et al. [63] found a very low compressive strength of 8 MPa for the mix with the AK/B ratio of 0.325 by mass; however, they reported that the high compressive strengths were in the range of 42 to 52 MPa, as the ratios of S/B by mass varied between 0.429 and 0.709. Thus, the use of a solution to binder ratio of 0.5 for all the mixtures produced acceptable compressive strength.

3.10. Effect of Molarity of Alkaline Activated Solution (NaOH Solution) on the Compressive Strength. Table 7 shows the effect of molarity of alkaline activated solution on the compressive strength.

The compressive strength of mix M4 with 14 molarities produced 17% higher than the mix M4A with 12 molarities. Other parameters except the molarity, such as binder, sand, and water, were kept constant for both the mixes. The use of high molarity based alkaline solution increases the compressive strength because of the release of silica and alumina [64]. From Figure 17 it was also found that the mixes M9, M12, and M16 with 14 molarities show higher compressive strength than the mixes M9A, M12A, and M16A with 12 molarities. All the parameters are same, respectively, except the molarity (NaOH solution). NaOH solution with high concentration increases the geopolymerization reaction [43].

4. Conclusions

This research into optimizing the use of MK, GGBS, and POFA as binders in the production of geopolymer mortars produced significant conclusions. Twenty-four geopolymer mortar mixtures incorporating sustainable binders—MK, GGBS, and POFA—were prepared. The cube compressive strength of the mortars was investigated up to a period of 28 days to study the feasibility of the replacement with GGBS and POFA in MK-based geopolymer mortar. Based on the tests conducted, the following conclusions were drawn:

- (i) The compressive strength of the geopolymer mortar increased with the MK content up to 20%, while further replacement of MK showed a significant reduction in the strength.
- (ii) Mix M12, with the addition of GGBS up to 35%, POFA up to 45% with 20% MK, produced the highest strength among the mixes.
- (iii) It is possible to improve the compressive strength of the geopolymer mortars at the early ages by introducing initial heating at 65°C for 24 h after demoulding. Improvements are more significant at 3 days.
- (iv) In most of the specimens, 90% of the compressive strength of the geopolymer mortar was achieved at the age of 7 days.
- (v) POFA produces a cohesive mix, in which the density of mortar decreases with the increase in the percentage of POFA, resulting in a decrease in density of approximately 12%.
- (vi) The finer particles of GGBS produce a dense mix; hence, the partial substitution of GGBS in the mortar should be maintained at 35%.
- (vii) The compressive strength increases with the increases of molarity of sodium hydroxide solution.
- (viii) It can also be concluded that the combined maximum volumes of MK, GGBS, and POFA can be used for the development of a sustainable construction material to replace OPC for the production of eco-environmentally friendly geopolymer mortars.

TABLE 7: Comparison of the compressive strength between different molarities.

Mortar designation	Binder mix proportion MK/GGBS/POFA (%)	M-sand (kg/m ³)	Alkali activator molarity	Compressive strength (MPa)	
				3-day	28-day
M4	10/45/45	1532	14	36.6	40.85
M6	15/35/50	1532	14	22.15	32.5
M9	20/25/55	1532	14	37.15	41
M12	20/35/45	1532	14	43.15	48
M16	25/35/40	1532	14	33.4	37.5
M18	30/35/35	1532	14	34	40.8
M4A	10/45/45	1532	12	30.8	34.1
M6A	15/35/50	1532	12	17.2	25.8
M9A	20/25/55	1532	12	32.5	37
M12A	20/35/45	1532	12	36	41.5
M16A	25/35/40	1532	12	27.6	33
M18A	30/35/35	1532	12	31.1	35.6

Note: MK: metakaolin; GGBS: ground granulated blast furnace slag; POFA: palm oil fuel ash.

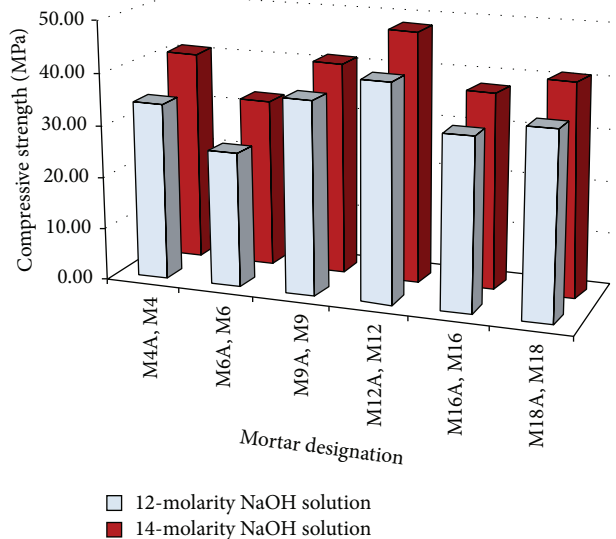


FIGURE 17: Effect of molarity in compressive strength.

This research work was focused on the development of the compressive strength of geopolymer mortar produced by different proportion of three pozzolanic materials and activated by two concentrated alkaline solutions. The test results were analysed based on the chemical compositions. Geopolymerization process could be affected by the particle size and reactivity rate of the binding materials, curing condition, and casting process. This could be recommended for further research work on the microstructural analysis for the proposed binding materials with different particle size and various curing conditions. Since water/binder ratio is an important factor and affects significantly the development of compressive strength for different proportion of binder/aggregate in concrete and mortar, mix design with different type and volume of aggregate could be carried on for optimization.

Conflict of Interests

The authors declare that there is no conflict of interests regarding the publication of this paper.

Acknowledgment

The authors are grateful to the University of Malaya for the financial support through the University of Malaya Research Project "RP018/2012B: Development of Geopolymer Concrete for Structural Application."

References

- [1] I. I. Bashar, U. J. Alengaram, M. Z. Jumaat, and A. Islam, "The effect of variation of molarity of alkali activator and fine aggregate content on the compressive strength of the fly ash: palm oil fuel ash based geopolymer mortar," *Advances in Materials Science and Engineering*, vol. 2014, Article ID 245473, 13 pages, 2014.
- [2] N. Ranjbar, M. Mehrali, A. Behnia, U. J. Alengaram, and M. Z. Jumaat, "Compressive strength and microstructural analysis of fly ash/palm oil fuel ash based geopolymer mortar," *Materials and Design*, vol. 59, pp. 532–539, 2014.
- [3] R. H. Kupaei, U. J. Alengaram, and M. Z. Jumaat, "The effect of different parameters on the development of compressive strength of oil palm shell geopolymer concrete," *The Scientific World Journal*, vol. 2014, Article ID 898536, 16 pages, 2014.
- [4] P. Chana, "Low carbon cements: the challenges and opportunities," in *Proceedings of the Future Cement Conference and Exhibition*, pp. 8–9, London, UK, February 2011.
- [5] L. G. Communications, *Sustainability Report 2013*, Lafarge, 2013.
- [6] J. Davidovits, "Global warming impact on the cement and aggregates industries," *World Resource Review*, vol. 6, no. 2, pp. 263–278, 1994.
- [7] E. Worrell, L. Price, N. Martin, C. Hendriks, and L. O. Meida, "Carbon dioxide emissions from the global cement industry,"

- Annual Review of Energy and the Environment*, vol. 26, no. 1, pp. 303–329, 2001.
- [8] D. M. Roy and G. M. Idorn, “Hydration, structure, and properties of blast furnace slag cements, mortars, and concrete,” *ACI Journal Proceedings*, vol. 79, no. 6, pp. 444–457, 1982.
- [9] L. K. Turner and F. G. Collins, “Carbon dioxide equivalent (CO₂-e) emissions: a comparison between geopolymer and OPC cement concrete,” *Construction and Building Materials*, vol. 43, pp. 125–130, 2013.
- [10] J. L. Provis and J. S. J. van Deventer, “Geopolymerisation kinetics. 1. In situ energy-dispersive X-ray diffractometry,” *Chemical Engineering Science*, vol. 62, no. 9, pp. 2309–2317, 2007.
- [11] J. Davidovits, “Geopolymer chemistry and sustainable development. The poly (sialate) terminology: a very useful and simple model for the promotion and understanding of green-chemistry,” in *Proceedings of the Geopolymer Conference*, pp. 9–15, Saint Quentin, France, September 2005.
- [12] P. Duxson, G. C. Lukey, and J. S. J. Van Deventer, “Physical evolution of Na-geopolymer derived from metakaolin up to 1000°C,” *Journal of Materials Science*, vol. 42, no. 9, pp. 3044–3054, 2007.
- [13] A. Islam, U. J. Alengaram, M. Z. Jumaat, and I. I. Bashar, “The development of compressive strength of ground granulated blast furnace slag-palm oil fuel ash-fly ash based geopolymer mortar,” *Materials & Design*, vol. 56, pp. 833–841, 2014.
- [14] J. L. Provis and J. S. J. van Deventer, *Geopolymers: Structures, Processing, Properties and Industrial Applications*, Elsevier, 2009.
- [15] J. L. Provis, “Geopolymers and other alkali activated materials: why, how, and what?” *Materials and Structures*, vol. 47, no. 1-2, pp. 11–25, 2014.
- [16] D. Hardjito, S. E. Wallah, D. M. J. Sumajouw, and B. V. Rangan, “On the development of fly ash-based geopolymer concrete,” *ACI Materials Journal*, vol. 101, no. 6, pp. 467–472, 2004.
- [17] E. I. Diaz, E. N. Allouche, and S. Eklund, “Factors affecting the suitability of fly ash as source material for geopolymers,” *Fuel*, vol. 89, no. 5, pp. 992–996, 2010.
- [18] J. Davidovits, “Properties of geopolymer cements,” in *Proceedings of the 1st International Conference on Alkaline Cements and Concretes*, pp. 131–149, Kiev, Ukraine, 1994.
- [19] H. Tchakoute Kouamo, A. Elimbi, J. A. Mbey, C. J. Ngally Sabouang, and D. Njopwouo, “The effect of adding alumina-oxide to metakaolin and volcanic ash on geopolymer products: a comparative study,” *Construction and Building Materials*, vol. 35, pp. 960–969, 2012.
- [20] S. A. Bernal, E. D. Rodríguez, R. Mejía De Gutiérrez, M. Gordillo, and J. L. Provis, “Mechanical and thermal characterisation of geopolymers based on silicate-activated metakaolin/slag blends,” *Journal of Materials Science*, vol. 46, no. 16, pp. 5477–5486, 2011.
- [21] W. Tangchirapat, T. Saeting, C. Jaturapitakkul, K. Kiattikomol, and A. Siripanichgorn, “Use of waste ash from palm oil industry in concrete,” *Waste Management*, vol. 27, no. 1, pp. 81–88, 2007.
- [22] A. S. M. A. Awal and M. W. Hussin, “The effectiveness of palm oil fuel ash in preventing expansion due to alkali-silica reaction,” *Cement and Concrete Composites*, vol. 19, no. 4, pp. 367–372, 1997.
- [23] U. J. Alengaram, H. Mahmud, and M. Z. Jumaat, “Enhancement and prediction of modulus of elasticity of palm kernel shell concrete,” *Materials & Design*, vol. 32, no. 4, pp. 2143–2148, 2011.
- [24] K. H. Mo, U. J. Alengaram, and M. Z. Jumaat, “A review on the use of agriculture waste material as lightweight aggregate for reinforced concrete structural members,” *Advances in Materials Science and Engineering*, vol. 2014, Article ID 365197, 9 pages, 2014.
- [25] W. Tangchirapat, S. Khamklai, and C. Jaturapitakkul, “Use of ground palm oil fuel ash to improve strength, sulfate resistance, and water permeability of concrete containing high amount of recycled concrete aggregates,” *Materials & Design*, vol. 41, pp. 150–157, 2012.
- [26] J. Cai, *Research of Effects and Mechanism of Micro Fines on Manufactured Fine Aggregate Concrete*, Wuhan University of Technology, Wuhan, China, 2006.
- [27] P. Nanthagopalan and M. Santhanam, “Fresh and hardened properties of self-compacting concrete produced with manufactured sand,” *Cement and Concrete Composites*, vol. 33, no. 3, pp. 353–358, 2011.
- [28] T.-L. Weng, W.-T. Lin, and A. Cheng, “Effect of metakaolin on strength and efflorescence quantity of cement-based composites,” *The Scientific World Journal*, vol. 2013, Article ID 606524, 11 pages, 2013.
- [29] A. Hawa, D. Tonnyapopas, and W. Prachasaree, “Performance evaluation and microstructure characterization of metakaolin-based geopolymer containing oil palm ash,” *The Scientific World Journal*, vol. 2013, Article ID 857586, 9 pages, 2013.
- [30] U. J. Alengaram, B. A. A. Muhit, and M. Z. B. Jumaat, “Utilization of oil palm kernel shell as lightweight aggregate in concrete—a review,” *Construction and Building Materials*, vol. 38, pp. 161–172, 2013.
- [31] R. Sahana, “Setting time compressive strength and microstructure of geopolymer paste,” in *Proceedings of the International Conference on Energy and Environment (ICEE '13)*, vol. 2, December 2013, An ISO 3297:2007 Certified Organization.
- [32] P. S. Deb, P. Nath, and P. K. Sarker, “The effects of ground granulated blast-furnace slag blending with fly ash and activator content on the workability and strength properties of geopolymer concrete cured at ambient temperature,” *Materials & Design*, vol. 62, pp. 32–39, 2014.
- [33] R. H. Kupaei, U. J. Alengaram, M. Z. B. Jumaat, and H. Nikraz, “Mix design for fly ash based oil palm shell geopolymer lightweight concrete,” *Construction and Building Materials*, vol. 43, pp. 490–496, 2013.
- [34] D. Hardjito and B. V. Rangan, *Development and Properties of Low-Calcium Fly Ash-Based Geopolymer Concrete*, Curtin University of Technology, Perth, Australia, 2005.
- [35] P. Chindaprasirt, T. Chareerat, and V. Sirivivatnanon, “Workability and strength of coarse high calcium fly ash geopolymer,” *Cement and Concrete Composites*, vol. 29, no. 3, pp. 224–229, 2007.
- [36] International A, “Standard test method for flow of hydraulic cement mortar,” ASTM C1437-13, ASTM International, West Conshohocken, Pa, USA, 2013.
- [37] A. S. Gill and R. Siddique, “Strength Properties and Sulphate Resistance of Self-Compacting Concrete Incorporating Silica Fume and Metakolin,” 2012.
- [38] E. Sakai, S. Hoshino, Y. Ohba, and M. Daimon, “The fluidity of cement paste with various types of inorganic powders,” in *Proceedings of the 10th International Congress on the Chemistry of Cement*, Gothenburg, Sweden, June 1997.
- [39] J. M. Khatib and S. Wild, “Sulphate resistance of metakaolin mortar,” *Cement and Concrete Research*, vol. 28, no. 1, pp. 83–92, 1998.

- [40] T. Bakharev, "Geopolymeric materials prepared using Class F fly ash and elevated temperature curing," *Cement and Concrete Research*, vol. 35, no. 6, pp. 1224–1232, 2005.
- [41] D. Khale and R. Chaudhary, "Mechanism of geopolymerization and factors influencing its development: a review," *Journal of Materials Science*, vol. 42, no. 3, pp. 729–746, 2007.
- [42] A. Fernández-Jiménez, A. Palomo, and M. Criado, "Microstructure development of alkali-activated fly ash cement: a descriptive model," *Cement and Concrete Research*, vol. 35, no. 6, pp. 1204–1209, 2005.
- [43] X. Guo, H. Shi, and W. A. Dick, "Compressive strength and microstructural characteristics of class C fly ash geopolymer," *Cement and Concrete Composites*, vol. 32, no. 2, pp. 142–147, 2010.
- [44] J. Davidovits, *Geopolymer Chemistry and Applications*, Geopolymer Institute, 2008.
- [45] P. D. Silva, K. Sagoe-Crenstil, and V. Sirivivatnanon, "Kinetics of geopolymerization: role of Al_2O_3 and SiO_2 ," *Cement and Concrete Research*, vol. 37, no. 4, pp. 512–518, 2007.
- [46] M. A. Caldarone, K. A. Gruber, and R. G. Burg, "High-reactivity metakaolin: a new generation mineral admixture," *Concrete International*, vol. 16, no. 11, pp. 37–40, 1994.
- [47] J. Kostuch, V. Walters, and T. Jones, "High performance concretes incorporating metakaolin: a review," *Concrete*, vol. 2, no. 1993, pp. 1799–1811, 2000.
- [48] S. Wild, J. M. Khatib, and A. Jones, "Relative strength, pozzolanic activity and cement hydration in superplasticised metakaolin concrete," *Cement and Concrete Research*, vol. 26, no. 10, pp. 1537–1544, 1996.
- [49] C. Li, H. Sun, and L. Li, "A review: the comparison between alkali-activated slag (Si + Ca) and metakaolin (Si + Al) cements," *Cement and Concrete Research*, vol. 40, no. 9, pp. 1341–1349, 2010.
- [50] V. F. F. Barbosa, K. J. D. MacKenzie, and C. Thaumaturgo, "Synthesis and characterisation of materials based on inorganic polymers of alumina and silica: sodium polysialate polymers," *International Journal of Inorganic Materials*, vol. 2, no. 4, pp. 309–317, 2000.
- [51] S. Austell, *A New Pozzolanic Material for the Cement and Concrete Industry, Use of Metastar for the Production of Highly Durable Concretes and Mortars*, ECC International product document, ECC International, Wareham, UK, 3rd edition, 1996.
- [52] S. Wild, J. Khatib, and M. Craythorne, "Strength development of mortar containing metakaolin," in *Proceedings of the 5th International Conference on Modern Building Materials, Structure and Techniques*, pp. 58–63, Vilnius, Lithuania, May 1997.
- [53] N. P. Ganapati, A. S. S. N. Prasad, S. Adishesu, and P. V. V. Satyanarayana, "A study on strength properties of geopolymer concrete with addition of G.G.B.S," *International Journal of Engineering Research and Development*, vol. 2, no. 4, pp. 19–28, 2012.
- [54] Z. Yunsheng, S. Wei, C. Qianli, and C. Lin, "Synthesis and heavy metal immobilization behaviors of slag based geopolymer," *Journal of Hazardous Materials*, vol. 143, no. 1-2, pp. 206–213, 2007.
- [55] K. H. Mo, U. J. Alengaram, and M. Z. Jumaat, "Utilization of ground granulated blast furnace slag as partial cement replacement in lightweight oil palm shell concrete," *Materials and Structures*, 2014.
- [56] M. W. Hussin and A. S. M. Abdul Awal, "Influence of palm oil fuel ash on sulfate resistance of mortar and concrete," *ACI Special Publication*, vol. 178, pp. 417–430, 1998.
- [57] M. A. M. Ariffin, M. W. Hussin, and M. A. R. Bhutta, "Mix design and compressive strength of geopolymer concrete containing blended ash from agro-industrial wastes," *Advanced Materials Research*, vol. 339, no. 1, pp. 452–457, 2011.
- [58] D. Tonayopas, F. Nilrat, K. Putto, and J. Tantiwitayawanich, "Effect of oil palm fiber fuel ash on compressive strength of hardening concrete," in *Proceedings of the 4th Thailand Materials Science and Technology Conference*, pp. 1–3, Pathumthani, Thailand, 2006.
- [59] J. C. Swanepoel and C. A. Strydom, "Utilisation of fly ash in a geopolymeric material," *Applied Geochemistry*, vol. 17, no. 8, pp. 1143–1148, 2002.
- [60] A. Kusbiantoro, M. F. Nuruddin, N. Shafiq, and S. A. Qazi, "The effect of microwave incinerated rice husk ash on the compressive and bond strength of fly ash based geopolymer concrete," *Construction and Building Materials*, vol. 36, pp. 695–703, 2012.
- [61] S. Wallah and B. V. Rangan, "Low calcium fly ash based geopolymer concrete—long term properties," Research Report GCI, Curtin University, Perth, Australia, 2006.
- [62] M. M. A. Abdullah, H. Kamarudin, H. Mohammed, I. Khairul Nizar, A. R. Rafiza, and Y. Zarina, "The relationship of NaOH molarity, $\text{Na}_2\text{SiO}_3/\text{NaOH}$ ratio, fly ash/alkaline activator ratio, and curing temperature to the strength of fly ash-based geopolymer," *Advanced Materials Research*, vol. 328–330, pp. 1475–1482, 2011.
- [63] A. Sathonsaowaphak, P. Chindaprasirt, and K. Pimraksa, "Workability and strength of lignite bottom ash geopolymer mortar," *Journal of Hazardous Materials*, vol. 168, no. 1, pp. 44–50, 2009.
- [64] P. Chindaprasirt, C. Jaturapitakkul, W. Chalee, and U. Rattanasak, "Comparative study on the characteristics of fly ash and bottom ash geopolymers," *Waste Management*, vol. 29, no. 2, pp. 539–543, 2009.

Research Article

Waste Cellulose from Tetra Pak Packages as Reinforcement of Cement Concrete

**Gonzalo Martínez-Barrera,¹ Carlos E. Barrera-Díaz,²
Erick Cuevas-Yañez,² Víctor Varela-Guerrero,² Enrique Viguera-Santiago,¹
Liliana Ávila-Córdoba,² and Miguel Martínez-López¹**

¹Laboratorio de Investigación y Desarrollo de Materiales Avanzados (LIDMA), Facultad de Química, Universidad Autónoma del Estado de México, km 12 de la Carretera Toluca-Atlacomulco, 50200 San Cayetano, Mexico

²Centro Conjunto de Investigación en Química Sustentable, Universidad Autónoma del Estado de México-Universidad Nacional Autónoma de México (UAEM-UNAM), Carretera Toluca-Atlacomulco km 14.5, 50200 San Cayetano, Mexico

Correspondence should be addressed to Gonzalo Martínez-Barrera; gonzomartinez02@yahoo.com.mx

Received 8 September 2014; Revised 19 December 2014; Accepted 8 January 2015

Academic Editor: Hao Wang

Copyright © 2015 Gonzalo Martínez-Barrera et al. This is an open access article distributed under the Creative Commons Attribution License, which permits unrestricted use, distribution, and reproduction in any medium, provided the original work is properly cited.

The development of the packaging industry has promoted indiscriminately the use of disposable packing as Tetra Pak, which after a very short useful life turns into garbage, helping to spoil the environment. One of the known processes that can be used for achievement of the compatibility between waste materials and the environment is the gamma radiation, which had proved to be a good tool for modification of physicochemical properties of materials. The aim of this work is to study the effects of waste cellulose from Tetra Pak packing and gamma radiation on the mechanical properties of cement concrete. Concrete specimens were elaborated with waste cellulose at concentrations of 3, 5, and 7 wt% and irradiated at 200, 250, and 300 kGy of gamma dose. The results show highest improvement on the mechanical properties for concrete with 3 wt% of waste cellulose and irradiated at 300 kGy; such improvements were related with the surface morphology of fracture zones of cement concrete observed by SEM microscopy.

1. Introduction

Due to the increment of awareness on environment, the use of waste materials is an attractive area of opportunity. Solid wastes are classified by their chemical nature as organic and inorganic; recovery of them has been under study for a long time. Use of waste in building materials, road construction, and pavement are beneficial because it reduces environmental pollution and solves the waste disposal problems [1, 2]. Such waste materials should show an effective recycling or reuse [3]. Several improvements have been reported for incorporating waste of recycled polymers, for example, in the case of asphalt pavement or in road performances [4–6].

Among waste materials are those containing cellulose as Tetra Pak packages; such packing is made up of three raw materials: paper (about 75%), low density polyethylene (about 20%), and aluminum (about 5%). Aseptic packages are recycled through a simple, well-established process

called hydropulping. In this process, the cellulosic fibers are separated from thin layers of polyethylene and aluminum. Early study on Tetra Pak garbage showed recovery of their components, being cardboard 63 wt%, polyethylene 30 wt%, and aluminum 7 wt% [7].

Degradation of cellulose or lingocellulosic materials produced huge number of water soluble or insoluble oxygenated compounds. The water content of aqueous phases is high, and it contains some valuable chemicals; one of them is phenolic compounds. It is convenient to mention that high-quality cellulosic fibers are used in the production of paper products such as tissue and paper towels and fine writing paper.

Some investigations are concerned with the use of cellulosic materials as fillers in composite materials. Most of the waste from the paper industry is known as paper sludge (PS) which is burnt and becomes PS ash. This is used as a soil improvement material and cement raw material. PS ash increased the strength of extremely stiff concrete; moreover,

it has high water absorption [8, 9]. Different composite materials have been produced by incorporating cellulosic materials for improvement of mechanical properties: (a) bending behavior is improved by incorporating cellulose fibers from waste paper; (b) toughness and tensile behavior of thin-sheet cement products are improved by adding fibers of recycled waste paper; (c) shore hardness (SH) values are increased as the resin concentration increases in composites elaborated with Tetra Pak and resin materials; and (d) maximum of strengthening is achieved for cement matrixes when adding plant-fibers and man-made cellulose fibers (from 8 to 10 wt%); the costs are reduced with this substitution [4, 5, 9, 10].

The mechanical improvements when using cellulose fibers are due mainly to their mechanical properties that include a modulus of elasticity up to 40 GPa. Moreover, fibers can be further subdivided by hydrolysis followed by mechanical disintegration into microfibrils with an elastic modulus up to 70 GPa. Such fibers are produced commercially by the pulp and paper industry [10].

With the exception of cotton, the main components of natural fibers are cellulose, hemicellulose and lignin, and, in minor concentration pectin, waxes and water soluble substances [10]. Linear cellulose molecules are linked laterally by hydrogen bonds to form linear bundles, giving rise to a crystalline structure. The degree of crystallinity of cellulose is one of the most important structural parameters; the rigidity of cellulose fibers increases, but flexibility decreases with increasing ratio of crystalline to amorphous regions. Therefore, the crystalline structure of cellulose is one important parameter for evaluating the physical and mechanical properties [11, 12].

The use of gamma radiation as a mechanism for reaction initiation and accelerator of the polymerization of a monomer in a ceramic matrix can bring considerable advantages. One of the most important objectives is to obtain higher adhesion between fibers and the matrix [13–18]. The first investigations focused on the influence of gamma radiation on lignocellulose materials, in terms of increasing the solubility of insoluble high-polymerized sugars such as cellulose [19]. Some investigations focused on effects of gamma radiation on physicochemical properties of cellulose, and the results show that an increment of 25 kGy (in average) caused a loss of 1% in cellulose crystallinity in the dose range of 0–1 MGy. Cellulose shows degradation (from 6 to 12%) up to 31.6 kGy and unchanged degree of crystallinity up to 300 kGy. The degree of polymerization (DP) is obtained up to 1 Gy; this decrease is above 10 kGy. Moreover, changes on specific gravity and in the lattice constant are observed up to 1 MGy, as well as complete degradation of cellulose at 6.55 MGy. In the case of lignin no changes are observed up to 31.6 kGy and only 15% of degradation at 19 MGy is observed [19].

In cellulose there is amorphous zones along the microfibril length, in which the crystallinity is interrupted. These zones allow the penetration of chemicals into the microfibrils. Furthermore, the gamma radiation caused break-up of cellulose to shorter chains, which are water-soluble, and it most likely leads to an “opening of additional microcracks,” in which water molecules can easily penetrate.

Some studies covering the effects of ionizing radiation on polymer-ceramic composite materials, for example, in gypsum/poly(methyl) acrylate composites showed that the yield of polymerization increased with increasing radiation dose and leveled off at a dose around 3–4 kGy, where a yield of 87–88% is achieved [9]. As this process is completed at room temperature, there is much economy of heat energy, besides the reduction in costs to keep the composite under pressure. The pressure is used to keep much of the monomer (usually with a high volatility) filling the interstices of the ceramic matrix during the conversion to ceramic-polymer composites.

The purpose of this work was to evaluate gamma radiation and waste cellulose as tools for improvement of mechanical properties of cement concrete. Waste cellulose was obtained from Tetra Pak packages and the gamma doses were covered up to 300 kGy. A simple and inexpensive process was expected as well as contribution on the environmental care.

2. Experimental Part

2.1. Specimen Preparation. Before preparing concrete specimens, one set of waste cellulose particles with average size of 0.5 mm was obtained from Tetra Pak packages and was used in concentrations of 3, 5, and 7% by weight; these values were selected in order to avoid problems concerning homogeneity and workability.

Different mixes were elaborated with Portland cement, silica sand, gravel, and water. The sand with uniform granulometry had an average diameter of 150 μm (mesh 60), while sizes of gravel were 0.5, 4.0, and 6.3 mm (mesh 35, 5, and 0.25", resp.). Proportion of components in the mixes was 1/2.75 for cement/aggregates, with water/cement ratio of 0.485. All materials were mixed according to practice ASTM C-305. Sand silica was obtained from a local company (GOSA, Atizapan, Mexico), and gravel aggregates were obtained from Tula Hidalgo México, respectively.

After mixing, concrete cylindrical specimens (2.0" diameter and 4.0" long) were molded. After 24 hours, they were placed in a controlled temperature room (at $23.0 \pm 2.0^\circ\text{C}$ and 95% of relative humidity according to ASTM C/192 M-00), with the surface exposed to moisture. The moist room conditions were the same as above, according to ASTM C-511. It is important to remark that waste cellulose was used as sand replacement.

2.2. Mechanical Tests. Compressive strength evaluation of all concrete cylindrical specimens was carried out in a universal testing machine model 70-S17C2 (Controls, Cernusco, Italy), according to ASTM C-39M-01, located at Laboratory of Research and Development of Advanced Materials (LIDMA) of the Autonomous University of the State of Mexico (UAEM). Specimens were tested after 7, 14, and 28 days of moist curing. Testing tolerance allowed for the specimens was 7 days ± 6 hrs, 14 days ± 9 hrs, and 28 days ± 12 hrs.

2.3. Irradiation Procedure. The concrete cylindrical specimens were irradiated at 200, 250, and 300 kGy using a ^{60}Co

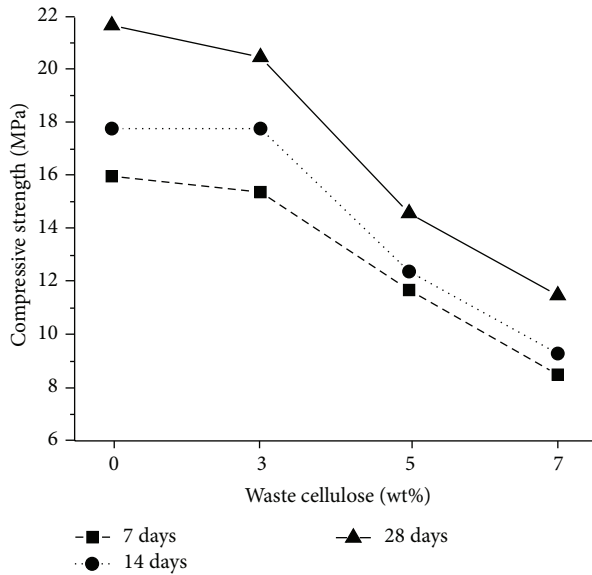


FIGURE 1: Compressive strength of concrete with waste cellulose.

source at the dose rate of 3.5 kGy/h; the experiments were made in air at room temperature. The irradiation was provided by a 651 PT Gammabeam Irradiator manufactured by NORDION (Chalk River, Ontario) and located at Institute of Nuclear Sciences of the National Autonomous University of Mexico.

2.4. Morphological Characterization. The surfaces of irradiated cellulose and those for fractured zones of concrete were analyzed, by a scanning electron microscopy (SEM) in a JEOL model JSM-5200 machine, in the secondary electron mode.

3. Results and Discussion

3.1. Compressive Strength. In Figure 1 compressive strength values of concrete with waste cellulose are shown. Concrete without waste cellulose at 28 days of curing time has the highest compressive strength value, namely, 21.7 MPa. Some behaviors are observed. (a) The values gradually decrease when more cellulose is added; (b) concrete with 3 wt% of waste cellulose has a minimal difference, 5%, with respect to control concrete (without cellulose); it does not happen for concrete with 7 wt% of waste cellulose, because it has 47% of reduction; and (c) independently of each cellulose percentage the compressive strength values increase when increasing curing time.

Such reductions in the values can be explained in terms of the waste cellulose added. The strength depends on the amount of waste cellulose and water cement ratio (w/c). By one hand cellulose has a hydrophobic nature and on the other hand the cellulose can substitute up to 7 wt% of sand in the mixture; thus more amount of water is available to interact into the surface of unhydrated grains of cement particles. Therefore, weak interfacial adhesion between cellulose and

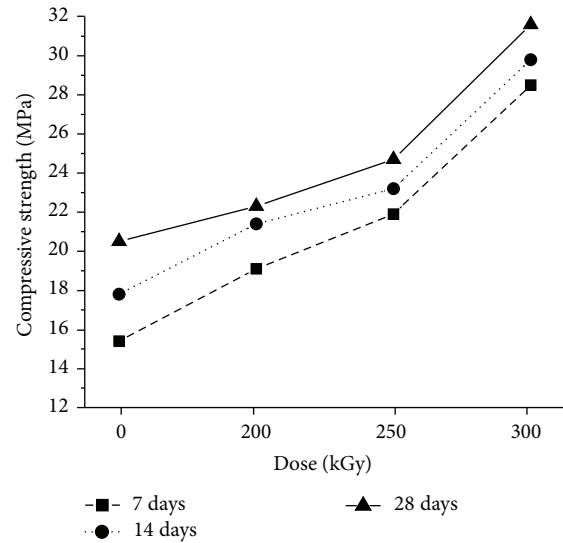


FIGURE 2: Compressive strength of concrete with waste cellulose at different irradiation doses.

hydrated cement particles is obtained; in consequence reduction on the compressive strength values is seen.

According to the highest compressive strength results for concrete with cellulose (seen previously in Figure 1), we decided to work with concrete with 3 wt% of waste cellulose in the second stage of this study, consisting on irradiating them up to 300 kGy. Some behaviors are shown in Figure 2. (a) The highest value is observed for concrete irradiated at 300 kGy at 28 days of curing time, namely, 31.6 MPa, which means an improvement of 45% with respect to control concrete; (b) the values increase when radiation dose increases too; (c) for each gamma dose the values increase when increasing curing time.

Such improvements of the compressive strength values can be explained in terms of the gamma radiation effects on the concrete components and waste cellulose. As we know, many types of chemical reactions take place during gamma irradiation of polymeric materials, cross-linking, and degradation by chain scission among others, but one or the other of these effects may be predominant in some materials. In the present investigation we argue the formation of cross-linking of the polymeric chains in the cellulose under the effect of irradiation dose and their repercussion on the cement and water molecules. We recall that cross-linking is the most important effect of polymer irradiation because it can usually improve the mechanical, thermal, and chemical properties. Moreover, application of high energy irradiation to cellulose creates free radicals by the scission of the weakest bonds; such radicals can react with some molecules in the cement matrix. The interaction between calcium silicate hydrate (formed during the hydration process) and the cellulose present in the pores during irradiation polymerization enhanced the interphase bonding and as a result, an improvement of the mechanical strength takes place.

3.2. Compressive Strain at Yield Point. Similar behavior for compressive strain is observed: (a) the values decrease when

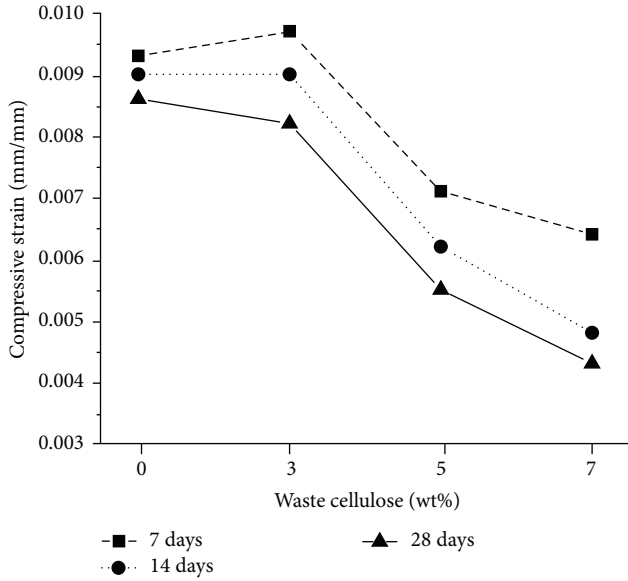


FIGURE 3: Compressive strain of concrete with waste cellulose.

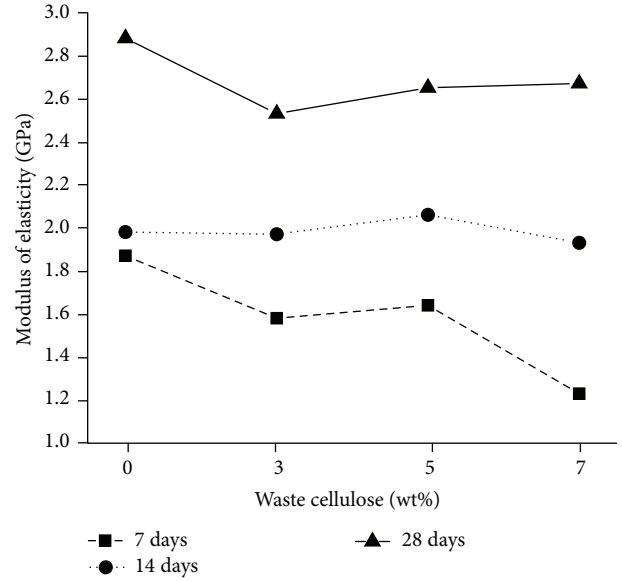


FIGURE 5: Modulus of elasticity of concrete with waste cellulose.

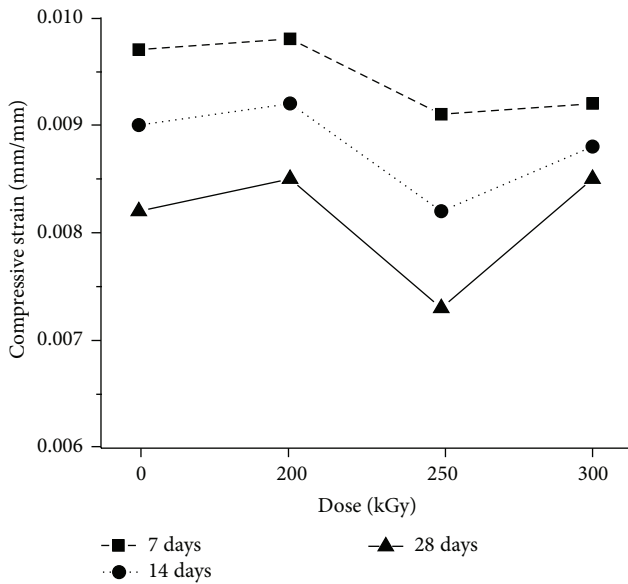


FIGURE 4: Compressive strain of concrete with waste cellulose at different irradiation doses.

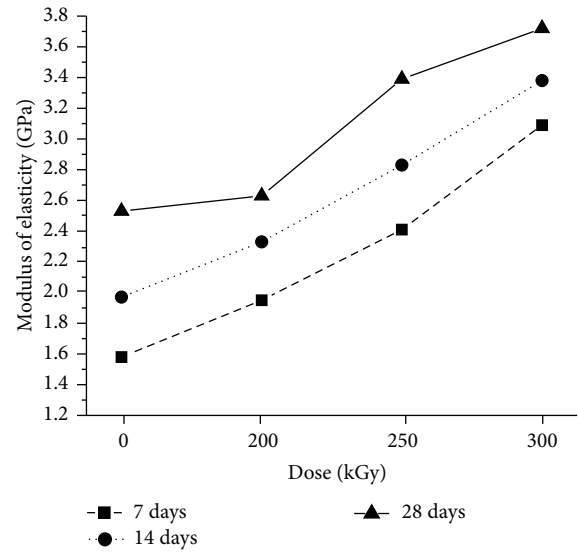


FIGURE 6: Modulus of elasticity of concrete with waste cellulose at different irradiation doses.

more waste cellulose concentration is added; (b) for each waste concentration, the values decrease according to curing time (Figure 3). The lowest value, 0.0043 mm/mm, is 116% minor with respect to compressive strain value of control concrete (without waste cellulose). Thus a hard concrete is produced when adding higher waste cellulose concentration.

For irradiated concrete a well-defined behavior is observed (Figure 4). The values show three stages: (a) in the first one the values increase at 200 kGy, (b) after they decrease at 250 kGy, and finally (c) they increase again at 300 kGy. The diminution at 250 kGy is 12% minor than those for control concrete.

3.3. *Modulus of Elasticity.* The moduli of elasticity values for concrete are shown in Figure 5. Depending on both parameters, waste cellulose concentration and curing time, different behaviors are observed. (a) For concrete with 7 days of curing time the values decrease according to the increase of waste cellulose too, being 35% minor when adding 7 wt% of waste cellulose; (b) for concrete with 14 days of curing time, the values are almost constant for any waste cellulose concentration; (c) for concrete with 28 days of curing time, the values diminish at 3 wt% of waste cellulose, and after increasing up to 7 wt% of waste cellulose, at this concentration the value is minor with respect to control

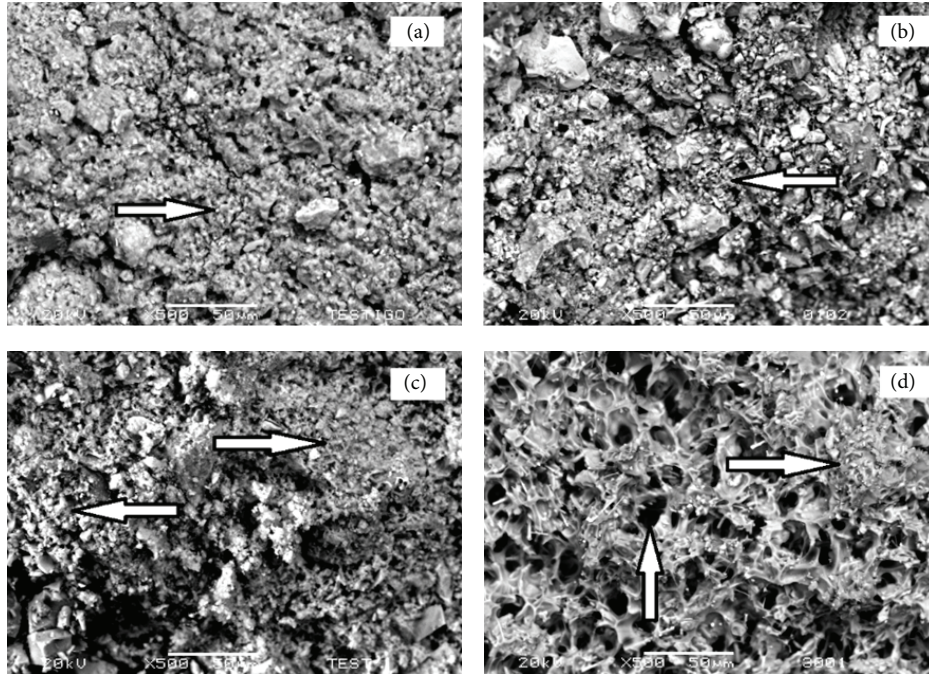


FIGURE 7: SEM images of fractured concrete: (a) nonirradiated; irradiated at (b) 200 kGy, (c) 250 kGy, and (d) 300 kGy.

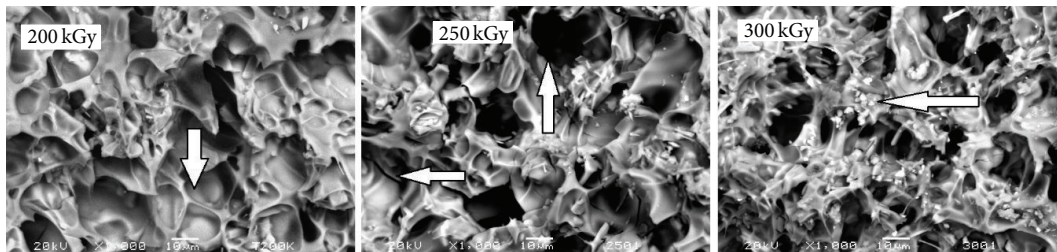


FIGURE 8: SEM images of irradiated cellulose at 200 kGy, 250 kGy, and 300 kGy.

concrete; and (d) for each waste cellulose concentration the values increase according to curing time increase.

In the case of irradiated concrete different behaviors are observed. (a) The values increase according to waste cellulose concentration increase. The highest value is observed for concrete with 28 days of curing time and irradiated at 300 kGy, which is 47% higher with respect to control concrete; (b) for each radiation dose the values increase according to curing time increasing (Figure 6). These results can be attributed to gamma irradiation effects on the waste cellulose. Improvement on modulus of elasticity values point out a predominant domain of cross-linking of polymer chains in cellulose. However, some shorter chains are produced which are water-soluble and in consequence increment on the solubility is done. In general terms, irradiated cellulose covers the sand particles; thus zone around them is affected by a stress concentration. Therefore, if the distance between particles is small enough, these zones join together and form a percolation network, which generate good adhesion between cement matrix and cellulose and in consequence increment in the modulus of elasticity is obtained.

The mechanical results can be related with morphological changes seen on the fractured zones of concrete specimens, as we see in Figure 7. For nonirradiated concrete a rough surface is shown (indicated by arrows) (Figure 7(a)); when applying 200 kGy of dose, the disperse particles are covered by irradiated cellulose (see arrow), as consequence of the cross-links of the polymer chains (Figure 7(b)). For higher dose, 250 kGy, the cellulose continues to form polymer films over the hydrating cement particles and thus interferes with the hydration process and thereby setting and hardening of cement (Figure 7(c)); finally at 300 kGy more evident is the presence of cellulose, through the cross-linked regions accompanied with larger quantities of voids in the interfacial zone (see arrows). Nevertheless strong bonds are progressively developed between cellulose and cement matrix (Figure 7(d)).

Figure 8 shows images of irradiated recycled cellulose obtained by Scanning Electron Microscopy (SEM). For irradiated cellulose at 200 kGy smooth and homogeneous surfaces (indicated by arrow) and some particles are seen. When increasing the radiation dose, at 250 kGy, some cracks

and more space between cellulose surfaces appear, giving an appearance of voids. Such modifications can be related with the main effects produced by gamma radiation: scission and cross-linking of molecular chains in cellulose. For higher dose, at 300 kGy, a higher number of dispersed particles, as well as rough surfaces, are observed.

4. Conclusions

Both waste cellulose concentration and gamma radiation are adequate tools for improvement of the mechanical properties of concrete, where sand is substituted by waste cellulose. In particular, compressive strength and modulus of elasticity values have an improvement of 45% and 47%, respectively, when adding 3 wt% of waste cellulose and applying 300 kGy of dose. Conversely, diminutions on the mechanical properties were seen for nonirradiated concrete. Through SEM images the influence of gamma radiation on waste cellulose and its effect on the mechanical properties of concrete was corroborated.

Conflict of Interests

The authors declare that none of them has a direct financial relationship with the commercial trademarks mentioned in this paper that might lead to a conflict of interests for any of the authors.

Acknowledgment

Financial support of the Autonomous University of the State of Mexico (UAEM), Toluca, by Grant UAEM 3408/2013M (Megaproyecto) is acknowledged.

References

- [1] C. Meyer, "Recycled materials in concrete," in *Developments in the Formulation and Reinforcement of Concrete*, S. Mindess, Ed., pp. 208–230, Woodhead Publishing, Cambridge, UK, 2009.
- [2] C. Meyer, "The economics of recycling in the US construction industry," in *Sustainable Construction Materials and Technologies*, Y.-M. Chun, P. Claisse, T. R. Naik, and E. Ganjian, Eds., pp. 509–513, Taylor & Francis, London, UK, 2007.
- [3] C. Barrera-Díaz, V. Varela-Guerrero, E. Cuevas-Yáñez, G. Martínez-Barrera, G. Roa-Morales, and M. A. García-Morales, "Use of recycled aluminum—polyethylene composite films as anodic electrodes for electrocoagulation of wastewater," *International Journal of Electrochemical Science*, vol. 9, no. 3, pp. 1034–1043, 2014.
- [4] M. Bentchikou, A. Guidoum, K. Scrivener, K. Silhadi, and S. Hanini, "Effect of recycled cellulose fibres on the properties of lightweight cement composite matrix," *Construction and Building Materials*, vol. 34, pp. 451–456, 2012.
- [5] A. Murathan, A. S. Murathan, M. Gürü, and M. Balbaşı, "Manufacturing low density boards from waste cardboards containing aluminium," *Materials and Design*, vol. 28, no. 7, pp. 2215–2217, 2007.
- [6] Z. N. Kalantar, M. R. Karim, and A. Mahrez, "A review of using waste and virgin polymer in pavement," *Construction and Building Materials*, vol. 33, pp. 55–62, 2012.
- [7] A. Korkmaz, J. Yanik, M. Brebu, and C. Vasile, "Pyrolysis of the tetra pak," *Waste Management*, vol. 29, no. 11, pp. 2836–2841, 2009.
- [8] H. Fujiwara, M. Maruoka, K. Koibuchi, and K. Fujita, "The application of paper sludge ash to extremely stiff consistency concrete product," in *Sustainable Construction Materials and Technologies*, Y.-M. Chun, P. Claisse, T. R. Naik, and E. Ganjian, Eds., pp. 303–311, Taylor & Francis, London, UK, 2007.
- [9] M. H. P. Gazineu, V. A. D. Santos, C. A. Hazin, W. E. D. Vasconcelos, and C. C. Dantas, "Production of polymer-plaster composite by gamma irradiation," *Progress in Nuclear Energy*, vol. 53, no. 8, pp. 1140–1144, 2011.
- [10] A. K. Bledzki and J. Gassan, "Composites reinforced with cellulose based fibres," *Progress in Polymer Science*, vol. 24, no. 2, pp. 221–274, 1999.
- [11] M. Åkerholm, B. Hinterstoisser, and L. Salmén, "Characterization of the crystalline structure of cellulose using static and dynamic FT-IR spectroscopy," *Carbohydrate Research*, vol. 339, no. 3, pp. 569–578, 2004.
- [12] E. Gümüşkaya, M. Usta, and H. Kirci, "The effects of various pulping conditions on crystalline structure of cellulose in cotton linters," *Polymer Degradation and Stability*, vol. 81, no. 3, pp. 559–564, 2003.
- [13] G. Martínez-Barrera, C. Menchaca Campos, and F. Ureña-Nuñez, "Gamma radiation as a novel technology for development of new generation concrete," in *Gamma Radiation*, F. Adrovic, Ed., pp. 91–114, InTech, Rijeka, Croatia, 2012.
- [14] L. I. Avila-Córdoba, G. Martínez-Barrera, F. Ureña-Nuñez, and C. E. Barrera-Díaz, "Electron microscopy for the evaluation of concrete surfaces modified by gamma radiation," in *Current Microscopy Contributions to Advances in Science and Technology*, A. Méndez-Vilas, Ed., pp. 1115–1122, Formatex Research Center, Badajoz, Spain, 2012.
- [15] G. Martínez-Barrera and W. Brostow, "Fiber-reinforced polymer concrete: property improvement by gamma irradiation," in *Gamma Radiation Effects on Polymeric Materials and Its Applications*, C. Barrera-Díaz and G. Martínez-Barrera, Eds., pp. 27–44, Research Signpost, Kerala, India, 2009.
- [16] G. Martínez-Barrera, C. Menchaca-Campos, C. E. Barrera-Díaz, and L. I. Avila-Cordoba, "Recent developments in polymer recycling," in *Gamma Rays: Technology, Applications and Health Implications*, I. Bikit, Ed., pp. 237–256, Nova Science Publishers, Hauppauge, NY, USA, 2013.
- [17] N. A. El-Faramawy and F. I. El-Hosiny, "The effect of the autoclaving process and addition of silica fume on portland cement in shielding gamma radiation," *Radiation Measurements*, vol. 29, no. 6, pp. 619–623, 1998.
- [18] M. Patel, P. R. Morrell, J. J. Murphy, A. Skinner, and R. S. Maxwell, "Gamma radiation induced effects on silica and on silica-polymer interfacial interactions in filled polysiloxane rubber," *Polymer Degradation and Stability*, vol. 91, no. 2, pp. 406–413, 2006.
- [19] R. Despot, M. Hasan, A. O. Rapp et al., "Changes in selected properties of wood caused by gamma radiation," in *Gamma Radiation*, F. Adrovic, Ed., pp. 281–304, InTech, Rijeka, Croatia, 2012.